HAL
open science

Flow in millimetric-channel : numerical and experimental study

Jafar Al-Muhammad

To cite this version:

Jafar Al-Muhammad. Flow in millimetric-channel : numerical and experimental study. Fluid mechanics [physics.class-ph]. Ecole Centrale Marseille, 2016. English. NNT : 2016ECDM0013 . tel-01531349

HAL Id: tel-01531349

https://theses.hal.science/tel-01531349v1

Submitted on 1 Jun 2017

HAL is a multi-disciplinary open access archive for the deposit and dissemination of scientific research documents, whether they are published or not. The documents may come from teaching and research institutions in France or abroad, or from public or private research centers.

L'archive ouverte pluridisciplinaire **HAL**, est destinée au dépôt et à la diffusion de documents scientifiques de niveau recherche, publiés ou non, émanant des établissements d'enseignement et de recherche français ou étrangers, des laboratoires publics ou privés.

École Doctorale : Sciences pour l'ingénieur : Mécanique, Physique, Micro et Nanoélectronique (ED353)

Laboratoires: IRSTEA UMR G-eau et IRPHE

THÈSE DE DOCTORAT

pour obtenir le grade de

DOCTEUR de l'ÉCOLE CENTRALE de MARSEILLE

Discipline : Mécanique et Physique des Fluides

Écoulement dans un canal millimétrique : étude numérique et expérimentale

Flow in millimetric-channel: numerical and experimental study

par

AL-MUHAMMAD Jafar

Directeur de thèse : ANSELMET Fabien

Soutenue le 8 décembre 2016

devant le jury composé de :

AIT MOUHEB Nassim	Chargé de recherche, IRSTEA UMR G-EAU	Invité
AMIELH Muriel	Chargée de recherche, CNRS de Marseille	Examinatrice
ANSELMET Fabien	Professeur à l'École Centrale de Marseille	Directeur de thèse
DANAILA Luminita	Professeur à l'Université de Rouen	Président du jury
ROÏG Véronique	Professeur à l'INP de Toulouse, IMFT	Rapporteur
SOLLIEC Camille	Maître de recherche, Ecole des Mines de Nantes	Rapporteur
TOMAS Séverine	Ingénieur de recherche, IRSTEA UMR G-EAU	Examinatrice

ACKNOWLEDGEMENTS

There are so many people that I would like to thank. Without them, the success of this research would not be possible.

First and foremost, I thank the Aleppo university and Irstea institute which both participated to fund three years of research.

I would like to express my sincerest gratitude to Professor Fabien ANSELMET, my academic advisor, and Dr Séverine TOMAS, my co-advisor at Irstea Institute, for their invaluable advice and guidance in my study and research. Their continuous encouragement and inspiration always helped me break through the difficulties I encountered in the research work, and Dr Muriel AMIELH and Dr Nassim AIT MOUHEB for their investment in this thesis. Thanks to them for their advice, their availability and the confidence they have given me throughout these four years.

I also thank my dissertation committee members Professor Véronique ROÏG and Dr Camille SOLLIEC, who agreed to make reports on this thesis, and professor Luminita DANAILA for accepting to evaluate this thesis, for their in-sightful comments and suggestions from their careful review of my research work and for their participation in the jury. I also thank Dr Jean-Jacques LASSERRE for the valuable advice he gave me for the setting of experimental manipulations.

This thesis was conducted at IRSTEA of Montpellier, in Plateforme de Recherche et d'expérimentation en Sciences et Technologies d'Irrigation, managed by the UMR G-EAU. I thank Bruno MOLLE, laboratory manager, for hosting me in his team. I thank Dominique ROLLIN , Sami BOUARFA and Olivier BARRETEAU, the heads of UMR G-eau and Eaux department at IRSTEA. My thanks also go to all members of Irstea and irrigation team for their kindness, their availability and their good humor: Patrice GARIN, Gilles BELAUD, Bruno CHEVIRON, Claire SERRA-WITTLING, Patrick ROSIQUE, Augustin LUXIN, marie-claude LAFFORGUE, Cyril DEJEAN, Carmen RENAUDEAU, Sophie LECLERC, Chantal MIRALES and Christine TAILLEFERIE. I would thank David TANG, the formidable technician in Irstea, who followed me throughout my experiments and helped me a lot for the development of experimental protocols. I do not forget Souha GAMRI, Nancy RIZK, Rami ALBASHA, Francisco FELIS, Yassin ELAMRI, Nour CHALGHOUMI, Claire RICHERT, Hind OUBANAS, Claire DEDIEU and Jean BORGARINO. I would also like to thank the team of Aix en Provence: Laurent HUET, Jacques GRANIER, Mathieu AUDOUARD, Pascal DI MAIOLO, Annie BORDAZ, Carole ISBÉRIE, Julien DEBORDE and Christophe STÉVENIN.

I am also very grateful to all the people and friends who gave me help and convenience during my PhD study. And thank finally all people interested in my work, hoping that they can find in my report useful explanations for their own work.

To my family

My deepest thanks go to my parents. Throughout my studies, they have always supported, encouraged and assisted me. They were able to give me every chance to succeed. Let they find, in the achievement of this work, the culmination of their efforts and accept my affectionate gratitude. They encouraged me to go to France to realize my dream of being a doctor in mechanical engineering and enrich my research experiences, but they never thought that this trip would last and the long distance between us would disrupt our lives because of the war in our country. I hope I have the occasion to see them safely.

I thank my family and especially my wife, Soumaya, for her support and encouragement during my four years' study and research at École Centrale de Marseille. I would not be able to concentrate on the research without the time and energy she spent selflessly on my family. I ended the years of the thesis with the good news of my life, the birth of my little soul Lina August 13, 2016 that filled our life together in full joy and happiness to whom I dedicate this thesis.

I also thank my brothers and my sister I've not seen for six years and I wish I will see soon. I dedicate this modest work to the children of my brother. I thank my uncles, my aunts, my grandfathers and my grandmothers. my father and my mother and my brothers, my sisters in law.

Also thanks to my family and friends in Syria who followed from far away the thesis but were there to change my mind.

TABLE OF CONTENTS

ACKNOWLEDGEMENTS **3**

DEDICATION **4**

TABLE OF CONTENTS **5**

Abstract **9**

Nomenclature **11**

Introduction **15**

I Context and objectives **17**

1 Challenges related to irrigation **21**
1.1 Irrigation and water consumption 21
1.2 Irrigation techniques 23
1.3 Clogging problems in micro-irrigation systems 28
1.4 Management of clogging problems 30
1.5 Conclusion: Emitter improvement 31

2 Labyrinth-channel hydrodynamics and thesis objectives **33**
2.1 Flow regime 33
2.2 Numerical analysis of the flow 34
2.3 Experimental analysis of the flow 35
2.4 Emitter design and geometry optimization objectives 35
2.5 Conclusion and thesis objectives 39

II Experimental methodology **41**

1 Experimental apparatus and conditions **45**
1.1 Introduction 45
1.2 Micro-Particle Image Velocimetry (micro-PIV) 45
1.3 Studied emitter and its geometry 47
1.4 Hydraulic equipments 49
1.5 Tracer particles 51
1.6 Flow Diagnostics 53
1.7 Experimental conditions 55
1.8 Pressure-discharge curves 55

2 Experimental settings **57**

2.1 Time delays between laser pulses . . . 57
2.2 Prototype positioning and image calibration . . . 59
2.3 Acquisition protocol . . . 60
2.4 Data analysis . . . 60
2.5 Data treatment . . . 62
2.6 Uncertainty analysis . . . 67
2.7 Conclusion . . . 70

III Numerical modelling **71**

1 Model presentation **75**
1.1 The equations of fluid motion . . . 75
1.2 Reynolds averaged equations . . . 75
1.3 Boussinesq hypothesis . . . 76
1.4 Spalart–Allmaras model . . . 77
1.5 $k - \epsilon$ models . . . 79
1.6 Reynolds stress model (RSM) . . . 81
1.7 Wall treatment . . . 83

2 Numerical resolution **89**
2.1 Geometry of the study . . . 89
2.2 Meshing . . . 90
2.3 Boundary conditions . . . 91
2.4 Solution methods . . . 92
2.5 Numerical calculation of the pressure losses . . . 95
2.6 Conclusion . . . 96

IV Results and discussion **97**

1 Pressure loss and discharge **101**
1.1 Introduction . . . 101
1.2 The pressure loss and discharge . . . 101
1.3 Geometric calculation of pressure losses . . . 103
1.4 Numerical calculation of pressure losses . . . 106
1.5 Conclusion . . . 108

2 Analysis of the labyrinth-channel flow **111**
2.1 Introduction . . . 111
2.2 Experimental visualization of instantaneous velocity fields . . . 112
2.3 Inlet flow . . . 113
2.4 Outlet flow . . . 121
2.5 Flow characterization inside the baffles . . . 123
2.6 Reynolds stresses . . . 131
2.7 Axial development of the flow . . . 137
2.8 Vertical evolution of the flow . . . 139
2.9 Turbulent kinetic energy . . . 140
2.10 Flow isotropy . . . 145
2.11 Turbulence properties . . . 146
2.12 Swirl detection and analysis . . . 148
2.13 Conclusion . . . 154

Conclusion and perspectives **157**

V Présentation en français **159**

Résumé **163**

1 Introduction générale, matériels et méthodes **165**
1.1 Introduction 165
1.2 Méthodologie expérimentale 166
1.3 Approche numérique 171
1.4 La résolution numérique 174

2 Résultats et conclusion générale **177**
2.1 Pertes de charge dans le labyrinthe 177
2.2 Caractérisation de l'écoulement dans le labyrinthe 179
2.3 Le développement axial de l'écoulement 183
2.4 L'évolution verticale de l'écoulement 184
2.5 Méthodes avancées de détection de vorticité 185
2.6 Conclusion générale et perspectives 188

Appendix A **191**
A.1 Optical system 191
A.2 Standard Wall function 194
A.3 Non-equilibrium wall function 195
A.4 Spalart-Allmaras: k and ϵ 196
A.5 RSM: supplementary informations 196
A.6 Image recording devices 197
A.7 Camera 197
A.8 Treatment method 198
A.9 Cross correlation 199
A.10 Comparative study between $1\mu m$ and $5\mu m$ particles diameters 200
A.11 Diagram 203
A.12 Friction factor k_f 203

Bibliography **205**

Abstract

In the present context of increasing water scarcity, a better water use efficiency is essential to maintain a sustainable economical growth. Moreover, water use efficiency covers also important environmental and social issues. Micro-irrigation system has the best water efficiency, nevertheless, its use is not much widespread. In the world, this system covers only 3% of land irrigated against 4% in France, as this system is sensitive to clogging, which increases the installation cost.

The baffle-fitted labyrinth-channel is largely used in micro-irrigation systems. The existing baffles, which play an important role for generating pressure losses and ensure the flow regulation on the irrigation network, produce vorticities where the velocity is low or zero. These vorticities favor the deposition of particles or other biochemical development causing emitter clogging. Flow topology characterization in the labyrinth-channel of emitter must be described to analyze emitter clogging sensibility which drastically reduces its performance.

Micro-PIV experiments, using $1\mu m$ particles, are conducted on ten-pattern repeating baffles to characterize the labyrinth-channel flow and to analyze regions which can be sensitive to clogging. An emitter works with a weak flow rate, and the labyrinth-channel cross-section is about $1\ mm^2$. Reynolds number varies from 400 to 800. So, this experimental investigation allows analyzing the flow regime and its influence. A treatment algorithm is developed to get the mean and fluctuating velocities. Advanced swirl analysis method is adapted to precisely detect the vorticity. Particular attention is focused on the technique acquisition and on pressure losses curves accuracy in the labyrinth-channel flow since this curve represents the emitter global performance.

Several turbulent models, implemented in ANSYS/Fluent, are used to perform modelling of the labyrinth-channel geometry. The micro-PIV and modeling results comparisons are presented in order to validate numerical model. The global objective of this manuscript is to identify the best model which allows to predict and analyze the sensitive areas in order to reduce them thanks to geometry optimization.

keywords

Clogging, CFD, micro-irrigation, micro-PIV, turbulence and swirl zone.

Nomenclature

Latin alphabet ——————————————————————-

A_{area}	Labyrinth-channel area	$[m^2]$
A_c	Cross-section area	$[m^2]$
A_{wall}	Wall area in 3D	$[m^2]$
A_μ, A_ϵ	Constants for Enhanced wall treatment	
C	Degree of pixel locking	
$\mathcal{C}$	Correlation coefficient	
C_f	Skin-friction coefficient	
C_ℓ, C_ℓ^*	Constants for Enhanced wall treatment	
C_p	Seeding particle concentration	[particle.m^{-3}]
C^+, E	Constants of the wall-law	
C_1, C_2 and C_s	Constants of RSM model	
C_{b1}, C_{b2}, $C_{\nu 1}$		
C_{w1}, C_{w2} and C_{w3}	Constants of Spalart-Allmaras model	
$C_{1\epsilon}$, $C_{2\epsilon}$ and C_μ	Constants of $k-\epsilon$ model	
d_{depth}	Depth of Labyrinth-channel	$[m]$
d_{inlet}	Inlet width of Labyrinth-channel	$[m]$
D_h	Hydraulic diameter	$[m]$
d_{outlet}	Outlet width of Labyrinth-channel	$[m]$
d_p	Particle diameter	$[m]$
D and E	Source terms of $k-\epsilon$ model	$[kg.m^{-1}.s^{-3}]$
f_1, f_2 and f_μ	Damping functions for Low-Reynolds $k-\epsilon$ model	
f_D	Darcy friction factor	
$f_{\nu 1}$, $f_{\nu 2}$ and f_w	Viscous damping functions	
f_ν,	Viscous damping function	
fr	Frequency	[Hz]
g	Gravity acceleration	$[m.s^{-2}]$
G_k	Generation of turbulence kinetic energy	$[kg.m^{-1}.s^{-3}]$
G_ν	Production of turbulent viscosity for Spalart-Allmaras model	$[kg.m^{-1}.s^{-2}]$
G_χ	Generation of turbulence viscosity	$[kg.m^{-1}.s^{-3}]$
I	Turbulent intensity	
k	Turbulent kinetic energy	$[m^2.s^{-2}]$
k_d	Discharge coefficient	
L_e	Turbulent entrance-length	$[m]$
ℓ	Pipe length	$[m]$
ℓ	Length scale	$[m]$
ℓ_{mean}	Mean width of Labyrinth-channel	$[m]$
ℓ_μ	Characteristic length scale	$[m]$
ℓ_ϵ	Characteristic length scale	$[m]$
$\dot{m}$	mass flow rate	$[kg.s^{-1}]$
M	Magnification factor	
N	Total image number	
N_v	Valid image number	
N_w	Interrogation window number	
p	Instantaneous pressure	$[Pa]$
$\overline{p}$	Mean pressure	$[Pa]$
p'	Fluctuating pressure	$[Pa]$
p_w	Wetted perimeter	$[m]$

q	Emitter discharge	$[m^3.s^{-1}]$ or $[\ell.h^{-1}]$
q_1	Flowrate	$[ml.min^{-1}]$
Q_v	Volumetric flow rate	$[m^3.s^{-1}]$
R and R_p	Residues	
Re	Reynolds number, $Re = U_m D_h/\nu$	
Re_y	Reynolds number based on y, $Re_y = \frac{\rho y\sqrt{k}}{\mu}$	
Re_t	Turbulent Reynolds number, $Re_t = \frac{\rho k^2}{\mu\epsilon}$	
Re_τ	Reynolds number based on the friction velocity, $Re_\tau = \frac{u_\tau D_h}{\nu}$	
Re_ϵ	Reynolds number based on ϵ, $Re_\epsilon = \frac{\rho(\mu\epsilon/\rho)^{1/4}y}{\mu}$	
S_f	Scale factor	
S	Modulus of the mean rate-of-strain tensor	$[s^{-1}]$
$\tilde{S}$	Identical to S for Spalart-allmaras model	$[s^{-1}]$
S_{ij}	Mean strain rate tensor	$[s^{-1}]$
St	Stokes number	
t	Time	$[s]$
T	Temperature	$[^oC]$
u_i, u_j	Instantaneous velocity	$[m.s^{-1}]$
$\overline{u_i}, \overline{u_j}$	Mean velocity	$[m.s^{-1}]$
u'_i, u'_j	Fluctuating velocity	$[m.s^{-1}]$
$\lvert u\rvert$, $\lvert\overline{u}\rvert$	Instantaneous and mean velocity modulus	$[m.s^{-1}]$
U_g	Sedimentation velocity	$[m.s^{-1}]$
U_m	Bulk velocity	$[m.s^{-1}]$
U	Flow velocity	$[m.s^{-1}]$
u^+	Dimensionless velocity	
u_τ	Friction velocity	$[m.s^{-1}]$
$\overline{u'^2_\tau}$, $\overline{u'^2_\eta}$, $\overline{u'^2_\lambda}$	Reynolds stresses at the wall adjacent cell	$[m^2.s^{-2}]$
V	Volume of Labyrinth-channel fluid	$[m^3]$
x	Emitter exponent	
x_i, x_j	Point coordinates	
y	Distance normal to the wall (general situation) or distance along the flow direction in the entrance region of the labyrinth-channel	$[m]$
y^+	Wall unit, $y^+ = \frac{u_\tau \rho y}{\mu}$	
$y^\star$	Wall unit defined by Eq.A.12	
Y_ν	Destruction term for S-A model	

Greek alphabet

α	Constant depending on geometry dimensions	
β	Constant for RNG $k-\epsilon$ model	
δ	Distance	$[m]$
δ_{ij}	Kronecker symbol	
δ_ν	Viscous length scale	$[m]$
ΔP	Working pressure head	$[bar]$
Δp	Pressure loss	$[Pa]$
Δt	Time delays between laser pulses	$[s]$
Δx	Window size used in micro-PIV	$[m]$
Δz	Thickness of the laser sheet	$[m]$
ϵ	Dissipation of turbulence kinetic energy	$[m^2.s^{-3}]$
$\bar{\epsilon}$	Dissipation due to the mean velocity gradient	$[m^2.s^{-3}]$

η	Kolmogorov length scale	$[m]$
η and η_0	Coefficients for RNG $k-\epsilon$ model	
κ	Von kárman constant	
$\lambda_{1,2,3}$	Eigenvalues of tensor : $A = S^2 + \Omega^2$	
λ_{abs}, λ_{em}	Absorption and emission wavelengths	$[nm]$
μ	Dynamic fluid viscosity	$[kg.m^{-1}.s^{-1}]$
μ_t	Turbulence viscosity	$[kg.m^{-1}.s^{-1}]$
ν	Kinematic viscosity	$[m^2.s^{-1}]$
ν	Identical to kinematic viscosity for Spalart-allmaras model	$[m^2.s^{-1}]$
$\tilde{\nu}$	Turbulent kinematic viscosity	$[m^2.s^{-1}]$
ρ	Fluid density	$[kg.m^{-3}]$
ρ_p	Particle density	$[kg.m^{-3}]$
σ_k and σ_ϵ	Turbulent Prandtl numbers for k and ϵ	
$\sigma_{\tilde{\nu}}$	Turbulent Prandtl numbers for $\tilde{\nu}$	
τ_{ij}	Viscous stress tensor	$[N.m^{-2}]$
τ_p	Characteristic time of a particle	$[s]$
τ_w	Wall shear stress	$[N.m^{-2}]$
τ_k	Characteristic time of the flow or Kolmogorov time scale	$[s]$
Φ	Dissipation rate	$[Pa]$
$\overline{\phi}$	Dissipation rate due to the turbulent fluctuations	$[Pa]$
$\overline{\varphi}$	Dissipation rate due to the overall movement fluctuations	$[Pa]$
ϕ_{max}	Maximum angle for the mesh	
ϕ_{min}	Minimum angle for the mesh	
φ	Minor head loss coefficient	
χ	Coefficient for Spalart-Allmaras model	
ξ	Pressure loss coefficient	
ω	Vorticity	$[s^{-1}]$
Ω_{ij}	Mean rate-of-rotation tensor	$[s^{-1}]$

Abbreviations

exp	Exponential function
tanh	Hyperpolic tangent
S-A	Spalart-Allmaras model
AKN	Abe, Kondoh and Nagano model as low-Reynolds number $k-\epsilon$ model
Abid	Abid model as low-Reynolds number $k-\epsilon$ model
CHC	Chang, Hsieh and Chen model as low-Reynolds number $k-\epsilon$ model
LS	Launder and Sharma model as low-Reynolds number $k-\epsilon$ model
RNG	Re-Normalization Group method as high-Reynolds number $k-\epsilon$ model
RSM	Reynolds stress model

Acronymes

FAO	Food and Agriculture Organization
GR	Industrial name, not an acronyme
IRSTEA	Institut national de Recherche en Sciences et Technologies pour l'Environnement et l'Agriculture
Micro-PIV	Micro Particle Image Velocimetry

Introduction

Micro-irrigation is a pressurized irrigation system which distributes water by emitters near the roots of the plants. Despite many advantages of this system such as high water efficiency, water saving and labor reduction, the percentage of use is weak in comparison with the other methods. In this technique, emitters are the most important and critical components. Emitters diameter is of the order of $1\ mm$, so they can be easily clogged by physical particles which are not captured by filtering systems or by biochemical development. As a result, the irrigation uniformity is perturbed and the investment cost is increased. Thus, the main drawback of this technique is clogging. This clogging is related to flow. Flow analysis allows to identify and to avoid as much as possible the areas vulnerable to clogging. The global objective of this study is to understand and to analyse the flow in the labyrinth-channel. This step is essential to optimize the labyrinth-channel geometry and to improve the geometry emitter which allows to have an anti-clogging emitter.

This manuscript is divided into four parts.

The first part is dedicated to the presentation of the overall context in which the study takes place, with emphasis the importance of micro irrigation use and the drawbacks associated with clogging in general and physical clogging in particular. Clogging is influenced by the labyrinth-channel geometry. Therefore, a comparative study about the geometry influence is presented from the litterature. The geometry, which is supposed to have the best performance and to be the best in view of avoiding clogging, is chosen to perform the numerical and experimental study. The optimization of this geometry will help to have anti-clogging emitter with high performance.

The second part is devoted to experimental methodology. The first chapter of this part presents the experimental apparatus and conditions. Labyrinth-channel designing and manufacturing are explained. The verification of the experimental conditions and the appropriate tools to have a better acquisition are presented. The micro-PIV principle is the subject of the second chapter. Experimental settings in relation with this technique are detailed. Finally, micro-PIV errors are also analysed.

The third part is devoted to numerical modelling. In the literature, the choice of turbulent model differs from one study to another. A presentation of the turbulent models is introduced in the first chapter. Several turbulent models such as Spalart-Allmaras, low-Reynolds $k-\epsilon$, high-Reynolds $k-\epsilon$ and RSM models are detailed. The advantage of each model is discussed. Then, the modelling of the near wall region which is an important factor to better predict the flow in this region is approached. The different functions used to model the flow in this region are presented and detailed. Wall boundary conditions are, also, explained. The numerical application of these models is presented in the second chapter. The different steps to perform the modelling begin by the geometry design in 2D and 3D. Mesh creation is an important issue to obtain good convergence results. A new method to calculate the pressure drop based on the numerical results is demonstrated and developed. This method allows to know and determine all the processes which contribute to pressure drop.

The fourth part deals with the overall results. Firstly, the pressure-discharge curve, which is the key of the emitter performance, is presented. A comparative study between the models used in the study is presented and discussed. The experimental and numerical pressure drop results are compared to those obtained by the pressure drop due to the labyrinth-channel geometry. The later is calculated from the formula developed by Zhang et al. (2011) [112]. The last chapter of this part includes the mean and fluc-

tuating second-order moments velocities comparison between experimental and numerical approaches. This study allows to validate the numerical results and to determine the best model which will be advised to use thereafter in geometry optimization. A detailed analysis at the inlet is discussed and compared with other studies to determine the flow regime. Then, analyses are performed at the outlet to determine the influence of baffle number on the outlet condition. A comparison between the flow characteristics along the different baffles is conducted to detemine whether the flow varies from one baffle to the other. A deep analysis in the first three baffles is performed. Swirl analysis and advanced detection methods are, then, introduced and detailed in order to identify the swirl zone and to compare with the streamlines fields obtained previously. Some turbulence properties are also discussed in the different baffles.

This manuscript ends with a general conclusion on the experimental and numerical results and perspectives for future work.

Part I

Context and objectives

Table of Contents

1 Challenges related to irrigation **21**
1.1 Irrigation and water consumption . . . 21
1.1.1 Water consumption and water resources deficit in the world . . . 21
1.1.2 The agricultural area in the world . . . 22
1.2 Irrigation techniques . . . 23
1.2.1 Surface irrigation . . . 24
1.2.2 Sprinkler irrigation . . . 25
1.2.3 Micro-irrigation . . . 25
1.3 Clogging problems in micro-irrigation systems . . . 28
1.3.1 Biological clogging . . . 29
1.3.2 Chemical clogging . . . 29
1.3.3 Physical clogging . . . 29
1.4 Management of clogging problems . . . 30
1.4.1 Water quality . . . 30
1.4.2 Filtration . . . 31
1.4.3 Chemical treatment . . . 31
1.5 Conclusion: Emitter improvement . . . 31

2 Labyrinth-channel hydrodynamics and thesis objectives **33**
2.1 Flow regime . . . 33
2.2 Numerical analysis of the flow . . . 34
2.3 Experimental analysis of the flow . . . 35
2.4 Emitter design and geometry optimization objectives . . . 35
2.4.1 Influence of labyrinth-channel geometry . . . 35
2.4.2 Geometry optimization . . . 38
2.5 Conclusion and thesis objectives . . . 39

Chapter 1

Challenges related to irrigation

1.1 Irrigation and water consumption

The micro-irrigation technique is an important practice to reduce the water quantity consumed in irrigated agriculture. The development of this system is necessary in view of the challenge associated with the water deficit and population growth. Presently, this irrigation system is little used, depending of countries around the world, in comparison with surface irrigation; nevertheless, its improvement should allow it to be more used by farmers.

1.1.1 Water consumption and water resources deficit in the world

Obviously, irrigation is the activity that mobilizes the largest volumes of water. Worldwide, 70% of the water withdrawn is used for irrigation, 20% is for the industry and the remaining 10% is used by households. This percentage varies from one continent to another. The regional variations are significant: 32.4% of the water withdrawn are for agriculture in Europe against 84.1% in Africa and 87.6% in the Middle East (MAFF)[1] in 2012 [1]. In France, it is the part which consumes a major part of the water withdrawn: 48% of the volumes consumed against 24% for households. In summer, this consumption can reach 79%. This can lead to restrictions between activity domains which use water (agricultural, industrial, energy and households) (Fig.I.1.1).

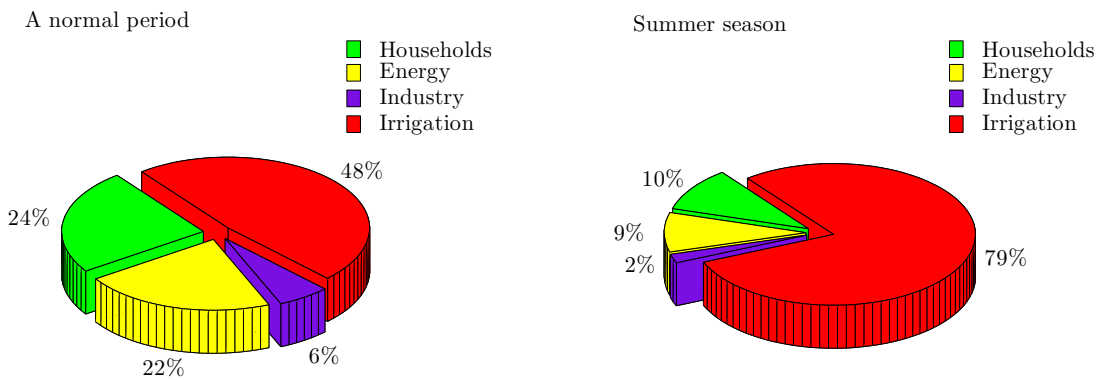

Figure I.1.1: Water consumption in France
- source : Agence de l'Eau - 2010

Access to water worldwide is a concern because of the reduction in available water resources

[1]Ministry of Agriculture, Food and Forestry in France. Ministère de l'agriculture, de l'agroalimentaire et de la forêt

(Fig.I.1.2). Water availability refers to the volume of water in the rivers compared with the amount of water we are using. This indicator is derived by calculating the ratio of water demand to water availability at the sub-drainage area scale on an annual basis. This diminution is related to the over-exploitation of water resources and the pollution by human activities. The poor management of water is one of major origin of this problem adding to the other origins such as the population growing and climate change. The rates of lowering water availability depend on two factors: social-economic development of the countries included in the region and climatic conditions of the region (Shiklimanov, 2000)[96] . However, better irrigation management could reduce this demand.

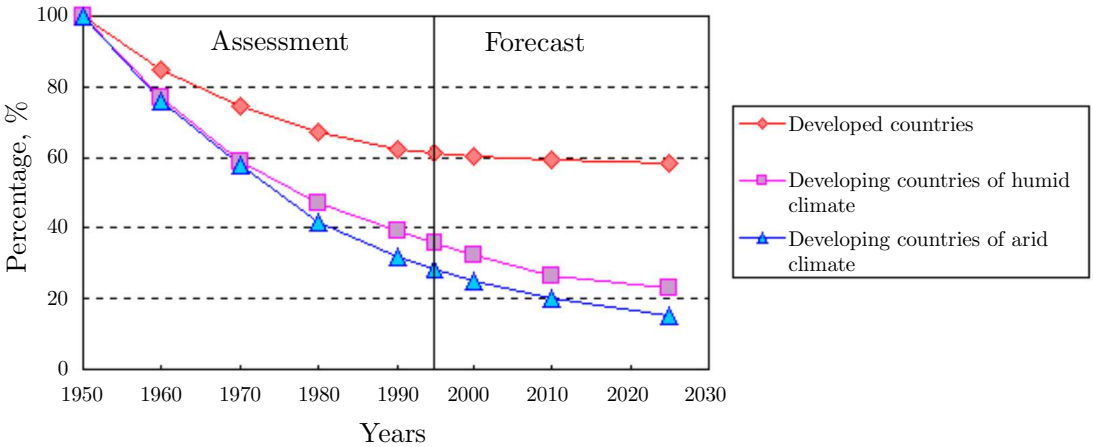

Figure I.1.2: Water availability - source FAO - 2010

1.1.2 The agricultural area in the world

The land in the world is limited:130 billions km^2 (The World Bank 2014). Globally, only one third of the land area is devoted to agricultural use. In 2011, it was about 38.5% of the total land area (FAO [2] 2011) (Fig.I.1.3). As the population is growing, we need to increase the percentage of agricultural land to meet the needs of everyone. Nevertheless, the entire agricultural land is not equipped with irrigation systems. Only 6.5% of agricultural area is equipped for irrigation according to the last data published by FAO 2011.

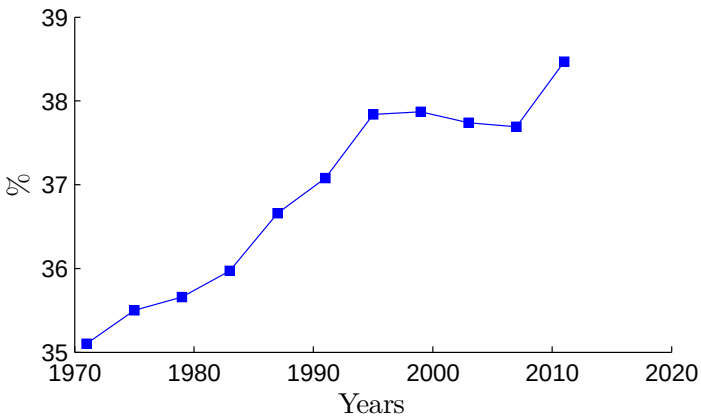

Figure I.1.3: Agricultural area as a % of land area
- source : FAO - 2011

[2]Food and Agriculture Organization of the United Nations

From 1961 to 2009, the cultivated area, globally, has increased by 12%, while agricultural production has increased by a factor of 2.5 to 3. With the population growth, the land area cultivated per person decreased to less than 0.25 ha (Fig.I.1.4) (FAO). Irrigated area takes part in 40% of world production (with a productivity 2.7 times higher than that of the lands watered by the rain). From today to 2050, an increase of 80% in agricultural production should result in a productivity improvement on land. Irrigation should, therefore, play a more strategic role. Irrigation is an important and essential activity to increase the food yields (Chengappa et al., 2007)[28] . This technique has been largely developed since the 1960s (Fig.I.1.5). This percentage needs to be even more increased in order to reach the world objective in food satisfaction. In France, land equipped [3] with irrigation systems is 2706×10^3 ha which amounts 9.0% of agricultural land area which is about 53.8% of total land area (Fao 2015).

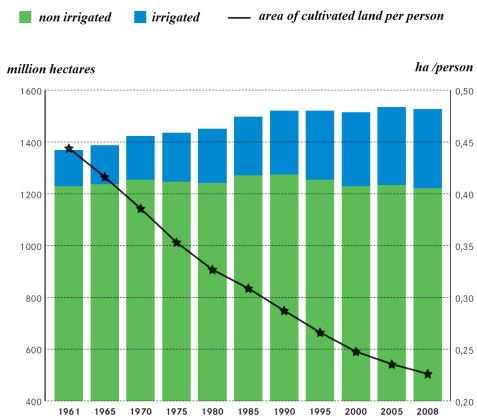

Figure I.1.4: Evolution of irrigated and non-irrigated cultivated land - source FAO - 2008 (extracted from [1])

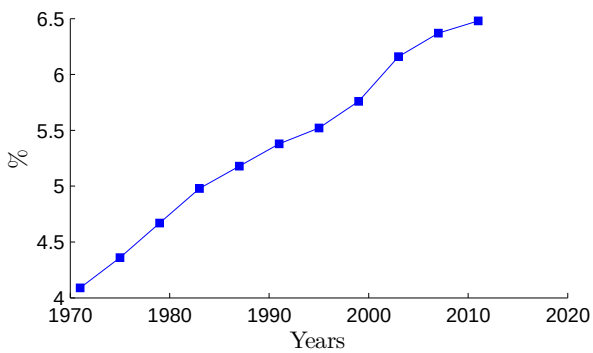

Figure I.1.5: Area equipped for irrigation as a % of agricultural area - source : FAO - 2011

1.2 Irrigation techniques

The best management, the best practice and the adoption of new techniques are required to preserve water resources and increase water efficiency [4]. This can be achieved thanks to three ways: better control of the water use, improving the performance of irrigation materials and finding alternative resources such as wastewater reuse. Irrigation systems are generally classified into two categories: surface

[3]It includes areas equipped for full control irrigation, equipped lowland areas, and areas equipped for spate irrigation. It does not include non-equipped cultivated wetlands and inland valley bottoms or non-equipped flood recession cropping areas.

[4]Water efficiency is a tool of water conservation that results in more efficient water use and thus reduces water demand. Water efficiency differs from water conservation in that it focuses on reducing waste (Vickers, 2002)[100].

irrigation systems and pressurized irrigation systems (sprinkler and micro-irrigation). The choice of one system or the other depends on several parameters: the cost of installation, technical capacity and the conditions of the land and culture. Worldwide, micro-irrigation and sprinkler irrigation account for about 20% of the total area equipped for irrigation. In France, sprinkler irrigation is the most widespread. It is practiced on 91% of irrigated area according to Fao data (Fig.I.1.6).

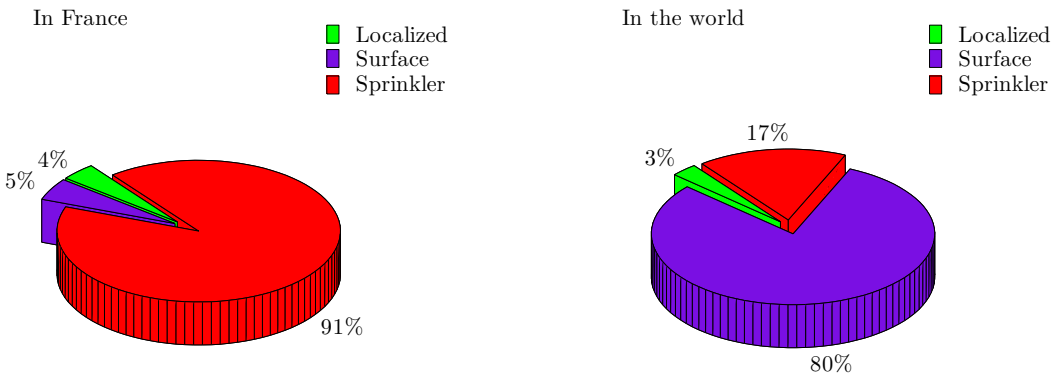

Figure I.1.6: Irrigation systems (by irrigated area)
- source : Fao - 2007

1.2.1 Surface irrigation

With this technique, water moves across the surface of agricultural lands in order to wet it and infiltrate into the soil. The land can be subdivided into furrow, border ship or basin with slight slope Fig.I.1.7(a). The distribution of water is ensured by the land topography and the hydraulic properties of soil and labor force.

Advantages of surface irrigation are to include lower initial investment of equipment and lower pumping costs per m^3 of water pumped. Disadvantages include larger labor costs and lower application efficiency (about 30%(62%) for undeveloped (developed) gravity system) compared to sprinkler and subsurface drip irrigation (for more detail about efficiency terms used in irrigation, see Lankford et al. (2004)[62]). This is the most common method to irrigate agricultural land and still is the most widespread in the world. It covers about 80% of global irrigated area (FAO 2012).

(a) (b) (c)

Figure I.1.7: Irrigation systems : a) Surface irrigation b) Sprinkler irrigation c) Micro-irrigation
- source: Irstea-2016

1.2.2 Sprinkler irrigation

In sprinkler irrigation, water is supplied under pressure and piped to one or more central locations within the field and distributed by overhead high-pressure sprinklers or guns reproduce rain irrigation. Agricultural sprinklers (Fig.I.1.8) typically have flow rates from 240 to 2700 $l.h^{-1}$, at nozzle pressures of 135 to 700 kPa, while gun sprinklers may have flow rates up to 120000 $l.h^{-1}$ or more at pressure up to 750 kPa or more (Merkley and Allen, 2003 [73]). It artificially produces natural rain (Fig.I.1.7(b)). This technique is characterized by larger efficiency than surface irrigation of 55 to 85% (Compaoré, 2006) [31]; but it requires higher energy expenditure and technical mastery. In addition, the winds deteriorate water distribution homogeneity and thus sprinkler irrigation efficiency.

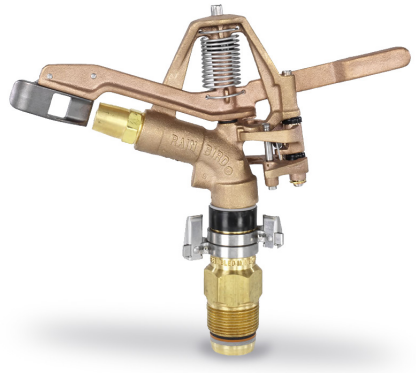

Figure I.1.8: An example of irrigation sprinkler http://www.rainbird.com

1.2.3 Micro-irrigation

1.2.3.1 Micro-irrigation definition

It is known as drip irrigation or localized irrigation (Fig.I.1.7(c)). Modern micro-irrigation is a system where water is distributed under low pressure through a pipe network, in a pre-determined pattern, and applied at a small discharge to each plant or adjacent to it in the vicinity of plants roots. This system has been developed from the 1950s, where plastics molding techniques and cheap polyethylene tubing made micro-irrigation systems possible for the first time [2]. This system is the most efficient irrigation system, with practically no water losses. In addition, the amount of water supplied to the roots can be perfectly controlled with this system. However, these facilities, often expensive, are more used on vegetables and are quite unsuited to cereal crops (Üzen et al., (2013)[99]. Some advantages of this system are the following:

- It waters a fraction of the soil,
- It requires a low flow rate and low pressure,
- It implements fixed and light equipment,
- It does not wet the foliage as sprinkler irrigation does,
- It requires little labor and energy once it is operational.

In France, micro-irrigation accounts for 4% to 5% of the area equipped for full control irrigation, about 107500 ha (in 2007). Compared with other techniques of irrigation, micro-irrigation helps to reduce water losses. This system controls the amount of water necessary for the plant and efficiency varies between 70% and 95% (Compaoré, 2006) [31]. Fertilizers can also be associated with water intake to

improve crop yields. However, the high cost of facilities and sensitivity of distributors to clogging are the main drawbacks associated with the use of this type of irrigation (see section I.1.3).

1.2.3.2 Micro-irrigation emitters

Emitters are the principal elements of micro-irrigation. These devices are used to control the discharge of water from the drip lateral pipes to the plants (FAO). So, the uniformity of water distribution and the water quantity are adjusted by these elements. They are inserted in the ramps, usually polyethylene pipes, at constant intervals. There are two cases, depending on whether the two functions, transmission and distribution, are handled by two different elements (tubing and emitters) or by the same element. The emitters have a flow rate between 1 and 8 $l.h^{-1}$ at a pressure of 0.5 to 4 bars, the most frequently used. They can be pressure-compensated or not Fig.I.1.9. Pressure compensating emitters facilitate water control, as each emitter performs to a pre-set flow rate (e.g. 2 $l.h^{-1}$), allowing water emitted over a length of time to be easily calculated. This ensures more efficient watering and reduces the risk of over-watering or under-watering. Pressure compensating emitters provide the same amount of water all the way down the slope, providing more even watering on uneven terrain. Pressure compensation occurs when the silicone diaphragm inside the emitter flexes to regulate water output. Flow control is achieved by a membrane, according to the pressure, which is deformed and closes more or less the water passage orifice. Non-pressure compensating emitters use longer tortuous channels which provide greater durability and longevity along with clogging resistance and low maintenance thanks to the absence of moving parts. Non-pressure compensating emitters will have varying output flow at varying inlet pressures. Ideal for vineyards and other permanent crop applications that require minimal elevation and pressure variations. Through non-pressure compensating emitter, water follows a complex path more or less long (0.1 to 1 m), which induces pressure dissipation. The GR[5] emitters, as called industrially, are equipped with a control system called labyrinth-channel in which water follows a long and complex path that leads to pressure dissipation in the form of head losses. Labyrinth-channels are characterized by a small section in the order of mm^2.

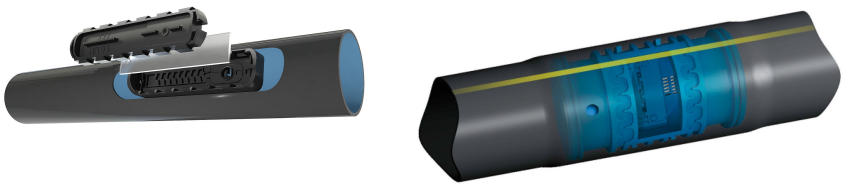

(a) Pressure compensating emitter. (b) Non-pressure compensating emitter.

Figure I.1.9: Emitter categories according to pressure sensitivity http://www.hydrotech-irrigazione.it

Hydraulic operation : The emitters are divided according to the operating hydraulic (Rieul and Ruelle, 2003)[94]:

- Circuit -uniform emitter: the water passage cross-section is constant along the path. The pressure losses are caused by the friction of the water along the walls of capillary tube.
- Circuit - non uniform emitter: in the emitter, there is a labyrinth-channel or baffles. Abrupt changes in direction of the liquid cause local head losses which add to the friction along the walls to generate the pressure losses. One can also find short circuit emitters. The conception of an integrated emitter allows to decrease emitter congestion and thus the pressure losses generated in the drip tubing.

[5]This is the industrial name, not an acronym

Mounting type : There are three fixing modes of the emitter on the ramp (Rieul and Ruelle, 2003)[94]:

- On-line emitter: This emitter is installed on a deviation. It is fixed on the ramp via a mouthpiece called 'Spot Watering' (Fig.I.1.10(a)). In this case, the emitter will be installed on the ramp in the ground. It is not suitable for devices that need to be handled (risk of tearing).
- In-line emitter: It is made of molded dripper, bearing two grooved ends that are inserted into the ramp. This mounting is carried out on the field, after cutting the pipe at regular intervals which vary across cultures which are intended facilities (spacing of $0.3\ m$ to $2.5\ m$). This system is not widespread (Fig.I.1.10(b)).
- Integrated emitter: The item with the path is set up in the pipe during its extrusion. The pipe is made around the emitter, the gaps are imposed. The emitter GR is part of this category, Fig.I.1.10(c) and other flat integrated emitters are shown Fig.I.1.10(d).

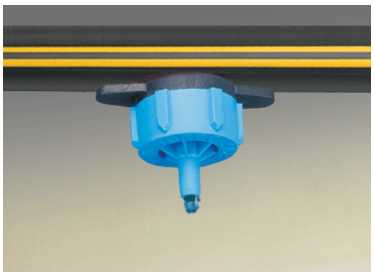

(a) On-line emitter
http://www.bombayharbor.com

(b) In-line emitterhttp://www.rivulis.com

(c) Round integrated emitter
http://www.indiamart.com

(d) Flat integrated emitter
http://tradesolutionzone.com

Figure I.1.10: Emitter shapes and types

Discharge-pressure curve : The relationship between the emitter discharge and pressure head in the ramp at the level of emitter is a power-law, Karmeli (1977) [54]:

$$q = k_d \Delta P^x \quad ; \tag{I.1.1}$$

in which : q is the emitter discharge $[\ell.h^{-1}]$,
k_d is the constant of proportionality that characterizes each emitter,
ΔP is the working pressure head at the emitter $[bar]$, and
x is the emitter discharge exponent.

In order to determine k_d and x, the discharges $(q_1, q_2, ...)$ at different operating pressure heads $(\Delta P_1, \Delta P_2, ...)$ must be measured. The exponent x is determined by the slope of log-plot of ΔP in function of q, see Fig.I.1.11.

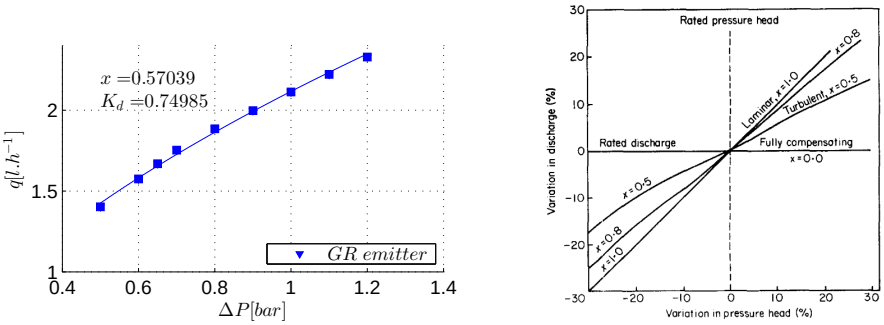

(a) GR emitter (b) x exponent

Figure I.1.11: Discharge-pressure curve for a GR emitter, performed at Irstea[6] institute and discharge variations resulting from pressure changes for emitters having different discharge exponents Karmeli (1977)[54].

This curve is important since it determines the emitter performance. It characterizes the flow regime and is a function of the emitter design (Merkley and Allen, 2003)[73]. In general, non-self-regulating emitters are characterized by x values varying from 0.38 to 0.8 (Rieul and Ruelle, 2003)[94].

- x is 0.5 in the case of purely turbulent orifice flow, assuming the pressure head is fully converted to velocity head,
- $x \leq 0.5$ for pressure-compensating emitters,
- $x \approx 0.7$ for long-path, laminar flow emitters. If the flow was completely laminar, the exponent would be 1.0,
- $x \approx 0.4$ for a vortex-type emitter.

The self-regulating distributors are practically independent of the pressure. Beyond certain flow rates, they are characterized by values of x close to 0.

1.3 Clogging problems in micro-irrigation systems

Micro-irrigation is the most efficient method to supply water and nutrients to plants, but this depends greatly on maintaining an uniform water application. However, the performance of drip irrigation, such as irrigation efficiency, distribution uniformity, in the field is often quite different from that obtained in experimental stations. It depends on the ability of farmers to change irrigation practices and economic and social reasons (Benouniche et al., 2014) [14]. The discharge variation within the system is influenced by the emitter clogging. The narrow flow passages and small orifice are inherent to all emitters. Therefore, all emitters are highly susceptible and vulnerable to clogging. Clogging is the major cause of performance degradation at the plot level (Pitts et al., 1990) [84] and thus determines the life of distribution system. Even a small percentage of clogged emitters can greatly reduce the uniformity of water application (Nakayama and Bucks, 1981 [75]; Bralts et al., 1981 [17]) and decrease the amount of applied water. Clogging also decreases the amount of salt leaching around the lateral line in case of saline water. The problem of clogging can be produced by physical, chemical and/or biological causes (Dosoretz et al., 2011)[36]. It is difficult and complex to determine the exact cause of emitter clogging because the various agents in the water can interact with each other. In irrigation emitter or device, these three forms of clogging can be observed simultaneously (Gilbert et al., 1981)[41]. The physical factors are the dominant cause of emitter clogging using reclaimed water. Biological and chemical factors are of secondary importance in case of conventional water (Gilbert et al., 1981)[41].

1.3.1 Biological clogging

Biological clogging is caused by the organic material present in the surface water, or by the development of algae and biofilm. Although the biological clogging represents a small percentage of emitter clogging using pure water, this percentage increases in the context of the use of treated waste water where organic clogging is mainly caused by biofilm development (Gamri et al., 2014)[39] (Fig.I.1.12). Biofilm development in irrigation systems is a serious source of clogging. Indeed, its presence promotes the physical and chemical deposits (Adin and Sacks, 1991[6]; Gilbert et al., 1981 [41]).

Figure I.1.12: Biological clogging (Gamri et al., 2014)[39]

1.3.2 Chemical clogging

The irrigation water contains various dissolved chemical elements. These compounds are in chemical equilibrium in their original environment. When pumping, this equilibrium can be broken by venting or adding entrants. Chemical precipitation may occur depending on water quality parameters such as temperature, pH and the concentration of salt. These parameters may induce the precipitation and sedimentation of mineral elements to generate clogging. Most encountered products are calcium carbonates and precipitated iron ferric form Fig.I.1.13 , rarely sulphate precipitates (Burt et al., 1995 [20]; Burt and Styles, 1994 [19]; Hills et al., 1989 [48]; Nakayama and Bucks, 1986[76]). The clogging with chemical factors is weak in comparison with the other types of clogging (Gilbert et al., 1981)[41] even in combination with the other forms.

Figure I.1.13: Chemical clogging

1.3.3 Physical clogging

The physical type is produced by mineral particles which deposit. Mineral particles suspended in the water are classified according to their diameter in several categories:

- Clay particles are the smallest particles, having diameters of less than $0.002\ mm$
- Silt particles have diameters between $0.002\ mm$ and $0.05\ mm$

- Sand particles, the largest particles, are larger than $0.05\ mm$ in diameter.

They can act on the obstruction of the emitters in two different ways:

- Direct obstruction: when one of the particles dimensions is greater than the passage section of the water through the emitter, sand particles or agglomerated particles are the major factor (Gilbert et al., 1981)[41]. Plastic particles are another important factor of clogging, but the filtering of irrigation water can reduce this factor (see section I.1.4.)
- Slow clogging or silting: when the finer particles settle gradually in areas where the water velocity is low. The point of grip on the tubing will be a trap to support the following particles and disturb the flow within the emitter. Deposits are located either in the labyrinth, or at the inlet gate grid designed to prevent large particles from entering the labyrinth (Fig.I.1.14).

Clays and fine silt particles are normally too small to plug the drippers. However, under certain physicochemical conditions, clays may aggregate downstream of the filtration system and form aggregates causing clogging (Pitts et al., 1990 [84]; Bounoua et al., 2016 [16]), either directly or indirectly holding other particles such as silt. In addition, it is likely that the fertilizer used during fertigation operations has a compounding effect on this mechanism. Physical clogging is responsible of 55% of emitter clogging (Gilbert et al., 1981)[41]. So, in this study, the flow characterization within the labyrinth-channel emitter, which is the first step to understand the physical clogging, is approached.

Figure I.1.14: Physical clogging (Bounoua, 2010)[15]

1.4 Management of clogging problems

Clogging phenomena can be managed by controlling the water quality in addition to the use of filtration and processing (Bucks et al., 1979 [18]; Nakayama and Bucks, 1991 [77]; Ravina et al., 1997 [92]; Levy el al., 2011 [69]). In this section, the different techniques are presented.

1.4.1 Water quality

Controlling the water quality varies according to the water origin. There are several sources of irrigation water by groundwater, surface water and wastewater. While the first category is rich in dissolved minerals (bringing chemical clogging), the second one is often charged with mineral particles (bringing physical clogging). High levels of algae and bacteria can be contained in this water category causing organic clogging. The last one is from a wastewater treatment plant. This category requires some special treatment to avoid as much as possible the emitter clogging.

Puig-Bargués et al. (2005)[88] show that the clogging phenomena are influenced by tertiary treatment in comparison with a secondary treatment. So, an advanced treatment of wastewater can reduce

clogging risk. The two first sources require a chemical treatment with various filtrations to reclaim and prevent clogging.

1.4.2 Filtration

A good filtration system is an essential component of a micro-irrigation system. The filters remove unwanted physical contaminants such as suspended solids, undissolved organic and inorganic materials that can clog the various components of irrigation devices. In selecting the type, size and capacity of the filtration units, the primary factors to be considered are the initial water quality and emitter design.

Various types of filters are available such as sand filters, disc filters, mesh filters, etc. The influence of filter is studied by Puig-Bargués et al. (2005)[88]. Similar work is performed by Carpa and Scicolone (2004 [21], 2005 [22]), by Adin and Sacks (1991)[6], and by Dehghanisanij el al. (2004)[35] and shows that the filtration reduces the risk of clogging and its performance depends on the type of filter used. However, filters require cleaning procedures and periodic chlorination because of their sensitivity to clogging.

1.4.3 Chemical treatment

The use of treatment procedures is a common technique in agriculture to eliminate components that clog irrigation systems (Bucks et al., 1979 [18]; Ravina et al., 1992 [91]; Rav-Acha et al., 1995 [90]). Chemical treatment by adding acid into the irrigation water is used to remove the precipitates that form in the irrigation systems (filter, tubing, or emitter). The chlorination treatment is generally used to control bacterial growth. The doses applied must be strictly observed (Carpa and Scicolone, 2004 [21], 2005 [22]) to avoid degrading cultures (Ravina et al., 1992 [91] and 1997 [92]).

1.5 Conclusion: Emitter improvement

Using high water quality, a good filtration and chemical treatment, the clogging risk can be reduced and controlled. If direct obstruction caused by sand particles is eliminated using a good filter and treatment, slow clogging is produced by clay and the formation of silt-sized aggregates is not prevented. Slow clogging is initially influenced by the emitter design or emitter geometry. However, several emitters provided with different labyrinth-channels were studied in previous researches. The emitter clogging occurs by different ways. For example, a physical particle, in the low-velocity zones of emitter where the physical particles tend to deposit, can catch by other particles to build a particle aggregate or organic material to develop a biofilm. This influence changes in the emitter labyrinth-channel according to the emitter geometry. Emitter improvement includes eliminating the most vulnerable zone to clog along the baffles of labyrinth-channel emitters.

Chapter 2

Labyrinth-channel hydrodynamics and thesis objectives

The emitter improvement or geometry optimization requires numerical and experimental methods to analyze the flow within the labyrinth-channel. All these methods aim to characterize the low velocity zones. In this section, the different numerical models and experimental techniques are presented.

2.1 Flow regime

In fluid mechanics, the determination of flow regime is necessary to qualify and quantify the fluid motion. The transition from laminar to turbulent flow depends on the geometry, surface roughness, flow velocity, type of fluid, among other things. Osborne Reynolds (Pope, 2000)[85] discovered that the flow regime depends mainly on the ratio of inertial forces to viscous forces in the fluid. This ratio is called the Reynolds number which is a dimensionless number. For flow in pipe or tube, the Reynolds number is, generally, defined by:

$$Re = \frac{U_m D_h}{\nu} \quad , \tag{I.2.1}$$

where U_m [1] is the average flow velocity of the fluid $[m.s^{-1}]$,

D_h is the hydraulic diameter of the pipe (or the tube)$[m]$, defined in Eq.II.1.9,

ν is the kinematic viscosity $[m^2.s^{-1}]$.

The Reynolds number at which the flow becomes turbulent is called the critical Reynolds number, Re_{cr}. The value of the critical Reynolds number is different for different geometries and flow conditions. In a circular pipe, the flow is laminar for $Re \leq 2300$, turbulent for $Re \geq 4000$ and transional in between when the pipe is smooth and straight. Micro-irrigation works with a nominal discharge of $2\ell.h^{-1}$. The labyrinth-channel cross-section A is in the order of $1\ mm^2$. So, the bulk velocity is given as:

$$U_m = q/A_c$$

where q is the discharge of emitter $[m^3.s^{-1}]$,

A_c is the cross-sectional area $[m^2]$.

For $2\ l.h^{-1}$, this gives a Reynolds number $Re = 555$, the flow should be laminar according to the standard classification mentioned above. But, labyrinth-channel geometry, in general, is complex. It is composed of several baffles, therefore the critical Reynolds number is different from that in straight pipes. There are not yet appropriate theories to calculate the critical Reynolds number in such geometries.

[1] In this thesis manuscript, the velocity modulus is defined by the symbol $|\overline{u}|$ for micro-PIV and modelling results. But, in this preamble analysis, the symbol U_m is used to define the average flow velocity (bulk velocity). Scientific notation of mean values, in fluid mechanics, is specific to turbulent flows.

Nishimura et al. (1984)[78] investigated the complex channel or tube with a symmetric wavy wall (Fig.I.2.1). They found that the transition from laminar to turbulent flow occurs when the Reynolds number reaches 350.

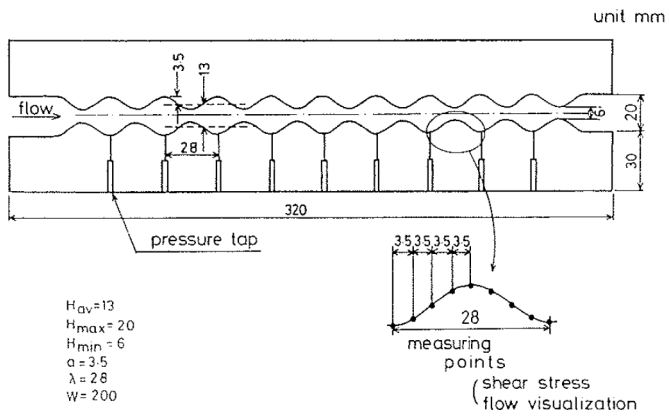

Figure I.2.1: Geometry studied by Nishimura et al. (1984)[78]

Some studies (Pfahler et al., 1990 [82]; Harley et al., 1995 [47]; Kandilikar et al., 2003 [53]) indicated that the transition from laminar to turbulent regime in channels with a section of about $1.0\ mm^2$ occurs at a Re ranging from 100 to 700. The flow is rather turbulent in the labyrinth-channel. However, there are several geometries for the labyrinth-channel as mentioned above. The turbulence varies according to the geometry.

2.2 Numerical analysis of the flow

The characteristics of the flow in the labyrinth-channel have a great bearing on the hydraulic performance and the anti-clogging properties of the emitter, so the flow state in the labyrinth-channel should be well understood before designing a high-performance emitter. However, the choice of the laminar flow model or the turbulence model is not evident. Flow characterization, numerically, can be performed by computational fluid dynamics (CFD), which is a commonly used method. In the labyrinth-channel, the choice of CFD modelling differs from one study to another. For example, Palau Salvador et al. (2004)[81] employ the laminar model, while the choice of turbulence model has been advised by most of the researchers working on this problem. Wei et al. (2006)[101] choose the standard $k-\epsilon$ model to describe the flow in the emitter with Reynolds number range $75-550$. They considered that this model is typically used for most engineering calculations even if it has been developed for fully turbulent flows. While Wei et al. (2012)[102] and Ali (2013)[9] employ the RNG $k-\epsilon$ model, Dazhuang et al. (2007)[34] use the realizable $k-\epsilon$ model for Reynolds number range $(325-650)$. The RNG $k-\epsilon$ model generally improves the accuracy for strongly strained and swirling flows. These features make the RNG $k-\epsilon$ model more accurate and reliable for a wider class of flows than the standard $k-\epsilon$ model. The realizable $k-\epsilon$ model is applied in various flow simulations; including vortex steady shear flow, free flow containing jet and mixed flow, pipe flow, boundary layer flow, and segregated flow. But all of these models calculate the turbulent stress with isotropic turbulent viscosity assumption, and the variation of surface curvature along the channel is not taken into account. That is why the Reynolds stress model (RSM) is also used in several studies (Zhang et al., 2007 [110]; Philipova et al., 2009[83]; Zhang et al., 2010 [111]). This model can account for the effects of streamline curvature, swirl, rotation and rapid changes in strain rate in a more rigorous way. Other more complex simulations such as LES model (Large Eddy Simulation) have been used by Wu et al. (2013)[107] and compared with standard $k-\epsilon$ model. They concluded that the LES model could obtain higher computational accuracy and the LES model was more effective in describing the flow characteristic of the fluid in the passage and optimizing

the path structure.

The geometry complexity reveals that there is not really a suitable numerical model to resolve the Navier Stokes equations in order to characterize and analyze the flow and determine the pressure and velocity fields, but it is deducted from the bibliography and the fact that a lot of turbulence models are used (see part III). The importance to have consensually adapted numerical tools (numerical model) for modelling the labyrinth-channel flow, is essential to achieve the main objective, geometry optimization.

2.3 Experimental analysis of the flow

The experimental results must be checked and their analysis validates the numerical model. Especially, in the study of emitter labyrinth-channel for which the choice of a laminar or turbulent model is not established. There are two approaches to check and validate the experimental results; global one using the discharge-pressure loss curves ($q = f(\Delta P)$) (used by Wei et al. (2012) [102]), and local one determining the velocity fields in the labyrinth-channel. Experimental tools and techniques are important to visualize the flow fields and to make a comparison with the numerical models. Unfortunately, most studies performed on the emitter and its geometries, are numerical. Nevertheless, there are also a few experimental studies. PIV (Particle Image Velocimetry) or micro-PIV and LDV (Laser-Doppler Velocimetry) techniques are the experimental tools to analyze the flow in the labyrinth-channel. The LDV method has been used by Zhang et al. 2007 [110] on an arch-type labyrinth-channel. PIV technique was used by Liu et al. (2009) [72] to analyze the flow characteristics of labyrinth-channel in drip irrigation on two geometries, Fig.I.2.7. Micro-PIV technique was used by Wei el al. (2012) [102] to visualize the flow but the analysis is still qualitative. However, the success of the experimental techniques, effectively, depends on the parameters used.

2.4 Emitter design and geometry optimization objectives

The two basic emitter design objectives are, (i) to have a low value of the exponent x Eq.I.1.1 (if the exponent is less than 0.5, it compensates better than a simple orifice) and, (ii) to have flushing properties to prevent clogging. These objectives tend to be conflicting; because the more pressure is compensated the less particles are flushed. In this section, the influences of labyrinth-channel geometry and the hydrodynamic conditions on clogging are presented.

2.4.1 Influence of labyrinth-channel geometry

Emitter performance, which is presented by the power-law of Karmeli Eq.I.1.1, is influenced by the labyrinth-channel geometry. In reality, the value of the exponent x (Eq.I.1.1) depends on the conception of the emitter and thus its geometry. In order to quantify and qualify this effect, three different simple geometries, namely, triangular, rectangular and trapezoidal, shown in Fig.I.2.2, have been studied by Wei et al. (2006) [101].

Trapezoidal Rectangular Triangular

Figure I.2.2: Three emitters studied by Wei et al. (2006)[101]

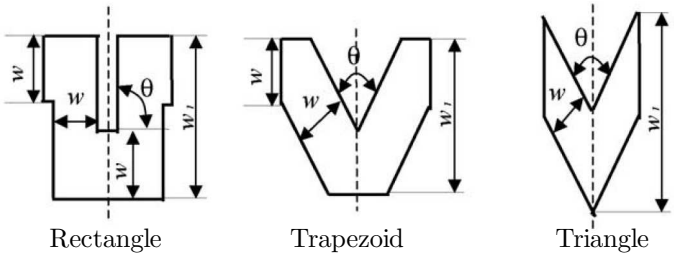

Figure I.2.3: Three geometries numerically studied by Wei et al. (2006)[101]

Table I.2.1: Structure parameters of three labyrinth-channels Fig.I.2.2.

Emitter type	$w(mm)$	$\theta(^o)$	$w_1(mm)$	$d(mm)$
Rectangle	1.0	90	4.0	0.5
Trapezoid	0.7	60	2.7	0.7
Triangle	0.7	60	4.0	0.7

The cross-section area of the three types of labyrinth-channel emitters is in the order of $1\ mm^2$ and the parameters notation (except the depth d), displayed in Fig.I.2.3, is detailed in table I.2.1. The nominal flow rate ranges from 2 to 8 $\ell.h^{-1}$. Consequently, Re ranges from 75 to 550. These authors found that the pressure loss caused by the triangular geometry is greater than the trapezoidal geometry and the latter is larger than the rectangular geometry. As a result, a greater dissipation per unit length occurs in the triangular channel than in the trapezoidal and rectangular channels. They concluded that the pressure loss occurs mainly at the channel corners. Therefore, the corner structure is the main element that affects the efficiency of hydraulic energy dissipation for the labyrinth-channel emitter (Liu et al., 2009) [72].

In order to define the emitter performance, simulations and experiments are performed to calculate x and k_d (Eq.I.1.1). Numerically, the geometries have the exponents 0.585, 0.478 and 0.465 for respectively rectangular, trapezoidal and triangular channels. Nevertheless, the three geometries have, experimentally, the exponents 0.611, 0.483 and 0.460. The triangular geometry achieves the first objective, but the conflicts between the first and second objectives have not been studied by the authors. To analyze partially the second objective, the flow velocity fields are obtained by Wei et al. (2006)[101] on Fig.I.2.4.

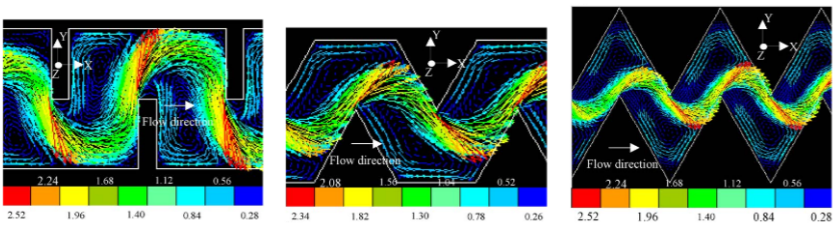

Figure I.2.4: Velocity fields in partial channels from the study of Wei et al. (2006) [101]

One can conclude that the flow in the labyrinth-channel is composed of a mainstream flow and recirculation regions. The mainstream flow has a high velocity. At the corner, the velocity reaches its maximum value. Recirculation regions are characterized by low velocity. The flush of dead zones, where the speed is low, appeared less frequently in the triangular geometry. So, this geometry is vulnerable to clogging more than the other geometries. The trapezoidal geometry is considered as the good geometry which gives a good performance with anti-clogging properties.

So the trapezoidal geometry is analyzed in detail for several dentate parameters by Dazhuang et al. (2007) [34], Fig.I.2.5. The dentate parameters are presented in table I.2.2 for a dentate angle $\theta = 32^o$. The hydraulic performance and effective hydraulic energy dissipation is satisfied by the type $\mathcal{II}$, see table I.2.2, (Fig.I.2.6), where the exponent x is the smallest. The type $\mathcal{I}$ has a large region of low velocity which is not beneficial for energy dissipation when increasing dentate height, the low velocity region is significantly reduced. But, when increasing the dentate height more than $1.6\ mm$, the region of reverse flow at the back of dentations is prolonged and the flow velocity is more reduced. They concluded that the flow path of type $\mathcal{II}$ has a good performance and effective energy dissipation. This type has low velocity region comparing with type $\mathcal{I}$ and the boundary scouring is high in comparison with type $\mathcal{III}$ and $\mathcal{IV}$.

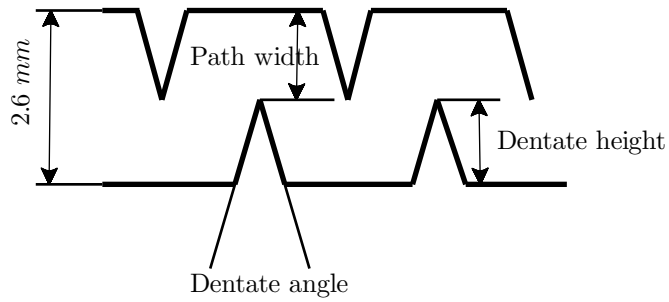

Figure I.2.5: Parameters of geometries studied by Dazhuang el al. (2007)[34]

Table I.2.2: Dentate parameters Fig.I.2.5.

Code	$\mathcal{I}$	$\mathcal{II}$	$\mathcal{III}$	$\mathcal{IV}$
$H\ (mm)$	1.0	1.3	1.6	2.0
$D\ (mm)$	1.6	1.3	1.0	0.6
H/D	0.6	1.0	1.6	3.3

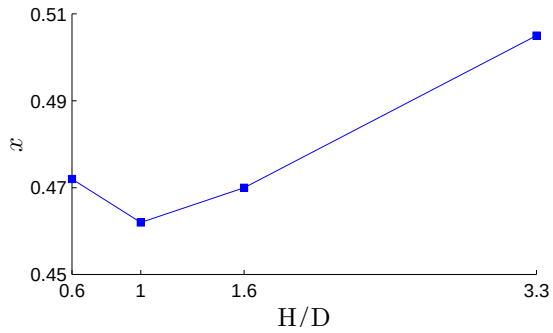

Figure I.2.6: Three geometries studied by Dazhuang el al. (2007)[34]

Dentate angle is important for designing the labyrinth-channel geometry. Four different dentate angles (32°, 41°, 53° and 63°) are then selected in the study of Dazhuang et al. (2007) [34]. The flow exponents for these geometries are 0.462, 0.461, 0.428 and 0.427. The best hydraulic performance is achieved when the angle values are 53° and 63°. But, this improvement gives a poor anti-clogging property. Type $\mathcal{II}$, in table I.2.2, seems to be the ideal pattern for both anti-clogging capacity and good hydraulic performance. However, the clogging tests are not performed in this study and the flow modelling results are analyzed to provide the anti-clogging capacity. The mentioned studies show the

best emitter geometry. Then, the dimensions of this form (trapezoidal geometry) have been changed in order to have the best performance.

The velocity fields in the recirculation zone are analyzed in detail by Liu et al. (2009)[72]. These analyses are performed for two patterns Fig.I.2.7, the first one is K_5 where the triangular shape repeats 5 times, while for the second one (M_4 model) the rectangular shape repeats 4 times. They found there are a certain number of flow stagnation regions which should be eliminated as much as possible in the design of the emitter, while the vortex flow should be fully developed Fig.I.2.8 and Fig.I.2.9. With reference to the anti-clogging performance and the energy emitter dissipation efficiency in the path of the emitter, the M-type flow path is better than the K-type.

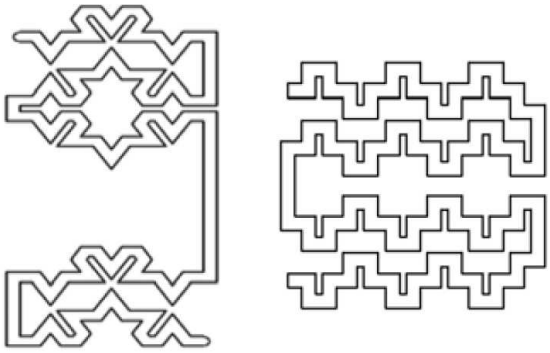

K_s M_4

Figure I.2.7: Two geometries studied by Liu et al. (2009)[72], where $A_c = 1.31\ mm^2$ for K_5 and $A_c = 0.8\ mm^2$ for M_4

Table I.2.3: The flow path geometry parameters Fig.I.2.7.

Flow path	K_5	M_4
Width of path $W(mm)$	1.20	0.90
Depth of path $D(mm)$	1.09	0.89
Area of path $A(mm^2)$	1.31	0.80
Length of path $L(mm)$	120	128

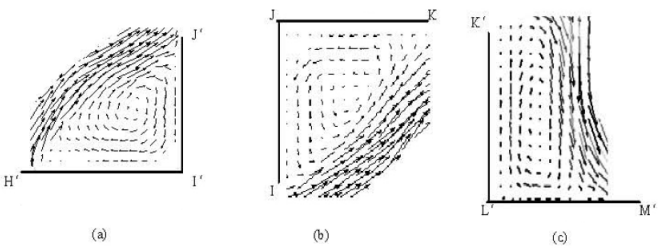

Figure I.2.8: The vortex distribution in the M-type flow path (Liu et al., 2009)[72].

2.4.2 Geometry optimization

Geometry optimization is necessary to avoid emitter clogging and to maintain emitter performance. Emitter efficiency which determines the lifetime of material equipment is related to the geometry.

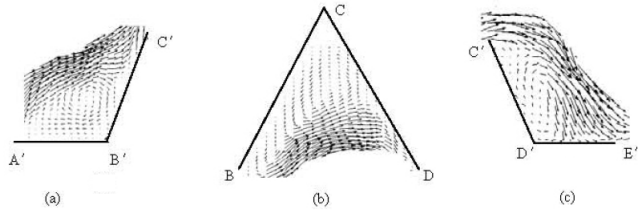

Figure I.2.9: The vortex distribution in the K-type flow path (Liu et al., 2009)[72].

An optimal emitter should have an anti-clogging geometry with a high performance for operating pressure. Therefore, manufacturers try to design emitters for which the flow rate is not directly dependent on the pressure head ($x < 0.5$). At the same time, they should design anti-clogging emitter by eliminating as much as possible the low velocity vortex regions where particles are trapped and organic development occurs.

The emitter design requires flow analysis of a high hydraulic performance emitter in order to optimize the geometry. Wei et al. (2012) [102] have conducted an important numerical comparison between a rectangular geometry and an optimized rectangular geometry by replacing the rectangle corner by arcs Fig.I.2.10. They found that there are no vortices nor stagnant regions in the optimized rectangular labyrinth-channel and the anti-clogging performance is obviously improved satisfying both objectives. The same idea is applied on a triangular geometry. The anti-clogging performance is improved. This is proven by the absence of vortices and stagnant regions in the rectangular channel.

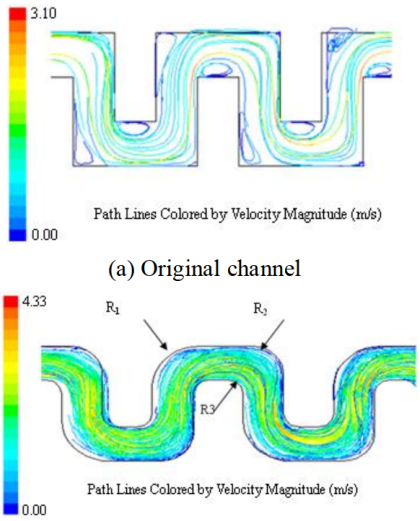

(a) Original channel

(b) Optimal channel

Figure I.2.10: Velocity path lines in a rectangular labyrinth-channel and the optimized one numerically analyzed by Wei et al. (2012)[102]

2.5 Conclusion and thesis objectives

The development of modern irrigation systems is important for struggling against the deficit of water resources. Micro-irrigation system is the most efficient system in comparison with other systems (sprinkler and surface irrigation). The main disadvantage of this system is the clogging which decreases the hydraulic performance and uniformity of water distribution. The physical clogging, in the case of fresh water (to distinguish it from waste waters), is the major responsible of clogging. The choice of a good irrigation filtration and chemical treatment adapted to irrigation water at the plot are important and essential to reduce clogging. However, when taking into account these treatments, the emitter design

plays a significant role to reduce the clogging. The clogging is related and influenced by the hydrodynamic conditions. The labyrinth-channel geometry changes and controls these conditions. Nevertheless, the design of anti-clogging emitter could reduce the hydraulic performance. Therefore, the emitter designed must have a good hydraulic performance and an anti-clogging capacity.

Several labyrinth-channel geometries have been studied in the literature, the trapezoidal geometry is chosen for its performance and anti-clogging capacity. The geometry parameters are chosen according to the previous research advices and results. The geometry chosen, in this study, is close to the type II analyzed by Dazhuang et al. (2007) [34]. Geometry optimization gives a good anti-clogging capacity. This optimization is realized by eliminating the low-velocity zones where the small particles deposit. In order to determine and identify these zones, the flow must be analyzed experimentally and numerically.

The objective of this study is to develop the simplest numerical model that will be used to better define flow regions that generate pressure losses and determine the low velocity zones. In the literature, there is no pertinent and reliable model for modelling the flow in the labyrinth-channel. Each numerical model has advantages and disadvantage. Therefore, several models are chosen to perform the modelling. Experimentally, micro-PIV technique is presently used to analyze the flow in the labyrinth-channel. This technique is a powerful tool in experimental fluid mechanics. The numerical results will be validated by comparison with the experimental results. Then, the adapted model, simple and fairly inexpensive in computation time, will be used in the future to optimize the baffles shape in terms of discharge/pressure loss and to limit the zones where low velocity is likely to be the principal cause to generate emitter clogging.

Part II

Experimental methodology

Table of Contents

1 Experimental apparatus and conditions **45**
1.1 Introduction . . . 45
1.2 Micro-Particle Image Velocimetry (micro-PIV) . . . 45
1.2.1 Introduction . . . 45
1.2.2 Principle of Particle Image Velocimetry PIV or micro-PIV . . . 46
1.3 Studied emitter and its geometry . . . 47
1.4 Hydraulic equipments . . . 49
1.5 Tracer particles . . . 51
1.5.1 Particle properties . . . 51
1.5.2 Seeding particles . . . 53
1.5.3 Concentration of seeding particles . . . 53
1.6 Flow Diagnostics . . . 53
1.7 Experimental conditions . . . 55
1.8 Pressure-discharge curves . . . 55

2 Experimental settings **57**
2.1 Time delays between laser pulses . . . 57
2.2 Prototype positioning and image calibration . . . 59
2.2.1 Prototype positioning . . . 59
2.2.2 Image calibration . . . 59
2.3 Acquisition protocol . . . 60
2.4 Data analysis . . . 60
2.4.1 Cross-correlation . . . 61
2.4.2 Vector validation . . . 62
2.5 Data treatment . . . 62
2.5.1 Derived quantities . . . 62
2.5.2 Statistical quantities . . . 62
2.5.3 Data convergence and image number . . . 63
2.6 Uncertainty analysis . . . 67
2.6.1 Peak locking . . . 67
2.6.2 Signal-to-noise ratio . . . 70
2.7 Conclusion . . . 70

Chapter 1

Experimental apparatus and conditions

1.1 Introduction

The experimental investigation of fluid flow has been developed in the last 30 years as a result of scientific and technical progress achieved in optics, laser, electronics, video and computer techniques. Laser Doppler Velocimetry (LDV), Doppler Global Velocimetry (DGV), Laser Induced Fluorescence (LIF), Particle Image Displacement Velocimetry (PIDV) and Particle Tracking Velocimetry (PTV) are the most known methods applied in fluid dynamics. PIDV or, as it is now most often called, Particle Image Velocimetry (PIV) technique, has been developed after the invention of the laser in the 1960s. This technique is used to obtain instantaneous velocity measurements and related properties of fluid flows. It allows to visualize and to describe the flow with quantitative and qualitative information.

A practical guide (Raffel et al., 2007)[89] presents the theory of this method with some experiments performed in this domain. PIV technique used to diagnose the micro-fluidic scales is called micro-PIV where spatial resolutions are in the order of several microns. In addition, the micro-PIV visualization is characterized by the illumination of the whole volume studied. The field of view definition is obtained by the camera focal plane. The first successful micro-PIV experiment was conducted by Santiago et al. (1988) [95]. This technique will be used in the present work since the labyrinth-channel has small dimensions. The experimental apparatus of a micro-PIV system typically consists in several subsystems. The micro-PIV system is divided in two parts: one is the hydraulic system and the other is the optical system. Both systems are consisted of hardware and software components. Hydraulic system is detailed in section II.1.4, while the optical system is presented in section II.1.6.

1.2 Micro-Particle Image Velocimetry (micro-PIV)

1.2.1 Introduction

The principle of PIV is based on the direct determination of the two fundamental dimensions of the velocity: length and time. This technique is indirect as it determines the particle velocity instead of the fluid velocity. Therefore, fluid mechanical properties of the particles have to be examined in order to avoid significant discrepancies between fluid and particle motion. In addition, there are several parameters and calibration to adjust. In this chapter, the principle of micro-PIV is presented in section II.1.2.2, while tracer particles and experimental conditions are detailed in section II.1.5 and section II.1.7 respectively. The specific data analysis procedures used in this study and experimental parameters are discussed in chapter II.2. The different steps and parameters of calibration and acquisition will be detailed.

1.2.2 Principle of Particle Image Velocimetry PIV or micro-PIV

The PIV technique is based upon the definition of velocity, i.e. the first derivative of position with respect to time. It consists in measuring the displacement of fluid ($\Delta\overrightarrow{x}$) over a given time interval (Δt). Either the fluid flow naturally contains particles or tracer particles have to be added to the fluid flow as in most of the applications. These particles are assumed to be small enough and light enough to move with local flow velocity. The movement of the fluid is imaged through the light scattered by these particles illuminated by a laser light sheet.

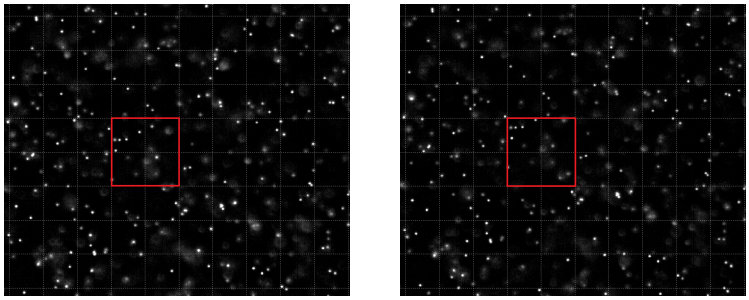

(a) At t, frame 1 (b) At $t + \delta t$, frame 2

Figure II.1.1: Particles images recorded on two frames

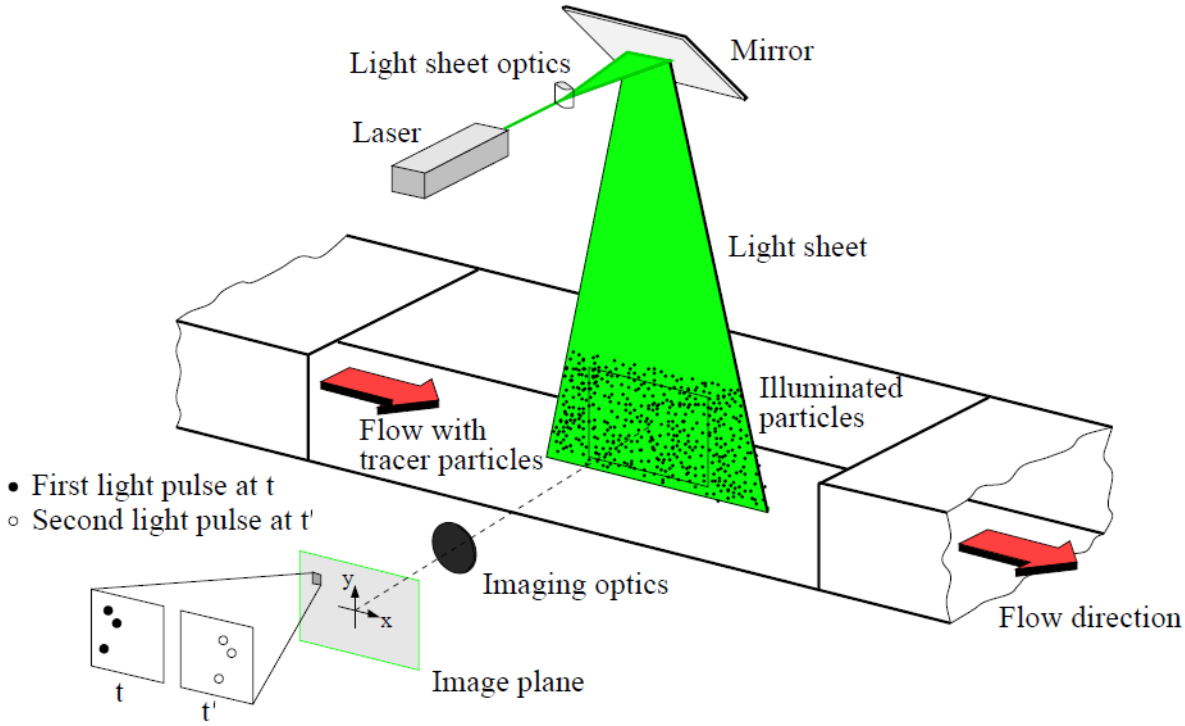

Figure II.1.2: Experimental setup for PIV recording in a wind tunnel or a water channel (Raffel et al., 2007)[89]

A plane within the flow is illuminated twice by means of two superimposed laser light sheets. The light scattered by the particles is recorded on two separate frames on a special cross-correlation CCD camera sensor, Fig.II.1.1. These digital images are divided in small areas, namely, ' interrogation windows '. Then, the two components of the 2D displacement vector of the particles images between the two frames are determined for each interrogation window by means of a spatially statistical cross-correlation function. Given the time interval between the two laser pulses and the image magnification

obtained from camera calibration, the projection of the local flow velocity vector onto the plane of the light sheet, attributed to the center of the interrogation window, can then be deduced. Neighboring interrogation windows must be partially overlapping in order to reduce the spacing between two vectors in the resulting vector grid. Typically, a 50% overlap is used, which doubles the number of vectors in each direction and thus quadruples the total number of vectors. The PIV at small length scales is named micro-PIV. The laser plane is not fine enough to illuminate the flow in 2D. The optics of the camera (depth of field) allows to locate the measurement area. It is quite specific to the micro-PIV. A complete micro-PIV experiment can be divided in the following steps:

- flow seeding;
- illumination;
- image recording;
- post treatment (analysis of the data recorded).

1.3 Studied emitter and its geometry

The emitter chosen is an integrated one with non-uniform section produces a turbulent flow. This emitter is the most widespread in micro-irrigation. This emitter is displayed in Fig.II.1.3. The emitter is composed of 60 baffles (labyrinth-channel units). Each three baffles pattern composes the basic unit which is repeated 20 times. This is the emitter least sensitive to clogging as discussed in section I.2.4.

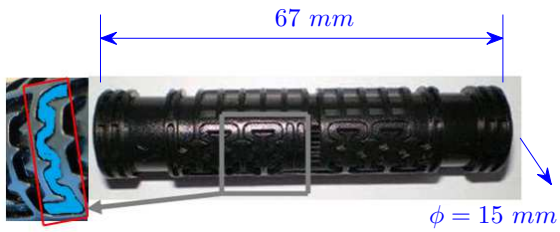

Figure II.1.3: Emitter studied (industrial geometry)

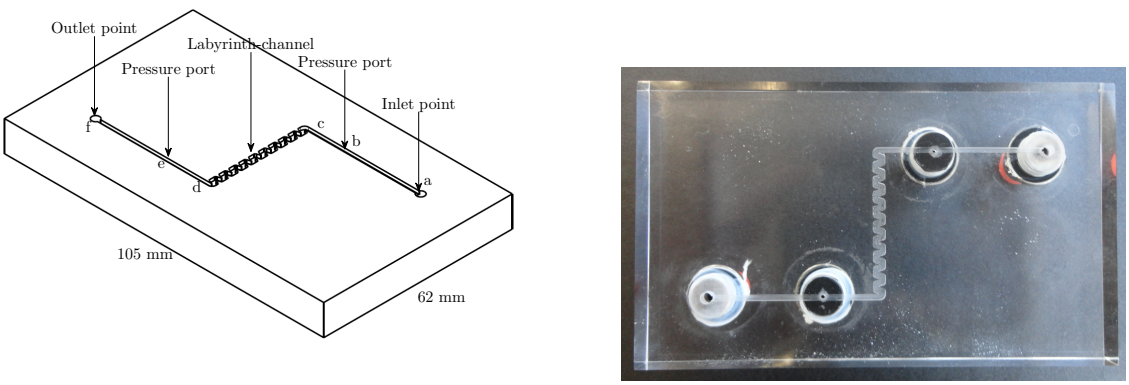

(a) Labyrinth-channel design

(b) Labyrinth-channel plate

Figure II.1.4: Labyrinth-channel fabrication (for laboratory experiment)

In order to study this emitter, three-pattern and ten-pattern labyrinth-channel units have been designed Fig.II.1.4(a) and fabricated by machining Fig.II.1.4(b). The first type, which is the same as used in modelling section III.2.1, allows to determine the pressure losses and will be used to obtain the pressure-discharge curves. Then, the pressure losses, within the whole emitter, can be deduced from this prototype because it is the repetitive pattern. Whereas, the second type is designed for the flow visualization by micro-PIV technique. This allows to know whether the flow variables will evolve along the different labyrinth-channel units or whether the flow is established. A second plate is used to seal these prototypes.

To allow optical access for micro-PIV, the material is transparent PMMA (poly methyl methacrylate). Sealing is assured by pressing the two PMMA plates between two 5 mm thick steel plates (Fig.II.1.5). A detailed geometry in 2D, with all dimensions, of the labyrinth-channel used for micro-PIV experiments is shown in Fig.II.1.6. All the dimensions are presented in table II.1.1, while the lines coordinates are presented in table II.1.2. Labyrinth depth is different from one prototype to another because of machinery low precision. That is why most of the results will be normalized to allow comparison.

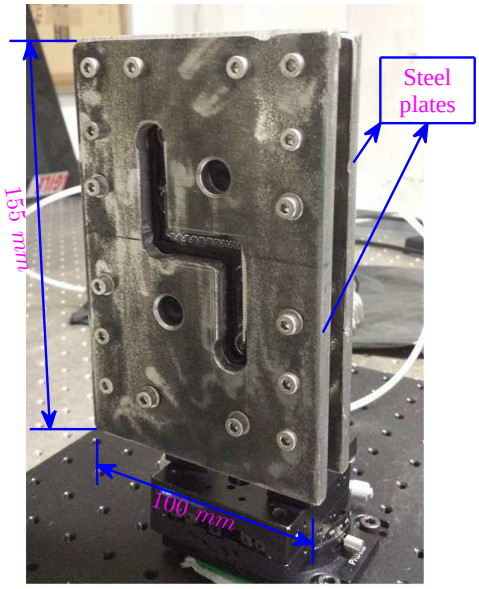

Figure II.1.5: Prototype

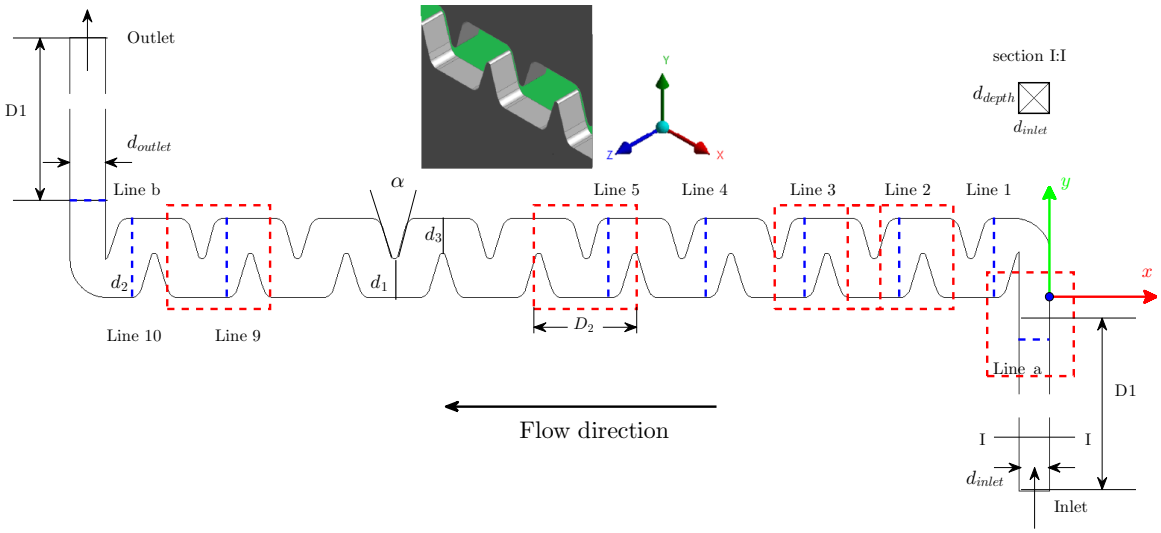

Figure II.1.6: Labyrinth-channel

Table II.1.1: The labyrinth-channel dimensions.

		Geometry 1 (for $5\mu m$)	Geometry 2 (for $1\mu m$)	Modelling	
Inlet width	d_{inlet}	1.07	1.20	1.00	mm
Outlet width	d_{outlet}	1.25	1.40	1.20	mm
Labyrinth-channel depth	d_{depth}	0.80	1.15	1.00	mm
	d_1	1.34	1.34	1.31	mm
	d_2	2.72	2.80	2.67	mm
	d_3	1.20	1.20	1.17	mm
	D_1	10.00	10.00	4.00	mm
Labyrinth-channel unit length	D_2		3.24		mm
Labyrinth-channel angle	α		33		^{o}

Table II.1.2: Lines coordinates.

	x_1 mm	x_2 mm	y_1 mm	y_2 mm	z mm
Line a	0	-1.13	-0.40	-0.40	0.5
Line 1	-2	-2	0	2.75	0.5
Line 2	-5.24	-5.24	0	2.75	0.5
Line 3	-8.5	-8.5	0	2.75	0.5
Line 5	-15	-15	0	2.75	0.5
Line 9	-28.0	-28.0	0	2.75	0.5
Line b	-32.2	-33.6	4.5	4.5	0.5

1.4 Hydraulic equipments

The hydraulic system provides the fluid flow with seeding particles. The scheme of this system is shown in Fig.II.1.7. It is composed of different elements to filter, pump and measure the flow rate, pressure losses and relative pressure. The experimental setup is shown in Fig.II.1.8. The pump is the driving part of this system. Pump type is a diaphragm metering pump (SIMDOS 10) Fig.II.1.9. Pump accuracy is of 2% of the set value. It pumps water from a $1\ \ell$ tank. The water quantity in the pipes and the labyrinth-channel is about $50\ ml$. The flow rate is adjusted by the pump. The pump has the ability to provide a flow rate between 10 and 100 $ml.min^{-1}$ (or $0.6 - 6\ l.h^{-1}$).

Just before the pump, there is an in-line filter to protect it, especially during seeding. The filter (KNF-FS25X) performs with a high-quality uniform mesh. The mesh size of $35\ \mu m$ is chosen. The pump induces flow pulsations. Theses flow pulsations must be absorbed before going through the studied prototype. In order to avoid them, two dampers are added to the circuit. A commercial damper of type: $PML\ 9962 - FPD10$, with a maximum efficiency of 97% was firstly checked. However, with this damper, the pulsations were not completely damped. For this reason, a second damper, hand-made was constituted of a pipe which contains air to damp the initial pump pulsations. Finally, peak-to-peak amplitude decreases from 17 $ml.min^{-1}$ without pulsations dampers to 1 $ml.min^{-1}$, when the two dampers are used, for flow rate of 100 $ml.min^{-1}$.

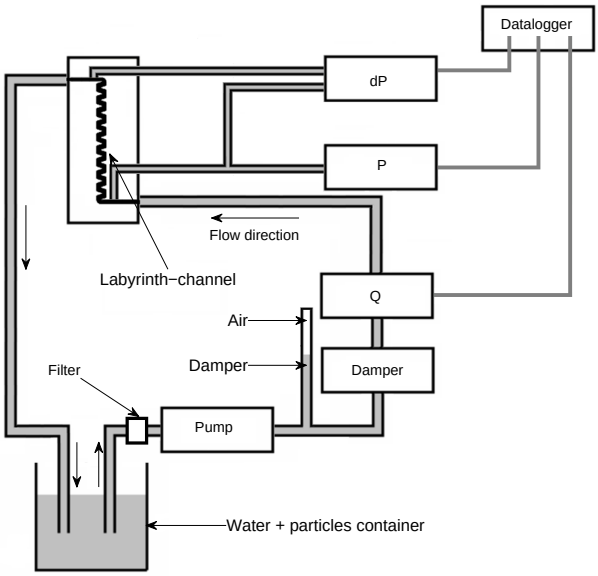

Figure II.1.7: Hydraulic scheme

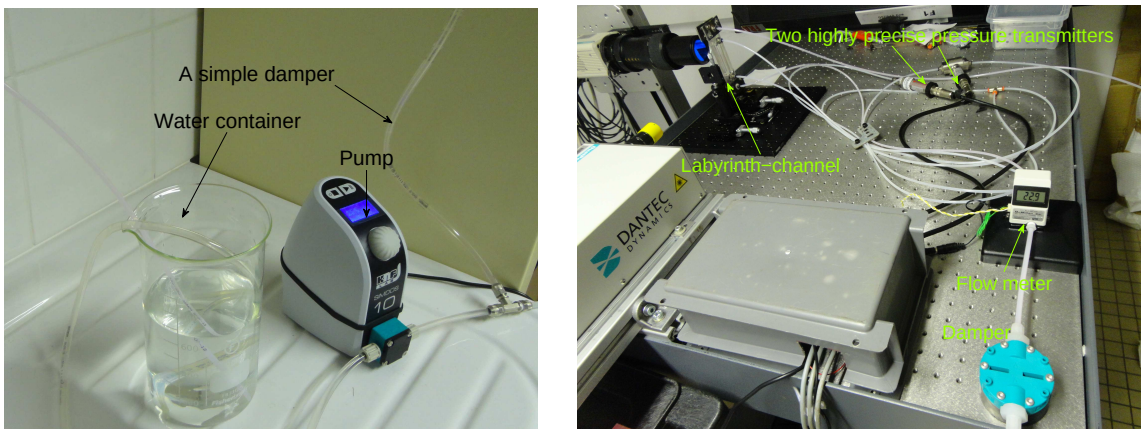

Figure II.1.8: Experimental setup

Figure II.1.9: A SIMDOS 10 metering pump

Figure II.1.10: Two pressure sensors

A flowmeter (Mc Millan, accuracy of $\pm 3\ ml.min^{-1}$) is used to measure the flow rate. The flowmeter is connected to a data logger. The signal of flow rate is in volts. In order to convert the flow

rate signal to $ml.min^{-1}$, we use calibration factor, which is equal to 20 $[ml.min^{-1}.V^{-1}]$. Instantaneous velocity vectors and fields obtained by micro-PIV depend on the volume flow rate of water. Therefore, any error in measuring the flow rate affects the bulk velocity estimation. Measurements are performed to calculate the standard deviation between the flowmeter value and the real flow rate. The errors come from two sources:

1 flowmeter device,

2 flow rate variations.

The error due to flowmeter device is given, by the manufactures, as equal to 2% of the set value in the operation manual. The flow rate value measured by the flowmeter deviates from the fixed value by a small error. It is the deviation of the average value due to the flow rate variation. This error is about $0.1 - 0.3\%$ for 48 $ml.min^{-1}$ (table II.1.3). One conclude that the last error is negligible in comparison with the first error which is weak likewise.

Table II.1.3: Error of flow rate variations

	nominal $ml.min^{-1}$	Measured $ml.min^{-1}$			
Flow rate	48	$48,06$	$47,87$	$48,03$	$48,05$
Error		0.1%	0.3%	0.1%	0.1%
Flow rate	24	$23,96$	$24,26$	$24,6$	$24,06$
Error		0.2%	1.1%	2.5%	0.25%

The pressure at the inlet (the relative pressure) as well as the pressure drop, in the labyrinth-channel, is measured by two highly precise pressure transmitters Keller, ($PR - 33x/80794$ and $PD - 33x/80920$, accuracy of 0.01 %), see Fig.II.1.10. These pressure sensors are connected to a data logger. The signals of pressure are in V. In order to convert the pressure signal to bar, we use the calibration factor, which is equal to $0.1[bar.V^{-1}]$.

1.5 Tracer particles

1.5.1 Particle properties

When velocity measurements by micro-PIV require seeding the flow with small particles, these particles must scatter the light. The fluid velocity is inferred from the particle displacements captured by the optical measurement. Therefore, the particles must be large enough to scatter the light and small enough to follow the flow. Polystyrene particles are preferred thanks to their density closer to the water density (1.05 $kg.m^{-3}$) against (1.19 $kg.m^{-3}$) for PMMA particles (Poly methyl methacrylate). These two types of particles are hydrophobic (and insoluble in acids and bases). Polystyrene-based (PS) fluorescent particles have narrow size distribution and they are available in a wide diameter range, intensive color and bright fluorescence (table II.1.4). In this thesis, two particle diameters are used. Supplier is *micro particles GmbH*. Fluorescent particles are used to improve sensitivity and detectability for analytical methods and to have feature bright, high-contrast colors. Using particles of $1\mu m$ diameter allows to have a high precision and to decrease the interrogation window size in order to better predict the flow when shear stress is high and in the swirl zone. Nevertheless, beyond the third baffle, these particles lose a lot of brightness and the signal-to-noise is bad. Therefore, these are replaced by particles of $5\mu m$ diameter to visualize the flow from the third baffle.

The choice of particles size is done by validating two criteria. The first criterion is the Stokes number at which Stokes velocity is verified. Stokes number (Eq.II.1.1) is defined as the ratio of the

characteristic time of a particle (Eq.II.1.2) to a characteristic time of the flow, namely, the Kolmogorov time scale (Eq.II.1.3).

Table II.1.4: Particles properties, where λ_{abs} and λ_{em} are the absorption and emission wavelengths respectively.

Particle diameter d_p $[\mu m]$	Particle material	Particle components	abs/em $[nm]$	Particle density ρ_p $[kg.m^{-3}]$	Hydrophilicity / Hydrophobicity
5	Polystyrene	Red Fluorescent	$\lambda_{abs} = 530$, $\lambda_{em} = 607$	1.05×10^3	hydrophobic
1		Rhodamine B	$\lambda_{abs} = 542$, $\lambda_{em} = 612$		

Table II.1.5: Turbulent dissipation, obtained numerically by RSM model

Flow rate q_1 $[ml.min^{-1}]$	Reynolds number Re	kinematic viscosity ν $[m^2.s^{-1}]$	turbulent dissipation ϵ $[m^2.s^{-3}]$	Kolmogorov time scale τ_k $[ms]$
24	400	10^{-6}	60	0.13
48	800		500	0.045

$$St = \frac{\tau_p}{\tau_k} \tag{II.1.1}$$

$$\tau_p = d_p^2 \frac{\rho_p}{18\mu} \tag{II.1.2}$$

$$\tau_k = \left(\frac{\nu}{\epsilon}\right)^{1/2} \tag{II.1.3}$$

where τ_p is the characteristic time of a particle $[s]$,
τ_k is the Kolmogorov time scale $[s]$.

Stokes number for the flow rates reported in table II.1.5 are 0.015 (6×10^{-4}) for $Re = 800$ and 0.005 (2×10^{-4}) for $Re = 400$ for $d_p = 5\mu m$ and $d_p = 1\mu m$ respectively. The dissipation rate ϵ in table II.1.5 is the results obtained by RSM model. The Stokes number values, thus, tend toward zero, so that τ_p is indeed, as expected, much smaller than τ_k.

After the verification of this important criterion, the sedimentation velocity, eventually, must be calculated for both particles types. The difference between the fluid density ρ and particles density ρ_p can be neglected in many practical applications even if an error of estimation is occurred between the fluid velocity and particle velocity due to the gravitational acceleration. Error estimation depends on the sedimentation velocity. Sedimentation velocity U_g is calculated from Stokes drag law under the gravitational acceleration, we assume spherical particles into a viscous fluid at a very low particle Reynolds number. This yields :

$$U_g = d_p^2 \frac{(\rho_p - \rho)}{18\mu} g \tag{II.1.4}$$

where g is the acceleration due to gravity $[m.s^{-2}]$,
μ is the dynamic viscosity of the fluid $[Pa.s]$,
d_p is the diameter of the particle $[m]$.

In table II.1.4, the particles density is $\rho_p = 1.05 \times 10^3\ kg.m^{-3}$. U_g is calculated for the big particles $d_p = 5\mu m$, we found that $U_g = 7.5 \times 10^{-10} m.s^{-1}$, which is a very low velocity because the particles density is selected to be very close to that of water.

All of these verifications show that the particles behave like tracers with a very small error in the velocity estimation.

1.5.2 Seeding particles

Tracer particles are added to water in a tank with a defined concentration. In order to avoid the deposition in the tank and to ensure a good recirculation of particles, a magnetic stirrer is put below the seeding beaker. A stir bar is immersed in the liquid (water + particles) to spin very quickly, and thus stir it.

1.5.3 Concentration of seeding particles

The particle concentration plays a key role in micro-PIV measurements. If it is too high, the particles are not discernible on the images. However, if the concentration is too low, the particles are not distributed everywhere; so it is difficult to estimate the velocity distribution in each point of the studied field. In general, the maximal concentration C_p to ensure good seeding for micro-PIV is given by the relationship:

$$\sqrt{\frac{1}{\Delta z C_p}} \gg \frac{d_p}{M}$$

where Δz is the thickness of the laser sheet $[m]$,
d_p is the particles diameter $[m]$,
M is the magnification factor.
In practice, particles are added to the water until there are four particles by interrogation window which has the dimension of 64×64 pixels for $d_p = 5\ \mu m$ (32×32 pixels for $d_p = 1\ \mu m$). This concentration is obtained by mixing $1\ ml$ ($0.25\ ml$) of raw solution charged with particles added to $150\ ml$ of pure water.

1.6 Flow Diagnostics

Optical system or micro-PIV equipments are composed of a laser source which is a pulsed Litron Nd:YAG Laser of $135\ mJ$ ($532\ nm$), doubled in frequency Fig.II.1.11 (Dantec Dynamics). Nd:YAG Lasers are the most commonly used solid-state lasers for micro-PIV in which the beam is generated by Nd^{3+} ions. The Nd^{3+} ion can be incorporated into various host materials. Nd:YAG lasers have a high amplification and good mechanical and thermal properties.

Figure II.1.11: Laser device of Dantec Dynamics type

HiSence 4M camera is used. The Dantec Dynamics HiSence camera offers high resolution (2048×2048 pixels) combined with high sensitivity. Well proven CCD sensors are combined with

Table II.1.6: Camera specifications - source: www.dantecdynamics.com

Model	Frame rate at full resolution	Sensor resolution (pixels)	Pixel size	Min. inter-frame time	Peak QE	Lens mount	Dynamic range
HiSence 4M	11 fps	2048×2048	$7.4\ \mu m$	$200\ nm$	55%	F-mount	12 bit

Peltier cooling to provide excellent image quality in the most demanding applications. Camera features are listed in table II.1.6. This camera is equipped with a Canon MP-E $65\ mm\ f/2.8$ lens. The lens can

Table II.1.7: Depth of fields (mm) - source: CANON lens manual guide

Magnification M for $f/2.8$	$1\times$	$2\times$	$3\times$	$4\times$	$5\times$
Depth of fields (mm)	0.396	0.148	0.088	0.062	0.048

provide a magnification of up to $5\times$. table II.1.7 shows the depth of fields of each magnification. Three extension rings (extension tube) $12,\ 20,\ 32\ mm$ have been added to increase magnification up to 7.7 and thus visualize $1\ \mu m$ PIV particles. The tubes do not contain any optical elements; their purpose is to move the lens farther from the image plane. The farther away the lens is, the closer the focus, the greater the magnification, and also the greater the loss of light (requiring a longer exposure time) (see annex A.1 for more detail).

A filter is used to visualize only particle emission wavelength. We remove the green laser light ($532\ nm$) to have only at the issue the fluorescent particle emission ($\lambda = 607 - 612\ nm$) table II.1.4. The high-pass filter used has the following properties: $T_{avg} > 93\ \%$ on 575–1266 nm, OD > 6 [1] at $561\ nm$, its diameter is of $50\ mm$, and its thickness is of $3.5\ mm$. More details on camera specifications and components are presented in Annex A.1.

The camera is mounted on a 3D traverse system Fig.II.1.12. The minimum displacement that the traverse system can be moved is in the order of $0.01\ mm$ on 3 axes. The maximum displacements are $600\ mm$. The labyrinth-channel is placed on the optical table; the laser and the camera are combined with the optical table.

Figure II.1.12: Traverse system
- source: www.dantecdynamics.com

[1] Optical Density (OD) is a measure of transmitted light. It describes the blocking characteristic of a filter and depends on the amount of energy transmitted by the filter.

1.7 Experimental conditions

The temperature is that of ambient room T = 20°C. The water used for the experiments is a distilled water for which pH is 5.8. The present experiments will be conducted with three flow rates $24\,ml.min^{-1}$ $(1.44\,l.h^{-1})$, $36\,ml.min^{-1}$ $(2.16\,l.h^{-1})$ and $48\,ml.min^{-1}$ $(2.88\,l.h^{-1})$ which correspond to Reynolds numbers 435, 642 and 867 when experiments are performed on geometry 1 and Reynolds numbers of 346, 510 and 687 when experiments are performed on geometry 2, (see table II.1.1); where $q_1 = 24\,ml.min{-}1$ and $q_1 = 48\,ml.min{-}1$ are taken around $q_1 = 36\,ml.min^{-1}$ corresponding to the nominal flow.

1.8 Pressure-discharge curves

An experimental set-up has been developed to determine the pressure loss Fig.II.1.8. In this set-up, the repeating-pattern labyrinth-channel prototype, which is composed of three baffles, has been used.

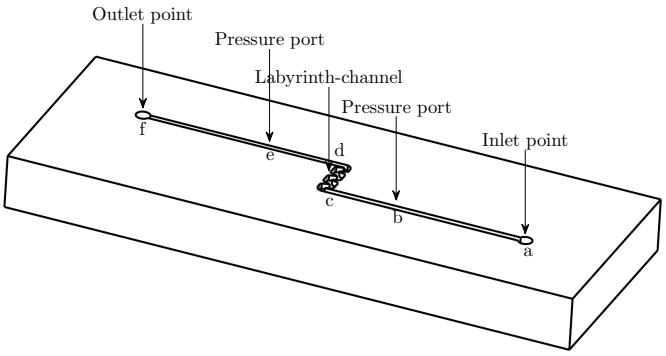

Figure II.1.13: Labyrinth-channel composed of three baffles.

The test duration is fixed to 10 min. The hydraulic circuit is turned on 30 min before acquiring the data to ensure that the flow has reached its steady state. The number of measuring points is about 20000. Then, the averaged value of each parameter (pressure drop and flow rate) is calculated. This test is repeated three times in three different days. The pressure drop for each flow rate is measured by pressure transmitter between the points b and e, Δp_{be} Fig.II.1.13.

The value recorded by pressure transmitter contains three contributions, namely, the pressure drop caused by the labyrinth-channel Δp_{cd} compared with numerical results in section III.2.5, the pressure drop between b and c, and the pressure drop between d and e. The measured pressure drop Δp_{be} can be written as:

$$\Delta p_{be} = \Delta p_{bc} + \Delta p_{cd} + \Delta p_{de} \quad . \tag{II.1.5}$$

The Darcy-Weisbach equation is the best empirical relation for pipe-flow head loss (White, 2010)[105]. The equation used to calculate the pressure drop between b and c; between d and e, can be written as:

$$\Delta p = f_D \frac{\ell}{D_h} \frac{\rho U_m^2}{2} \quad , \tag{II.1.6}$$

where f_D, the Darcy friction factor, is a dimensionless coefficient varying with the flow nature.
For a laminar flow, the friction factor is a function of Reynolds number Re only and is independent of the roughness of the pipe surface. In fully developed laminar flow, $f_D = \alpha/Re$.
where $\alpha = 48$, for a square section, as the cross-sectional inlet and outlet.
The pressure losses, Δp_{bc} and Δp_{de} are written as:

$$\Delta p_{bc} = f_{bc} \frac{\ell_{bc}}{D_{hbc}} \rho \frac{U_{mbc}^2}{2} \quad , \tag{II.1.7}$$

$$\Delta p_{de} = f_{de} \frac{\ell_{de}}{D_{hde}} \rho \frac{U_{mde}^2}{2} \quad , \tag{II.1.8}$$

where $f_{bc} = 48/Re_{bc}$ and $f_{de} = 48/Re_{de}$.
The hydraulic diameter is given by the relationship:

$$D_h = \frac{4A_c}{p_w} \quad , \tag{II.1.9}$$

where A_c, is the cross-sectional area of the pipe $[m^2]$ and p_w is its wetted perimeter $[m]$. For a rectangular section, the hydraulic diameter is written as:

$$D_h = \frac{4a \times b}{2a + 2b} = \frac{2a \times b}{a + b} \quad , \tag{II.1.10}$$

where a is d_{inlet} or d_{outlet} and b is d_{depth} for the labyrinth-channel geometry.
By replacing the labyrinth-channel dimensions, the hydraulic diameter, at the inlet section, is:

$$D_{hbc} = 0.92\ mm \quad ,$$

and at the outlet section is :

$$D_{hde} = 0.98\ mm \quad ,$$

$\ell_{bc} = \ell_{de} = D_1 = 10\ mm$ and $U_m = q_1/A_c$.
The two previous equations can be written as:

$$\Delta p_{bc} = 5.58 \times q_1 \quad , \tag{II.1.11}$$

$$\Delta p_{de} = 4.20 \times q_1 \quad , \tag{II.1.12}$$

where Δp_{bc} and Δp_{de} are pressure drops in [Pa], and q_1 is the measured flow rate $[ml.min^{-1}]$. In a summary, verification of pressure values by pressure sensors is important to accurately perform the discharge-pressure experiment.

Chapter 2

Experimental settings

2.1 Time delays between laser pulses

Time delay between the illumination pulses is an important factor for the micro-PIV treatment success. So, more attention has to be paid to determine this time. In general, the time is defined by flow velocity:

$$\Delta t = \frac{\Delta x}{U} \quad , \tag{II.2.1}$$

where $\Delta x =$ Window size$/4$ is a particle displacement $[m]$,

U is the flow velocity $[m.s^{-1}]$.

It has to be long enough to enable the displacements between the images of the tracer particles to be determined with sufficient resolution and short enough to avoid particles with an out-of-plane velocity component leaving the light sheet between two subsequent illuminations.

The difficulty of the time delay between the illumination pulses determination is that the flow, in labyrinth-channel, is complex. According to Al-Muhammad et al. (2016)[10], it consists in two different regions: one is the main flow and the other is the vortices zones. The velocity profile is plotted on an arbitrary line (the line 3 presented in Fig.III.2.1) in Fig.II.2.1. This profile corresponds to the modelling results obtained by the RSM model for a Reynolds number $Re = 800$ (see part III). We chose two velocities corresponding to the extreme values for estimating Δt. Then, Δt is calculated from the Eq.II.2.1 in order that a particle moves a quarter of interrogation window ((table II.2.1 and table II.2.2).

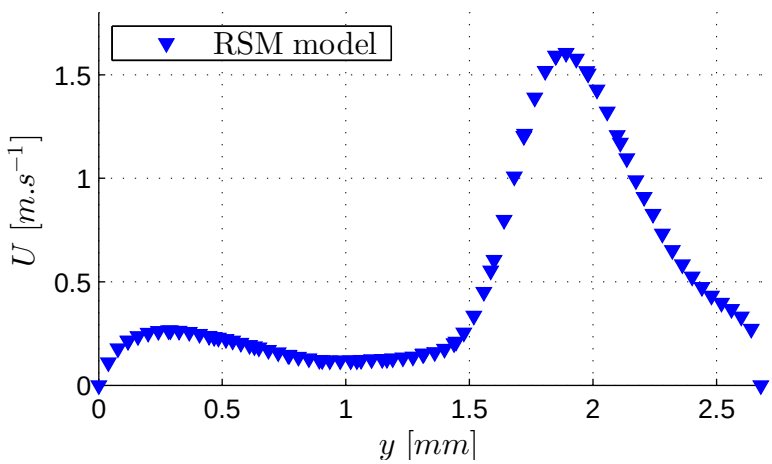

Figure II.2.1: Velocity modulus profile for $Re = 800$ along the line 3 (see lines position on Fig.II.1.6)

The experiments are conducted with two particles diameters. Therefore, these will be treated by two ways (interrogation window size).

Table II.2.1: Acquisition configuration

Acquisition type zoom	Fields of view $(mm \times mm)$	Particle diameter (μm)	Interrogation window $(pixels)$	A window quarter (μm)
$\times 5$	3×3	5	64×64	$\Delta x_1 = 23.28$
$\times 7.7$	2.2×2.2	1	32×32	$\Delta x_2 = 8.59$

Table II.2.2: Time delays between two laser pulses in a pair

Flow rate $q\ (ml.min^{-1})$	Re	Velocity $U\ (m.s^{-1})$	A window quarter $\Delta x_1\ (\mu m)$	A window quarter $\Delta x_2\ (\mu m)$	time $\Delta t_1\ (\mu s)$	time $\Delta t_2\ (\mu s)$
48	800	1.6	23.28	8.59	15	6
		0.264			88	33
36	600	1.168	23.28	8.59	20	8
		0.17			137	51
24	400	0.76	23.28	8.59	30	12
		0.093			250	93

Nevertheless, the velocities estimated from the modelling are slightly varying according to the chosen model. Therefore, the values presented in table II.2.2, for RSM model, are only indicative. Tests are carried out to determine which time delay will be better for micro-PIV experiments. The tests began from the largest time delay for each flow rate, table II.2.2 (which corresponds to the low velocity in the vortex zone) to the time delay which corresponds to the velocity in the mainstream flow. It has been observed that the velocity profiles measured do not evolve anymore when the time delay is lower than that of the mainstream flow (for example 15 μs for flow rate of 48 $ml.min^{-1}$). Therefore, the smallest time delay, presented in table II.2.2, has been taken to perform all the experiments.

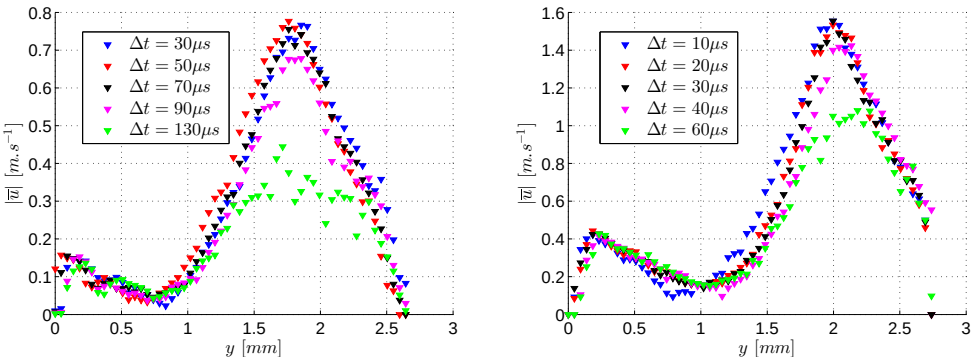

(a) $Re = 435$ (b) $Re = 863$

Figure II.2.2: Velocity modulus profiles for several delays between two laser pulses along the line 3, with particles of 5 μm

Then, frequency between two-image couples is calculated by taking into account that images have to be non-correlated. The calculation of frequency is based on the low-velocity particles in order to ensure that the particles leave the image to avoid the correlated images. A particle in the center of the recirculation zone needs time to get out of this recirculation zone. This time is calculated for the flow modeled by the RSM model. The distance and the spatial averaged velocity on the recirculation zone

allow to calculate this time, and thus the frequency. We thus choose to fix fr $= 1$ Hz according to this principle.

2.2 Prototype positioning and image calibration

2.2.1 Prototype positioning

Firstly, the prototype support, Fig.II.1.5, is installed to be parallel to the laser light sheet and perpendicular to the camera. Then, the distance between the laser source and the prototype support is adjusted. This distance allows having the finest laser highlight at the nearest prototype side. This distance is equal to 30 cm. In order to cover a full baffle, the camera is zoomed. At this position, the depth of field is 48 μm and the field of view has the dimension of 3×3 mm^2. Thus, a pixel is equivalent to a distance of 1.45 μm for a particle diameter of $5\mu m$. For $1\mu m$, fields of view have the dimension of 2.2×2.2 mm^2. Thus, a pixel is equivalent to a distance of 1.09 μm. Finally, the channel middle is defined measuring the distance between the channel bottom and the side between the two plates which was 0.65 mm equivalent to 0.8 mm (channel depth). As a consequence, this distance will be divided by two to have the channel middle distance from one side. These adjustments have been validated by determining channel middle at the prototype inlet and outlet thanks to velocity profiles in the z-direction. This profile has been obtained from the maxima of velocity profiles in the $(x,\ y)$ plane taken at different z-values Fig.II.2.3.

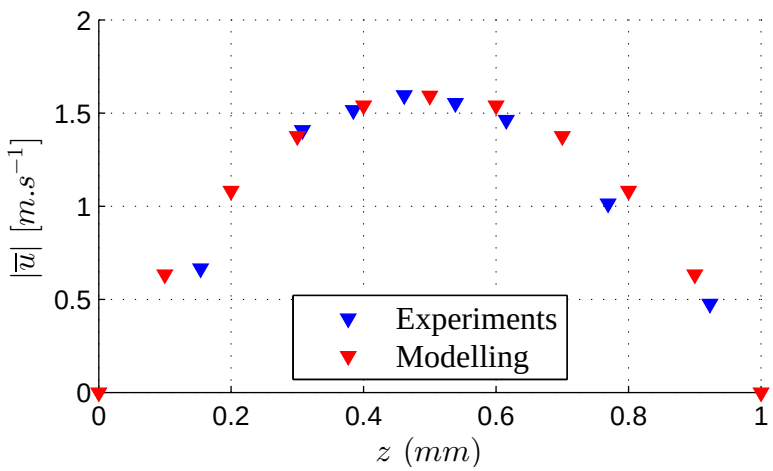

Figure II.2.3: Velocity profile at the entrance in the depth direction to determine the middle of the channel, $Re = 800$

2.2.2 Image calibration

In order to determine the resolution on the PIV image, an image calibration is taken. A known distance must be defined, this allows to calculate the scale factor S_f. In these experiments, a calibration is performed using a millimetric paper as calibration target. This scale factor will help to determine the distance between two image series or rather the distance Δx in $[mm]$ from the distance acquired in pixels. In Fig.II.2.4, the distance between A and B is 2 mm. This gives a scale factor of 0.1976 which will be used later for the velocity calculation. For each experiment, it is advised to perform the image calibration. The velocity value is directly proportional to the scale factor; therefore relative error in the measuring of scale factor gives a relative error in the velocity (error due to calibration only).

Experiments are performed with a camera magnification (M) $\times 5$ ($\times 7$) for $5\mu m$ ($1\mu m$). So from

the equation $S_f = \frac{1}{M}$, it yields $S_f = 0.2$. Table II.2.3 presents the calibration results achieved with $M = 5$ referred to $5\mu m$ particles diameter, where the width $\%$, used in the calibration, is the ratio of the studied image width to the standard image width which corresponds to the ratio of the two scale factors. When comparing the scale factor obtained with the theoretical value $S_f = 0.2$, the calibration error is insignificant. However, the theoretical value $S_f = 0.2$ can not reach. That is why the scale factor is compared to the average of three tests performed. The average of the three scale factors is about 0.1971.

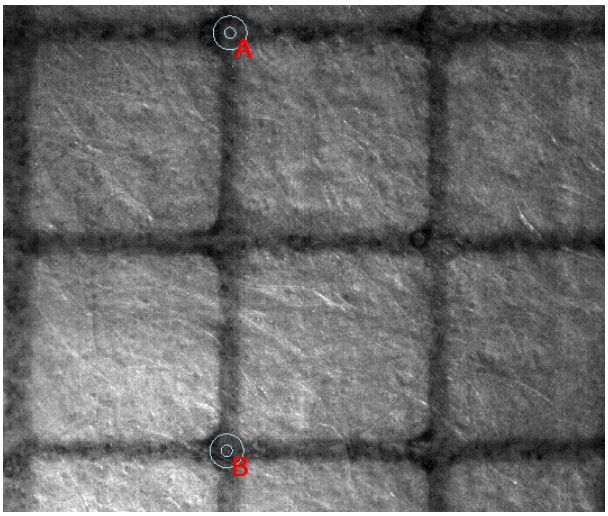

Figure II.2.4: Millimetric paper for calibration.

Table II.2.3: Image calibration data

Description	Scale Factor	% Difference	Width %
Standard calibration	0.2	NA	NA
Calibration 1	0.1976	−0.24	98.8
Calibration 2	0.1968	−0.32	98.4
Calibration 3	0.1970	−0.30	98.5

2.3 Acquisition protocol

One of the difficulties of this experiment is the existence of bubbles in the circuit. Water and seeding particles are moving in the circuit. Air bubbles must be extracted from the circuit because air bubbles in the water disrupt the measurement signals. Another difficulty is to have a perfect prototype-camera-laser positioning to ensure having good images. Acquisition techniques are the following: firstly, the prototype positioning is performed so that the labyrinth-channel is parallel to the camera level. Secondly, the prototype is positioned at a precise distance from the laser objective for which the finest laser light sheet is in the middle of the studied baffle. The minimum width of laser light is $1\ mm$ which is equal to the labyrinth-channel depth.

2.4 Data analysis

Once the micro-PIV images are acquired, the instantaneous particle-displacement fields are calculated using the autocorrelation definition within the data acquisition software (Dantec Dynamic Studio). Firstly, a mask is applied. This mask is used to hide the outside of the flow. The peak detection and vector validation are, then, processed using the Dantec software (see annex A.8). Finally, a Matlab program

is developed to plot velocity vectors and calculate derived statistical quantities such as velocity mean values and variances or the turbulence kinetic energy. An algorithm of data processing is presented in Fig.II.2.5.

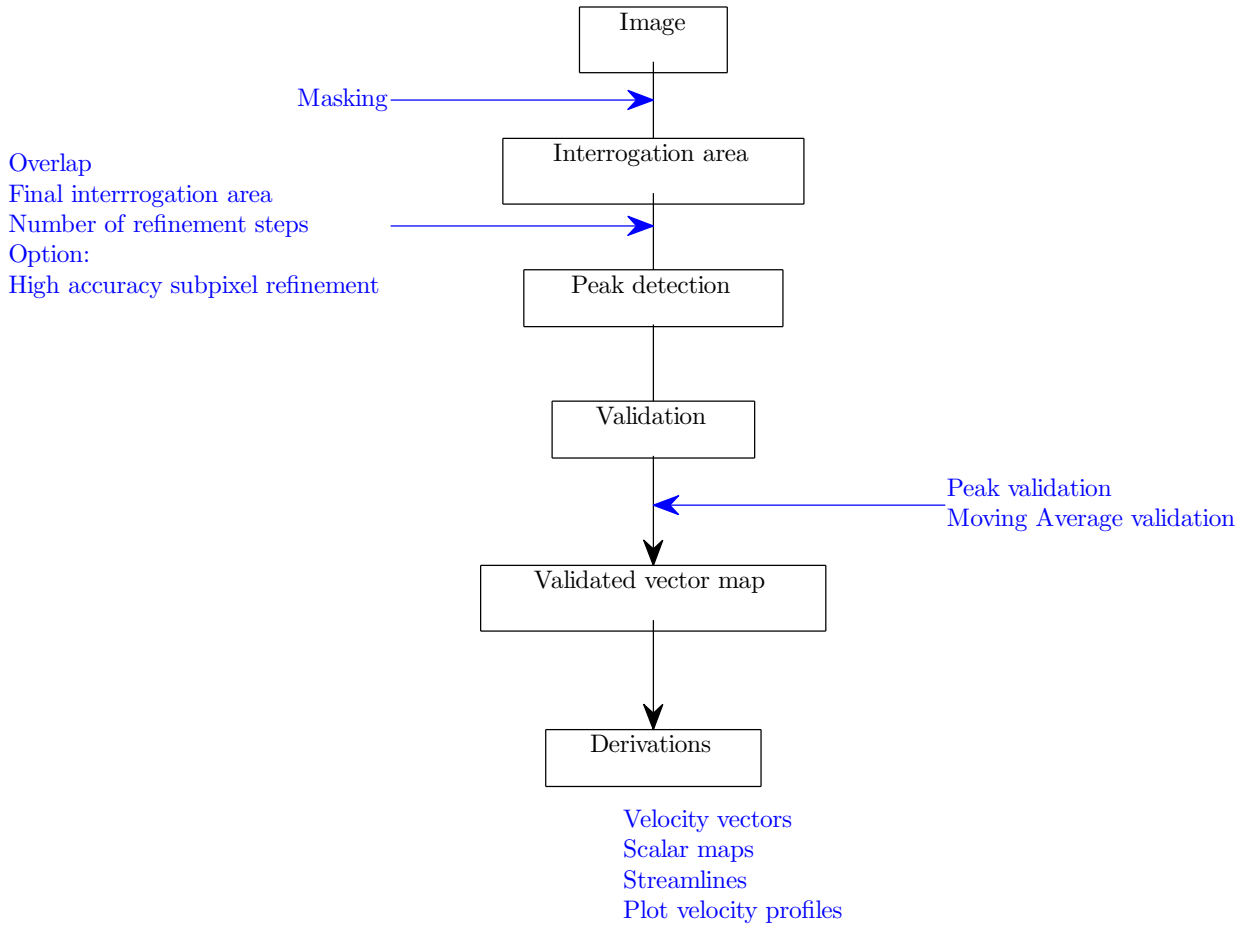

Figure II.2.5: Chart of micro-PIV Data Processing

2.4.1 Cross-correlation

The technique of micro-PIV is the same than PIV one. It is based on a correlation method. Correlation of two functions $f(x)$ and $g(x)$ is defined as the integral of the product of $f^{\star}(x)$ with $g(x)$, the latter being shifted over some distance Δx

$$f = C_{fg}(\Delta x) = \int_{-\infty}^{+\infty} f^{\star}(x) g(x + \Delta x) dx \quad . \tag{II.2.2}$$

The asterisk means that the complex conjugate value is taken (see Bastiaans (1993) [13] and Press et al., (1992)[87], also see annex A.9 for more details).

In the present thesis, adaptive correlation is chosen to treat micro-PIV images. An overlap of 50% is chosen. Process is performed in three steps starting from a first treatment with an interrogation area of 512×512 pixels (256×256 pixels) until 64×64 pixels (32×32 pixels) for $5\mu m$ ($1\mu m$) particles diameter respectively.

2.4.2 Vector validation

Every instantaneous displacement field contains a percentage of spurious vectors which deviate in magnitude and orientation from their physically-consistent neighbors. Spurious vectors occur when the paired-particle displacement peak is exceeded by a noise peak in the cross-correlation, saturated pixel of too few pairs in an interrogation window. The validation of peak correlation chosen by Dynamic Studio software, is the relative height of the highest peak compared to that of the second highest " peak validation " (see Fig.A.7 in annex A.8). In many cases of few particles, this criterion cannot be satisfied. For higher particle concentration, it is often quite satisfactory to use 1.1. If a very strict validation is required a value as high as 2 can be used. The local neighborhood validation is used. This method is used to validate vector maps by comparing each vector with the average of other vectors in a defined neighborhood "Moving Average validation" (see Fig.II.2.5). Vectors that deviate too much from their neighbors can be replaced by the average of the neighbors as a reasonable estimate of true velocities. Valid vectors are converted to velocities using magnification information from the calibration and times between two laser pulses. The percentage of non-valid vectors is about $0-5\%$ ($30-40$ %) for particle $1\mu m$ and $5\mu m$ respectively. Then, the post processing is performed on the valid vectors only.

2.5 Data treatment

2.5.1 Derived quantities

The micro-PIV experiments allow to determine the velocity fields in the studied region of the fluid flow. Each velocity vector or field contains an x-y grid of u and v velocities. From these instantaneous velocity fields, the velocity modulus $|u|$, the velocity fluctuations about the mean (u' and v') are derived and calculated.

$$|u| = \left(u^2 + v^2\right)^{1/2},$$

This formulae can be applicable for the mean velocity $(\overline{u})$ instead of instantaneous velocity (u) to find $|\overline{u}|$, and

$$u' = u - \overline{u},$$

and

$$v' = v - \overline{v}.$$

2.5.2 Statistical quantities

Several statistical quantities are calculated from ensembles of instantaneous velocity fields containing the mean x and y velocity components ($\overline{u}$ and $\overline{v}$), the second-order moments of the fluctuating velocities $\overline{u'^2}$, $\overline{v'^2}$ and $\overline{u'v'}$ and the mean velocity modulus $|\overline{u}|$. These statistical quantities serve to calculate the convergence residues. While the final statistical quantities which serve to plot and calculate the velocity fields and vectors are calculated from:

$$\overline{u_j(x,y)} = \frac{1}{\mathcal{N}_v}\sum_{k=1}^{\mathcal{N}_v} u_{jk}(x,y)$$

j=1,2

$$\overline{|u(x,y)|} = \frac{1}{\mathcal{N}_v}\sum_{k=1}^{\mathcal{N}_v} |u_k(x,y)|$$

where k is the image number, $\mathcal{N}_v$ is the valid image number which is different from the total image number $\mathcal{N}$.

The root-mean-squared velocity fluctuations are defined as:

$$\overline{u_i'v_j'(x,y)} = \frac{1}{\mathcal{N}_v}\sum_{k=1}^{\mathcal{N}_v}\Big(u_{ik}(x,y) - \overline{u_i(x,y)}\Big) \times \Big(u_{jk}(x,y) - \overline{u_j(x,y)}\Big)$$

i and j=1,2.

Interrogation window number, determining the velocity vector number, is related to the image size (L pixels), the interrogation window size (l pixels) and the overlap percent $x = n/d$. The interrogation windows number $\mathcal{N}_w$ is calculated from the formula:

$$\mathcal{N}_w = (\frac{L}{l} * d - n)^2$$

For example, if the micro-PIV data has been acquired with particles diameter of 5 μm. Then, the data has been treated with interrogation windows of 64^2 and overlap percent of $50\% = 1/2$. Therefore, $d = 2$ and $n = 1$. It yields that $\mathcal{N}_w = 3969$ vectors.

2.5.3 Data convergence and image number

The number of image pairs is chosen to ensure convergence criteria toward mean velocity and its components u and v added to the three second-order moments of the fluctuating velocity. In these experiments, we analyze 250 image series for 5 μm and 1 μm. Then, 500 image series are also analyzed for 1 μm.

The number of image pairs should be sufficient to meet the data convergence. Its determination allows to reduce the recording time, to respect the computer memory and to avoid the huge quantity of data in the phase of treatment.

The convergence study is performed and based on two residue types:

- The residues calculated from the mean velocities $\overline{u}$,$\overline{v}$ and $|\overline{u}|$.
- The residues calculated from the second-order fluctuating velocities $\overline{u'^2}$,$\overline{v'^2}$ and $\overline{u'v'}$.

2.5.3.1 Mean velocity

The formula used to calculate the residue value, $\mathcal{R}$, for the mean velocity, is the following:

$$\mathcal{R}_{u_i} = \frac{\left[\frac{1}{i}\sum\limits_{k=1}^{i} u_k - \frac{1}{i-1}\sum\limits_{k=2}^{i} u_{k-1}\right]^2}{\left[\frac{1}{i}\sum\limits_{k=1}^{i} u_k\right]^2} \tag{II.2.3}$$

$\mathcal{R}$ based on v or $|u|$ is calculated from the same relationship replacing only u.

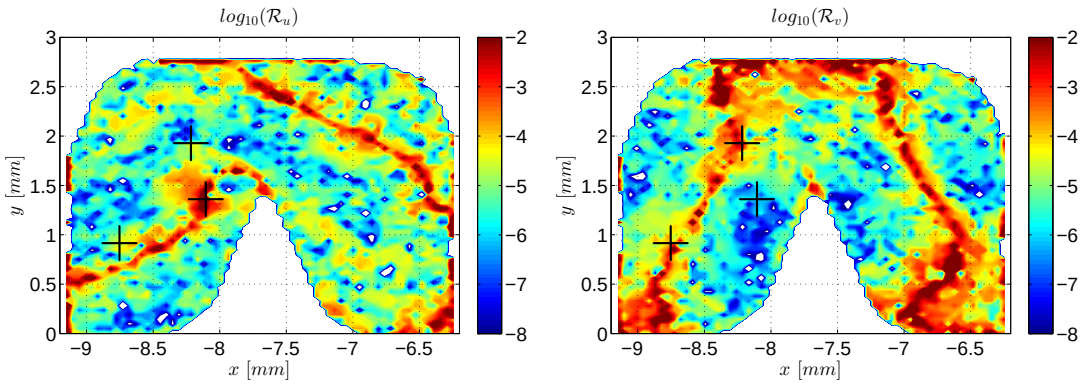

(a) $log_{10}(\mathcal{R}_u)$ (b) $log_{10}(\mathcal{R}_v)$

Figure II.2.6: Mean velocity residues fields, $Re = 863, dp = 5\mu m$, 250 images

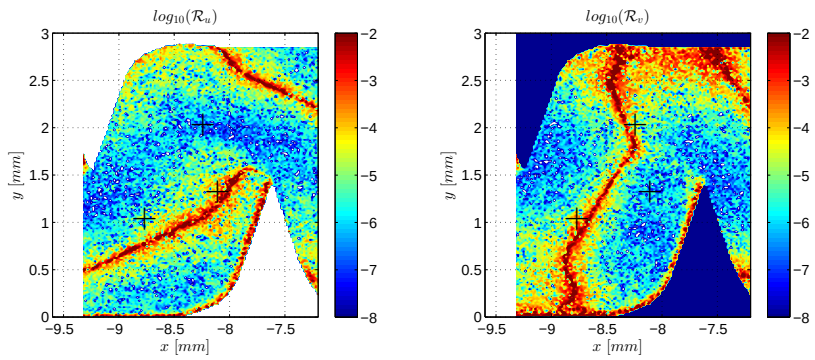

(a) $log_{10}(\mathcal{R}_u)$ (b) $log_{10}(\mathcal{R}_v)$

Figure II.2.7: Mean velocity residues fields, $Re = 687$, $dp = 1\mu m$, 500 images

The mean velocities residues fields, $\mathcal{R}_u$ and $\mathcal{R}_v$ are calculated from Eq.II.2.3. Then, logarithmic values of residues are plotted for the data acquired with $d_p = 5\ \mu m$ and with 250 pairs of images number in Fig.II.2.6 and for the data acquired with $d_p = 1\ \mu m$ and with 500 pairs of images number in Fig.II.2.7. The improvement of residues prediction is obtained from both the using of smaller particles and the increase of pairs of images number. In the case of $5\mu m$, the residues values are globally about 10^{-5}, while for $1\mu m$, the residues have the values of 10^{-7} with 500 pairs of images. The colored-red regions, in these figures, are those for which the residues are superior to 10^{-2}. In fact, these maximums are due to almost zero values of velocity fields (see Fig.II.2.8). The residues evolution along images for 3 points located in these regions p1(-8.75,1) mm, p2(-8.1,1.4) mm and p3(-8.25,2) mm [1], are plotted in Fig.II.2.9 and Fig.II.2.10. p2 and p3 are chosen for which $\mathcal{R}_u > 10^{-2}$ and $\mathcal{R}_v > 10^{-2}$ respectively. Then, the velocities convergences are plotted in Fig.II.2.11 and Fig.II.2.12. The $\overline{u}$ and $\overline{v}$ velocities are almost zero in p2 and p3 respectively. Therefore, as it is noted above the high value of residues obtained in these 2 points are due to the velocity values which are closer to zero.

[1]The 3 points are shown on all the residue fields with a (+) sign.

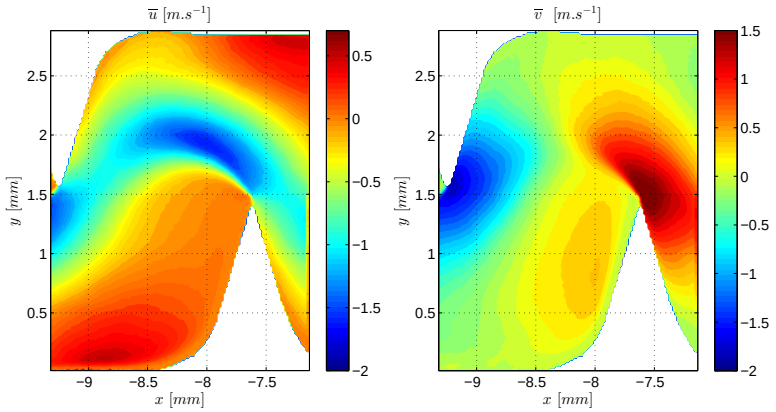

(a) $\overline{u}$ (b) $\overline{v}$

Figure II.2.8: Mean velocity fields, $Re = 687$, $dp = 1\mu m$, 500 images

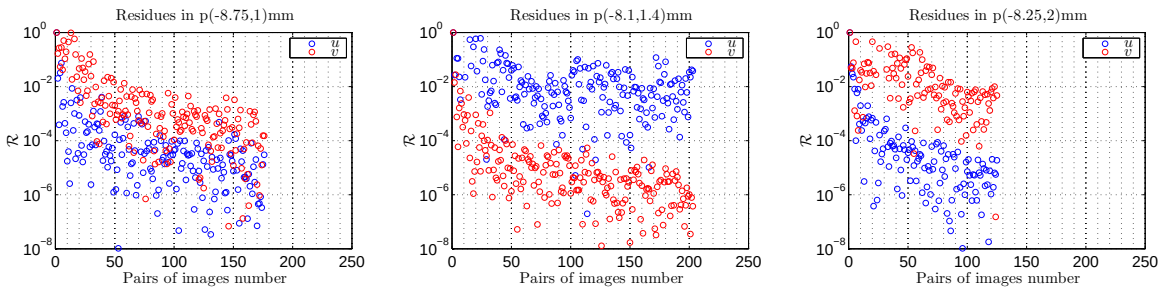

(a) Point 1 (b) Point 2 (c) Point 3

Figure II.2.9: Convergence of the mean velocity residues, $Re = 863$, $dp = 5\mu m$, 250 images

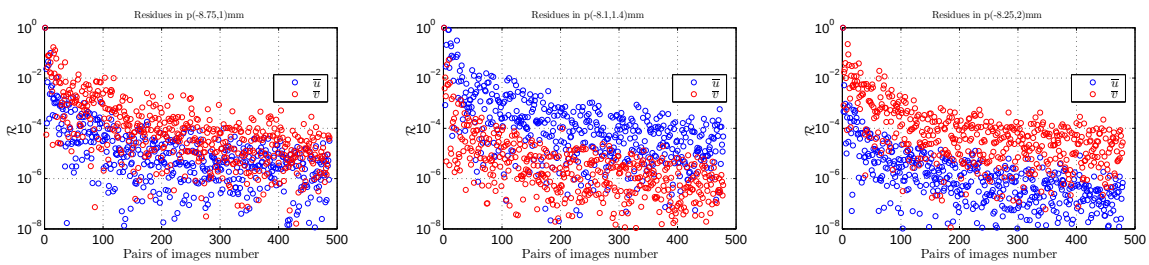

(a) Point 1 (b) Point 2 (c) Point 3

Figure II.2.10: Convergence of the mean velocity residues, $Re = 687$, $dp = 1\mu m$, 500 images

For all studied points, the number of samples is inferior to 250 (500) as the spurious instantaneous vectors are eliminated when the convergence study is performed. When using $d_p = 5\mu m$ particles. In p1 and p3, u and v do not reach the mean value since only 170 and 130 vectors are valid respectively. Nevertheless, with $d_p = 1\mu m$, all velocities values reach the mean value after 200 pairs of image.

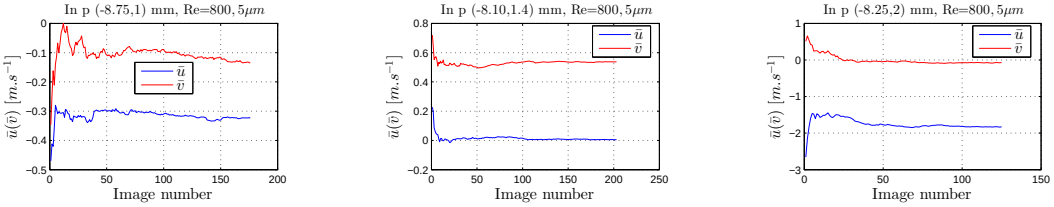

(a) Point 1 (b) Point 2 (c) Point 3

Figure II.2.11: u and v velocities components, $Re = 863$, $d_p = 5\mu m$, 250 images

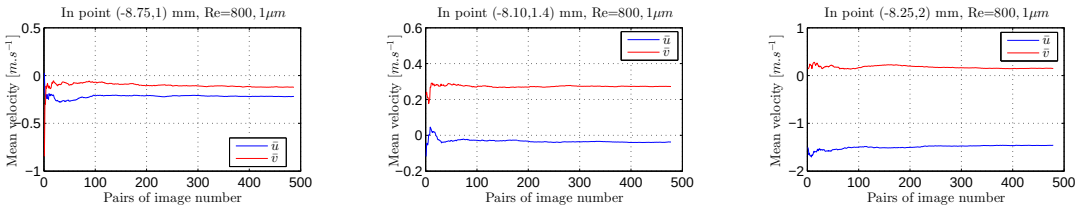

(a) Point 1 (b) Point 2 (c) Point 3

Figure II.2.12: u and v velocities components, $Re = 687$, $d_p = 1\mu m$, 500 images

2.5.3.2 Fluctuating velocity

The second-order moments of fluctuating velocities residues are calculated by the formula:

$$\mathcal{R}_{u_i'^2} = \frac{\left[\frac{1}{i}\sum_{k=1}^{i} u_k'^2 - \frac{1}{i-1}\sum_{k=2}^{i} u_{k-1}'^2\right]^2}{\left[\frac{1}{i}\sum_{k=1}^{i} u_k'^2\right]^2} \tag{II.2.4}$$

$\mathcal{R}$ based on v'^2 or $u'v'$ is calculated from the same relationship replacing only u'^2. The values obtained, by this formula, are plotted on Fig.II.2.13 and Fig.II.2.14. The evolution of residues according to the second-order moments fluctuating velocities is more important than for the mean velocity (point 3). The second-order moments of fluctuating velocities for three points in the flow are plotted on Fig.II.2.15 and Fig.II.2.16. The second-order fluctuating velocities reach a stable value in the main flow. However, such a behavior is not achieved in the recirculation zone (point 2).

The residue values obtained are 10^{-5}, for fluctuating velocities which is, probably, enough when all velocity vectors are valid, especially, in the mainstream flow where the mean and fluctuating velocities reach a state stable. However, additional images are advised to better analyze the recirculation zone.

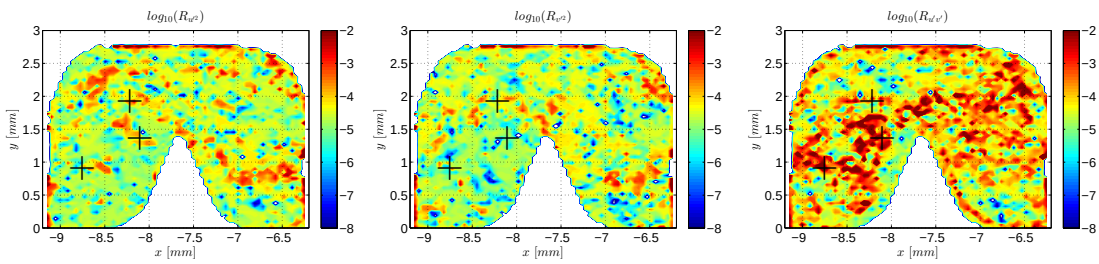

(a) $log_{10}(\mathcal{R}_u'^2)$ (b) $log_{10}(\mathcal{R}_v'^2)$ (c) $log_{10}(\mathcal{R}_{u'v'})$

Figure II.2.13: Convergence based on the second-order moments of the fluctuating velocity, $Re = 863$, $5\mu m$, 250 images

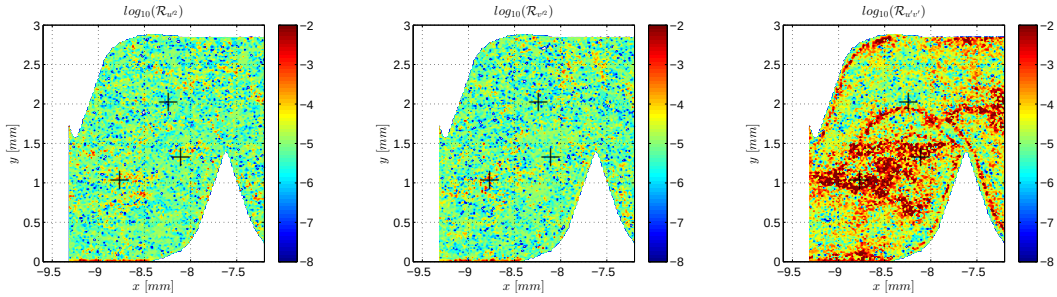

(a) $log_{10}(\mathcal{R}_u'^2)$ (b) $log_{10}(\mathcal{R}_v'^2)$ (c) $log_{10}(\mathcal{R}_{u'v'})$

Figure II.2.14: Convergence based on the second-order moments of the fluctuating velocity, $Re = 687$, $1\mu m$, 500 images

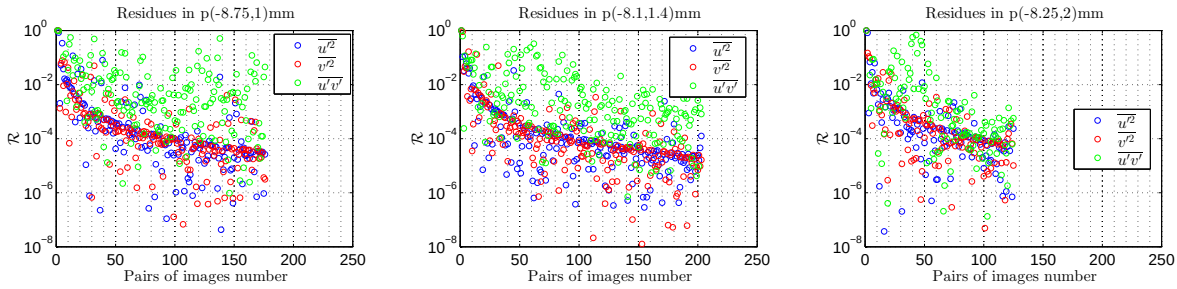

(a) Point 1 (b) Point 2 (c) Point 3

Figure II.2.15: Convergence based on the second-order moments of the fluctuating velocity, $Re = 863$, $5\mu m$, 250 images

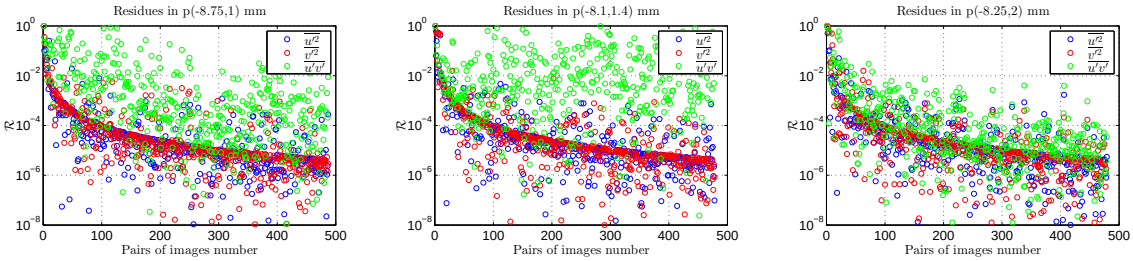

(a) Point 1 (b) Point 2 (c) Point 3

Figure II.2.16: Convergence based on the second-order moments of the fluctuating velocity, $Re = 687$, $1\mu m$, 500 images

2.6 Uncertainty analysis

2.6.1 Peak locking

The recording of the particle signal on the discrete grid of a CCD sensor leads to introduce new bias. Indeed, the recording on a sensor implies a spatial sampling of the signal scattered by the particles. If the sampling frequency satisfies the Nyquist criterion, the original signal can be reconstructed without alteration. However, images of particle size less than 2 pixels can cause a frequent defect called ”peak-locking” which appears when calculating the displacement field from the integer pixel values

(Westerweel, 2000) [104]. Significantly, peak-locking reduces the accuracy of micro-PIV measurements. Although the effects on the mean velocity flow statistics may be within acceptable limits. In other words, the mean velocity fields and profiles are the only statistics that are insensitive to peak locking as it is found by Christensen (2004) [30]. The peak-locking effect can lead to awkward results for instantaneous spatial derivative data such as velocity gradient and turbulent velocity fluctuations. The easiest way to demonstrate this phenomenon is to plot a histogram of the fractional part of velocity components (displacement), which is between -0.5 and $+0.5$ pixel units. Fig.II.2.17, Fig.II.2.19 present the displacement percentage in the third baffle, for $d_p = 5\mu m$, for both $Re = 400$ and $Re = 800$. While the histograms of displacements, for $d_p = 1\mu m$, are presented in Fig.II.2.18 and Fig.II.2.20. The degree of peak locking can be quantified as:

$$C = 1 - \frac{N_{min}}{N_{max}} \tag{II.2.5}$$

where N_{min} (minimum of %) and N_{max} (maximum of %) are the lowest and highest percent of counts in the fractional histogram. Hence, if $C = 0$, this indicates the absence of peak-locking, whereas $C = 1$ indicates very strong peak locking. Four levels of peak-locking can be distinguished:

- $C < 0.2$, virtually no peak-locking occurs,
- $0.2 < C < 0.4$ mild peak-locking occurs,
- $0.4 < C < 0.6$ strong peak-locking occurs,
- $C > 0.6$ severe peak-locking.

The figures for the peak-locking analysis in this study show that there is no peak-locking for estimating velocity in the x and y directions in the third baffle, for the two particles diameters ($d_p = 5\mu m$ and $d_p = 1\mu m$). Therefore, the second-order moments of the fluctuating velocity fields and profiles are insensitive to peak-locking.

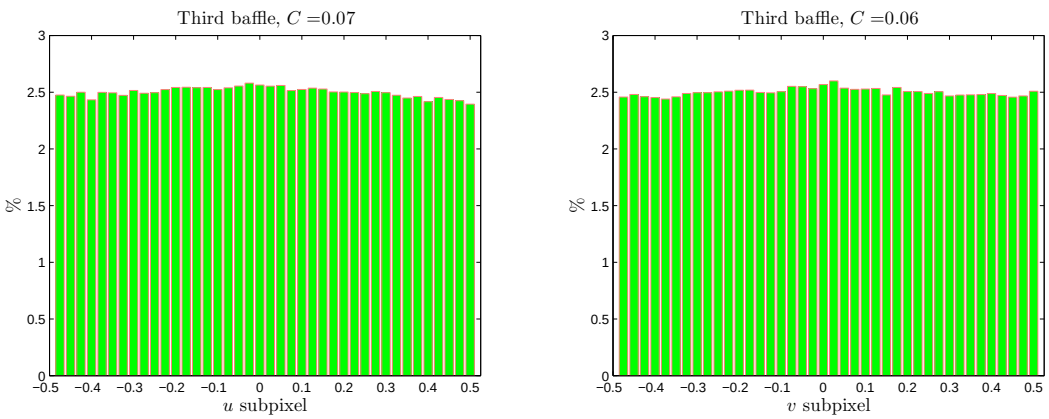

(a) u subpixel (b) v subpixel

Figure II.2.17: The subpixel analysis in the third baffle, $Re = 435$, $d_p = 5\mu m$

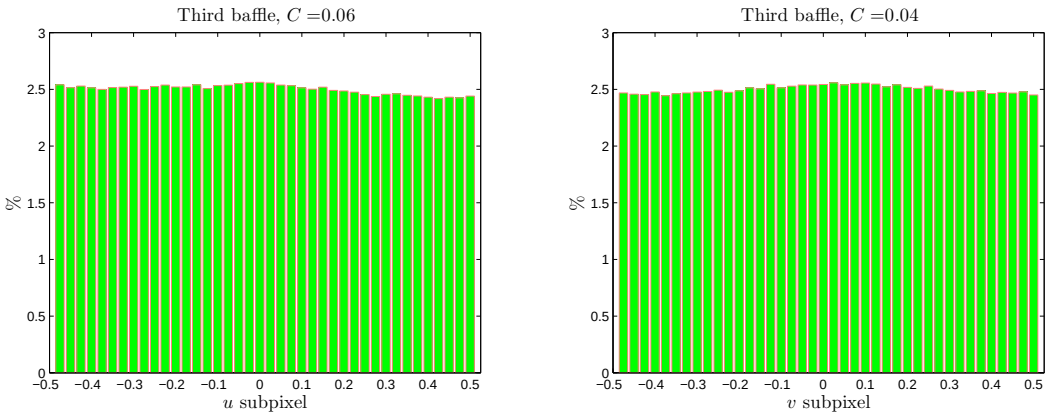

(a) u subpixel (b) v subpixel

Figure II.2.18: The subpixel analysis in the third baffle, $Re = 346$, $d_p = 1\mu m$

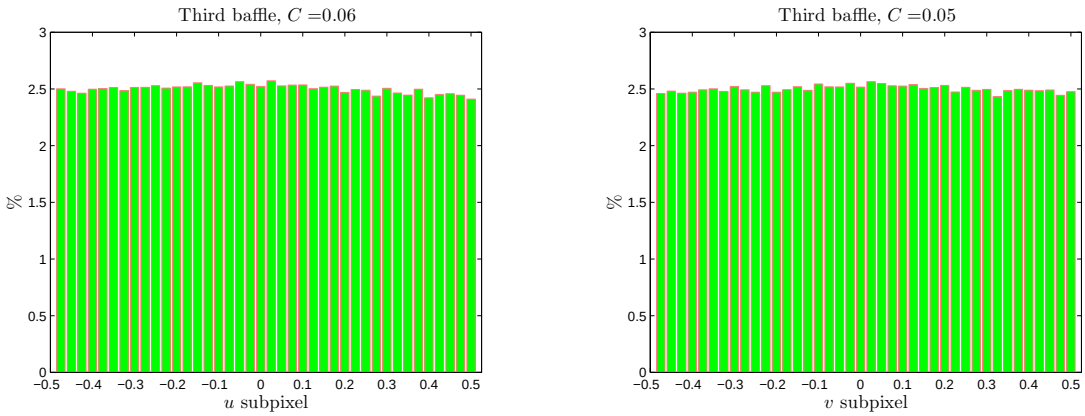

(a) u subpixel (b) v subpixel

Figure II.2.19: The subpixel analysis in the third baffle, $Re = 863$, $d_p = 5\mu m$

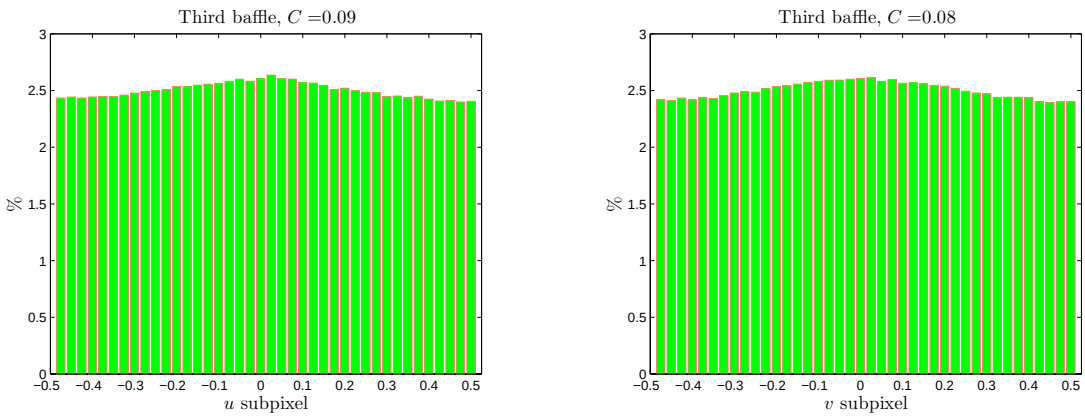

(a) u subpixel (b) v subpixel

Figure II.2.20: The subpixel analysis in the third baffle, $Re = 687$, $d_p = 1\mu m$

2.6.2 Signal-to-noise ratio

Signal-to-noise ratio (abbreviated SN Ratio) is used in micro-PIV to compare the level of a desired signal to the level of background noise. In PIV, the measurement signal is contained in the recorded intensity of the particle image pattern superimposed on a variety of noise sources. The primary peak ratio (PPR) Fig.II.2.21 from which SN ratio is determined, is defined as (Kumer and Hassebrook, 1990)[61]:

$$PPR = \frac{C_{max}}{C_2} \tag{II.2.6}$$

where C_{max} is the primary peak height (the signal part);
C_2 is the height of the secondary peak (the noise part).

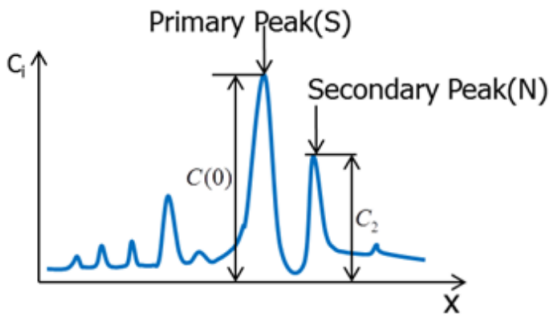

Figure II.2.21: Example of $1D$ graphical representation of correlation SNR by the PPR method (Xue et al., 2013) [108].

The information about the true displacement in the correlation plane is contained in the correlation of the fluctuating intensities, and random correlation peaks also come from the correlation of the fluctuating intensities only. The image background noise has no contribution to neither the signal part nor the noise part of the cross-correlation. So, in order to obtain a more accurate signal-to-noise ratio of the cross-correlation plane, eliminating the effect of image background noise is necessary. The subtraction of the mean image from the raw images helps to eliminate the background noise. Nevertheless, some information about the particles signal is also lost when subtracting the mean image without having an influence on the final results. The SNR have the values 15 for $d_p = 5\mu m$ and 7 for $d_p = 1\mu m$ which is good in comparison with the background noise. In PIV, each signal with a SNR close to 4, is considered as noise.

2.7 Conclusion

In this chapter, the experimental setting is explained and detailed. Firstly, the choice of several important parameters used in micro-PIV is justified. Then, the acquisition and treatment protocol is detailed. Afterwards, extensive study of data convergence is presented. This analysis allows to determine the residues of mean and fluctuating second-order moments velocities. The residues based on the mean velocities are about $10^{-6} - 10^{-7}$ using $1\mu m$ particle, $10^{-4} - 10^{-6}$ using $5\mu m$ for mean velocities. The residues based on the fluctuating second-order moments velocities are about 10^{-5} for $\overline{u'^2}$ and $\overline{v'^2}$, nevertheless the residues are $10^{-3} - 10^{-4}$ for $\overline{u'v'}$. Some errors are quantified such as peak locking and signal-to-noise ratio. It appears that there is no peak-locking and the signal-to-noise ratio is about 7 which is satisfactory for micro-PIV experiments.

Part III

Numerical modelling

Table of Contents

1 Model presentation **75**
- 1.1 The equations of fluid motion . . . 75
- 1.2 Reynolds averaged equations . . . 75
- 1.3 Boussinesq hypothesis . . . 76
- 1.4 Spalart–Allmaras model . . . 77
  - 1.4.1 Introduction . . . 77
  - 1.4.2 Spalart–Allmaras equations . . . 77
- 1.5 $k - \epsilon$ models . . . 79
  - 1.5.1 High-Reynolds number $k - \epsilon$ models . . . 79
  - 1.5.2 Low-Reynolds number $k - \epsilon$ models . . . 80
  - 1.5.3 $k - \epsilon$ modelled equations . . . 80
- 1.6 Reynolds stress model (RSM) . . . 81
  - 1.6.1 Introduction . . . 81
  - 1.6.2 RSM equations . . . 81
- 1.7 Wall treatment . . . 83
  - 1.7.1 Near-wall layers . . . 83
  - 1.7.2 Wall functions . . . 84
  - 1.7.3 Wall Boundary conditions . . . 86
  - 1.7.4 Damping functions . . . 86

2 Numerical resolution **89**
- 2.1 Geometry of the study . . . 89
- 2.2 Meshing . . . 90
- 2.3 Boundary conditions . . . 91
- 2.4 Solution methods . . . 92
  - 2.4.1 Solver choice . . . 92
  - 2.4.2 Pressure-velocity coupling . . . 93
  - 2.4.3 Interpolation methods for gradients . . . 93
  - 2.4.4 Interpolation methods for pressure . . . 94
  - 2.4.5 Spatial discretization . . . 94
  - 2.4.6 Convergence . . . 94
- 2.5 Numerical calculation of the pressure losses . . . 95
- 2.6 Conclusion . . . 96

Chapter 1

Model presentation

As mentioned in the chapter I.2, there is not a fixed model in the literature to model such a labyrinth-channel flow. Labyrinth-channel geometry is complex and the flow undergoes several direction changes, these changes induce vortex zones. The prediction of these vortices is difficult with a laminar model so that turbulence models are chosen to perform the modelling. In this chapter, the different turbulence approaches to model the flow in the labyrinth-channel are presented and explained. All boundary conditions and approximations imposed are also justified.

1.1 The equations of fluid motion

The differential form of the continuity equation and Navier-Stokes momentum equations for compressible Newtonian fluid can be written as (Pope, 2000) [85]:

$$\frac{\partial \rho}{\partial t} + \frac{\partial \rho u_i}{\partial x_i} = 0 \tag{III.1.1}$$

The equations for momentum:

$$\frac{\partial \rho u_i}{\partial t} + \frac{\partial \rho u_i u_j}{\partial x_j} = -\frac{\partial p}{\partial x_i} + \frac{\partial \tau_{ij}}{\partial x_i} \tag{III.1.2}$$

where ρ is the fluid density $[kg.m^{-3}]$.

The instantaneous velocity $u_i(x_j, t)$, where $(i = 1, 2, 3)$ and the pressure $p(x_j, t)$ at any time t and in any point x_j (where $j = 1, 2, 3$) of the flow field are treated independently of the temperature.

The viscous stress tensor τ_{ij}, is proportional to the symmetric part of the deformation rate tensor (Newtonian fluid) with Stokes hypothesis and is given by:

$$\tau_{ij} = \mu \left(\frac{\partial u_i}{\partial x_j} + \frac{\partial u_j}{\partial x_i} - \frac{2}{3} \frac{\partial u_k}{\partial x_k} \delta_{ij} \right) \tag{III.1.3}$$

where μ is the dynamic fluid viscosity $[kg.m^{-1}.s^{-1}]$,
δ_{ij} is the Kronecker symbol.

1.2 Reynolds averaged equations

In the Reynolds decomposition (Reynolds, 1895) [93], all of the solution variables in the instantaneous (exact) Navier-Stokes equations are decomposed into the mean (ensemble-averaged or time-averaged) and fluctuating components.

$$u_i = \overline{u_i} + u_i' \tag{III.1.4}$$

where $\overline{u_i}$ and u_i' are the mean and fluctuating velocities ($i = 1, 2, 3$).
For a scalar such as pressure, this decomposition is written as:

$$p = \overline{p} + p' \tag{III.1.5}$$

Substituting the equations of velocities and pressure decomposition Eq.III.1.4 and Eq.III.1.5 into the instantaneous continuity and momentum equations Eq.III.1.1 and Eq.III.1.2 and taking the average yields the Reynolds-averaged Navier-Stokes (RANS) equations (dropping the overbar on the mean velocity):

$$\frac{\partial \rho}{\partial t} + \frac{\partial \rho u_i}{\partial x_i} = 0 \tag{III.1.6}$$

$$\frac{\partial \rho u_i}{\partial t} + \frac{\partial \rho u_i u_j}{\partial x_j} = -\frac{\partial p}{\partial x_i} + \frac{\partial \tau_{ij}}{\partial x_j} + \frac{\partial}{\partial x_j}\left(-\rho \overline{u_i' u_j'}\right) \tag{III.1.7}$$

In theory, the average should also involve the fluid density. In the present study, the fluid has a constant density, therefore the application of the density decomposition makes no sense because the density does not vary. These equation terms have the same general form as the exact Navier-Stokes equations. Nevertheless, additional terms appear to represent turbulence effects. These terms are called the Reynolds stresses $\rho \overline{u_i' u_j'}$.

1.3 Boussinesq hypothesis

A closure problem arises in the Reynolds-averaged Navier-Stokes (RANS) equations because of the non-linearity of the Reynolds stress terms $\rho \overline{u_i' u_j'}$. Closing and modelling the RANS equations (Eq.III.1.7) require modelling the Reynolds stresses. Joseph Boussinesq has introduced the concept of eddy viscosity to model the Reynolds stresses. In this method, called the Boussinesq hypothesis (Hinze, 1975)[49], the Reynolds stresses are related linearly to the mean velocity gradients. A new proportionality constant $\mu_t > 0$, the turbulence (eddy) viscosity, has been introduced:

$$-\rho \overline{u_i' u_j'} = 2\mu_t S_{ij} - \frac{2}{3}\rho k \delta_{ij} \tag{III.1.8}$$

where μ_t is the turbulence viscosity(eddy viscosity) $[kg.m^{-1}.s^{-1}]$,
k is the mean turbulent kinetic energy $[m^2.s^{-2}]$. This is given by the formula:

$$k = \frac{1}{2}\overline{u_i' u_i'} \tag{III.1.9}$$

i and $j = 1, 2, 3$.
The mean strain rate tensor, S_{ij} can be written in the following way:

$$S_{ij} = \frac{1}{2}\left[\frac{\partial u_i}{\partial x_j} + \frac{\partial u_j}{\partial x_i}\right] - \frac{1}{3}\frac{\partial u_k}{\partial x_k}\delta_{ij} \quad . \tag{III.1.10}$$

In order to obey the definition of turbulence kinetic energy for modelling compressible flow, the last term, in Eq.III.1.10 is included. The same equation Eq.III.1.8 can be written more explicitly as:

$$-\rho \overline{u_i' u_j'} = \mu_t\left(\frac{\partial u_i}{\partial x_j} + \frac{\partial u_j}{\partial x_i}\right) - \frac{2}{3}\left(\rho k + \mu_t \frac{\partial u_k}{\partial x_k}\right)\delta_{ij} \tag{III.1.11}$$

This hypothesis is employed in several turbulent models, such as algebraic models, the Spalart-Allmaras model, the $k - \epsilon$ models and the $k - \omega$ models. The Boussinesq hypothesis is both the strength and the weakness of models that have used this hypothesis. The effect of turbulence on the mean flow is represented in the same way as molecular viscosity affects a laminar flow. The hypothesis also allows

to introduce intuitive scalar turbulence variables like the turbulent energy and its dissipation rate and to relate these variables to even more intuitive variables like turbulence intensity and turbulence length scale. Nevertheless, the Boussinesq hypothesis is not, always, valid. The Reynolds stress tensor is proportional to the strain rate tensor in simple flows like flat plate boundary layers and wakes, but in complex flows, like flows with strong curvature, or strongly accelerated or decelerated flows, this assumption is not valid. Applying this hypothesis, two-equation models predict with non-separable problems strongly rotating flows and other flows where curvature effects are significant. That is the main weakness of the Boussinesq hypothesis. Another weakness is that μ_t is assumed positive, which is not always the case (for some flows, there are areas with a counter-gradient, so that $\mu_t < 0$). For incompressible and steady flow, the Reynolds-averaged Navier-Stokes equations (RANS), according to these approximations, are:

$$\frac{\partial u_i}{\partial x_i} = 0 \quad , \tag{III.1.12}$$

$$\rho u_j \frac{\partial u_i}{\partial x_j} = -\frac{\partial p}{\partial x_i} + \frac{\partial}{\partial x_j}\left[(\mu + \mu_t)\left(\frac{\partial u_i}{\partial x_j} + \frac{\partial u_j}{\partial x_i}\right)\right] \tag{III.1.13}$$

1.4 Spalart–Allmaras model

1.4.1 Introduction

The Spalart–Allmaras model is a simple one-equation model that solves a modeled transport equation for the turbulent kinematic viscosity. This embodies a relatively new class of one-equation models in which it is not necessary to calculate a length scale related to the local shear layer thickness. The Spalart-Allmaras model was designed specifically for wall-bounded flows and has been shown to give good results for boundary layers subjected to adverse pressure gradients. The Spalart–Allmaras model is effectively a low-Reynolds-number model, requiring the viscosity-affected region of the boundary layer to be properly resolved[1].

In turbulence models that employ the Boussinesq approach, the central issue is how the eddy viscosity is computed. The model proposed by Spalart and Allmaras (1992)[97] solves a transport equation for a quantity that is a modified form of the turbulent kinematic viscosity.

1.4.2 Spalart–Allmaras equations

The transported variable in the Spalart-Allmaras model, $\tilde{\nu}$, is identical to the turbulent kinematic viscosity except in the near-wall (viscous-affected) region. The transport equation for $\tilde{\nu}$ is :

$$\frac{\partial}{\partial x_i}(\rho\tilde{\nu}u_i) = G_\nu + \frac{1}{\sigma_{\tilde{\nu}}}\left[\frac{\partial}{\partial x_j}\left\{(\mu + \rho\tilde{\nu})\frac{\partial\tilde{\nu}}{\partial x_j}\right\} + C_{b2}\rho\left(\frac{\partial\tilde{\nu}}{\partial x_j}\right)^2\right] - Y_\nu \tag{III.1.14}$$

The turbulent viscosity μ_t, is computed from:

$$\mu_t = \rho\tilde{\nu}f_{\nu 1} \tag{III.1.15}$$

where the viscous damping function, $f_{\nu 1}$, is given by:

$$f_{\nu 1} = \frac{\chi^3}{\chi^3 + C_{\nu 1}^3} \tag{III.1.16}$$

[1] ANSYS FLUENT Theory Guide, ANSYS Inc., 2003, chapter 10.

and

$$\chi = \frac{\tilde{\nu}}{\nu} \tag{III.1.17}$$

The production of turbulent viscosity term, G_ν is modelled as:

$$G_\nu = C_{b1}\rho\tilde{S}\tilde{\nu} \tag{III.1.18}$$

where

$$\tilde{S} = S + \frac{\tilde{\nu}}{\kappa^2 d^2} f_{\nu 2} \tag{III.1.19}$$

and

$$f_{\nu 2} = 1 - \frac{\chi}{1 + \chi f_{\nu 1}} \tag{III.1.20}$$

where d is the distance from the wall, and S is a scalar measure of the deformation tensor. In the original model proposed by Spalart-Allmaras, S is based on the magnitude of the vorticity. However, modifications take into account the effect of mean strain on the turbulence production (Dacles-Mariani et al., 1995)[32]:

$$S = |\Omega_{ij}| + C_{prod} min\left(0, |S_{ij}| - |\Omega_{ij}|\right) \tag{III.1.21}$$

where $C_{prod} = 2.0$,$|\Omega_{ij}| = \sqrt{2\Omega_{ij}\Omega_{ij}}$, $|S_{ij}| = \sqrt{2S_{ij}S_{ij}}$ where Ω_{ij} is the mean rate-of-rotation tensor which is defined by:

$$\Omega_{ij} = \frac{1}{2}\left(\frac{\partial u_i}{\partial x_j} - \frac{\partial u_j}{\partial x_i}\right) \quad ; \tag{III.1.22}$$

and the main strain rate, S_{ij}, is defined as:

$$S_{ij} = \frac{1}{2}\left(\frac{\partial u_j}{\partial x_i} + \frac{\partial u_i}{\partial x_j}\right) \quad . \tag{III.1.23}$$

The destruction term, Y_ν, that occurs in the near-wall region due to wall blocking and viscous damping, is modelled as :

$$Y_\nu = C_{w1}\rho f_w \left(\frac{\tilde{\nu}}{d}\right)^2 \quad ; \tag{III.1.24}$$

$$f_w = g\left[\frac{1 + C_{w3}^6}{g^6 + C_{w3}^6}\right]^{1/6} \quad ; \tag{III.1.25}$$

$$g = r + C_{w2}\left(r^6 - r\right) \quad ; \tag{III.1.26}$$

$$r \equiv \frac{\tilde{\nu}}{\tilde{S}^2 d^2} \quad ; \tag{III.1.27}$$

where C_{w1}, C_{w2} and C_{w3} are constants (tableIII.1.1).

Table III.1.1: The constants of Spalart-Allmaras model.

C_{b1}	C_{b2}	$\sigma_{\tilde{\nu}}$	$C_{\nu 1}$	C_{w1}	C_{w2}	C_{w3}
0.1355	0.622	2/3	$\frac{C_{b1}}{\kappa^2} + \frac{(1+C_{b2})}{\sigma\tilde{\nu}}$	7.1	0.3	2.0

1.5 $k - \epsilon$ models

Two-equation turbulence $k-\epsilon$ models are some of the most common turbulence models. They are used for most types of engineering problems. These models include two additional transport equations for the turbulent kinetic energy k, defined in Eq.III.1.9, and the turbulent dissipation rate ϵ, defined in Eq.III.1.28, in order to represent the turbulent properties of the flow.

$$\epsilon = \nu \overline{\frac{\partial u_i'}{\partial x_j} \frac{\partial u_i'}{\partial x_j}} \tag{III.1.28}$$

Hereby, ϵ is the isotropic turbulent dissipation rate or, is the rate at which turbulence kinetic energy is converted into thermal internal energy. Therefore, this variable is related to the fluctuating velocities. While the total dissipation, discussed in section.IV.1.4, is produced by the mean and fluctuating velocities. The first transported variable determines the energy in the turbulent velocity field, whereas the second variable, determines the length or the time scale of turbulence. The modelled transport equation for k is derived from the exact equation, while the modelled transport equation for ϵ is obtained using physical reasoning and bears little resemblance to its mathematically exact counterpart. $k - \epsilon$ models also often have problems to predict strongly decelerated flows like stagnation flows.

1.5.1 High-Reynolds number $k - \epsilon$ models

1.5.1.1 Standard $k - \epsilon$

The standard $k - \epsilon$ model was initially proposed by Launder and Spalding (1972)[66] and it was developed by Launder and Jones (1972)[64]. Standard $k - \epsilon$ model is recommended for high Reynolds number flows (Launder and Spalding, 1974) [67]. It is considered as a powerful tool for prediction of many complex flow problems including jets, wakes, wall flows. This model was derived by assuming that the flow is fully turbulent. Therefore, the effects of molecular viscosity are negligible (Launder and Spalding 1972) [66]. This model provides robustness, economy and reasonable accuracy for a wide range of turbulent flows.

1.5.1.2 RNG $k - \epsilon$

The weakness of the standard $k - \epsilon$ is known. For example, the effects of swirl or rotation are not taken into account. This model is inaccurate in the case of strained and swirling flows. Therefore, modifications have been introduced to improve its performance. RNG $k-\epsilon$ is one of model variant. This model was developed using Re-Normalization Group (RNG) methods by Yakhot and Orszag (1986) [109] to renormalize the Navier-Stokes equations, to account for the effects of smaller scales of motion. The calculation of turbulent diffusion, in the standard $k - \epsilon$ model, is occurred only at the specified scale, whereas in reality all scales of motion will contribute to the turbulent diffusion. RNG $k - \epsilon$ model uses a specific technique to derive a turbulence model similar to the standard $k - \epsilon$ model but it results in a modified form of the epsilon equation which attempts to account for the different scales of motion through changes in the production term. The effect of swirl is also accounted for in the RNG $k-\epsilon$ model enhancing the accuracy for swirling flows. The RNG $k-\epsilon$ model uses an analytically derived differential formula for the effective turbulent viscosity which can be used for low-Reynolds number flows. So, the RNG $k - \epsilon$ model is more accurate and more reliable than the standard $k - \epsilon$ model for a wider range of flows. These models require additional semi-empirical parameterization, namely, wall functions detailed in section 1.7.

Table III.1.2: The constants involved in all $k-\epsilon$ models used in this study.

	High-Reynolds number $k-\epsilon$ models		Low-Reynolds number $k-\epsilon$ models	
Model	Standard	RNG	AKN	Abid, LS and CHC
$C_{1\epsilon}$	1.44	1.42	1.50	1.44
$C_{2\epsilon}$	1.92	1.68	1.90	1.92
σ_k	1.00	0.72	1.40	1.00
σ_ϵ	1.30	0.72	1.40	1.30
C_μ	0.09	0.085	0.09	0.09

1.5.2 Low-Reynolds number $k-\epsilon$ models

The standard $k-\epsilon$ model is modified, in the low-Reynolds number $k-\epsilon$ models, to account for the low-Reynolds number effects which appear in the vicinity of a wall. The low-Re $k-\epsilon$ models have no wall functions as they compute the entire boundary layer including the viscous sub-layer. Damping functions are designed to damp certain terms near the wall and correct the behavior of the eddy viscosity. Therefore, the equations are integrated to the wall without assuming an universal law for the velocity profile nor an equilibrium condition for k and ϵ. There are quite a few low-Reynolds number $k-\epsilon$ models. The following low-Reynolds number $k-\epsilon$ models are used in this study: [Abid] (Abid, 1991) [4], [LS] (Launder and Sharma, 1974) [65], [AKN] (Abe; Kondoh and Nagano, 1994) [3] and [CHC] (Chang; Hsieh and Chen, 1995) [24].

1.5.3 $k-\epsilon$ modelled equations

As it was mentioned above, $k-\epsilon$ model is based on the equations Eq.III.1.12, Eq.III.1.13 and two additional equations for solving k and ϵ (Eq.III.1.29 and Eq.III.1.30). Nevertheless, as previously stated, there are two types of $k-\epsilon$ models; high-Reynolds number $k-\epsilon$ models and low-Reynolds number $k-\epsilon$ models. In the case of incompressible steady-state flow, buoyancy and gravity are not taken into account. The modelled equations for the turbulence kinetic energy k and the dissipation rate ϵ, for $k-\epsilon$ models, are then:

$$\underbrace{\rho u_j \frac{\partial k}{\partial x_j}}_{\text{advection}_k} = \underbrace{\frac{\partial}{\partial x_j}\left[\left(\mu + \frac{\mu_t}{\sigma_k}\right)\frac{\partial k}{\partial x_j}\right]}_{\text{diffusion}_k} + \underbrace{G_k}_{\text{production}_k} - \underbrace{\rho\epsilon}_{\text{destruction}_k} - \underbrace{D}_{\text{source term}_k} \quad ; \tag{III.1.29}$$

$$\underbrace{\rho u_j \frac{\partial \epsilon}{\partial x_j}}_{\text{advection}_\epsilon} = \underbrace{\frac{\partial}{\partial x_j}\left[\left(\mu + \frac{\mu_t}{\sigma_\epsilon}\right)\frac{\partial \epsilon}{\partial x_j}\right]}_{\text{diffusion}_\epsilon} + \underbrace{C_{1\epsilon} f_1 \frac{\epsilon}{k} G_k}_{\text{production}_\epsilon} - \underbrace{C_{2\epsilon} f_2 \rho \frac{\epsilon^2}{k}}_{\text{destruction}_\epsilon} + \underbrace{E}_{\text{source term}_\epsilon} \quad . \tag{III.1.30}$$

G_k represents the generation of turbulence kinetic energy. This term is defined from the exact equation for k as:

$$G_k = -\rho \overline{u_i' u_j'} \frac{\partial u_j}{\partial x_i} \tag{III.1.31}$$

This term is modelled with the Boussinesq hypothesis, from the fact that this term is related to the mean velocity gradients by the following way:

$$G_k = \mu_t S^2 \tag{III.1.32}$$

where S is the modulus of the mean rate-of-strain tensor, defined as:

$$S = \sqrt{2 S_{ij} S_{ij}} \quad ; \tag{III.1.33}$$

The turbulent viscosity can be written as a general term multiplied by a damping function, f_μ:

$$\mu_t = \rho f_\mu C_\mu \frac{k^2}{\epsilon} \quad . \tag{III.1.34}$$

The model constants for all $k-\epsilon$ models used in this work are summarized in table III.1.2, while the damping functions are discussed in section 1.7.4. These damping functions replace the wall function used for high-Reynolds number $k-\epsilon$ models detailed in section 1.7.

1.6 Reynolds stress model (RSM)

1.6.1 Introduction

RSM does not assume that the flow is turbulent isotropic as $k-\epsilon$, and for an anisotropic turbulence, the Reynolds stress tensor, $\rho\overline{u_i'u_j'}$, is usually anisotropic. Therefore, the Boussinesq hypothesis is not used in the RSM model. This model closes the Reynolds-averaged Navier-Stokes equations by solving transport equations for the Reynolds stresses, together with an equation for the dissipation rate ϵ. Since the RSM accounts for the effects of streamline curvature, swirl, rotation and rapid changes in strain rate, it has greater potential to give accurate predictions for complex flows. The modelling of the pressure-strain correlation and the turbulence kinetic energy dissipation ϵ from its own transport equation, as in $k-\epsilon$ turbulence model, is particularly challenging, and often considered as one of the drawbacks of the RSM model. This may compromise the accuracy of RSM predictions.

1.6.2 RSM equations

The symbolic form of exact transport equations for the Reynolds stress tensor $\rho\overline{u_i'u_j'}$, for incompressible steady-state flow without taking into account buoyancy and gravity, may be written as follows:

$$\underbrace{C_{ij}}_{\text{Convection}} = \underbrace{D_{T,ij}}_{\text{Turbulent diffusion}} + \underbrace{D_{L,ij}}_{\text{Molecular diffusion}} + \underbrace{P_{ij}}_{\text{Stress production}} + \underbrace{\phi_{ij}}_{\text{Pressure strain}} - \underbrace{\epsilon_{ij}}_{\text{Dissipation}} \tag{III.1.35}$$

The terms that do not require modelling are:

$$C_{ij} = \frac{\partial}{\partial x_k}\left(\rho u_k \overline{u_i'u_j'}\right) \tag{III.1.36}$$

$$D_{L,ij} = \frac{\partial}{\partial x_k}\left(\mu \frac{\partial \overline{u_i'u_j'}}{\partial x_k}\right) \tag{III.1.37}$$

$$P_{ij} = -\rho\left(\overline{u_i'u_k'}\frac{\partial u_j}{\partial x_k} + \overline{u_j'u_k'}\frac{\partial u_i}{\partial x_k}\right) \tag{III.1.38}$$

The other terms, in Eq.III.1.35, have the following definitions:

$$D_{T,ij} = -\frac{\partial}{\partial x_k}\left[\rho\overline{u_i'u_j'u_k'} + \overline{p'\left(\delta_{kj}u_i' + \delta_{ik}u_j'\right)}\right] \quad , \tag{III.1.39}$$

$$\phi_{ij} = \overline{p'\left(\frac{\partial u_i'}{\partial x_j} + \frac{\partial u_j'}{\partial x_i}\right)} \quad , \tag{III.1.40}$$

$$\epsilon_{ij} = 2\mu\overline{\frac{\partial u_i'}{\partial x_k}\frac{\partial u_j'}{\partial x_k}} \quad . \tag{III.1.41}$$

However, $D_{T,ij}$, ϕ_{ij} and ϵ_{ij} need to be modelled to close the equations.
The turbulent diffusion $D_{T,ij}$ is usually modelled using a simplified Daly and Harlow model [33]

$$D_{T,ij} = C_s \frac{\partial}{\partial x_k}\left(\rho \overline{u'_k u'_\ell} \frac{k}{\epsilon} \frac{\partial \overline{u'_i u'_j}}{\partial x_\ell}\right) \quad ; \tag{III.1.42}$$

with $C_s = 0.22$.
However, numerical instabilities can result from this equation, so another simplification using a scalar turbulent diffusivity is made (Lien and Leschziner, 1994)[71]:

$$D_{T,ij} = \frac{\partial}{\partial x_k}\left(\frac{\mu_t}{\sigma_k} \frac{\partial \overline{u'_i u'_j}}{\partial x_k}\right) \quad ; \tag{III.1.43}$$

ϕ_{ij} is the term from the pressure-strain correlation. Chou (1945)[29] showed that this term could be divided into three contributions; the first one contains only turbulent interactions, the second one is generated by interactions between turbulence and the averaged velocity gradient and the last one acts only with the presence of walls. Applying the divergence on the fluctuating velocity equations, we obtain the Poisson equation for the fluctuation of pressure:

$$\frac{\partial^2 p'}{\partial x_i \partial x_i} = \underbrace{-2\rho \frac{\partial \overline{u_i}}{\partial x_j}\frac{\partial u'_j}{\partial x_i}}_{\text{rapid}} \underbrace{- \rho \frac{\partial u'_i}{\partial x_j}\frac{\partial u'_j}{\partial x_i}}_{\text{slow}} + \underbrace{\rho \frac{\partial \overline{u'_i \partial u'_j}}{\partial x_j \partial x_i}}_{\text{wall}} \quad . \tag{III.1.44}$$

The pressure-strain term, ϕ_{ij}, is modelled on the basis of the proposals of Gibson and Launder (1978) [40] , Fu et al. (1987) [38] and Launder (1989) [63]. The modelling is composed from several terms as the following:

$$\phi_{ij} = \phi_{ij,1} + \phi_{ij,2} + \phi_{ij,w} \tag{III.1.45}$$

where $\phi_{ij,1}$ is the slow pressure-strain term, namely the return-to-isotropy term while $\phi_{ij,2}$ is called the rapid-strain term, and $\phi_{ij,w}$ is the wall-reflection term. $\phi_{ij,w}$ is defined in annex 2.6.
The slow pressure-strain, $\phi_{ij,1}$, is modelled as:

$$\phi_{ij,1} = -C_1 \rho \frac{\epsilon}{k}\left(\overline{u'_i u'_j} - \frac{2}{3}k\delta_{ij}\right) \quad . \tag{III.1.46}$$

The rapid pressure-strain,$\phi_{ij,2}$, is modelled as:

$$\phi_{ij,2} = -C_2\left(P_{ij} - \frac{2}{3}P_k\delta_{ij}\right) \quad ; \tag{III.1.47}$$

where the constants C_1 and C_2 are 1.8 and 0.6 respectively. The turbulent viscosity, μ_t, is computed similarly to the $k-\epsilon$ models with the usual assumption that:

$$\epsilon_{ij} = \frac{2}{3}\delta_{ij}\epsilon \quad . \tag{III.1.48}$$

The values of k and ϵ are solved by the following modelled equations:

$$\frac{\partial}{\partial x_i}(\rho k u_i) = \frac{\partial}{\partial x_j}\left[\left(\mu + \frac{\mu_t}{\sigma_k}\frac{\partial k}{\partial x_j}\right)\right] + \frac{1}{2}G_k - \rho\epsilon \quad ; \tag{III.1.49}$$

$$\frac{\partial}{\partial x_i}(\rho \epsilon u_i) = \frac{\partial}{\partial x_j}\left[\left(\mu + \frac{\mu_t}{\sigma_\epsilon}\frac{\partial \epsilon}{\partial x_j}\right)\right] + \frac{1}{2}C_{\epsilon 1}G_k\frac{\epsilon}{k} - C_{\epsilon 2}\rho\frac{\epsilon^2}{k} \quad ; \tag{III.1.50}$$

where $C_\mu = 0.09$, $\sigma_k = 0.82$, $\sigma_\epsilon = 1.00$, $C_{\epsilon 1} = 1.44$ and $C_{\epsilon 2} = 1.92$.

1.7 Wall treatment

Turbulent flows are significantly affected by the presence of walls since molecular viscosity effects become more and more predominant relative to turbulence effects - which vanish at the wall - as the wall is approached. The mean velocity field must satisfy the non-slip condition at the wall. However, the turbulence is also changed by the presence of the wall. Very close to the wall, viscous damping reduces the tangential velocity fluctuations, while kinematic blocking reduces the normal fluctuations. Toward the outer part of the near-wall region, however, the turbulence is rapidly augmented by the production of turbulence kinetic energy due to the large gradients in mean velocity. The treatment of the near-wall region can be performed using wall functions, only in the wall region, or using damping functions modifying the turbulence properties closer to the wall while the turbulence properties, in core flow, remain unchanged. Near-wall layers and the wall and damping functions are presented in this section.

1.7.1 Near-wall layers

Numerous experiments have shown that the wall region involves three sub-regions, namely, the viscous sub-layer, the buffer layer, and the fully turbulent region (Fig.III.1.1). In the viscous sub-layer, molecular viscosity plays a dominant role. In the fully turbulent region, turbulence plays the major role. Finally, there is a region between the viscous sub-layer and the fully turbulent layer where the effects of molecular viscosity and turbulence are equally important. This region is called the buffer region. In the viscous sub-layer, $u(y=0) = u' = v' = 0$, therefore the wall friction is written as:

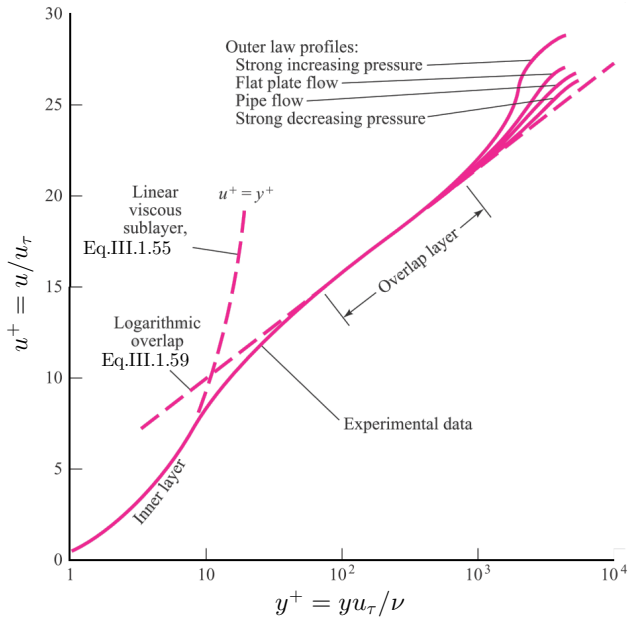

Figure III.1.1: Subdivisions of the Near-Wall Region (White, 2010)[105]

$$\tau_{xy}(y=0) \approx \tau_w = \mu \frac{d\overline{u}}{dy}_{y=0} \quad . \tag{III.1.51}$$

where y is the distance from the wall [m]. Close to the wall, it is evident that the viscosity ν and the wall shear stress τ_w are important parameters. From these quantities (and ρ) we define the appropriate velocity and length scales in the near-wall region. This is the friction velocity :

$$u_\tau = \sqrt{\frac{\tau_w}{\rho}} \quad , \tag{III.1.52}$$

and the viscous length scale :

$$\delta_\nu = \nu\sqrt{\frac{\rho}{\tau_w}} = \frac{\nu}{u_\tau} \quad . \tag{III.1.53}$$

The distance from the wall measured in viscous lengths- or wall unit - is denoted by:

$$y^+ = \frac{y}{\delta_\nu} = \frac{u_\tau \rho y}{\mu} \quad . \tag{III.1.54}$$

The dimensionless velocity is also used, $u^+ = u/u_\tau$, which is the velocity u parallel to the wall (function of y), divided by the friction velocity u_τ.
As it can be inferred from equations Eq.III.1.13 and Eq.III.1.51 that the total friction is constant, the mean velocity is written as:

$$\overline{u}(y) = y\frac{\tau_w}{\mu} \quad . \tag{III.1.55}$$

The profile is, thus, a linear function of the distance to the wall. This linear law is written:

$$u^+ = y^+ \quad . \tag{III.1.56}$$

The viscous sub-layer is extended up to a thickness of $y^+ = 5$.
In the fully turbulent region or log-law region, the friction is fundamentally turbulent. Shear stress can be written as:

$$\tau_{xy} \approx -\rho\overline{u'v'} \approx \tau_w \quad . \tag{III.1.57}$$

Using the friction velocity, the Reynolds stress is written:

$$-\overline{u'v'} = u_\tau^2 = \nu_t\frac{d\overline{u}}{dy} = \ell^2\left(\frac{d\overline{u}}{dy}\right)^2 \quad , \tag{III.1.58}$$

where ℓ is a lengthscale $[m]$.
This friction velocity appears as a characteristic scale of velocity fluctuations. As the molecular viscosity is not involved in this layer, the mean velocity gradient in this region is:

$$\frac{du^+}{dy^+} = \frac{1}{\kappa y^+} \quad , \tag{III.1.59}$$

$$u^+ = \frac{1}{\kappa}lny^+ + C^+ \quad or \quad u^+ = \frac{1}{\kappa}lnEy^+ \quad , \tag{III.1.60}$$

where $\kappa = 0.41$ is the Von kármán constant with the assumption that the integral length scale l is such that $\ell = \kappa y$;
$C^+ = 5.45$ is a constant;
$E = 9.8$ is a constant.
This log-law region extends over the region $50 < y^+ < 300$ to 500.
The buffer layer is the intermediate layer where the fully turbulent layer and the viscous sub-layer merge. In this region, the viscous stresses have the same order of magnitude as the turbulent stresses. Knudsen and Katz (1985) [59] propose the following formula:

$$u^+ = 5lny^+ - 3.05 \quad . \tag{III.1.61}$$

1.7.2 Wall functions

1.7.2.1 Standard wall function

The wall function is based on the work of Launder and Spalding (1974)[67]. Standard wall functions have been widely used in industrial flows. Using this function, k and ϵ equations are not solved in the sub-layer and buffer layer. Empirical functions are used instead of the analytical relationships. This function is valid for $30 < y^* < 300$[2]. The equations of this function are detailed in A.2.

[2]Switch between those two zones occurs for specified y^+, in the FLUENT code this value is established as $y^* = 11.225$. FLUENT uses wall unit y^* instead of y^+ and U^* instead of U^+.

1.7.2.2 Non equilibrium wall function

The standard wall function is not applied when the flows are under severe pressure gradients, and are in strong non-equilibrium, which means that the turbulence production term and the dissipation term are not equal. The non-equilibrium wall function takes into account this effect. This function is, also, valid for $30 < y^* < 300$. The equations of this function are detailed in A.3.

1.7.2.3 Enhanced wall treatment

Enhanced wall treatment combines a two layer model with enhanced wall functions. The near-wall mesh must be fine enough to be able to resolve the viscous sub-layer (first node placed at $y^+ \approx 1$)[3]. But, when high-Reynolds number flows are considered, and especially for complex flows, the mesh grid cannot, in general, be refined sufficiently in the near-wall region for this approach to be implemented. For $Re_y > 200$, defined in Eq.III.1.66, the flow is assumed to be fully turbulent and the $k-\epsilon$ models are used. Otherwise, for $Re_y < 200$, the one-equation model of Wolfshtein (1969) is used [106] Fig.III.1.2. The turbulent kinetic energy is then calculated with a transport equation, but the turbulent viscosity is determined using a characteristic length scale ℓ_μ, so that

$$\mu_t = \rho C_\mu \ell_\mu \sqrt{k} \tag{III.1.62}$$

where ℓ_μ is computed from Chen and Patel (1988)[27] by:

$$\ell_\mu = y C_\ell (1 - exp^{(-Re_y/A_\mu)}) \tag{III.1.63}$$

with A_μ a constant.
On the contrary, ϵ is not computed with a transport equation, but it is evaluated through an algebraic relation, namely,

$$\epsilon = k^{3/2}/\ell_\epsilon$$

where the length scale ℓ_ϵ is inferred from a relation similar to that for ℓ_μ, but with a constant A_ϵ instead of A_μ:

$$\ell_\epsilon = y C_\ell^* (1 - exp^{(-Re_y/A_\epsilon)}) \quad . \tag{III.1.64}$$

The constants in previous equations are taken from Chen and Patel (1988)[27] and are as follows: $C_\ell^* = \kappa C_\mu^{-3/4}$, $A_\mu = 70$, $A_\epsilon = 2C_\ell^*$ (see Hanjalic and Launder (2011) for more details [46]).

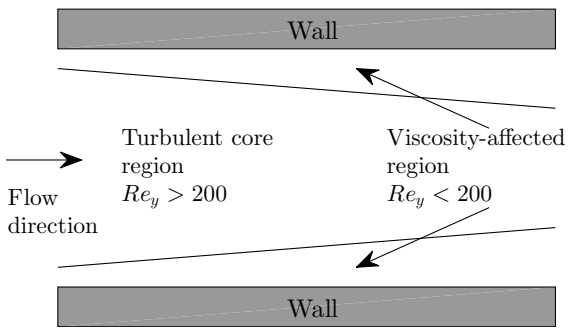

Figure III.1.2: Two-layer zonal model

[3] ANSYS FLUENT Theory Guide, ANSYS Inc., 2003, chapter 12.

1.7.3 Wall Boundary conditions

The modified turbulent kinematic viscosity, $\tilde{\nu}$, is set to be zero at the wall, for the Spalart-Allmaras model. The laminar sub-layer is resolved Eq.III.1.56 when the mesh is fine enough, but the law-of-the-wall is employed when the mesh is too coarse Eq.III.1.60.

Wall boundary conditions for all low-Reynolds $k-\epsilon$ models are presented in table III.1.3. While wall functions, used for $k-\epsilon$ models, are also used for the RSM model. The RSM model requires boundary conditions for individual Reynolds stresses $\rho\overline{u_i'u_j'}$, and for the turbulence dissipation rate, ϵ. These quantities can be input directly or derived from the turbulence intensity and characteristic length. Using standard wall function or non-equilibrium wall function, the Reynolds stresses at the wall-adjacent cells are computed, for a local coordinate system, as follows:

$$\frac{\overline{u_\tau'^2}}{k} = 1.098, \frac{\overline{u_\eta'^2}}{k} = 0.247, \frac{\overline{u_\lambda'^2}}{k} = 0.655, -\frac{\overline{u_\tau' u_\eta'}}{k} = 0.255$$

where τ is the tangential coordinate to the wall,
η is the normal coordinate at the wall, and
λ is the binormal coordinate at the wall.

Turbulence kinetic energy k is calculated from k equation Eq.III.1.49 and in the flow core, k is calculated by Eq.III.1.9 after the calculation of Reynolds stress. The Reynolds stresses, alternatively, can be explicitly specified in term of wall-shear stress:

$$\frac{\overline{u_\tau'^2}}{u_\tau^2} = 5.1, \frac{\overline{u_\eta'^2}}{u_\tau^2} = 1.0, \frac{\overline{u_\lambda'^2}}{u_\tau^2} = 2.3, -\frac{\overline{u_\tau' u_\eta'}}{u_\tau^2} = 1.0 \quad .$$

When using enhanced wall treatments as the near-wall treatment, zero flux wall boundary conditions to the Reynolds stress equations are applied.

1.7.4 Damping functions

For low -Reynolds number $k-\epsilon$ models, the μ_t, k and ϵ equations are modified using algebraic functions to represent physical reality. Near the wall, Re_t (defined in Eq.III.1.65) and μ_t tend towards zero, therefore, $\epsilon \simeq$ diffusion of k. While further from the wall, $\mu_t \gg \mu$, therefore, $\epsilon \simeq$ production of k. In addition, very close to the wall, k tends towards zero, but ϵ has a non-zero defined value. In order to take into account these complex effects, one must adapt the standard equations by adding the damping functions. Indeed, the equations are integrated to the wall without assuming an universal law for the velocity profile nor an equilibrium condition for k and ϵ. The damping functions f_μ, f_1 and f_2 for low-Reynolds number $k-\epsilon$ models are summarized in table III.1.4. The damping functions are written in terms of the turbulence Reynolds numbers[4]:

$$Re_t = \frac{\rho k^2}{\mu\epsilon} \quad , \tag{III.1.65}$$

$$Re_y = \frac{\rho y\sqrt{k}}{\mu} \quad , \; and \tag{III.1.66}$$

$$Re_\epsilon = \frac{\rho\left(\mu\epsilon/\rho\right)^{1/4} y}{\mu} \quad . \tag{III.1.67}$$

[4]

$$\epsilon = \tilde{\epsilon} + D$$

Different models use different damping functions (f_μ, f_1 and f_2) and different extra terms (D and E). Many models solve for $\tilde{\epsilon}$ rather than for ϵ where D is equal to the wall value of ϵ which gives an easy boundary condition $\tilde{\epsilon} = 0$. Other models which solve ϵ, use no extra source in the k equation, i.e. D= 0.

This approach based on modelled equations for k and for ϵ together with damping functions is developed for low-Reynolds number flows.

Table III.1.3: The source terms and boundary conditions of low-Reynolds number $k-\epsilon$ models and high-Reynolds number $k-\epsilon$ models, where $\eta = Sk/\epsilon$, $\eta_0 = 4.38$ and $\beta = 0.012$.

Model	Source terms		Wall boundary conditions	
Abid	$D = 2\nu\left(\partial\sqrt{k}/\partial y\right)^2$	$E = 0$	$k = 0$	$\epsilon = 2\nu\left(\partial\sqrt{k}/\partial y\right)^2$
AKN	$D = 0$	$E = 0$	$k = 0$	$\epsilon = 2\nu\left(\partial\sqrt{k}/\partial y\right)^2$
CHC	$D = 0$	$E = 0$	$k = 0$	$\epsilon = \nu\left(\partial^2 k/\partial y^2\right)$
LS	$D = 2\nu\left(\partial\sqrt{k}/\partial y\right)^2$	$E = 2\nu\nu_t\left(\partial^2 u/\partial y^2\right)^2$	$k = 0$	$\epsilon = 0$
RNG	$D = 0$	$E = \left(\frac{C_\mu \eta^3(1-\eta/\eta_0)}{1+\beta\eta^3}\frac{\epsilon^2}{k}\right)$	Wall function "Enhanced wall treatment"	
Standard	$D = 0$	$E = 0$	Wall function "Enhanced wall treatment"	

Table III.1.4: The damping functions of low-Reynolds number $k-\epsilon$ models and high-Reynolds number $k-\epsilon$ models

Model	f_μ	f_1	f_2
Abid	$tanh\left(0.008Re_y\right)\left(1+4\left(Re_t^{-0.75}\right)\right)$	1	$\left[1-\frac{2}{9}exp\left(-\frac{Re_t^2}{36}\right)\right]\times\left[1-exp\left(\frac{-Re_y}{12}\right)\right]$
AKN	$\left[1-exp\left(-Re_\epsilon/14\right)\right]^2\times\left[1+5exp\left(-Re_t/200\right)^2/Re_t^{3/4}\right]$	1	$\left[1-exp\left(-Re_\epsilon/3.1\right)\right]^2\times\left[1-0.3exp\left(-\left(Re_t/6.5\right)^2\right)\right]$
CHC	$\left[1-exp\left(-0.0215Re_y\right)\right]^2\times\left(1+31.66/Re_t^{5/4}\right)$	1	$\left[1-0.01exp\left(Re_t^2\right)\right]\times\left[1-exp\left(-0.0631Re_y\right)\right]$
LS	$exp\left[-3.4/\left(1+Re_t/50\right)^2\right]$	1	$1-0.3exp\left(-Re_t^2\right)$
RNG	1	1	1
Standard	1	1	1

Chapter 2

Numerical resolution

The numerical study is performed using the commercial computational fluid dynamics software ANSYS/ Fluent V14.0. Where the models studied are implemented. Simulations are performed in two dimensions (2D) and three dimensions (3D). The main advantage of 2D is that it runs faster than 3D. However, the real labyrinth is narrow and thus considering that the walls in the transverse direction are very distant from the simulated plane, as it is supposed in 2D, could result in wrong predictions.

2.1 Geometry of the study

The geometry is shown in Fig.III.2.1. A three-pattern labyrinth-channel is designed. Inlet and outlet sections are offset from the studied region in order to prevent perturbations. Labyrinth-channel dimensions are detailed in table II.1.1.

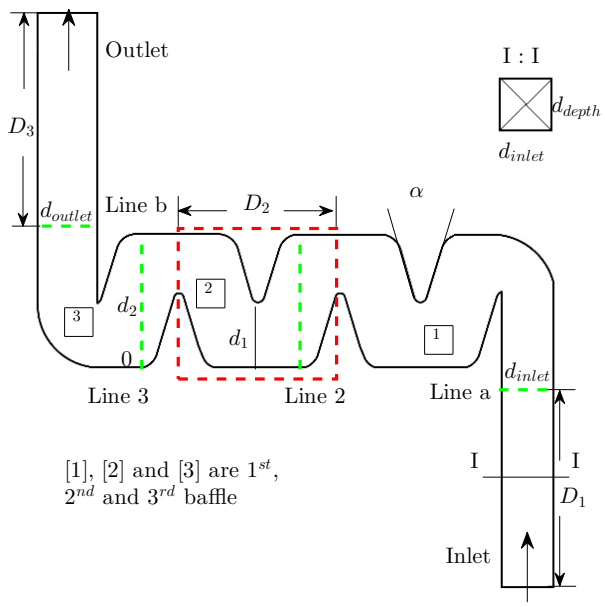

Figure III.2.1: Labyrinth-channel used in modelling

2.2 Meshing

The mesh is generated and its quality is examined Fig.III.2.2. The skewness, based on the deviation from a normalized equilateral angle Eq.III.2.1, is around 0.75 and 0.56 in two and three dimensions respectively, which states that mesh quality is acceptable. The skewness for a quadratic cell is computed from the relation Bakker (2002) [12].

$$\text{Skewness} = \max\left[\frac{\phi_{max} - 90}{90}, \frac{90 - \phi_{min}}{90}\right] \tag{III.2.1}$$

where ϕ_{max} and ϕ_{max} are presented in Fig.III.2.3.

For all models, we opt for a quadratic-dominant (in two dimensions) and prism with quadrilateral base (in three dimensions) mesh type. The mesh is chosen with $y^+ < 5$ for high-Reynolds number $k-\epsilon$, Spalart-Allmaras and RSM models. Low-Reynolds number $k-\epsilon$ models require fine mesh, $y^+ \leq 1$ at the wall-adjacent cell. Modelling by low-Reynolds number $k-\epsilon$ models requires more mesh refinement close to the wall in order to have a sufficient number of points in the region $0 < y^+ < 10$.

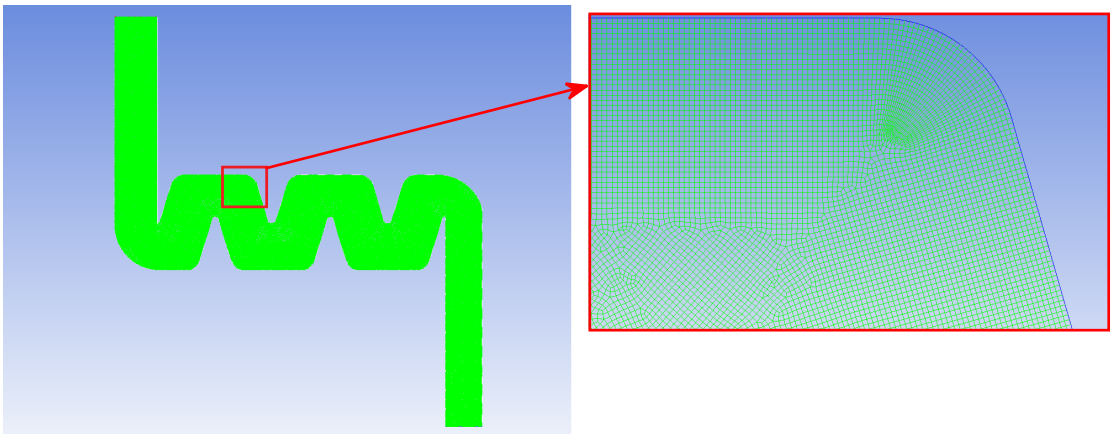

Figure III.2.2: Mesh generated in 2D for modelling.

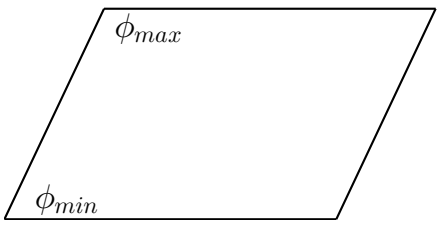

Figure III.2.3: quadratic cell.

The independence of the results to the meshing has been verified. For example, the velocity modulus profiles are plotted on line 2 for different mesh cell numbers (Fig.III.2.4). The variation of the velocity is weak when the mesh cell number is at least 1.33×10^5 and then the smallest mesh size is $15.6\ \mu m$. Therefore, the effect of mesh can be neglected. The chosen cell numbers, for all models, are presented in table III.2.1. That way, the results will not depend on meshing to ensure that the differences will be due to the model.

Table III.2.1: Mesh cell number.

Model	2D		3D	
	Cell number	max of y^+	Cell number	max of y^+
Standard $k-\epsilon$, RSM	1.33×10^5	3.5- 4	5.3×10^5	7-8
Low-Reynolds $k-\epsilon$, S-A	5.33×10^5	1.8- 2.5	5.3×10^5	8
LS $k-\epsilon$	5.33×10^5	1.8- 2.5	1.2×10^6	8

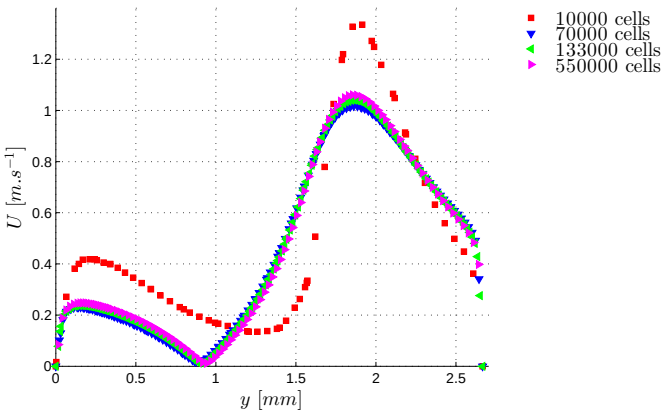

Figure III.2.4: The velocity modulus $[m.s^{-1}]$ for four mesh cell sizes; [LS] $k-\epsilon$ model for $Re = 800$ on line 2.

2.3 Boundary conditions

The flow rate $[kg.s^{-1}]$[1] is imposed at the inlet, and at the outlet. All simulations are performed with an initial inlet flow rate of $0.4\ [kg.s^{-1}]$ in 2D ($0.0004\ [kg.s^{-1}]$ in 3D), then it is regularily increased until $0.8\ [kg.s^{-1}]$ in 2D ($0.0008\ [kg.s^{-1}]$ in 3D); which corresponds to a Reynolds number ranging from 400 to 800. The flow rates are taken around the nominal flow rate of emitter 2 $[l.h^{-1}]$, which is equivalent to $0.55\ [kg.s^{-1}]$. The turbulent intensity and hydraulic diameter are chosen for the specification method of turbulence to calculate the turbulence effect for all $k-\epsilon$, S-A and RSM models. The direction of specification method is taken normal to boundary. While, additional conditions for Reynolds-stress specification method are chosen to be k and turbulent intensity.

The hydraulic diameter is used when handling flow in non-circular channels or tubes. It is equivalent to the pipe diameter. It is defined by Eq.II.1.10. In 3D, from Fig.III.2.1 and at the inlet, one can write :

$$D_h = \frac{2\ d_{inlet} \times d_{depth}}{d_{inlet} + d_{depth}} \quad . \tag{III.2.2}$$

As, $d_{depth} = d_{inlet} = 1\ mm$, it yields :

$$D_h = 1\ mm \quad . \tag{III.2.3}$$

[1] $[kg.s^{-1}]$ is the flow rate unit used in Fluent. This unit is converted to $[l.h^{-1}]$ to have the same unit used in the experimental acquisition. It is important to note that:

- in 2D, $1\ [kg.s^{-1}]$ is equivalent to $3,6\ [l.h^{-1}]$
- in 3D, $1\ [kg.s^{-1}] = 3600\ [l.h^{-1}]$

Generally, in 2D, where $d_{depth} \gg d_{inlet}$. Eq.III.2.2 can be written dividing the equation by d_{depth}:

$$D_h = \frac{4\, d_{inlet}}{\frac{2\, d_{inlet}}{d_{depth}} + 2} \quad ; \tag{III.2.4}$$

But, d_{depth} is infinite, d_{inlet}/d_{depth} tends towards zero. Therefore, $D_h = 2d_{inlet}$, it yields:

$$D_h = 2\ mm \quad . \tag{III.2.5}$$

The turbulent intensity is described by the formulae:

$$I = \frac{u'}{|\overline{u}|} \quad ; \tag{III.2.6}$$

where:

$$u' = \sqrt{\frac{1}{3}\left(\overline{u'^2} + \overline{v'^2} + \overline{w'^2}\right)} \quad ; \tag{III.2.7}$$

or, if the turbulence is isotropic as supposed for $k - \epsilon$ models, by :

$$I = \frac{\left(\overline{u'^2}\right)^{1/2}}{|\overline{u}|} \quad . \tag{III.2.8}$$

A turbulent intensity (5%) is imposed. This turbulent intensity is obtained from the experimental results.

2.4 Solution methods

The algorithm of the solution process is shown in Fig.III.2.5. The solution parameters consist in the choice of the solver and the spatial discretization scheme[2].

2.4.1 Solver choice

The types of solver available in Fluent are:

- Pressure based: with this solver, the momentum and pressure are resolved as the primary variables. However, there are two algorithms for pressure-based solvers; segregated solver and coupled solver where the variables are resolved sequentially and simultaneously, respectively. The pressure-based segregated solver is applicable for a wide range of flow regimes, requires less memory and allows flexibility in the solution procedure. While, the pressure-based coupled solver is applicable for most single phase flows and requires more memory than the segregated solver.
- Density based: the variables are solved in vector form; the pressure is obtained through an equation of state. This solver is applicable when there is a strong coupling, or interdependence, between density, energy, momentum, and/or species.

Therefore, pressure-based segregated solver is chosen for this study.

[2]The solution methods is extracted from the following document:
ANSYS FLUENT Theory Guide, ANSYS Inc., 2003, chapter 26.

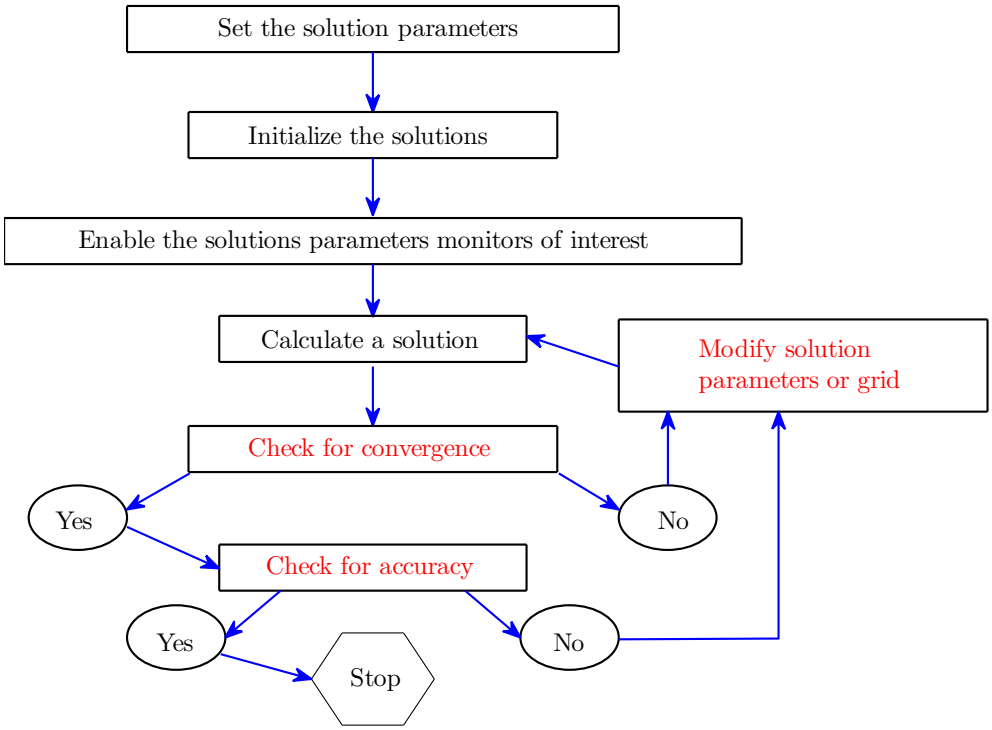

Figure III.2.5: Algorithm of solution process.

2.4.2 Pressure-velocity coupling

This method indicates the numerical algorithm which uses a combination of continuity and momentum equations to derive an equation for pressure (or pressure correction) when using the pressure-based solver. There are various algorithms as:

- SIMPLE (Semi-Implicit Method for Pressure-Linked Equations) which is a robust scheme.
- SIMPLEC (SIMPLE-Consistent) which allows faster convergence for simple problems (e.g. laminar).
- PISO (Pressure-Implicit with Splitting of Operators) which is useful and recommended for unsteady flow or for meshes containing cells with higher than average skewness.
- Coupled which is also a scheme to solve this coupling but if the pressure-based coupled solver is enabled.

In present simulations, the SIMPLE method is used for pressure-velocity coupling.

2.4.3 Interpolation methods for gradients

The gradients of solution variables, at cell center, can be determined using three approaches:

- Green-Gauss cell-Based: it is the least computationally intensive.
- Green-Gauss Node-Based: this method is more accurate and minimizes false diffusion. It is specially recommended for unstructured meshes.
- Least-Squares cell-Based: this method has the same accuracy as Node-based gradients and is less computationally intensive.

To calculate gradients, the Least-Squares cell-Based method is selected.

2.4.4 Interpolation methods for pressure

When using the pressure-based solver, several interpolation schemes for calculating cell-face pressures, are available:

- Standard: this method is acceptable for most cases.
- Second-Order: this method is recommended for compressible flows.
- Body force weighted: when problems involving large body forces are studied, Body force weighted is recommended.
- PRESTO: it is preferred for the flow features which include strong streamline curvature and rotation.
- Linear: if one of these methods is not adapted, linear is used.

In the present simulation, Standard is set as spatial interpolation for pressure.

2.4.5 Spatial discretization

Field variables at cell center must be interpolated. Interpolation schemes to solve momentum, turbulent kinetic energy and turbulent dissipation rate equations are:

- First-Order Upwind: this method is easiest to converge, but is first-order accurate.
- Power Law: this method is more accurate than first-order for flows where $Re_{cell} < 5$.
- Second-Order Upwind: with triangle/tetrahedron mesh or when flow is not aligned with grid, Second-Order Upwind is recommended.
- MUSCL (Monotone Upstream-Centered Schemes for Conservation Laws): it is more accurate in predicting secondary flows, vortices, forces, etc. It is advised for unstructured meshes.
- QUICK (Quadratic Upwind Interpolation) : QUICK is applied to quadrilateral/hexahedron and hybrid meshes, useful for rotating/swirling flows, 3rd-order accurate on uniform mesh.

In the present simulation, MUSCL is set as spatial discretization. This method is accurate and adapted for all mesh types.

2.4.6 Convergence

The transport equation of any variable ϕ is presented as follows:

$$a_p\phi_p + \sum_{nb} a_{nb}\phi_{nb} = b_p \tag{III.2.9}$$

The coefficients a_p and a_{nb} depend on the solution. These coefficients vary in each iteration. The equality is not exact, the gap in between is called the residual R_p, which is given as:

$$R_p = a_p\phi_p + \sum_{nb} a_{nb}\phi_{nb} - b_p \tag{III.2.10}$$

The total residual is the sum of cell residuals:

$$R = \sum_{cells} |R_p| \tag{III.2.11}$$

The convergence accuracy is not fixed. It changes from one model to another. However, it is always less than 10^{-6} and can reach 10^{-12} in some cases Fig.III.2.6.

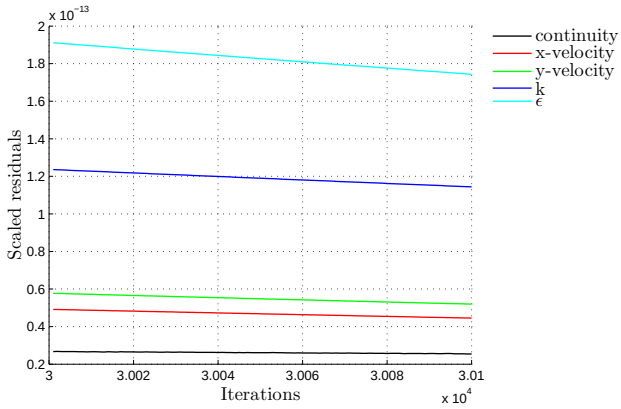

Figure III.2.6: Residues obtained after 3×10^4 iterations.

2.5 Numerical calculation of the pressure losses

Numerically, the pressure loss, between two lines in 2D or two sections in 3D, is the pressure at the upstream line (section) minus the downstream pressure. Nevertheless, to understand the origins of pressure losses, one must analyze what happens between the two lines (sections). In a pipe flow, two processes may dissipate the mean flow kinetic energy, the first is by volume dissipation or the internal dissipation and the second is by friction at the wall (Chassaing, 2000[25]; White, 2010 [105]). In general, these two mechanisms occur together. Pressure drop is related to tube length. For a labyrinth-channel, it can be written as:

$$\frac{dp}{dx} = -\frac{1}{Q_v}\int_A \Phi \times dA_c - \frac{\tau_w}{\delta} \tag{III.2.12}$$

where $\delta = d/2$, d is not constant among the labyrinth-channel.

$$\Phi = 2\mu S_{ij} S_{ij} \tag{III.2.13}$$

Φ is the dissipation rate generated by turbulent fluctuations added to that of the overall motion. It can be written as follows:

$$\Phi = \overline{\phi} + \overline{\varphi} \quad ; \tag{III.2.14}$$

where:

$$\overline{\Phi} = 2\mu \overline{S_{ij}}\ \overline{S_{ij}} \text{ and } \overline{\varphi} = 2\mu \overline{s_{ij} s_{ij}} \quad .$$

Eq.III.2.12 can be written, with approximations, as:

$$|\frac{dp}{dx}| \approx \frac{\rho}{Q_v}\int \epsilon_t \times dA_c + \frac{\tau_w}{\delta} \tag{III.2.15}$$

with $\epsilon_t = \bar{\epsilon} + \epsilon$.
In Eq.III.2.15, the sign $(\approx)$ is set instead of $(=)$ because it is assumed that turbulent kinetic energy production equals turbulent dissipation. The term, on the left-hand side, is the pressure loss absolute value per length unit. On the right-hand side, the first term is the dissipation rate integrated on the cross-section where $Q_v = U_m \times A_c$ is the volumetric flow rate $[m^3.s^{-1}]$, A_c is the cross-section area $[m^2]$.

The total dissipation rate, ϵ_t, is also composed of two contributions. The first contribution, $\bar{\epsilon}$, is the dissipation due to the mean flow: in general, it is of order Re^{-1} compared with the other terms, and therefore negligible. The second contribution, ϵ, is the dissipation due to the fluctuating flow. ϵ is the variable in Eq.III.1.30 for $k-\epsilon$ models and in Eq.III.1.50 for RSM model and $\bar{\epsilon}$ is defined by the formula: $\bar{\epsilon} = \nu S^2$, where S is the modulus of the mean rate-of-strain tensor (Eq.III.1.33) in the flow core. The second term is the energy dissipated at the wall, by friction, divided by δ. The wall friction is given by

formula: $\tau_w = \mu S$, where S is the modulus of the mean rate-of-strain tensor at the wall (Eq.III.1.33). The volume of fluid, V, in the labyrinth-channel, can be written by different ways:

$$V = A_c \times L = A_{area} \times d_{depth} = \ell_{mean} \times L \times d_{depth} \quad , \tag{III.2.16}$$

where L is the path length of the fluid (m), and $\ell_{mean} = A_{area}/L$, which is the mean width over the entire area of the labyrinth-channel (m).
For the geometry in Fig.III.2.1, $A_{area} = 32.44\, mm^2$ and $L = 26.48\, mm$. Therefore, $\ell_{mean} = 1.22\, mm$ (Eq.III.2.16). By multiplying and handling Eq.III.2.15 by the total volume of fluid V, we obtain:

$$(p_{inlet} \times d_{inlet} - p_{outlet} \times d_{outlet}) \times d_{depth} \approx (\bar{\epsilon} + \epsilon)\, \frac{\rho A_{area}}{U_m} \times d_{depth} + \frac{\tau_w \times A_c \times L}{\delta} \tag{III.2.17}$$

In 2D, $A_c/\delta = 2\, d_{depth}$. The previous equation can be written as:

$$p_{inlet} \times d_{inlet} - p_{outlet} \times d_{outlet} \approx (\bar{\epsilon} + \epsilon)\, \frac{\rho A_{area}}{U_m} + \tau_w \times L_{wall} \tag{III.2.18}$$

with $L_{wall} = 2L$.
In 3D, $A_c/\delta = (2\, \ell_{mean} + 2\, d_{depth})$ Eq.III.2.17 can be written as:

$$p_{inlet} \times A_{inlet} - p_{outlet} \times A_{outlet} \approx (\bar{\epsilon} + \epsilon)\, \frac{\rho V}{U_m} + \tau_w \times A_{wall} \tag{III.2.19}$$

with $A_{wall} = (2\ell_{mean} + 2d_{depth}) \times L$.
Some approximations are taken into account for the development of equations Eq.III.2.18 and Eq.III.2.19:

- The pressure on such line p_{inlet} or p_{outlet} (or surface), is the average pressure calculated on this line (surface).
- The velocity U_m is the average flow velocity on the surface in $2D$, or on the volume, in $3D$.
- Turbulent dissipation ϵ is the average value calculated on the surface in $2D$, or on the volume, in $3D$.
- Modulus of the rate-of-strain in flow core, which serves to calculate the average dissipation $\bar{\epsilon}$, is the average value calculated on the surface in $2D$, or on the volume, in $3D$.
- Modulus of the rate-of-strain at the wall, which serves to calculate the wall friction τ_w is the average value calculated on the wall line in $2D$, or on the wall surface, in $3D$.

2.6 Conclusion

Firstly, several turbulence models, wall treatment and damping functions were presented and discussed in chapter III.1. In this chapter, the geometry design and dimensions was introduced. Then, the mesh was verified. The choice of solution method was justified. Finally, some relationships were developed to calculate numerically the different terms of pressure losses. These relationships allow to define the responsible terms of pressure losses and to compare these terms among them.

Part IV

Results and discussion

Table of Contents

1 Pressure loss and discharge **101**
1.1 Introduction . . . 101
1.2 The pressure loss and discharge . . . 101
1.3 Geometric calculation of pressure losses . . . 103
1.4 Numerical calculation of pressure losses . . . 106
1.5 Conclusion . . . 108

2 Analysis of the labyrinth-channel flow **111**
2.1 Introduction . . . 111
2.2 Experimental visualization of instantaneous velocity fields . . . 112
2.3 Inlet flow . . . 113
2.3.1 Mean flow properties . . . 113
2.3.2 Turbulence statistics . . . 118
2.4 Outlet flow . . . 121
2.5 Flow characterization inside the baffles . . . 123
2.5.1 Experimental analysis . . . 123
2.5.2 Numerical analysis . . . 125
2.5.3 Comparative study . . . 130
2.6 Reynolds stresses . . . 131
2.6.1 Experimental analysis . . . 131
2.6.2 Numerical analysis . . . 134
2.6.3 Comparative study . . . 136
2.7 Axial development of the flow . . . 137
2.7.1 Experimental flow consistency . . . 137
2.7.2 Numerical flow consistency . . . 139
2.8 Vertical evolution of the flow . . . 139
2.9 Turbulent kinetic energy . . . 140
2.9.1 Experimental analysis . . . 140
2.9.2 Numerical analysis . . . 141
2.10 Flow isotropy . . . 145
2.11 Turbulence properties . . . 146
2.12 Swirl detection and analysis . . . 148
2.12.1 Strain rate and vorticity . . . 148
2.12.2 Advanced criterion . . . 151
2.13 Conclusion . . . 154

Chapter 1

Pressure loss and discharge

1.1 Introduction

The emitter global performance is determined by the pressure drop inside the baffles chapter I.1. This pressure drop determines the flow rate. This is why the pressure drop analysis is very important. It allows to understand the mechanism or the role of the baffles in generating this pressure drop. This chapter introduces the discharge-pressure curves obtained numerically and experimentally. Then, the contributions of each type of pressure loss are analyzed. Finally, the geometric calculations of pressure losses are performed and the results obtained are compared with the numerical calculations for some turbulence models.

1.2 The pressure loss and discharge

The static pressure contours are plotted in Fig. IV.1.1 using RSM model in 3D. Hereby the evolution of static pressure along the baffles is presented. The influence of Reynolds numbers on this pressure is discussed. The pressure is slightly decreased at the inlet and the outlet since the pressure drop is only generated by the friction at the wall (Pope, 2000)[85]. It is sharply decreased along baffles where the contributions of each type of pressure loss intervene (Eq.III.2.15). The pressure reaches its minimum value at the outlet behind the last baffle, the dark blue-colored zone (Fig.IV.1.1). The results in the literature on a similar labyrinth-channel give quantitatively the same pressure fields (Wei et al., 2006)[101].

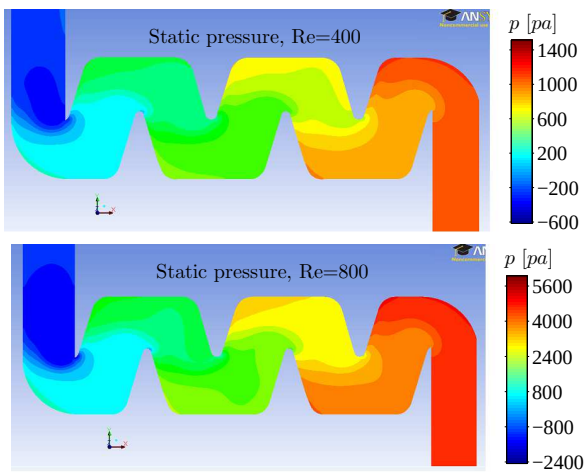

Figure IV.1.1: Static pressure contour using RSM model in 3D

The ratio of pressure losses for two Reynolds numbers ($Re = 400$ and $Re = 800$) is approximately 4. This ratio is related to the square of ratio of Reynolds number or rather the square of bulk velocity. One can conclude from this comparison that the Reynolds number in this range, relatively, has no effect on the pressure losses after the first baffle.

The discharge-pressure loss curves ($q = f(\Delta P)$) where ΔP stands for the inlet / outlet pressure losses are plotted for each turbulence model in 2D and four models in 3D and compared with the experimental data (Fig.IV.1.2). As mentioned above, in section I.1.2.3.2, from the paper of Karmeli (1977) [54], it can be noted that for long-path emitters, which are used for our study, the emitter discharge exponent x Eq.I.1.1 is between 1 and 0.5; the values respectively for laminar and rough fully turbulent wall flows. In 2D (Fig.1.2(a)), the exponents of standard, RNG and [LS] $k - \epsilon$ models, Spalart–Allmaras and RSM are those of rough fully turbulent regime (for which the friction factor C_f, defined and discussed in section IV.2.3.1, which is proportional to $\Delta P/q^2$, does not depend anymore on the Reynolds number Re) and they are close to, but slightly smaller than, the exponents of the [LS] $k - \epsilon$ model and the experiments ($0.57 - 0.59$, such that C_f slightly decreases with Re, see White (2010)[105]). [Abid], [AKN] and [CHC] $k - \epsilon$ models have a laminar behavior since the exponents of these models are close to 1 and therefore such that C_f strongly decreases with Re (see table IV.1.1). It appears that when the flow rate increases, all the $k - \epsilon$ models predict almost the same pressure drop. Even though it is quite difficult to comment and analyze in detail the results presented in Fig.1.2(a) and Fig.1.2(b), a clear distinction can be made between the two types of flow regimes, with the [LS] $k - \epsilon$ model being the only model which can simulate the turbulent regime for which C_f slightly decreases with Re.

In three dimensions, four models are chosen: standard $k - \epsilon$ model, [LS] $k - \epsilon$ model, S–A and RSM. It can be observed that the curve exponents, in 3D, are close to 0.5. These results indicate that the flow is turbulent. Experimental exponent of this curve is 0.59 which is close to the numerical results. Nevertheless, some differences in the pressure losses prediction can be observed between experimental and numerical values. One could suspect that this is due to the 2D hypothesis (Fig.1.2(a)). However, looking at 3D results, a larger gap is noted (Fig.1.2(b)): pressure losses are larger than in 2D. The pressure loss is related to the velocity. The velocity profiles and fields are discussed in chapter IV.2, and in order to understand these losses, the analysis of the main drivers of head losses has been developed and presented in section III.2.5. Then, the numerical application of this analysis is presented in section IV.1.4 for turbulence models.

Table IV.1.1: The exponent values in the Eq.I.1.1 for all models plotted in Fig.IV.1.2.

	Model	Standard	RNG	Abid	LS	AKN	CHC	S-A	RSM	experiment
x exponent	2D	0.50	0.49	0.99	0.56	0.98	0.86	0.51	0.46	–
	3D	0.50	–	–	0.54	–	–	0.52	0.48	0.59

In the thesis manuscript, the numerical results of four models are more deeply analyzed: the S-A, the standard $k-\epsilon$ and the RSM models (from the simplest to the most complex) as high Reynolds number models, the [LS] $k-\epsilon$ model as a low-Reynolds number $k-\epsilon$ model which behaves like a high-Reynolds number model and the [CHC] $k - \epsilon$ model as a low- Reynolds number $k - \epsilon$ model which tends to a laminar behavior.

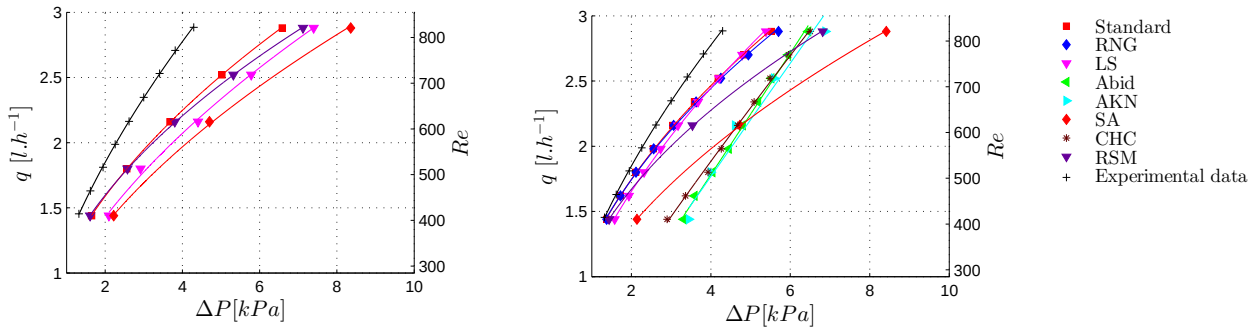

(a) 3D. (b) 2D.

Figure IV.1.2: Discharge-pressure loss curves in three dimensions (3D) (a) and two dimensions (2D) (b).

1.3 Geometric calculation of pressure losses

This section tends to understand how the labyrinth-channel geometry impacts on pressure losses. The overall head loss for the pipe system consists of the head loss due to viscous effects in the straight pipes, termed the major loss and denoted $h_{L-\text{major}}$, and the head loss in various pipe components, termed the minor loss and denoted $h_{L-\text{minor}}$. That is:

$$h_L = h_{L-\text{major}} + h_{L-\text{minor}} \quad . \tag{IV.1.1}$$

The head loss designations of *major* and *minor* do not necessarily reflect the relative importance of each type of loss. For a pipe system that contains many components and a relatively short length of pipe, the minor loss may be actually larger than the major loss. The major head loss, $h_{L-major}$ is given as (White, 2010)[105]:

$$h_{L-\text{major}} = f\frac{\ell}{D}\frac{U_m^2}{2g} \quad ; \tag{IV.1.2}$$

where f is a dimensionless parameter, called the Darcy friction factor. The above mentioned equation is called the Darcy-Weisbach equation. It is valid for any fully developed, steady, incompressible pipe flow, whether the pipe is horizontal or of different slopes.
Minor losses are expressed as (White, 2010)[105]:

$$h_{L-\text{minor}} = \zeta\frac{U_m^2}{2g} \tag{IV.1.3}$$

where ζ is the minor head loss coefficient.

Labyrinth-channel is usually composed of many channel units with the same shape. When the flow is fully developed, the head loss within each unit is identical (Takahiro and Shougo, 2006)[5]. Therefore, the total pressure drop ($h \times \rho g$) can be expressed as:

$$\Delta P = N(\Delta P_f + \Delta P_j) \quad ; \tag{IV.1.4}$$

where

$$\Delta P_f = f\frac{\ell}{d}\rho\frac{U_m^2}{2} \quad ; \tag{IV.1.5}$$

$$\Delta P_j = \zeta\rho\frac{U_m^2}{2} \quad ; \tag{IV.1.6}$$

$$U_m = \frac{Q}{A_c} \quad . \tag{IV.1.7}$$

Substituting Eq.IV.1.5,Eq.IV.1.6 and Eq.IV.1.7 into Eq.IV.1.4 gives:

$$\Delta P = N(f\frac{\ell}{d} + \zeta)\rho\frac{Q^2}{2A^2} \tag{IV.1.8}$$

Zhang et al. (2011, 2013)[112][113] have then presented a new variable which is called the pressure loss coefficient (PLC) of channel unit φ, which is defined as:

$$\varphi = (f\frac{\ell}{d} + \zeta) \tag{IV.1.9}$$

Zhang et al. (2011, 2013)[112][113] have developed a regression model to express φ in function of the geometry parameters represented in Fig.IV.1.3:

$$\varphi = -6.258 - 26.084(S/H) + 25.297\alpha + 4.406(D/W)^2 + 0.784(H/D)^2 + 9.549(S/H)^2 \\ - 6.332(D/W)\alpha + 6.366(H/D) \times (S/H) - 6.802(H/D)\alpha \quad . \tag{IV.1.10}$$

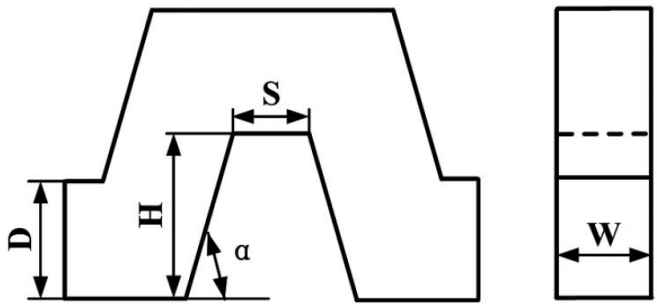

Figure IV.1.3: Characteristic parameters of the trapezoidal labyrinth-channel unit (Zhang et al., 2011, 2013)[112].

The value of φ can be easily calculated from this equation when the channel dimensions are given. When replacing the dimensions of the labyrinth-channel displayed on Fig.III.2.1 in this equation, the value of φ is in the range of $12.21 - 13.01$. This depends on the value of S (and thus H) presented in table IV.1.2. When the baffle is a sharp triangle (a trapeze) $S = 0$ ($S = 0.185$) which corresponds to case n^o1 (case n^o2).

Table IV.1.2: Labyrinth-channel dimensions

	D (mm)	W (mm)	H (mm)	S (mm)	α
case n^o1	1.31	1.00	1.72	0.00	73
case n^o2	1.31	1.00	1.43	0.185	73

Experimentally, the value of φ is calculated by the pressure drop measurements on the two prototypes with 3 and 10 channel units. Subtracting the pressure drops for the same flow rate gives the pressure drop corresponding to 7 channel units. The subtraction is necessary to eliminate the pressure drop due to the inlet and the outlet sections and eliminate Δp due to the first baffles when flow is not yet established (see section IV.2.7).

Table IV.1.3: Experimental values of pressure drop.

Flow rate $[ml.min^{-1}]$	Pressure drop for the prototype of 10 channel units $[pa]$	Pressure drop for the prototype of 3 channel units $[pa]$	Pressure drop for 7 channel units $[pa]$
30	8408	2102	6306
36	11253	2838	8415
42	14396	3657	10739
48	17821	4556	13265

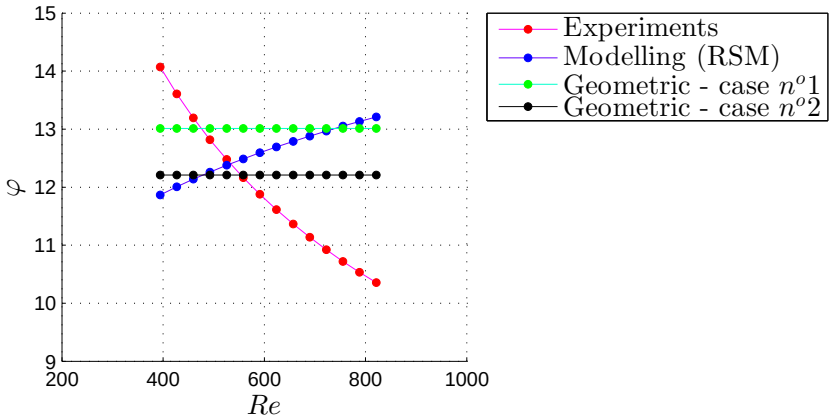

Figure IV.1.4: The variable φ for labyrinth-channel unit.

Numerically, φ is calculated from the results of simulation of 3 channel-units with RSM. The contributions of the inlet and the outlet are eliminated, but the first baffle has been taken into account. While φ is calculated experimentally from three baffles fully developed. φ values obtained from theoretical, experimental and numerical analyses are presented in Fig.IV.1.4. This figure explains clearly the difference in the pressure losses prediction between a fully developed flow where $x = 0.5$ in Eq.I.1.1. In this case, the φ value is in good agreement with the experimental and numerical values, even if the Reynolds number effect is not taken into account. Indeed, Eq.IV.1.10 assumes that the pressure drop does not depend on the Reynolds number; it depends only on the geometry dimensions. This case supports the hypothesis that the flow is fully turbulent and the pressure loss is identical in the different labyrinth-channel units. When $S \neq 0$ which corresponds to the case n^o2, the labyrinth-channel geometry generates a weaker pressure drop in comparison with case n^o1. The wall length in 2D (or surface in 3D) is more important in the case n^o1, φ is thus greater. However, the pressure loss occurs mainly at the channel corners (teeth of the baffle) (Wei et al., 2006) [101]. Therefore, the corner structure of the channel is the main factor that affects the efficiency of hydraulic energy dissipation for the labyrinth emitters. The equation Eq.IV.1.10 and the results represented in Fig.IV.1.4 confirm this conclusion. The contributions of wall friction and the dissipation rate in the core flow ϵ are discussed in the following section to better understand how the pressure loss occurs. When comparing curves tendency with the x values, one finds that for $x > 0.5$, as for the experimental data, φ decreases when Re increases. Pressure loss coefficient φ is calculated by Eq.IV.1.9 which depends on Reynolds number by the Darcy friction factor f. This state is represented by the Moody diagram A.14. In the last case, $x < 0.5$, φ increases with Re. This is the numerical case when RSM is used. A detailed analysis of the numerical pressure loss is introduced in the following section to understand this phenomenon. We can conclude that theoretical, experimental and numerical values of φ are of the same order of magnitude for all the studied Reynolds numbers Re. The theoretical equation Eq.IV.1.10 also assumes that the flow is identical in all the labyrinth-channel units. The axial flow homogeneity is discussed in section IV.2.7.

1.4 Numerical calculation of pressure losses

This section presents the results of the approach detailed in section.III.2.5. The S-A model can not be included in this analysis. Thus, only the dissipation rate and the wall friction for the standard, [LS], [CHC] $k-\epsilon$ models and RSM model are calculated, by Eq.III.2.18 and Eq.III.2.19[1], and presented in table IV.1.4, in 2D, and in table IV.1.5, in 3D, for standard, [LS] $k-\epsilon$ models and RSM, for $Re = 400$ and $Re = 800$ which are the extreme values of the performed simulations. The percentage is calculated as the ratio of each contribution to the pressure drop divided by the sum of the three contributions to the pressure drop. When the flow rate decreases, the percentage of the contribution due to the turbulent dissipation decreases, while the two other contributions increase. This can be explained by the decrease of turbulence effect. This result is true in both 2D and 3D. In the case of $Re = 800$, it can be observed that the turbulent dissipation rate for the [CHC] $k-\epsilon$ model is about 1.15-1.20 times higher than for the other $k-\epsilon$ models (see table IV.1.4) and about 1.02 in comparison with RSM model. The dissipation rate obtained from RSM model is closer to [CHC] $k-\epsilon$ model than Standard and [LS] $k-\epsilon$ models. This is explained by the fact that RSM model uses the same ϵ equation as the one used in $k-\epsilon$ models. For $Re = 400$, the dissipation rate is about 1.62-1.74 higher than the other $k-\epsilon$ models (Fig.2.59(c)) and about 1.75 in comparison with RSM model. But, the percentage of this dissipation is closer to the other models table.IV.1.4 and table IV.1.5. The dissipation by the mean flow is higher in RSM model. The third contribution is smaller for standard $k-\epsilon$ model than for the other models. For $Re = 400$, the dissipation is higher for [CHC] $k-\epsilon$ model. The other models have the same quantity. When the terms of pressure drop are compared for $Re = 400$ and $Re = 800$ for all the numerical models, the percentage of wall friction terms decreases when Re increases. The same tendancy is observed for the contribution due to the mean flow, while the contribution due to the turbulence increases, since this contribution is linked to the turbulence intensity. For $Re = 800$, the percentage of pressure loss generated by the turbulent dissipation is dominant, about $77-81.8$ % in 2D and about $59.1-73.5$ % in 3D, and even greater than the wall friction. Nevertheless, for $Re = 400$, this percentage reaches about $69.7-71.8$ in 2D and about $31.3-53.1$ in 3D. Therefore, turbulent dissipation is the main phenomenon which explains the pressure drop, unlike what is observed for standard channel flows (Pope, 2000)[85]. This specific distribution is due to the large swirling regions where wall friction is minimal. x values for S-A and Standard $k-\epsilon$ models are close. Nevertheless, S-A model dissipates more energy than standard $k-\epsilon$ model. The dissipation rate and thus the pressure losses are not influenced directly by the x exponent. However, the influence of the x and k_d values (Eq.I.1.1) on the dissipation rate and thus the pressure losses is discussed in section IV.2.5.

[1] We recall that:

$$p_{inlet} \times d_{inlet} - p_{outlet} \times d_{outlet} \approx (\bar{\epsilon} + \epsilon)\,\frac{\rho A_{area}}{U_m} + \tau_w \times L_{wall}$$

$$p_{inlet} \times A_{inlet} - p_{outlet} \times A_{outlet} \approx (\bar{\epsilon} + \epsilon)\,\frac{\rho V}{U_m} + \tau_w \times A_{wall}$$

.

Table IV.1.4: The pressure drop ΔP with ϵ, $\bar{\epsilon}$ and τ_w, in 2D.

Model	Unit	Standard				LS				CHC				RSM			
flow rate	$[ml.min^{-1}]$	48		24		48		24		48		24		48		24	
Re		800		400		800		400		800		400		800		400	
(1) $\epsilon \times \frac{\rho A_{area}}{U_{mean}}$	$[Pa.m]$	4.81	81.6%	1.07	71.8%	4.50	79.1%	1.15	70.6%	5.36	81.8%	1.86	71.3%	5.29	77%	1.06	69.7%
(2) $\bar{\epsilon} \times \frac{\rho A_{area}}{U_{mean}}$	$[Pa.m]$	0.27	4.6%	0.13	8.7%	0.21	3.7%	0.12	7.4%	0.26	4%	0.30	11.5%	0.59	8.6 %	0.12	7.9 %
(3) $\tau_w \times L_{wall}$	$[Pa.m]$	0.81	13.8%	0.29	19.5%	0.98	17.2%	0.36	22.0%	0.93	14.2%	0.45	17.2%	0.99	14.4 %	0.34	22.4 %
(1) + (2) + (3)	$[Pa.m]$	5.89		1.49		5.69		1.63		6.55		2.61		6.87		1.52	
$\Delta p \times \ell$	$[Pa.m]$	6.00		1.52		5.89		1.68		6.90		3.01		6.92		1.55	

Table IV.1.5: The pressure drop ΔP with ϵ, $\bar{\epsilon}$ and τ_w, in 3D

Model	Unit	Standard				LS				RSM			
flow rate	$[ml.min^{-1}]$	48		24		48		24		48		24	
Re		800		400		800		400		800		400	
(1) $\epsilon \times \frac{\rho V}{U_{mean}}$	$[Pa.m^2] \times 10^{-3}$	4.24	64.5 %	0.68	39.5%	4.26	59.1 %	0.60	31.3%	5.46	73.5 %	1.03	53.1 %
(2) $\bar{\epsilon} \times \frac{\rho V}{U_{mean}}$	$[Pa.m^2] \times 10^{-3}$	0.82	12.5 %	0.41	23.8%	0.85	11.8 %	0.50	26 %	0.60	8.1 %	0.28	14.4 %
(3) $\tau_w \times A_{wall}$	$[Pa.m^2] \times 10^{-3}$	1.51	23%	0.63	36.7%	2.10	29.1%	0.82	42.7%	1.37	18.4%	0.63	32.5%
(1) + (2) + (3)	$[Pa.m^2] \times 10^{-3}$	6.57		1.72		7.21		1.92		7.43		1.94	
$\Delta P \times S_{Section}$	$[Pa.m^2] \times 10^{-3}$	7.06		1.77		8.08		2.27		7.62		1.86	

The pressure drop for each part of labyrinth-channel is also calculated in tables IV.1.6, IV.1.7, IV.1.8 and IV.1.9 for the intermediate Reynolds number (i.e. $Re = 600$). The pressure drop in the second baffle which presents the labyrinth-channel unit is higher than for the first and third baffles. The first baffle contains the entrance which is a straight section. Thus, the dissipation rate is weak in this section. It seems that the flow is not yet developed in this part. However, the third baffle dissipates the energy in a way similar to the second baffle. The pressure drop in the third baffle is, generally, smaller than the sum of the three contributions causing this pressure drop. That is due to the pressure increase after the outlet turn since the outlet section is slightly larger than the section of the labyrinth-channel.

The approaches detailed in section.III.2.5 show that the pressure losses are a function of ϵ, $\bar{\epsilon}$ and τ_w Eq.III.2.18 and Eq.III.2.19. The pressure losses for the modelling, are thus calculated using these equations. The discrepancy between the experimental and numerical data Fig.IV.1.2 could be explained by the over-estimation of ϵ contribution (in relation to the assumption that turbulent production and dissipation are equal) which is the main responsible of pressure drop ($70 - 80\%$, for the high flow rates). The curves plotted in Fig.1.2(b) show that the pressure drop, in three dimensions, is increased in comparison with 2D cases. Especially, the pressure drop due to the wall friction is greater in three dimensions. That is to say that the 3D modelling generates a larger contribution of the wall friction, which is not surprising since the two lateral walls are then considered, while this is not the case for the 2D modeling. A significant shear-strain increase is observed with respect to the dissipation. The ratio of turbulent dissipation / shear-strain, for [LS] $k - \epsilon$ model, is decreased from $4.6/1$, in 2D, to $2/1$, in 3D for $Re = 800$ and from $3.3/1$, in 2D, to $0.75/1$, in 3D for $Re = 400$, while this ratio for RSM model, is decreased from $5.34/1$, in 2D, to $4/1$, in 3D for $Re = 800$ and from $3.12/1$, in 2D, to $1.63/1$, in 3D for $Re = 400$ (see table.IV.1.4 and table IV.1.5).

Table IV.1.6: Standard $k - \epsilon$ model for flow rate of 36 $ml.min^{-1}$, $Re = 600$, in 2D

Unit $[Pa.m]$	baffle 1	baffle 2	baffle 3	total
(1) $\epsilon \times \frac{\rho A_{area}}{U_{mean}}$	0.53	0.88	1.12	2.53
(2) $\bar{\epsilon} \times \frac{\rho A_{area}}{U_{mean}}$	0.07	0.05	0.07	0.19
(3) $\tau_w \times L_{wall}$	0.20	0.13	0.17	0.50
(1) + (2) + (3)	0.80	1.06	1.36	3.22
$\Delta P \times \ell$	0.91	1.26	1.10	3.27

Table IV.1.7: [LS] $k - \epsilon$ model for flow rate of 36 $ml.min^{-1}$, $Re = 600$, in 2D

Unit $[Pa.m]$	baffle 1	baffle 2	baffle 3	total
(1) $\epsilon \times \frac{\rho A_{area}}{U_{mean}}$	0.50	1.12	1.08	2.70
(2) $\bar{\epsilon} \times \frac{\rho A_{area}}{U_{mean}}$	0.08	0.05	0.04	0.17
(3) $\tau_w \times L_{wall}$	0.22	0.17	0.24	0.63
(1)+(2)+(3)	0.80	1.33	1.36	3.49
$\Delta P \times \ell$	1.22	1.31	1.09	3.62

1.5 Conclusion

The pressure drop along the baffles is analyzed in this chapter. The pressure losses, namely hydraulic performance, are an important factor in micro-irrigation emitter. This must be taken into account as part of an emitter optimization by CFD. The experimental exponents of the discharge-pressure are about 0.59 which is close to the fully turbulent developed regime. Some turbulence models as Standard,

Table IV.1.8: [CHC] $k-\epsilon$ model for flow rate of 36 $ml.min^{-1}$, $Re = 600$, in 2D

Unit $[Pa.m]$	baffle 1	baffle 2	baffle 3	total
(1) $\epsilon \times \frac{\rho A_{area}}{U_{mean}}$	0.10	1.79	2.43	4.32
(2) $\bar{\epsilon} \times \frac{\rho A_{area}}{U_{mean}}$	0.10	0.17	0.08	0.35
(3) $\tau_w \times L_{wall}$	0.20	0.24	0.27	0.71
(1) + (2) + (3)	0.37	2.20	2.78	5.35
$\Delta P \times \ell$	1.58	2.92	2.40	5.90

Table IV.1.9: RSM model for flow rate of 36 $ml.min^{-1}$, $Re = 600$, in 2D

Unit $[Pa.m]$	baffle 1	baffle 2	baffle 3	total
(1) $\epsilon \times \frac{\rho A_{area}}{U_{mean}}$	0.38	0.91	1.46	2.75
(2) $\bar{\epsilon} \times \frac{\rho A_{area}}{U_{mean}}$	0.06	0.06	0.08	0.20
(3) $\tau_w \times L_{wall}$	0.22	0.13	0.24	0.59
(1) + (2) + (3)	0.66	1.10	1.78	3.54
$\Delta P \times \ell$	1.00	1.55	1.19	3.74

[LS] $k-\epsilon$, RSM and S-A models give an exponent closer to the experimental one and others [Abid], [AKN] and [CHC] $k-\epsilon$ models are further away from this exponent. However, the models for which the values of x are close to 0.5 do not predict the same pressure losses, i.e standard $k-\epsilon$ and SA models where the first model predicts the smallest numerical pressure losses, while S-A model predicts the greatest one. Therefore, the velocity analysis must be discussed and explained to understand deeply the difference. Theoretical pressure drop estimated from emitter dimensions suppose the flow is rather fully turbulent. φ, thus, does not depend on Reynolds number, while experimental results show that the flow is related to Reynolds number. When calculating the experimental values of φ, it is found that the theoretical value is in the range of experimental φ. Numerical analysis points out an expected result: dissipation rate is the main driver of head losses, ahead of wall friction. However, dissipation modelling differs from one model to another which could explain variation between numerical results and the gap from experimental data. The discharge-pressure curves allows to eliminate some models as Abid, [AKN], and RNG $k-\epsilon$ which give results far from experimental results. It seems the numerical models standard and [LS] $k-\epsilon$ and RSM model are more adequate to model the flow in the labyrinth-channel. Extended analysis on the velocity fields is presented in the next chapter to confirm which is the best model.

Chapter 2

Analysis of the labyrinth-channel flow

2.1 Introduction

In order to analyze flow behavior, the instantaneous and mean velocity, fluctuating velocity second-order moments, turbulence intensity, turbulence kinetic energy and vorticity fields and profiles, obtained by the experimental and numerical methods, are presented and discussed in this chapter. The CFD simulations are performed on a three pattern labyrinth-channel which is the repetitive pattern of the whole emitter labyrinth-channel (section 2.1), while micro-PIV measurements are performed on a ten pattern labyrinth-channel which allows to see the flow evolution beyond the third labyrinth-channel. For both approaches, a range of three flow rates have been imposed, namely, 24 $ml.min^{-1}$, 36 $ml.min^{-1}$ and 48 $ml.min^{-1}$ which corresponds to Reynolds number ranging from 400 to 800. The flow in the labyrinth-channel is visualized, experimentally, by flow mixing with fluorescent particles and laser light sheet. The particles diameter is of $1\mu m$. Nevertheless beyond the third baffle, the $1\mu m$ particles have a low SNR as the laser diverges in plexiglass. Therefore, these are replaced by particles of $5\mu m$ diameter. A comparative analysis between the $1\mu m$ and $5\mu m$ results is presented in annex A.10 to validate that experimental results are not influenced by this diameter change. The acquired data are treated and analyzed by Dantec software (Dynamic Studio) and Matlab scripts.

Experimental mean velocity profiles presented in this manuscript are obtained by ensemble-averaging on 500 (or 250) instantaneous velocity fields, each field containing 127×127 vectors with $1\mu m$ particles diameter (63×63 vectors with $5\mu m$).

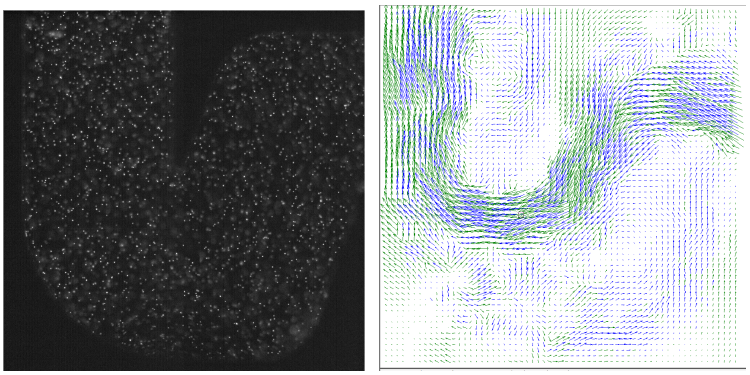

(a) Particle seeding. (b) Velocity vectors.

Figure IV.2.1: Flow seeding in the tenth baffle of the labyrinth-channel, $q = 48\ ml.min^{-1}$, $d_p = 5\mu m$

2.2 Experimental visualization of instantaneous velocity fields

The instantaneous velocity field in the labyrinth-channel and its fluctuation about the mean value are presented in this section. Fig.IV.2.1(a) shows, in the tenth baffle, a typical micro-PIV image. The images reveal the instantaneous flow ($10\ ns$) from a single laser sheet illumination and the time-averaged flow resulting from $1/11\ s$ exposure onto a Hisense camera. The flow is seeded by particles noted in table II.1.4. The corresponding velocity fields in the tenth baffle are presented on Fig.IV.2.1(b). The blue vectors refer to valid ones when green vectors to spurious ones. Two characteristic locations are noted in the labyrinth-channel unit labeled A and B on Fig.IV.2.2 to analyze the instantaneous flow in the zone where velocity vectors are dense and the zone where the velocity vectors are light and dispersed respectively. Four images of instantaneous velocity vectors are presented in Fig.IV.2.2. It is, as expected, shown that the vector magnitude and direction change from one image to another which explains the variation of instantaneous velocity which is presented in Fig.IV.2.3, where the bold lines are the cumulative averages based only on the valid vectors (blue ones). Therefore, the pair of images number presented in Fig.IV.2.3 is inferior to 250.

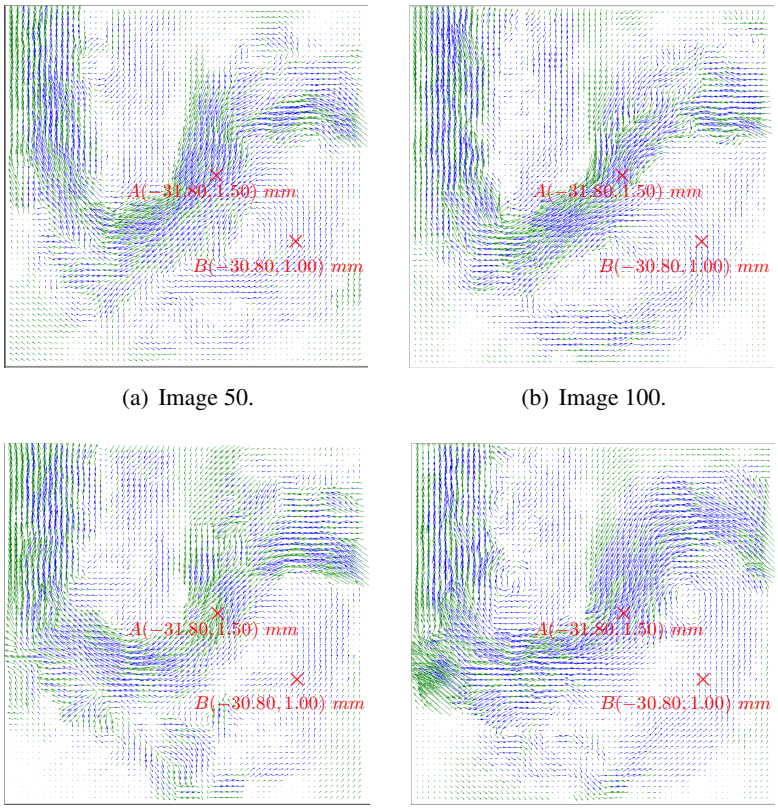

(a) Image 50. (b) Image 100.

(c) Image 150. (d) Image 200.

Figure IV.2.2: Velocity vectors inside the tenth baffle for different images, $q = 48\ ml.min^{-1}$, $d_p = 5\mu m$

Peak-to-peak amplitude and average value ratio for u and v $(max(u) - min(u))/\overline{u}$, are then calculated for these two points [1]. The velocity variation about the average value is more noticeable in point B (19 and 5.3 for u and v respectively). This means that the velocity components u and v vary from a value 19 and 5.3 times the average which has a low value in this point, while it reaches 2 and 0.8 (for u and v respectively) in point A which has a high value. Finally, the evolutions of instantaneous velocity are plotted in two points C and D, where the first one is in the middle of the inlet channel $C(-0.60, -1.50)mm$ and the other is near the wall $D(-1.16, -1.50)\ mm$ (Fig.IV.2.4). Obviously, the

[1] The coordinate system is shown on Fig.II.1.6.

variation of the u velocity is more notable near the wall. The velocity component u is almost zero.

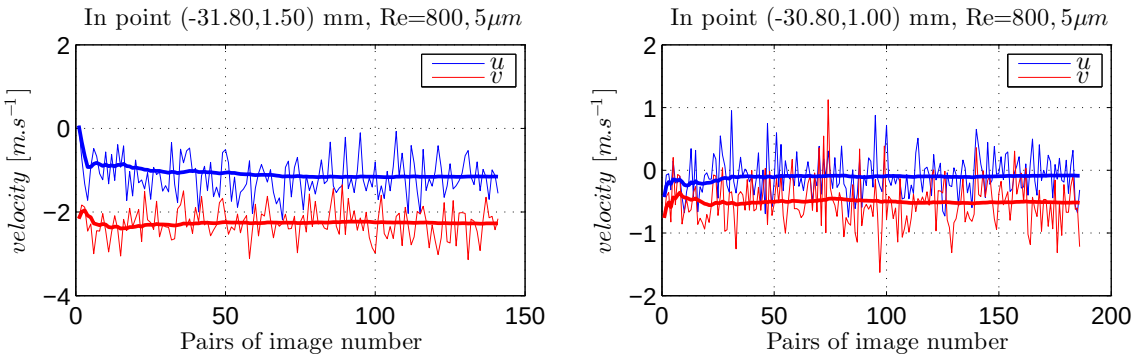

(a) $A(-31.80, 1.50)\ mm$ (b) $B(-30.80, 1.00)\ mm$

Figure IV.2.3: Instantaneous velocity in the tenth baffle of labyrinth-channel, $q = 48\ ml.min^{-1}$, $d_p = 5\mu m$

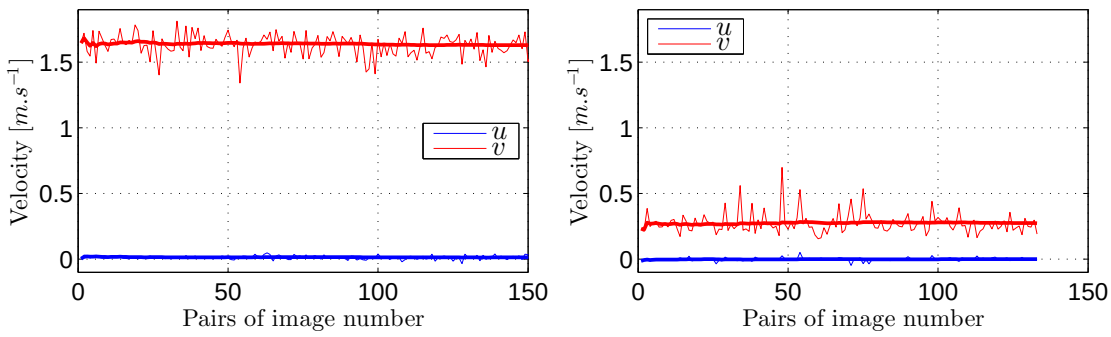

(a) Flow core $C(-0.60, -1.50)\ mm$. (b) Near-wall $D(-1.16, -1.50)\ mm$.

Figure IV.2.4: Instantaneous velocity in the entrance, $q = 48\ ml.min^{-1}$, $d_p = 5\mu m$

2.3 Inlet flow

2.3.1 Mean flow properties

Experimentally, the labyrinth-channel prototype is designed to ensure that the flow is established before the entrance into the baffle curve. The simulation is realized supposing the flow is turbulent, so the flow will be modeled following the equations of turbulence model even in the straight square section[2]. The turbulence models are based on hypotheses which vary from one model to another (chapter III.1). For example, $k - \epsilon$ model is based on the Boussinesq hypothesis and the hypothesis of isotropy. Nevertheless this hypothesis is not used for the RSM model. Therefore, the solution may depend on the model. The comparison between the experimental and numerical results allows to validate the numerical work.

The geometry 1 is used to visualize the flow in the inlet. The dimensions are presented in table II.1.1. The cross-section area A_c is equal to $0.86\ mm^2$, while A_c of geometry 2 is equal to $1.38\ mm^2$.

Mean properties such as the bulk mean velocity, skin-friction coefficient and correlation coeffi-

[2]Laminar model and LES were also conducted on the geometry shown in Fig.III.2.1. However both models did not give relevant results.

cient are treated. The bulk mean velocity is calculated from Eq.IV.2.1 for a square cross-section pipe:

$$U_m = \frac{1}{A_c}\int_0^{A_c} \overline{u}\mathrm{d}A \quad . \tag{IV.2.1}$$

However, this relationship leads to a simple formula from which the bulk mean velocity is easy to calculate if the mass flow rate $\dot{m}$ is known:

$$U_m = \frac{\dot{m}}{\rho A_c} = \frac{q}{A_c} \quad . \tag{IV.2.2}$$

By applying this formula, one finds the value of the mean bulk velocities U_m (or $|\overline{u}|_{inlet}$) presented in table IV.2.1. Since there are two geometries used in the experiments, therefore, Reynolds numbers slightly vary. They are calculated taking into account the dimension detailed in table II.1.1 and presented in table IV.2.1.

Table IV.2.1: Reynolds numbers.

flow rate	Modeling			Geometry 1			Geometry 2		
$ml.min^{-1}$	D_h $\times 10^{-3}m$	U_m $m.s^{-1}$	Re	D_h $\times 10^{-3}m$	U_m $m.s^{-1}$	Re	D_h $\times 10^{-3}m$	U_m $m.s^{-1}$	Re
24		0.4	400		0.48	435		0.295	346
36	1	0.6	600	0.916	0.71	642	1.17	0.435	510
48		0.8	800		0.94	863		0.585	687

Experimental velocity fields, at the inlet, are plotted for two Reynolds numbers Fig.IV.2.5 for micro-PIV data[3]. In order to see the velocity evolution along the channel inlet, velocity profiles, before the first baffle curve, are plotted along the inlet channel (y coordinate direction) to determine whether the flow evolves or not. These profiles are shown in Fig.IV.2.6 for $Re = 435$ and $Re = 863$ with $d_p = 1\ \mu m$. They show that the velocity is subjected to only a small change when approaching the curvature of the first baffle when $Re = 863$. However, velocity profiles do not evolve along a distance of 1.9 D_h. Therefore, the profile is considered to be established. The parabolic shape of velocity profile for $Re = 435$ ensures this fact. For $Re = 863$, it can be remarked that the velocity profile is flattened at the middle of the channel. The centerline velocities U_c are 1.03 $m.s^{-1}$, 1.39 $m.s^{-1}$ and 1.64 $m.s^{-1}$. Then, the ratio of the mean centerline velocity to the mean bulk velocity, U_c/U_m is almost 2.16 for $Re = 435$, 2 for $Re = 642$; and 1.743 for $Re = 863$ (Fig.IV.2.7). The ratios of U_c/U_m for the numerical results, [LS] $k-\epsilon$ and RSM models, are about $1.4-1.5$ when Reynolds number is in the range 400-800. LS $k-\epsilon$ and RSM models are chosen to perform these analyses at the inlet and at the outlet since (i) LS $k-\epsilon$ model is the closest to the experiments for the x exponent value, and since (ii) Chaudhary et al. (2013) [26] have demonstrated that RSM model with enhanced wall treatment offers a high accuracy with the added ability of capturing turbulence anisotropy and secondary flows, but its computational cost is very high. Their calculations are performed for a low-Reynolds number $Re = 4586$.

In a circular pipe, the mean bulk (average) velocity in fully developed laminar pipe flow is one-half of the mean centerline (maximum) velocity(White (2010) [105]). It is clear that the ratio U_c/U_m decreases when Re increases for experimental and numerical data Fig.IV.2.8 for a given x/D_h position. The experimental results obtained in this study, are closer to Targ's data in pipe Sparrow et al.(1964) [98] whereas the numerical results are closer to the case of plane channels (this ratio does not exceed 1.5), a result which we could not explain so far in a quantitative way even though it is probably related to insufficient entry length for modelling as illustrated in Fig.IV.2.8.

[3]The x-axis in the figure passes through the right side of the inlet section, while the y axis passes through the bottom side of the labyrinth-channel unit. The origin of coordinate system is pointed out in blue in Fig.II.1.6. Therefore the inlet is at $y = -35\ mm$ and $y = -4\ mm$ experimentally and numerically respectively.

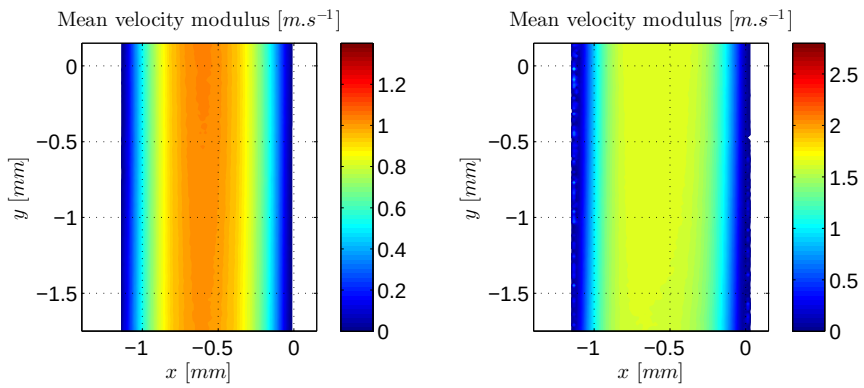

(a) $Re = 435$. (b) $Re = 863$.

Figure IV.2.5: Velocity fields at the inlet, $d_p = 1\ \mu m$

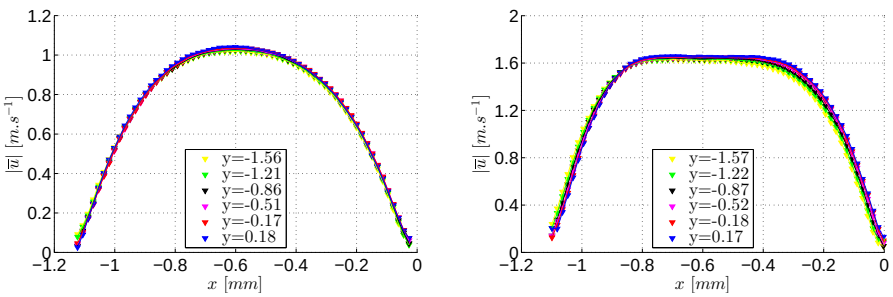

(a) $Re = 435$. (b) $Re = 863$.

Figure IV.2.6: Velocity profiles for various y positions at the inlet, $d_p = 1\ \mu m$

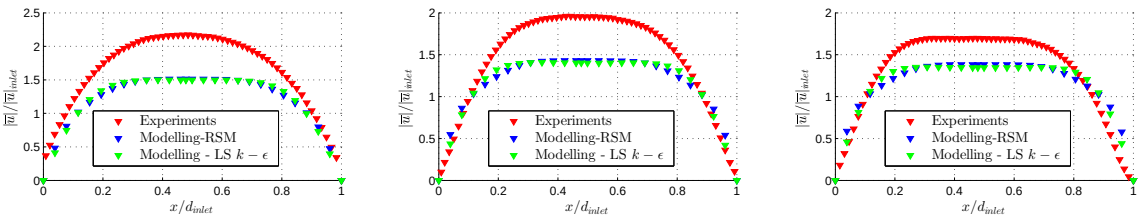

(a) $Re = 400$ (b) $Re = 600$ (c) $Re = 800$

Figure IV.2.7: Normalized velocity profiles on line a, $d_p = 1\mu m$, where the line a is at $y = 4\ D_h$ from the inlet in the numerical modeling and is at $y \simeq 38\ D_h$ for the micro-PIV experiments.

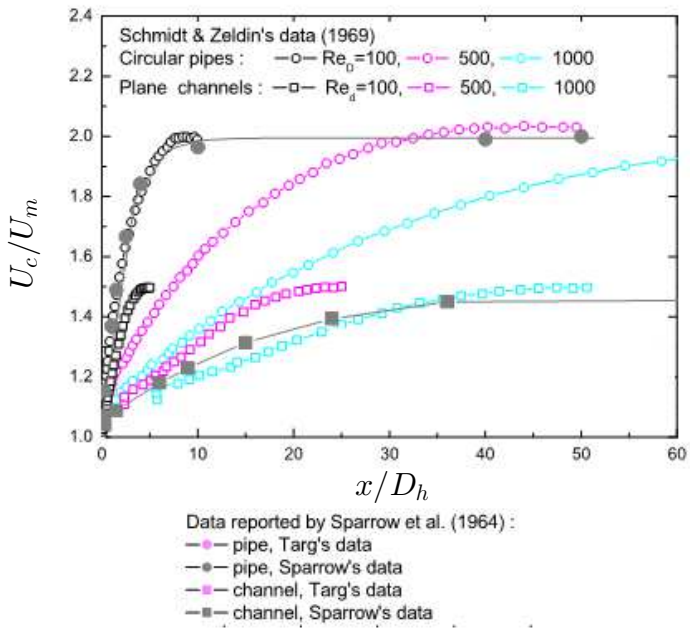

Figure IV.2.8: U_c/U_m from the study of Sparrow et al.(1964) [98]

The velocity profiles are strongly related to the distance from the pipe (or duct) inlet to the point at which the velocity profiles are taken. The length from the pipe inlet to the point where the flow velocity does change, is called hydrodynamic entrance length L_e and the region along this length is called hydrodynamic entrance region, while the region beyond the entrance region in which the velocity profile is fully developed and remains unchanged is called the hydrodynamically fully developed region. Dimensional analysis shows that the Reynolds number and pipe diameter are the only parameters affecting entrance length. For laminar flow, the accepted correlation between the entrance length and Reynolds number is:

$$\frac{L_e}{D_h} \simeq 0.06 Re_d \qquad \text{laminar} \tag{IV.2.3}$$

In turbulent flow, L_e is relatively shorter. Its dependence on the Reynolds number is weaker. For decades, it was favored a sixth-power-law estimate, $L_e/D_h \simeq 4.4 Re_d^{1/6}$, but recent CFD results (Anselmet et al., 2009 [11]) indicate that a better turbulent entrance-length correlation is:

$$\frac{L_e}{D_h} \simeq 1.6 Re_d^{1/4} \qquad Re_d \leq 10^7 \quad . \tag{IV.2.4}$$

In the present range of Reynolds numbers $400 - 800$, entrance length L_e must be between $24 - 48\ D_h$. Therefore, the experimental normalized velocity profile, Fig.2.7(c), is slightly different from Targ's data when Re is about 1000. The choice of turbulent boundary conditions (see section III.2.3) favors the flow development, therefore the entrance length will be shorter. The velocity profile is somewhat acceptable at $y = 4D_h$.

The skin friction coefficient is calculated from $C_f = \tau_w / \frac{1}{2}\rho U_m^2$. The wall shear stress, τ_w, is here given by:

$$\tau_w = \mu \left(\frac{\partial \overline{v}}{\partial x} \right)_{x=0} \quad ; \tag{IV.2.5}$$

where μ is the dynamic viscosity, $\overline{v}$ is the flow velocity parallel to the wall and x is the distance to the wall. Fig.IV.2.9 shows $\left(\frac{\partial \overline{v}}{\partial x}\right)$ along the line "a" for both Reynolds numbers used in the experiments, while numerical velocity gradients are presented in Fig.IV.2.10. These two figures allow to calculate the friction velocity, presented in table IV.2.2. The friction velocity is calculated by the formula $u_\tau = \sqrt{(\tau_w/\rho)}$.

Reynolds number based on the friction velocity is given as:

$$Re_\tau = \frac{u_\tau D_h}{\nu} \tag{IV.2.6}$$

Some details about the mean velocity properties are presented in table IV.2.2.

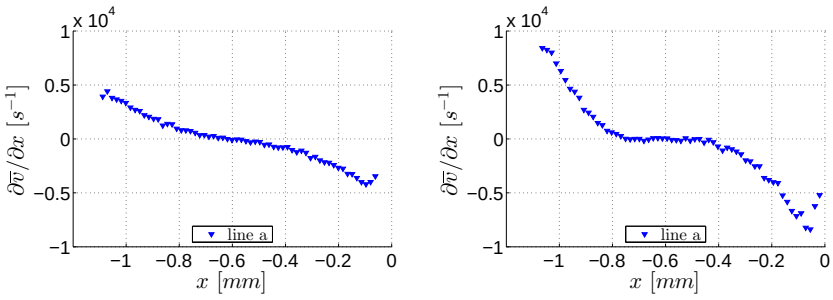

(a) $Re = 435$. (b) $Re = 863$.

Figure IV.2.9: Experimental velocity gradient $\left(\frac{\partial \overline{v}}{\partial x}\right)$ at $y \simeq 38D_h$, $d_p = 1\mu m$. This profile allows to calculate τ_w by Eq.IV.2.5. Worth noting that the maximum value is taken near the wall at $0 > x > -0.1\ mm$.

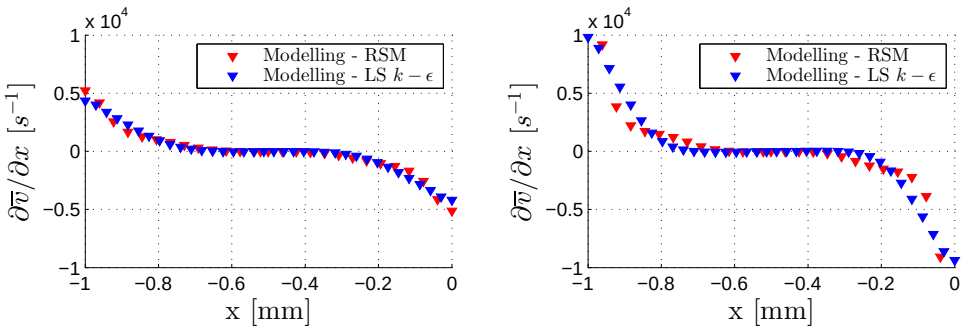

(a) $Re = 400$. (b) $Re = 800$.

Figure IV.2.10: Numerical velocity gradient $\left(\frac{\partial \overline{v}}{\partial x}\right)$ at $y = 4D_h$

Table IV.2.2: Mean flow variables

	Re	$\frac{\partial \overline{v}}{\partial x}$ s^{-1}	τ_w pa	u_τ $m.s^{-1}$	Re_τ	C_f	f	$C_f \times Re$	k_f
Micro-PIV	435	4197	4.197	0.065	59.4	36.44×10^{-3}	0.15	15.9	63.4
	863	8389	8.389	0.092	84.0	19.0×10^{-3}	0.08	16.4	65.6
RSM model	400	5220	5.220	0.072	72	65.25×10^{-3}	0.261	26.1	104.4
	800	12062	12.06	0.11	110	37.69×10^{-3}	0.151	30.2	120.8
LS $k-\epsilon$	400	4389	4.389	0.066	66	54.86×10^{-3}	0.220	22.0	88.0
	800	9907	9.907	0.10	100	30.96×10^{-3}	0.124	24.8	99.2

The friction factor f, which is presented in table IV.2.2, is related to the skin-friction coefficient C_f by the relation: $f = 4 \times C_f$. The friction factor is shown in the diagram Fig.A.13 (see annex A.11). As $f > 0.04$, the relationship between f and Re is $f = k_f/Re$, where $k_f = 64$ for a cicular pipe. k_f is calculated and presented in table IV.2.2 which is close to the theoretical value, about 60.4 for rectangular geometry with $a/b = 1.34$ used in experiments, where a and b are the length and the width of the cross-section (see annex A.12 for more details about k_f in function of geometry dimensions for fully laminar

flow). f justifies that the flow is rather laminar for the experimental profiles, while for RSM and LS $k-\epsilon$ models, k_f value is close to the value obtained when $a/b = \infty$ (this case corresponds to a plane channel flow). This result confirms the ratio obtained for U_c/U_m when comparing to Targ's data (Sparrow et al., 1964) [98]). These parameters and relationships are true when the flow is developed. Therefore, the experimental parameters are closer to the theoretical value.

2.3.2 Turbulence statistics

The turbulence statistics for fully developed flow in a straight square section include the root-mean square (rms) values of velocity fluctuations, the correlation coefficient of u' and v', the skewness and flatness factors of velocities. Showing the statistics of turbulence of the duct flow is useful for the detailed understanding of the velocity fluctuation properties. In particular, calculating the skewness factor is helpful to know the flow heterogeneity, while giving the rms values is helpful to know the velocity fluctuating amplitude in the two spatial directions, and the turbulent diffusivity that is further related to the velocity correlation coefficient (see Eq.IV.2.10).

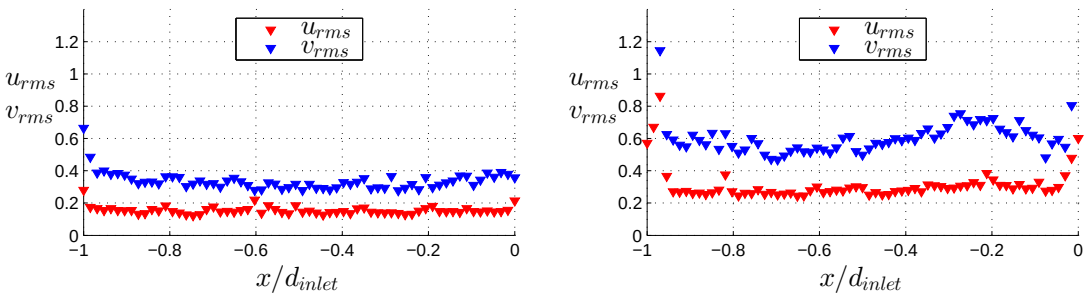

(a) $Re = 435$. (b) $Re = 863$.

Figure IV.2.11: Root-mean-square velocity fluctuations normalized by the wall shear velocity u_τ along the line a, $d_p = 1\mu m$

Huser and Biringen (1993)[51] (hereinafter denoted as HB) carried out the DNS of a fully developed turbulent duct flow at a Reynolds number of 10320 ($Re_\tau = 600$ based on the wall-shear velocity and the duct width). u_{rms}, v_{rms} and w_{rms} normalized by the wall-shear velocity reach 3, 1 and 0.8 respectively near wall. Kim el al. (1986)[58] (denoted as KMM) carried out simulations on a channel and they found that the root-mean-square velocity fluctuations profiles are symmetric about the middle of channel where the values are 0.8, 0.6 and 0.6. In the present study, u_{rms} and v_{rms} are about 0.4 and 0.2 for $Re = 435$ ($Re_\tau = 59.4$) and 0.8 and 0.3 for $Re = 863$ ($Re_\tau = 84$).

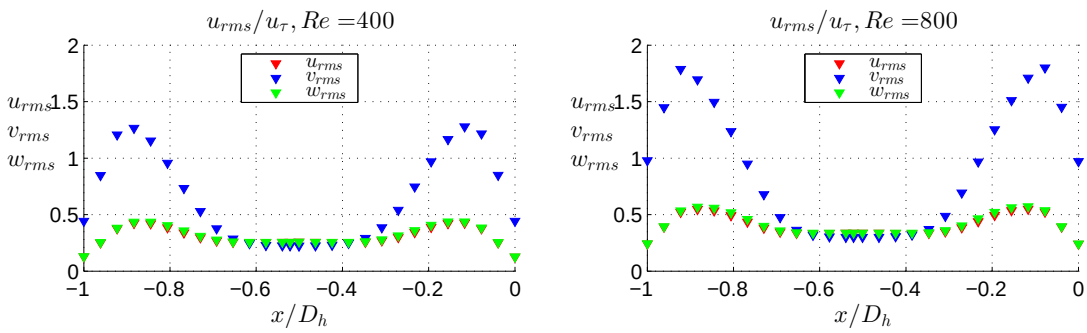

(a) $Re = 400$. (b) $Re = 800$.

Figure IV.2.12: Numerical root-mean-square velocity fluctuations normalized by the wall shear velocity u_τ along the line a, RSM model

In the study of KMM, u_{rms} and v_{rms} are zero at the wall and reach their maximum values in the boundary layer on a distance of $0.1\ y/\delta$ which is equivalent to $0.05\ mm$ from the wall in the present study. While, in our modeling performed by RSM model, the maximum value of u_{rms}, v_{rms} and w_{rms} is at $0.08\ mm$ from the wall Fig.IV.2.12. With the present experimental treatment, it is difficult to see the evolution of u_{rms} and v_{rms} along the boundary layer. The first point is at $0.0344\ mm$.

The fluctuating velocity second-order moments $\overline{u'^2}$, $\overline{v'^2}$ and $\overline{u'v'}$ are, then, treated and analyzed. These fluctuating velocity second-order moments are calculated as the mean of the squared fluctuating velocities at the inlet. The fluctuating velocity second-order moments show that the turbulence is weak; about $10^{-4}\ m^2.s^{-2}$ for both $\overline{u'^2}$ and $\overline{u'v'}$, while it reaches $10^{-2}\ m^2.s^{-2}$ ($10^{-3}\ m^2.s^{-2}$) for $\overline{v'^2}$ with $Re = 863$ ($Re = 435$ respectively). This term $\overline{v'^2}$, as expected, is larger than the other terms $\overline{u'^2}$ and $\overline{u'v'}$ (Fig.IV.2.13 and Fig.IV.2.14). Comparing the two components measured by micro-PIV, the fluctuating velocity second-order moment $\overline{v'^2}$ is greater than $\overline{u'^2}$. The ratios are 10 (20) for $Re = 435$ ($Re = 863$). Therefore, the fluctuating velocity variance perpendicular to the main flow axis is $10 - 20$ times lower than in the main flow direction.

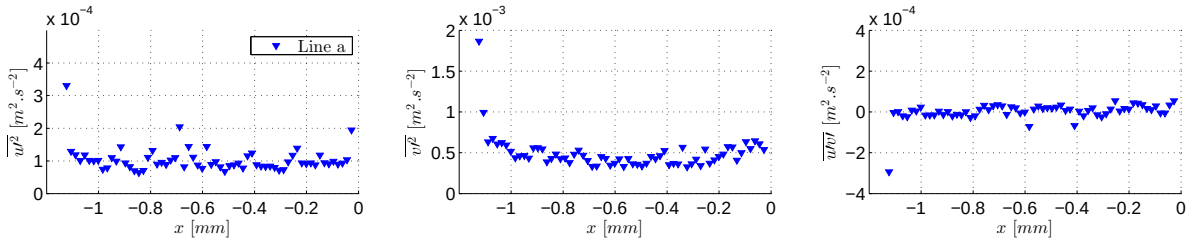

Figure IV.2.13: Fluctuating velocity second-order profiles along the line a, $Re = 435$, $d_p = 1\mu m$

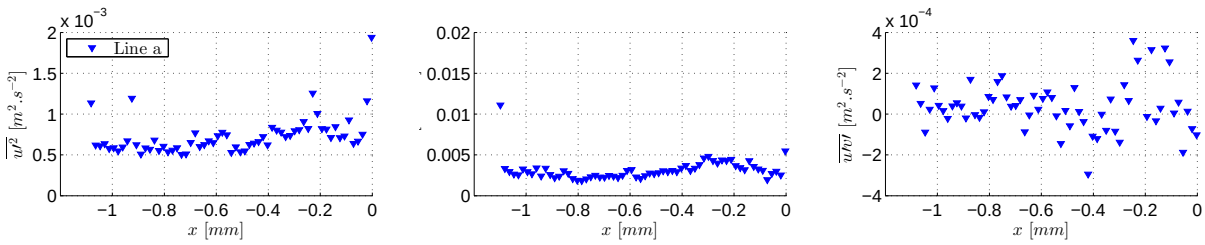

Figure IV.2.14: Fluctuating velocity second-order profiles along the line a, $Re = 863$, $d_p = 1\mu m$

The skewness factors of the velocity fluctuation $\mathcal{S}(u')$ and $\mathcal{S}(v')$ are plotted as a function of the global coordinate along the line a. It can be seen, from Fig.IV.2.15 and Fig.IV.2.16, that the skewness factors are in a fairly good agreement with the DNS results of KMM (see Kim et al. (1987)[58]). It is difficult to compare between the study of KMM and the present study since the flow in the study of KMM is fully developed, while the flow in the labyrinth-channel inlet is not well characterized due to the convergence study at the inlet[4]. The skewness $S(u')$ and $S(v')$ are symmetric about the channel center (see Kim et al. (1987) KMM [58]). $S(u')$ is about 1 near the wall whereas this reaches -0.5 at the middle of pipe, while $S(v')$ is about 0.5 on one side and it changes sign at the channel center to -0.5 on the other side of the channel.

[4]In the study of KMM, the channel is horizontal. The flow direction is in the x axis. Whereas in the present study, the flow is vertical at the inlet and the flow direction is in the y axis. Therefore, the comparison is performed between $\mathcal{S}(v')$ of our study and $\mathcal{S}(u')$ in the study of KMM.

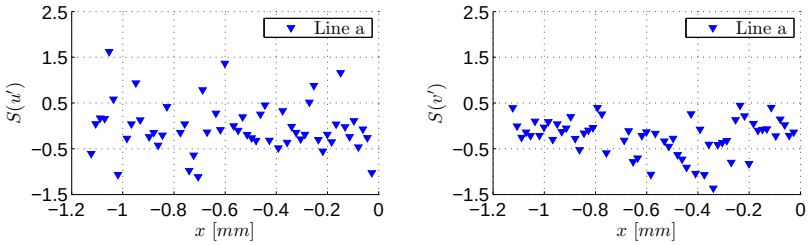

Figure IV.2.15: Skewness profiles in line a, $Re = 435$, $d_p = 1\mu m$

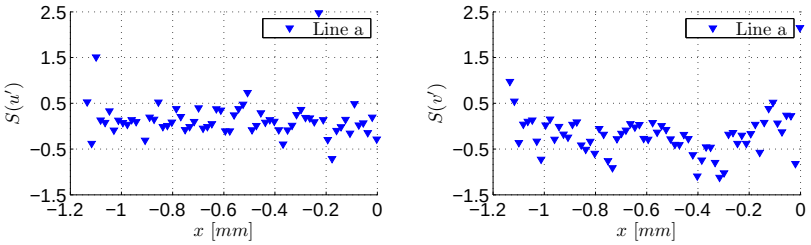

Figure IV.2.16: Skewness profiles in line a, $Re = 863$, $d_p = 1\mu m$

Correlation coefficient $\mathcal{C}$ is an important parameter to qualify the turbulence in pipes. This parameter is calculated by the following formula:

$$\mathcal{C} = \overline{u'v'} / \left(\sqrt{\overline{u'^2}} \times \sqrt{\overline{v'^2}} \right) \quad . \tag{IV.2.7}$$

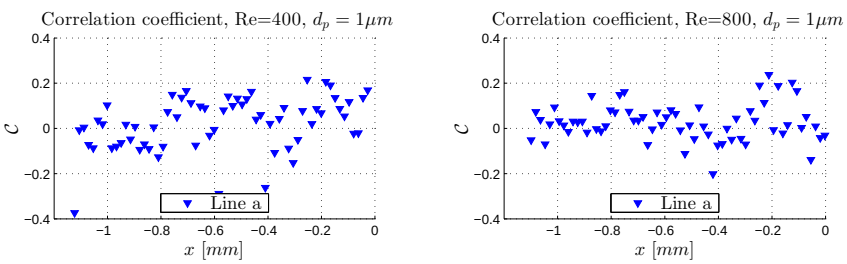

(a) $Re = 435$. (b) $Re = 863$.

Figure IV.2.17: Correlation coefficient profiles in line a, $d_p = 1\mu m$

In channel flow, this parameter has the maximum value 0.4 for KMM (Kim et al., 1987)[58] and it changes sign at the middle of channel where its value is zero. Fig.IV.2.17 shows the results obtained for this parameter using $d_p = 1\mu m$. The value of $\mathcal{C}$ is different from the values obtained by KMM (Kim et al., 1987) [58] as it is found for $\mathcal{S}(u')$ and $\mathcal{S}(v')$. However, this value is strongly related to $\overline{u'^2}$ and $\overline{u'v'}$. Therefore, it is better to see this parameter inside the baffle such as the outlet section since $\overline{u'^2}$ and $\overline{u'v'}$ have relatively high values in comparison with the inlet section (see sections IV.2.4 and IV.2.5). As a conclusion for the flow in the inlet, additional pairs of image would be required to be able to measure with more accuracy the various quantities as u_{rms}, v_{rms}, $\mathcal{C}$, $S(u'^2)$, $S(v'^2)$. The values of $S(u'^2)$, $S(v'^2)$ at the inlet, obviously, resulted from the poor convergence of u' and v'.

The turbulent intensity, I, is defined as the ratio of the root-mean-square of the velocity fluctuations, u', to the bulk velocity, U_m:

$$I = \frac{u'}{U_m} \tag{IV.2.8}$$

where:

$$u' = \sqrt{\frac{1}{3}\left(\overline{u'^2} + \overline{v'^2} + \overline{w'^2}\right)} \quad . \tag{IV.2.9}$$

As only two components of the fluctuating velocity are measured by two component micro-PIV, the third component has to be estimated from the first two. Therefore, it was decided to calculate the turbulent intensity by assuming axisymmetric flow (Hafeli et al. 2014)[44], i.e. the two components perpendicular to the main flow direction are considered equal ($\overline{u'^2} \simeq \overline{w'^2}$). This hypothesis is confirmed since u_{rms}, w_{rms} are superposed as it is seen in Fig.IV.2.12 using RSM model.

Turbulent intensity profiles are compared for [LS] model, RSM model and micro-PIV for $Re = 800$ and $Re = 400$. It is clearly shown in Fig.IV.2.18 that in the middle of channel, the numerical turbulent intensity results are both close to experimental results. The turbulent intensity is plotted on line a for $Re = 435$ and $Re = 863$ with $d_p = 1\mu m$ (Fig.IV.2.18). The turbulent intensity values reach $4 - 5$ % ($3 - 3.5$ %) at the middle and 10.0 % (6 %) near the wall for $Re = 863$ (respectively $Re = 435$). Near the wall, RSM model predicts better the turbulent intensity in the boundary layers. Since damping functions are used for [LS] $k - \epsilon$ model, this model predicts a weak turbulence intensity near the wall. As expected, the turbulent intensity is zero at the wall for both models.

A turbulent intensity of 5 % has been taken as boundary condition to model the flow in the labyrinth-channel. This value allows to perform the flow modeling maintaining the I value in the good order of magnitude.

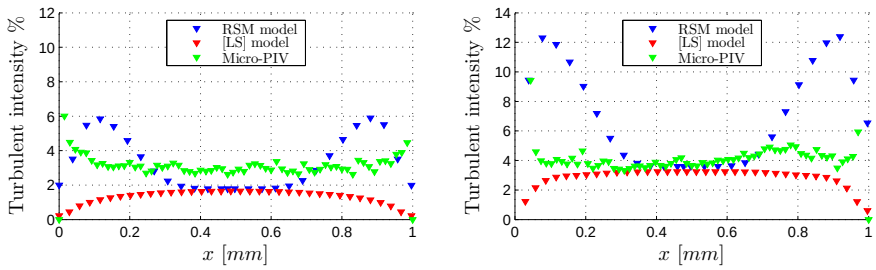

(a) $Re = 400$ (b) $Re = 800$

Figure IV.2.18: Numerical and experimental turbulent intensity profiles, $d_p = 1\mu m$. In x-axis, the coordinates are normalized by d_{inlet} to be 0 and 1 in the two sides. It is important to note that $d_{inlet} = 1\ mm$ and $1.2\ mm$ numerically and experimentally respectively.

2.4 Outlet flow

The outlet section has a rectangular form. Firstly, normalized mean velocity profiles are plotted along the line b (see Fig.II.1.6) for both Reynolds numbers $Re = 400$ and $Re = 800$ and are compared to RSM model results in Fig.IV.2.19. It clearly appears that the velocity is influenced by the presence of a vortex at the outlet where $|\overline{u}|$ is closer to zero between $x/d_{outlet} = 0.75$ and $x/d_{outlet} = 0.85$ [5] for $Re = 800$. The ratio of maximum velocity to the bulk velocity in the outlet is, experimentally, about 2.2 for both Reynolds numbers, while for RSM model this ratio increases from 1.83 for $Re = 400$ to 2.1 when $Re = 800$. The mean velocity results are somewhat comparable even if the outlet section is after 10 labyrinth-channel units for the experiments, while it is only after 3 labyrinth-channel units for modelling. Then, the fluctuating velocity second-order moments normalized by the friction velocity, calculated at the inlet (see section 2.3), are plotted along the line b, Fig.IV.2.20 for the experimental results and in Fig.IV.2.21 for RSM model. One can conclude that the numerical results have the same magnitude as the experimental results. The values of $\overline{u'^2}$,$\overline{v'^2}$ and $\overline{u'v'}$ are much larger in the outlet when comparing these values with the values obtained at the inlet. The ratio is about $40 - 50$. This trend is

[5] In the outlet section, the analysis is performed on geometry 2.

clear when calculating the turbulent intensity at the outlet (Fig.IV.2.22).

The analysis performed in the outlet shows clearly that the flow is turbulent and the turbulent intensity is about 50%. We suppose that this turbulence comes from the sharp changes of direction within the labyrinth-channel. Reynolds number effect on the results is low.

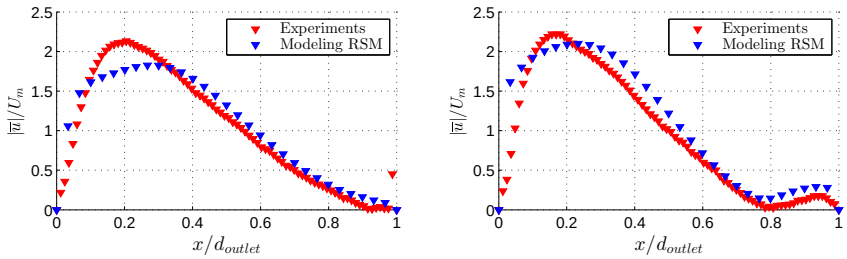

(a) $Re = 400$. (b) $Re = 800$.

Figure IV.2.19: Normalized mean velocity modulus profiles in line b

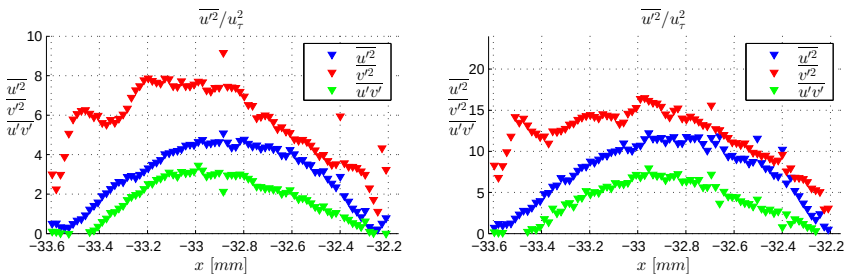

(a) $Re = 346$ (b) $Re = 687$

Figure IV.2.20: Normalized fluctuating velocity second order moments in line b, $d_p = 1\mu m$

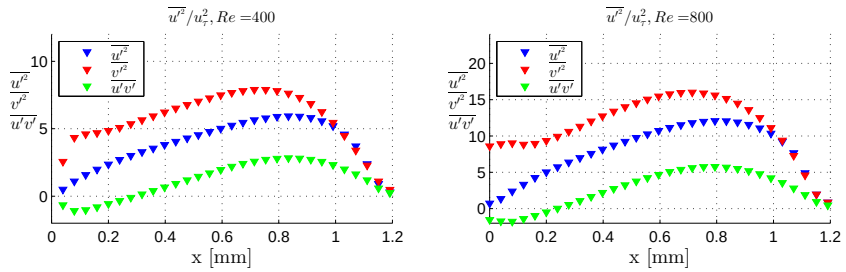

(a) $Re = 400$ (b) $Re = 800$

Figure IV.2.21: Normalized fluctuating velocity second order moments in line b, RSM model

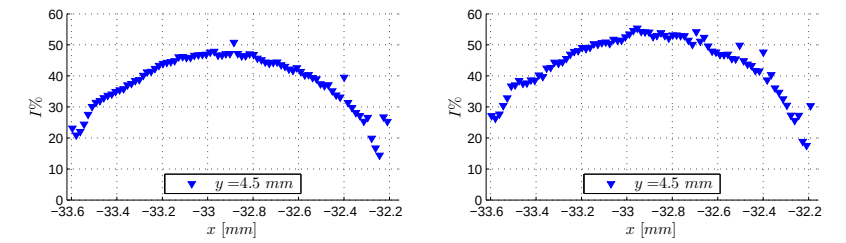

(a) $Re = 346$ (b) $Re = 687$

Figure IV.2.22: Turbulent intensity profiles in line b, $d_p = 1\mu m$

2.5 Flow characterization inside the baffles

2.5.1 Experimental analysis

The mean velocity modulus field and streamlines inside the first and third baffles using $1\mu m$ particles are shown in Fig.IV.2.23 to Fig.IV.2.26 (where the flow is numerically shown to be established). Behind the obstacle, namely baffle in this manuscript, the flow is composed of two small vortices for the first baffle and a single large vortex from the third baffle. This region is called a recirculation zone (red ellipse) which is characterized by a very low velocity. The mean velocity modulus varies from 0.05 to 0.2 $m.s^{-1}$ for $Re = 346$ (respectively 0.1 to 0.4 $m.s^{-1}$ for $Re = 687$). The mainstream flow is interrupted by a stagnation zone (black ellipse) in the first baffle. The vortex form, inside the third baffle, is not changed when increasing the flow rate. The vortex center moves a little towards the bottom wall for $Re = 346$. The vortex center is in $x = -8.78\ mm$ and $y = 0.76\ mm$ for $Re = 687$, and then in $x = -8.78\ mm$ and $y = 0.66\ mm$ for $Re = 346$. In the middle of the labyrinth-channel, the flow has a high velocity reaching 1.1 and 2.2 $m.s^{-1}$ for $Re = 346$ and $Re = 687$ respectively inside the third baffle. This narrow zone is called the mainstream flow. Some variations in prediction of the swirl zone is observed when Reynolds number changes (Fig.IV.2.23 and Fig.IV.2.24).

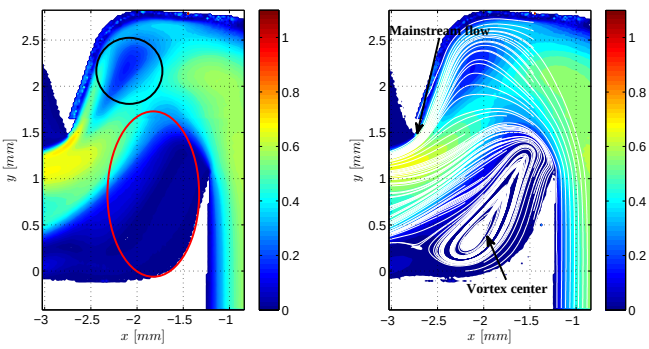

(a) Mean velocity modulus field (b) Mean velocity streamlines

Figure IV.2.23: Mean velocity modulus fields and streamlines $[m.s^{-1}]$ inside the first baffle, $Re = 346$, $d_p = 1\mu m$

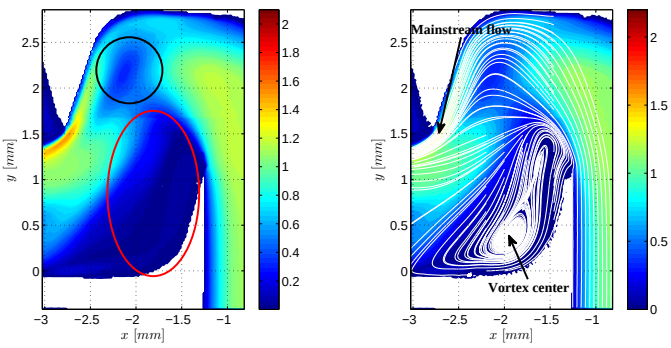

(a) Mean velocity modulus field (b) Mean velocity streamlines

Figure IV.2.24: Mean velocity modulus fields and streamlines $[m.s^{-1}]$ inside the first baffle, $Re = 687$, $d_p = 1\mu m$

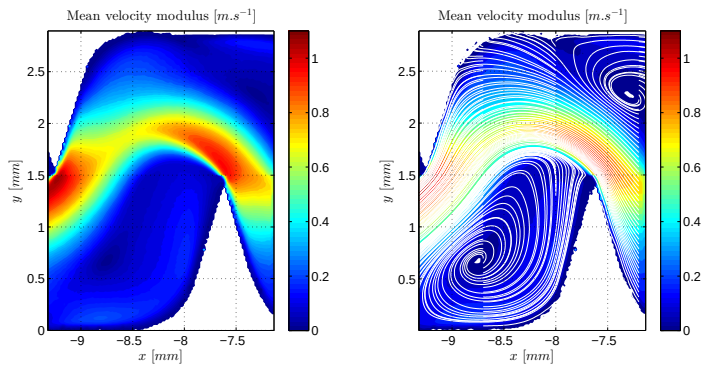

(a) Mean velocity modulus field (b) Mean velocity streamlines

Figure IV.2.25: Mean velocity modulus fields and streamlines $[m.s^{-1}]$ inside the third baffle, $Re = 346$, $d_p = 1\mu m$

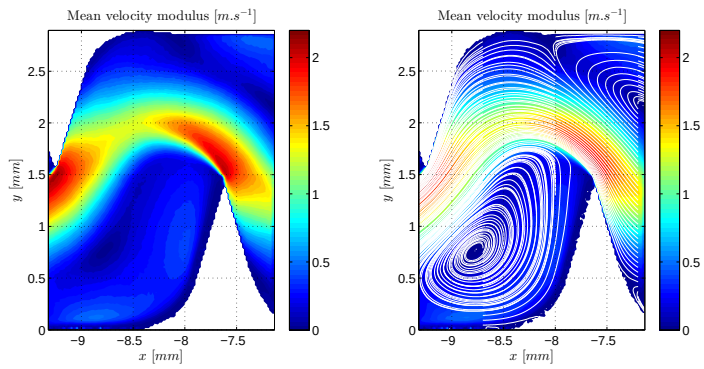

(a) Mean velocity modulus field (b) Mean velocity streamlines

Figure IV.2.26: Mean velocity modulus fields and streamlines $[m.s^{-1}]$ inside the third baffle, $Re = 687$, $d_p = 1\mu m$

The mean velocity modulus and components profiles are then plotted on the three lines (1, 2 and 3, see Fig.II.1.6) in order to see the evolution of the velocity in Fig.IV.2.27 for $Re = 346$ and in Fig.IV.2.28 for $Re = 687$. The flow for $Re = 687$ is developed faster than for $Re = 346$ where the velocity evolves more between the line 2 and the line 3 taken into the third baffle for which the flow is fully developed.

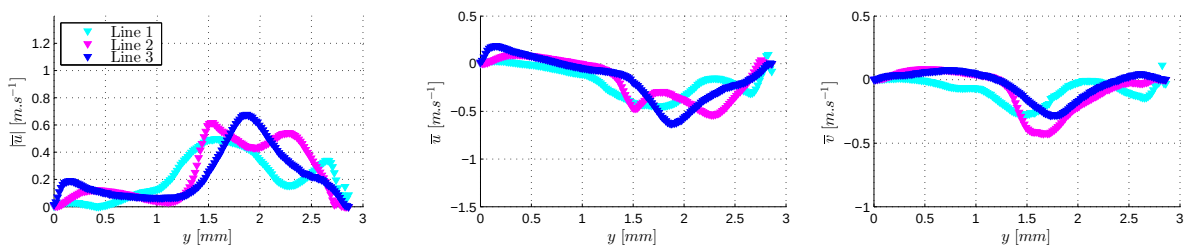

(a) $|\overline{u}|$ (b) $\overline{u}$ (c) $\overline{v}$

Figure IV.2.27: Velocity profiles for the first three baffles, $Re = 346$

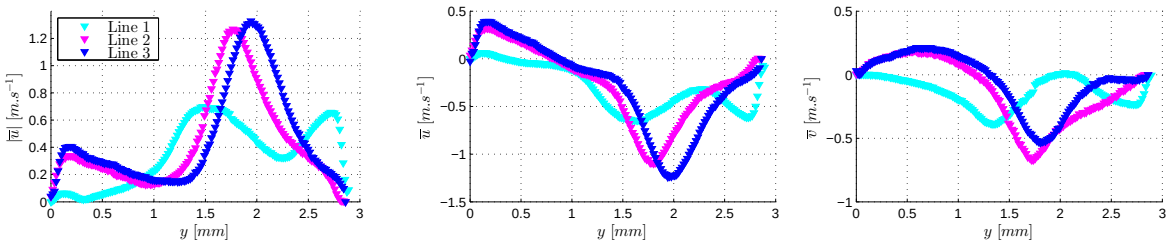

(a) $|\overline{u}|$ (b) $\overline{u}$ (c) $\overline{v}$

Figure IV.2.28: Velocity profiles for the first three baffles, $Re = 687$

The velocity $\overline{u}$ is negative in the mainstream flow because the flow is in the opposite direction of the x axis. $\overline{u}$ is positive in the lower part of the recirculation zone. $\overline{v}$ is negative in the mainstream flow (Fig.IV.2.27 and Fig.IV.2.28) for the second and the third baffles and is positive in the first baffle.

2.5.2 Numerical analysis

Two dimensions : Simulations are performed with standard, [LS] and [CHC] $k - \epsilon$, S-A and RSM models. The mean velocity fields obtained from the simulations for the minimum and the maximum flow rates, $Re = 400$ and 800 respectively, are shown on Fig.IV.2.29. These velocity fields also show that there are two regions. One is the main flow characterized by large velocity values. The other is the swirl region characterized by a low velocity modulus value and negative velocity values (see Fig.IV.2.32 and Fig.IV.2.33). The same flow typology is obtained with micro-PIV experiment. It can also be observed (Fig.IV.2.29) that the maximum velocity is at the corner of the labyrinth-channel, where the water hits the wall in the different baffles.

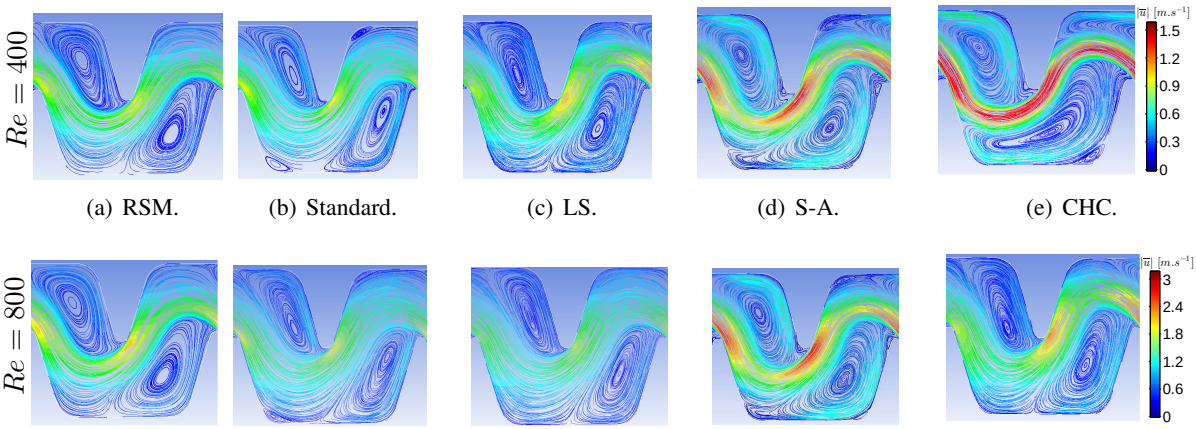

(a) RSM. (b) Standard. (c) LS. (d) S-A. (e) CHC.

(f) RSM. (g) Standard. (h) LS. (i) S-A. (j) CHC.

Figure IV.2.29: The mean velocity fields in the red square (Fig.III.2.1) in 2D, $[m.s^{-1}]$

The shape of the swirl can be split in two groups: the first one is an oval as depicted by the streamlines shown on Fig.IV.2.29 for standard and [LS] $k - \epsilon$ and RSM models, while the second form is rather extended, elongated and large (it occupies more space in the bottom of the baffle for S-A model). The swirl region form, for [CHC] $k - \epsilon$ model, is changed from the second form for $Re = 400$ (Fig.2.29(e)) to the first one for $Re = 800$ (Fig.2.29(j)), where it is smaller. Since the swirl region velocity is negative and higher, the main flow velocity is also higher (mass conservation).

Three dimensions : Simulations are performed with standard and [LS] $k-\epsilon$, RSM and S-A models. The swirl form remains of the first type for standard $k-\epsilon$ and RSM models, and of the second type for S-A model, while the form of swirl region for [LS] $k-\epsilon$ model is changed to the second group (Fig.IV.2.30). In order to characterize how the flow evolves within the labyrinth-channel depth, a cross section at the level of the line 2 is taken to analyze the flow in the z-axis. The flow is, generally, symmetrical in z-axis for all models, see Fig.IV.2.31. Nevertheless, an important variation of mainstream flow and swirl zone form appears mainly for [LS] $k-\epsilon$ model when Reynolds number changes. This variation changes from one model to another. As expected, with a larger swirl zone, the mainstream flow has a higher velocity (Fig.2.31(h)).

Link with discharge-pressure curves : The classification of swirl zone in two groups allows to perform the comparison with the x exponents of discharge-pressure curves Eq.I.1.1. x exponent does not depend on the swirl zone form, but it rather depends on changes of the zone size; for the following reasons. Firstly, the exponents of the standard and [LS] $k-\epsilon$, RSM and S-A models are almost identical in 2D and 3D (see table IV.1.1). The standard and RSM models in 2D and 3D, LS $k-\epsilon$ model in 2D have a first group swirl zone, whereas the S-A model, in 2D and 3D, and [LS] $k-\epsilon$ model in 3D have a swirl zone from the second group (Fig.IV.2.29 and Fig.IV.2.30). Secondly, the exponent x is calculated by varying the flow rate and thus Reynolds number and measuring the pressure losses in the emitter geometry. Therefore x depends necessarily on the variation of flow topology when the flow rate varies. To discuss the second reason, it is important to classify the x exponent in four categories:

- $x = 0.5$ as it is found for standard $k-\epsilon$ model. It seems that the swirl zone form does not change when Reynolds number changes in 2D and 3D (Fig.2.29(b) and Fig.2.31(f) in 2D, Fig.2.30(f) and Fig.2.31(b) in 3D).
- $0.5 > x > 0.6$ this is the case for [LS] $k-\epsilon$, S-A models in 2D and in 3D. For this category, the size of swirl zone reduces when Reynolds number increases remaining in the same form group.
- $x > 0.6$ [CHC] $k-\epsilon$ model, in 2D, undergoes this category of exponent. Its exponent is the most important ($x = 0.86$) (see table IV.1.1), we can see clearly the change of swirl zone form from the second group (larger) to the first group (smaller) when Reynolds number increases (Fig.IV.2.29).
- $x < 0.5$ RSM model is the only model to undergo this case in 2D and 3D. When looking at the swirl zone form for this model, we can observe that the swirl zone size increases slightly when the Reynolds number increases (Fig.IV.2.29 and in Fig.IV.2.30).

After this classification, it is important to analyze the influence of the swirl zone form on the exponent of the discharge-pressure curve, and consequently the pressure losses generated in the labyrinth-channel. The discharge-pressure curves show that S-A model dissipates more energy than the other models (Fig.IV.1.2). Nevertheless, the x exponent of this model is 0.51 and 0.52 in 2D and 3D respectively. This exponent is closer to that obtained by standard $k-\epsilon$ model for which the pressure losses are the smallest among the numerical models (Fig.IV.1.2).

Therefore, in order to explain and underline this difference in the pressure losses prediction when having the same x exponent for the different models, it is important and essential to analyse the influence of k_d in the power-law equation Eq.I.1.1. The k_d values are calculated and presented in table IV.2.3.

Table IV.2.3: The k_d values in the Eq.I.1.1 for all models plotted in Fig.IV.2.29 and in Fig.IV.2.30

	Model	Standard	LS	CHC	S-A	RSM	experiment
k_d	2D	1.237	1.119	0.554	0.981	1.226	–
	3D	1.123	0.985	–	0.952	1.156	1.232

We can observe that the constant k_d decreases in 3D modelling in comparison with 2D modelling. The swirl zone size is more important in 3D Fig.IV.2.30. We can conclude that when k_d increases the swirl zone size decreases. It seems that for the emitter geometry used in this work, the size of swirl zone for standard $k-\epsilon$ is the smallest.

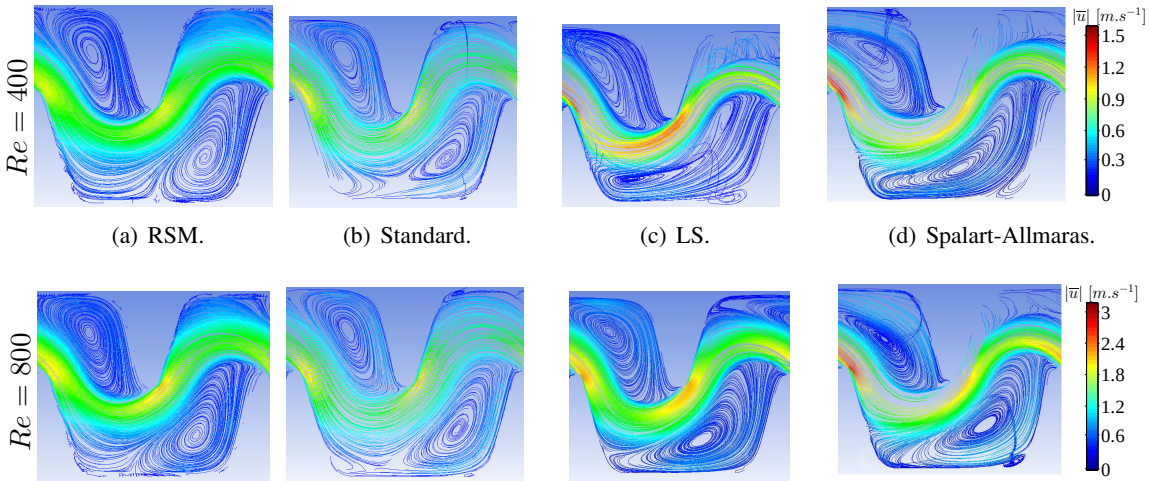

(a) RSM. (b) Standard. (c) LS. (d) Spalart-Allmaras.

(e) RSM. (f) Standard. (g) LS. (h) Spalart-Allmaras.

Figure IV.2.30: The mean velocity modulus fields in the red square (Fig.III.2.1) in 3D simulations

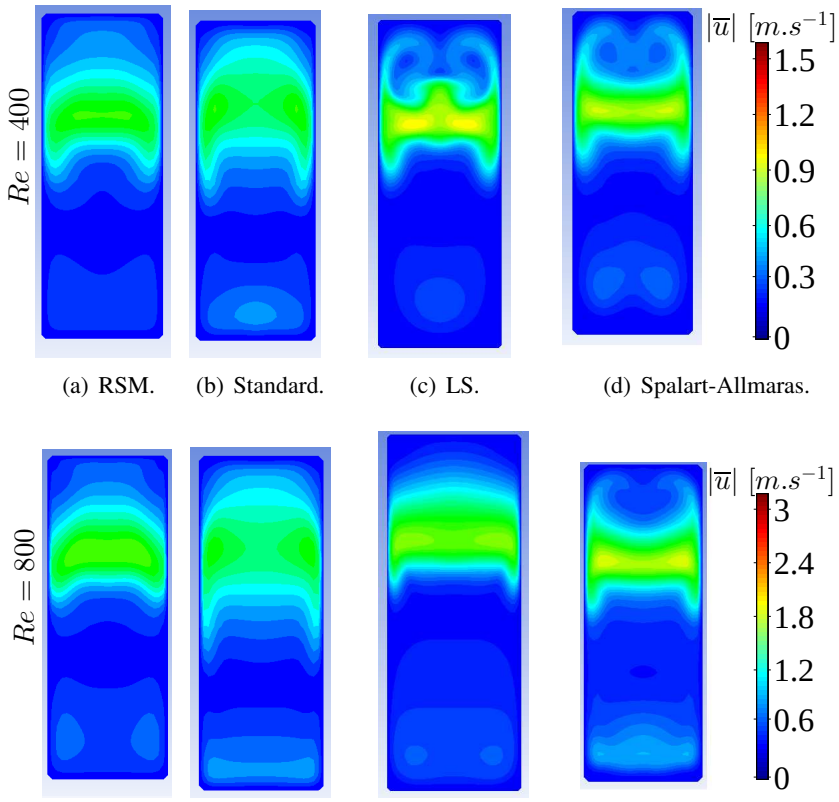

(a) RSM. (b) Standard. (c) LS. (d) Spalart-Allmaras.

(e) RSM. (f) Standard. (g) LS. (h) Spalart-Allmaras.

Figure IV.2.31: The mean velocity modulus in a perpendicular plane at line 2 (along the z axis), 3D simulations

The normalized mean velocity profiles are then plotted (Fig.IV.2.32 and Fig.IV.2.33) to understand the flow development along the baffle and to analyze the x exponent influence on velocity values in 2D and 3D. In 2D and 3D, it can be observed that the velocity for several models varies from line 2 to line 3 . That is to say that the flow is not yet developed and it changes from one baffle to another like for [LS] and [CHC] $k-\epsilon$ and S-A models (Fig.2.32(i) and Fig.2.33(i)). A developed state seems to be reached just after the first baffle for standard $k-\epsilon$ and RSM models. It can be noted that all the turbulence models studied have the same velocity profile at $Re = 800$ on line 3 (Fig.IV.2.32 and Fig.IV.2.33). Mean velocity reaches higher values in 3D than in 2D due to bigger swirl zone.

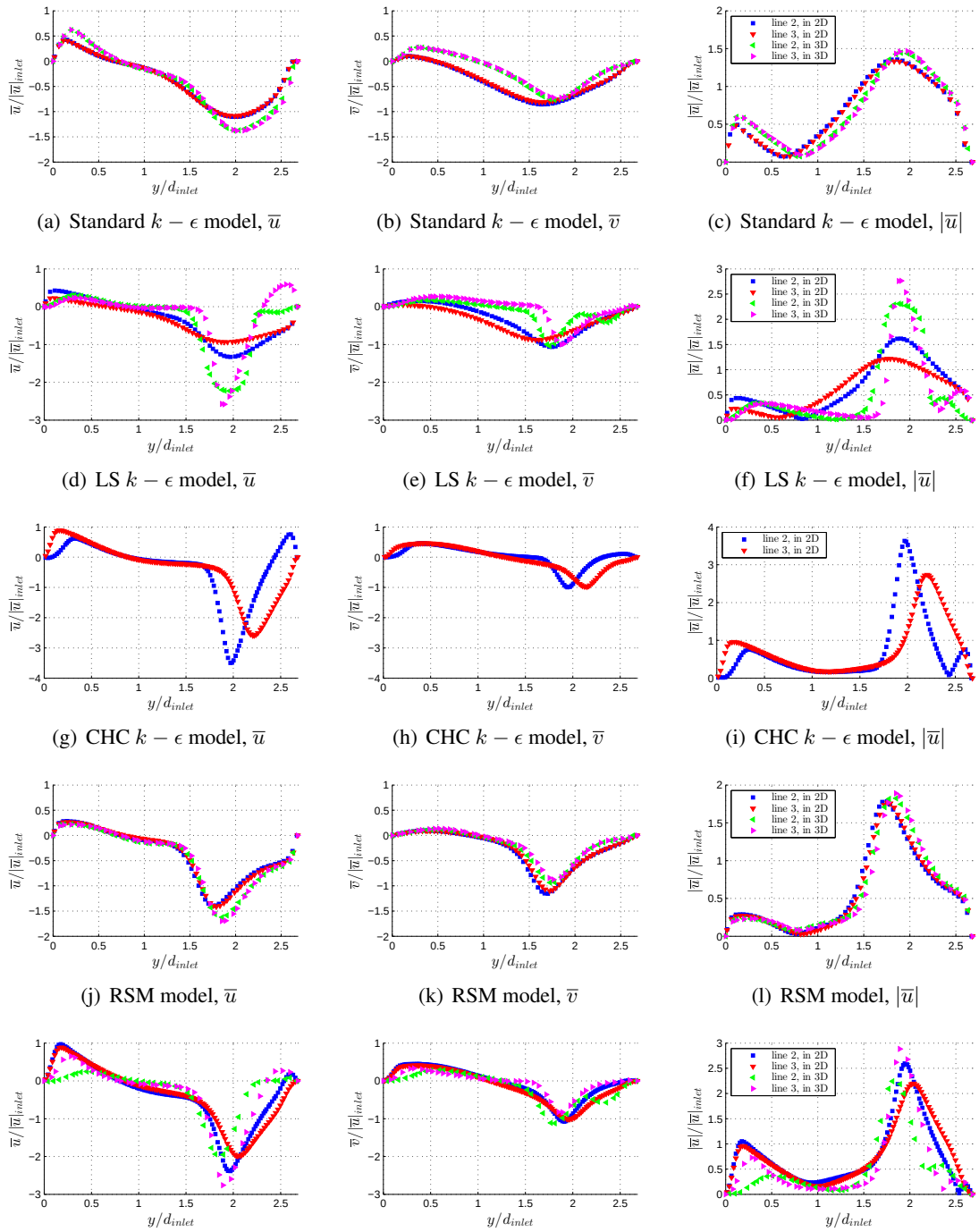

(a) Standard $k-\epsilon$ model, $\overline{u}$ (b) Standard $k-\epsilon$ model, $\overline{v}$ (c) Standard $k-\epsilon$ model, $|\overline{u}|$

(d) LS $k-\epsilon$ model, $\overline{u}$ (e) LS $k-\epsilon$ model, $\overline{v}$ (f) LS $k-\epsilon$ model, $|\overline{u}|$

(g) CHC $k-\epsilon$ model, $\overline{u}$ (h) CHC $k-\epsilon$ model, $\overline{v}$ (i) CHC $k-\epsilon$ model, $|\overline{u}|$

(j) RSM model, $\overline{u}$ (k) RSM model, $\overline{v}$ (l) RSM model, $|\overline{u}|$

(m) S-A model, $\overline{u}$ (n) S-A model, $\overline{v}$ (o) S-A model, $|\overline{u}|$

Figure IV.2.32: Evolution of the normalized x-axis, y-axis and mean velocity modulus profiles on lines 2 and 3 for $Re = 400$

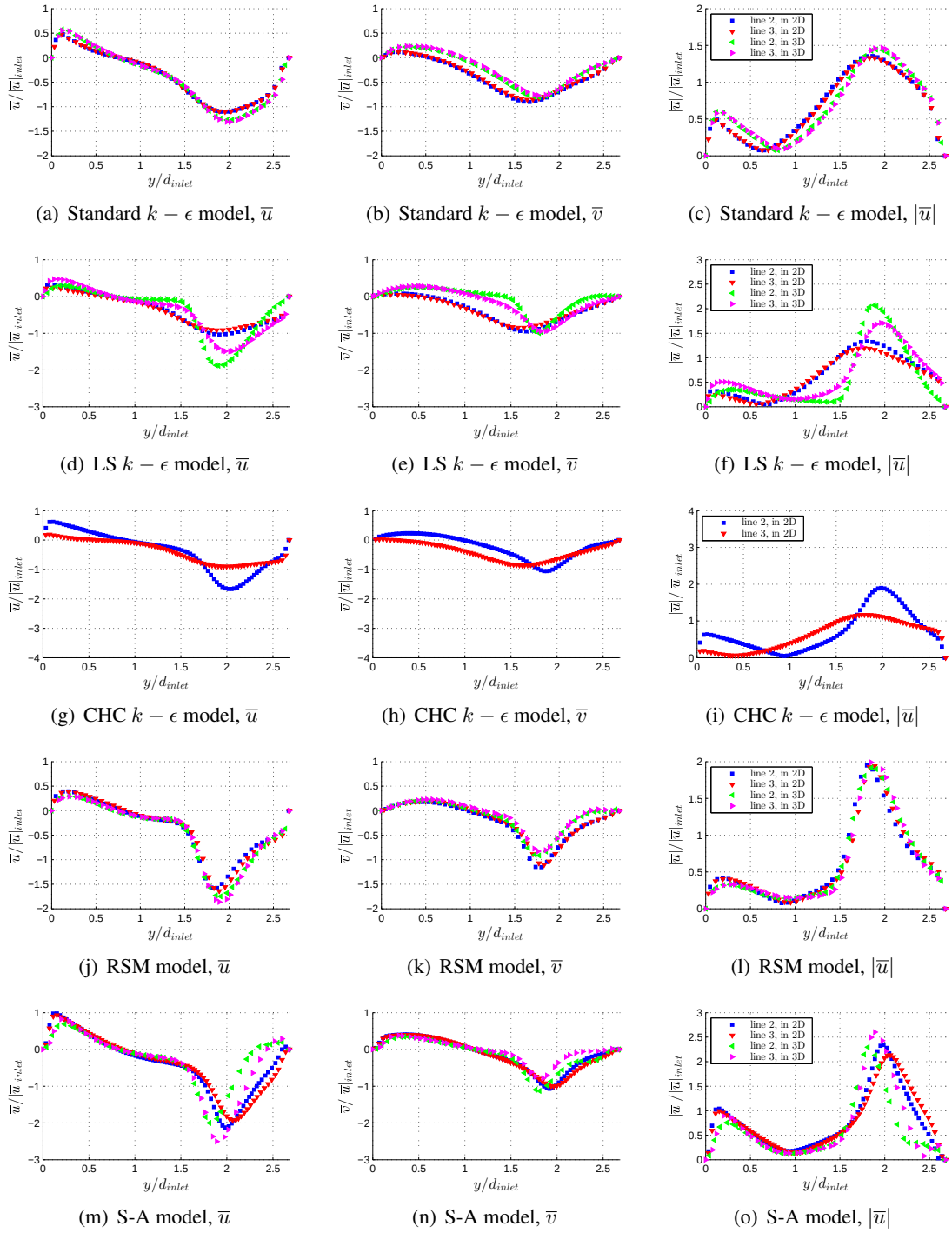

(a) Standard $k-\epsilon$ model, $\overline{u}$ (b) Standard $k-\epsilon$ model, $\overline{v}$ (c) Standard $k-\epsilon$ model, $|\overline{u}|$

(d) LS $k-\epsilon$ model, $\overline{u}$ (e) LS $k-\epsilon$ model, $\overline{v}$ (f) LS $k-\epsilon$ model, $|\overline{u}|$

(g) CHC $k-\epsilon$ model, $\overline{u}$ (h) CHC $k-\epsilon$ model, $\overline{v}$ (i) CHC $k-\epsilon$ model, $|\overline{u}|$

(j) RSM model, $\overline{u}$ (k) RSM model, $\overline{v}$ (l) RSM model, $|\overline{u}|$

(m) S-A model, $\overline{u}$ (n) S-A model, $\overline{v}$ (o) S-A model, $|\overline{u}|$

Figure IV.2.33: Evolution of the normalized x-axis, y-axis and mean velocity modulus profiles on lines 2 and 3 for $Re = 800$

For these lines, the velocity component $\overline{u}$ is the one which determines the flowrate. The relation between the velocity and the exponents x or/ and the constant k_d depends on this component. The normalization allows to compare the 2D modelling with the 3D modelling inside the baffle. $\overline{u}$ is greater in the mainstream flow with negative sign. $\overline{u}$ is greater in the 3D modelling when considering the line 3 (Fig.IV.2.32 and Fig.IV.2.33). k_d decreases for the 3D modelling using the same model, while the velocity component $\overline{u}$ increases in the mainstream flow. Therefore, the velocity component $\overline{u}$ increases when k_d decreases, while $\overline{v}$ behavior is contrary to what is observed for $\overline{u}$.

The different models vary in the prediction of pressure losses. It is clear that the model predicting

large recirculation region dissipates more energy such as obtained by [CHC] $k-\epsilon$ for $Re = 400$, and S-A model in 2D and in 3D for both Reynolds numbers $Re = 400$ and $Re = 800$. However, it seems, as observed on discharge-pressure curves, that at higher Reynolds number, the different $k-\epsilon$ models predict almost the same flow. The S-A model dissipates more energy in 3D since the value of k_d is smaller even though x exponent is closer to 0.5.

This evolution is due to the predictions of k and ϵ which obviously depend on the model and the damping factors for low-Reynolds number $k-\epsilon$ models, see section IV.2.9, where k and ϵ are weak in the two first baffles.

2.5.3 Comparative study

The micro-PIV results are compared with those of LS $k-\epsilon$ and RSM models only, since RSM model takes into account all Reynolds stresses, while LS $k-\epsilon$ model has an exponent closest to the experimental exponent. Streamlines obtained with micro-PIV are compared with the modeling by [LS] $k-\epsilon$ and RSM models in Fig.IV.2.34 for $Re = 800$. These models do not predict exactly the vortex zone form as micro-PIV does: the vortex center is not at the same position and velocity magnitude is greater than in the micro-PIV results (1.33 times greater), see Fig.IV.2.35 and Fig.IV.2.36.

The x exponent for the experimental data is 0.59. The swirl zone decreases when Reynolds number increases (Fig.IV.2.25 and Fig.IV.2.26). However, the forms of swirl zone RSM models are closer to that that obtained by micro-PIV, see Fig.IV.2.34 where the swirl zones belong to the first group cited previously.

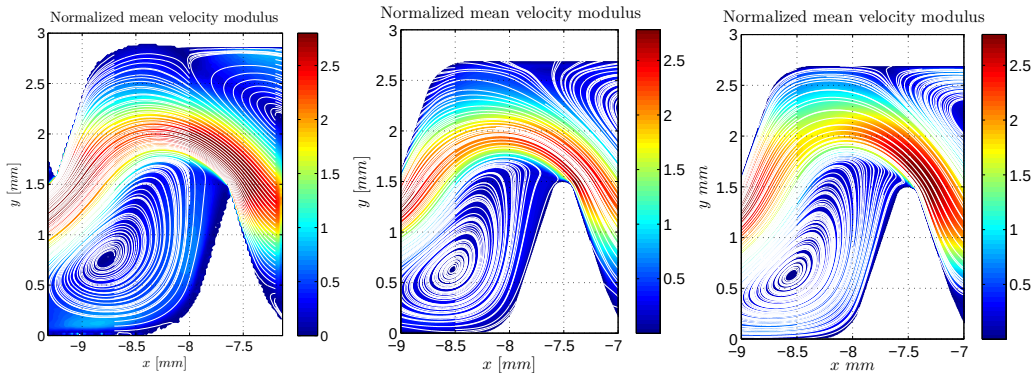

(a) Micro-PIV, $Re = 687$ (b) RSM model, $Re = 800$ (c) LS $k-\epsilon$, $Re = 800$

Figure IV.2.34: Velocity streamlines in the second baffle with the same flowrate 48 $ml.min^{-1}$

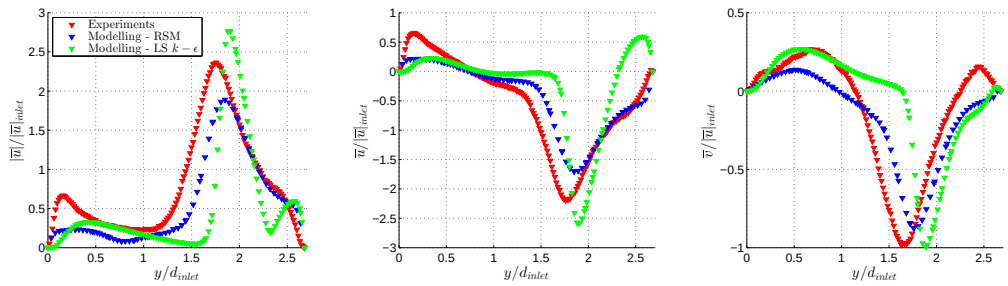

(a) $|\overline{u}|$ (b) $\overline{u}$ (c) $\overline{v}$

Figure IV.2.35: Normalized velocity profiles comparison between micro-PIV, RSM and LS $k-\epsilon$ models along the line 3, where $Re = 400$ for the modelling and $Re = 346$ for the experiment with the same flow rate 24 $ml.min^{-1}$.

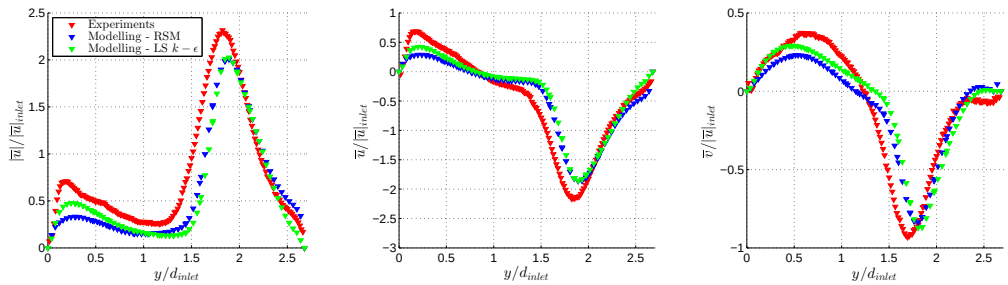

(a) $|\overline{u}|$ (b) $\overline{u}$ (c) $\overline{v}$

Figure IV.2.36: Normalized velocity profiles comparison between micro-PIV, RSM and LS $k-\epsilon$ models along the line 3, where $Re = 800$ for the modelling and $Re = 687$ for the experiment with the same flow rate 48 $ml.min^{-1}$.

The normalized mean velocities are then plotted along the line 3 to investigate with accuracy this comparison and to analyze the differences. The numerical results are closer to the experimental data for high Reynolds number $Re = 800$. The modelling under-predicts the velocity in the mainstream flow for $Re = 800$ with 20% in comparison with the experimental values. While, the difference is more important for the two models for $Re = 400$. The evolution of the LS $k-\epsilon$ model is more important when Reynolds number varies, and therefore x is greater than for the RSM model.

2.6 Reynolds stresses

2.6.1 Experimental analysis

Reynolds stresses or fluctuating velocity second-order moments fields $\overline{u'^2}$, $\overline{v'^2}$ and $\overline{u'v'}$ are calculated and plotted inside the first and third baffles for $Re = 346$ and $Re = 687$ (Fig.IV.2.37, Fig.IV.2.38, Fig.IV.2.39 and Fig.IV.2.40). It can be observed that the Reynolds stresses are three times higher for $Re = 687$ in comparison with $Re = 346$. For both, $\overline{u'^2}$ and $\overline{v'^2}$ are maximum in the main flow near the separation zone[6]. Reynolds stresses are close to zero in the vortex zones, thereby being likely to facilitate the particle deposition and emitter clogging. The magnitude scales of fluctuating velocity second-order moments are, in the first baffle, small when compared with the third baffle, e.g respectively $\overline{u'^2} = 0.15\ [m^2.s^{-2}]$ and $0.35\ [m^2.s^{-2}]$.

$\overline{u'v'}$ values are almost zero in the recirculation zone, from $y = 0$ to $y = 1.5\ mm$ for experimental data ($x = -2.1\ mm$, $x = -5.35\ mm$ and $x = -8.5\ mm$ for the first , second and the third line respectively). Then, they are positive, from $y = 1.5$ to $y = 2\ mm$ and negative for $y > 2\ mm$. A detailed analysis is performed to understand this sign change which is clearly seen on the line 3 (Fig.IV.2.41 and Fig.IV.2.42). In general, $\overline{u'v'}$ is related to the velocity gradient, through Boussinesq hypothesis, and the relation is given by:

$$-\overline{u'v'} = \nu_t \left(\frac{\partial \overline{u}}{\partial y} + \frac{\partial \overline{v}}{\partial x} \right) \quad . \tag{IV.2.10}$$

[6]Separation zone can result from such causes such as a rapidly expanding duct of pipe. Separation occurs due to an adverse pressure gradient encountered as the flow expands, causing an extended region of separated flow. The part of the flow that separates the recirculating flow and the flow through the central region of the duct is called the dividing streamline. The point where the dividing streamline attaches to the wall again is called the reattachment point. As the flow goes farther downstream, it eventually achieves an equilibrium state and has no reverse flow. These flow properties will be analyzed thoroughly in section IV.2.12.

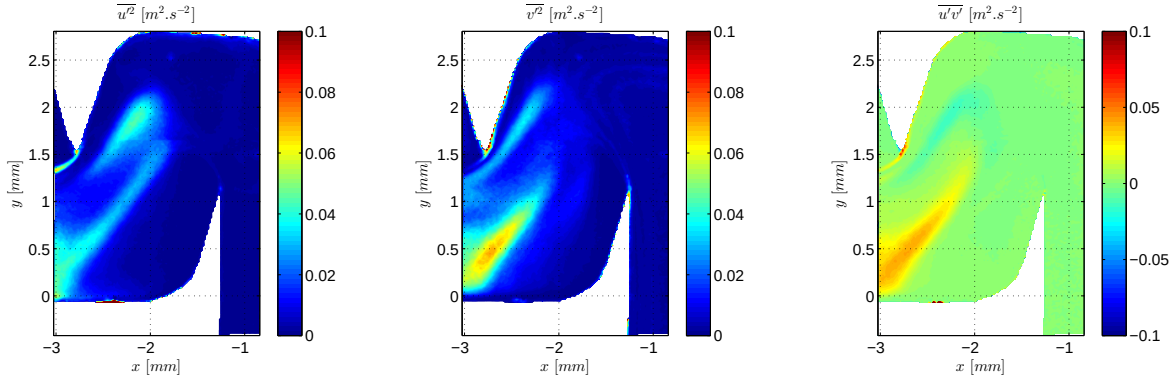

(a) $\overline{u'^2}$ (b) $\overline{v'^2}$ (c) $\overline{u'v'}$

Figure IV.2.37: Fluctuating velocity second-order moments fields inside the first baffle, $Re = 346$, $d_p = 1\mu m$

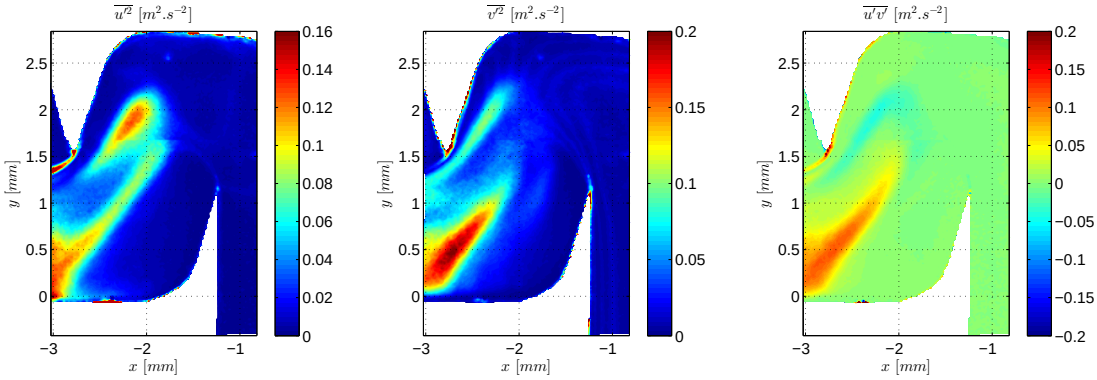

(a) $\overline{u'^2}$ (b) $\overline{v'^2}$ (c) $\overline{u'v'}$

Figure IV.2.38: Fluctuating velocity second-order moments fields inside the first baffle, $Re = 687$, $d_p = 1\mu m$

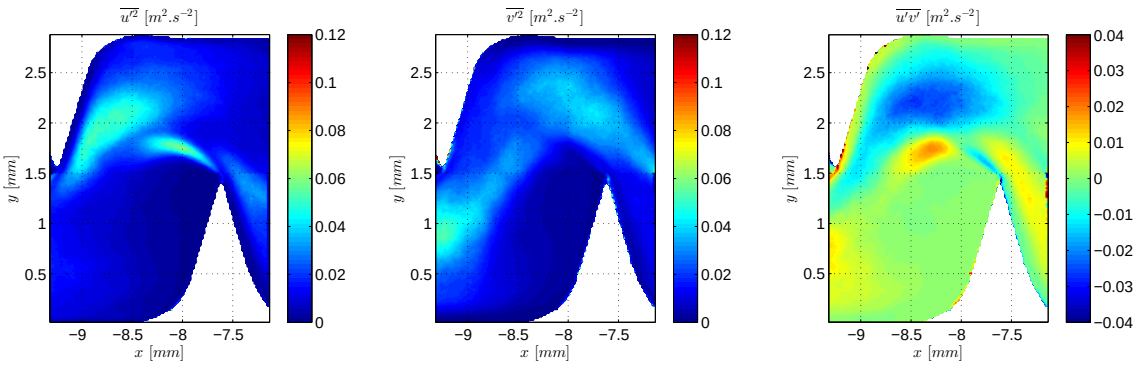

(a) $\overline{u'^2}$ (b) $\overline{v'^2}$ (c) $\overline{u'v'}$

Figure IV.2.39: Fluctuating velocity second-order moments fields inside the third baffle, $Re = 346$, $d_p = 1\mu m$

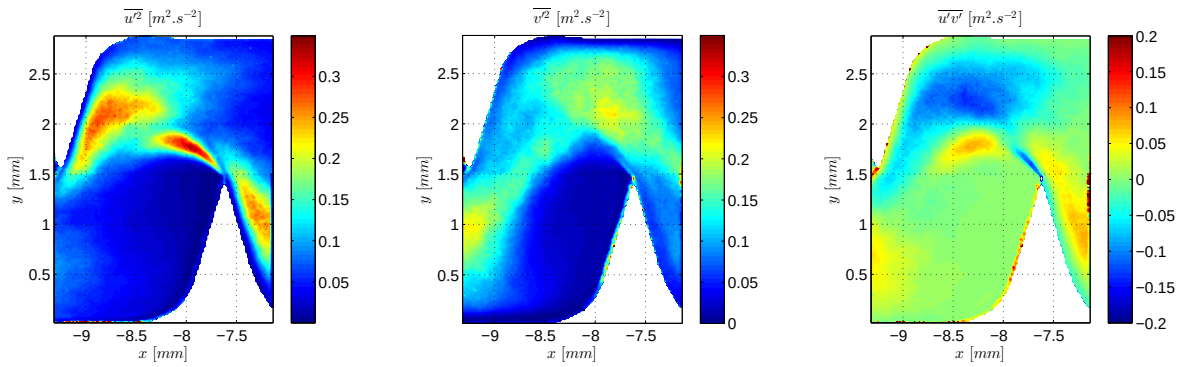

(a) $\overline{u'^2}$ (b) $\overline{v'^2}$ (c) $\overline{u'v'}$

Figure IV.2.40: Fluctuating velocity second-order moments fields inside the third baffle, $Re = 687$, $1\mu m$

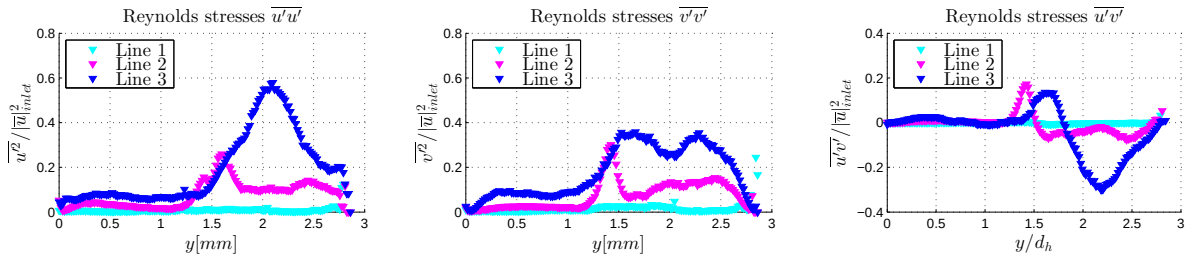

(a) $\overline{u'^2}$ (b) $\overline{v'^2}$ (c) $\overline{u'v'}$

Figure IV.2.41: Normalized fluctuating velocity second-order moments profiles for the first three baffles, $Re = 346$, $d_p = 1\mu m$

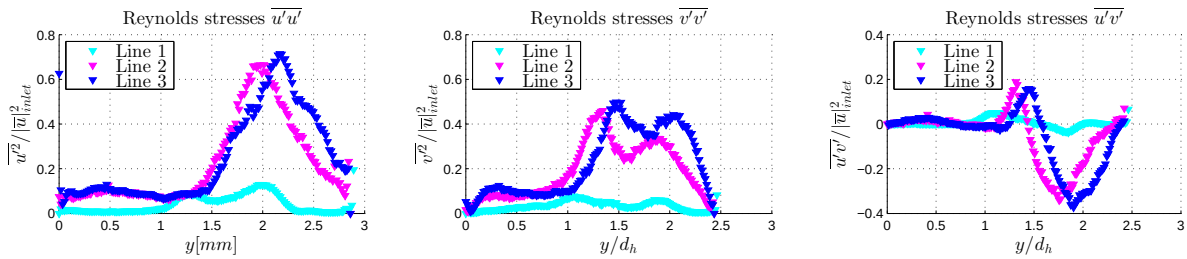

(a) $\overline{u'^2}$ (b) $\overline{v'^2}$ (c) $\overline{u'v'}$

Figure IV.2.42: Normalized fluctuating velocity second-order moments profiles for the first three baffles, $Re = 687$, $d_p = 1\mu m$

The profiles of $\frac{\partial \overline{u}}{\partial y}$ and $\frac{\partial \overline{v}}{\partial x}$ are plotted on the line 3 to determine the dominant term and/or the term values along this line Fig.IV.2.43. $\frac{\partial \overline{u}}{\partial y}$ and $\frac{\partial \overline{v}}{\partial x}$ have the same magnitude. For $y \leq 1.5mm$, one of the two terms eliminates the other, therefore, $\overline{u'v'}$ is almost zero. From $y = 1.5\ mm$ to $y = 2\ mm$, the value of $\frac{\partial \overline{u}}{\partial y}$ is responsible for the positive value of $\overline{u'v'}$, while for $y > 2\ mm$ both terms accumulate and give the strong negative value of $\overline{u'v'}$. We can conclude that $\overline{u'v'}$ values are well correlated with velocity gradients values and therefore depend on the different regions which have been already distinguished.

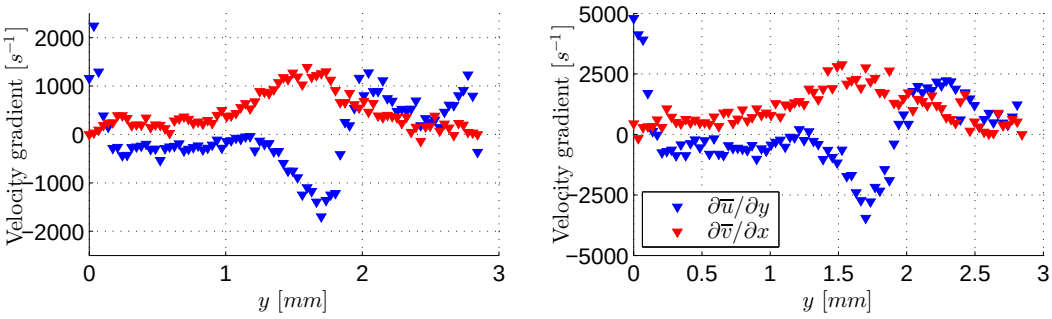

(a) $Re = 346$ (b) $Re = 687$

Figure IV.2.43: Velocity gradients along the line 3, $d_p = 1\mu m$

Correlation coefficient, $\mathcal{C}$ Eq.IV.2.7, is calculated, on the line 3 for both Reynolds numbers (Fig. IV.2.44). This coefficient has its maximum value of about 0.8 in modulus at $y = 2.25\ mm$ and it is not influenced by Reynolds number. Its values are much smaller (less than 0.25 in magnitude) for $y \leq 1.5\ mm$. In the study of KMM (Kim et al., 1987)[58], C reaches 0.5 near the wall and decreases to zero in the channel center.

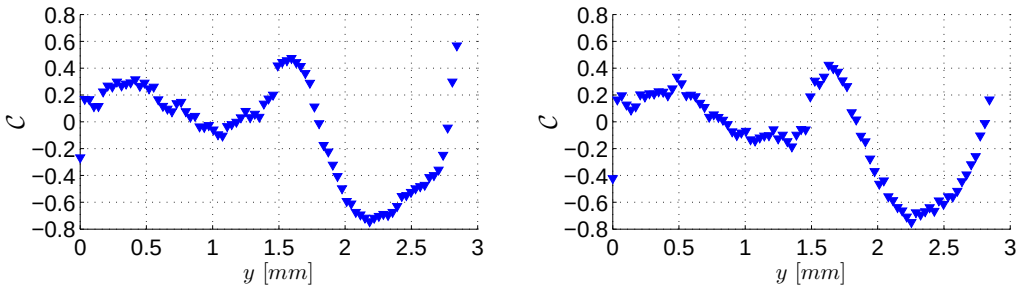

(a) $Re = 346$ (b) $Re = 687$

Figure IV.2.44: Correlation coefficient on the line 3, $1\mu m$

2.6.2 Numerical analysis

The Reynolds normal stresses for $k - \epsilon$ models are almost equal since the influence of $\frac{\partial \overline{u}}{\partial x}$, $\frac{\partial \overline{v}}{\partial y}$ and $\frac{\partial \overline{w}}{\partial z}$ is very small (Boussinesq's hypothesis) so that these stresses are mostly generated by pressure redistribution. This yields :

$$\overline{u'^2} = \overline{v'^2} = \overline{w'^2} = \frac{2}{3}k$$

For $k - \epsilon$ model, Reynolds stresses are important in the main flow as much as in the swirl region Fig.IV.2.45. Normalized Reynolds stresses downfall between these two regions in 2D Fig.2.45(b). But, in 3D the Reynolds stresses are higher in the main flow only, a trend which was also displayed by expeimental data. We observe that increasing Reynolds number does not change these profiles predicted by $k - \epsilon$ models. Reynolds stresses resulting from the RSM model are different. $\overline{v'w'}$ and $\overline{u'w'}$ are negligible. These are in the order of 10^{-9}, see Fig.IV.2.46 and Fig.IV.2.47. The Reynolds stresses are important in the swirl region simulated in 2D and less important in 3D, $\overline{u'v'}$ is negative in the main flow and positive between the swirl region and the bottom wall. For the RSM model, $\overline{v'^2}$ is important inside the recirculation region, the turbulence energy thus is generated in the y direction. In that case increasing Reynolds number seems to impact $\overline{v'^2}$ profiles in 2D moving the maximum from the mainstream flow ($Re = 400$) to the vortex zone ($Re = 800$), but has no influence in 3D.

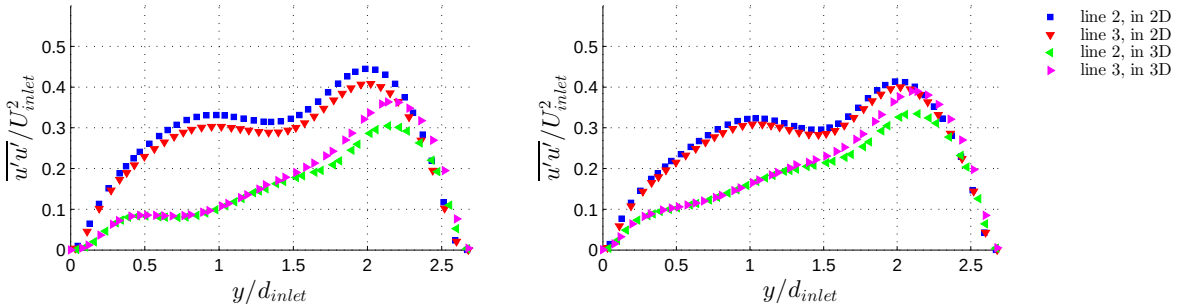

(a) $Re = 400$. (b) $Re = 800$.

Figure IV.2.45: Normalized Reynolds stresses for standard $k - \epsilon$ model

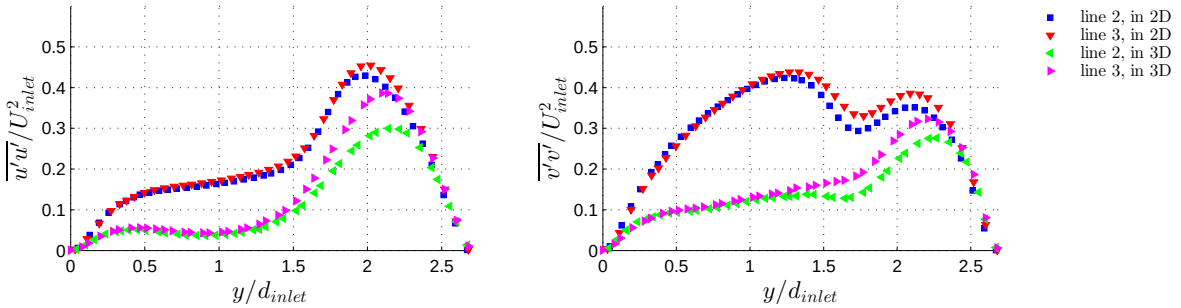

(a) $\overline{u'u'}$. (b) $\overline{v'v'}$.

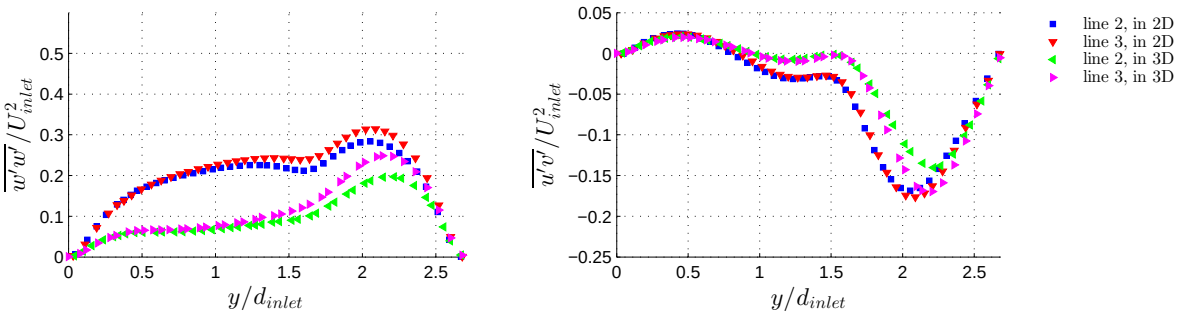

(c) $\overline{w'w'}$. (d) $\overline{u'v'}$.

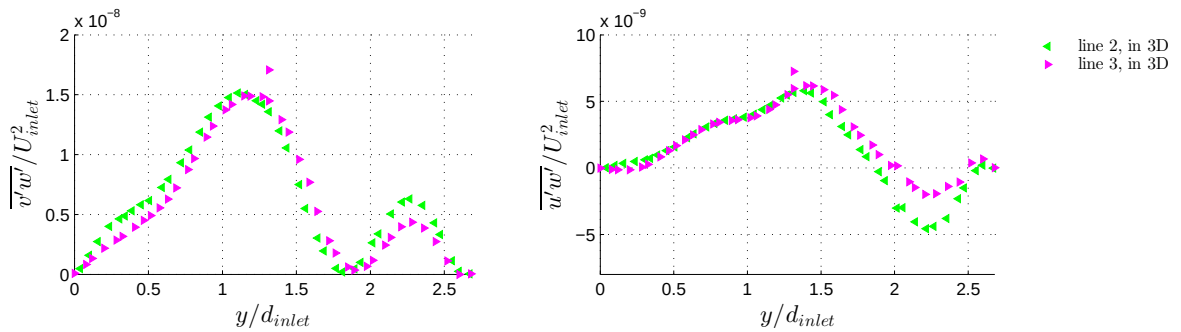

(e) $\overline{v'w'}$. (f) $\overline{u'w'}$.

Figure IV.2.46: Normalized Reynolds stresses for $Re = 400$, RSM model

The normalized values of Reynolds stresses are very high. $\overline{u'^2}/U^2_{inlet} \simeq 0.4 - 0.5$, which gives $\sigma_u/U_{inlet} \simeq 0.6 - 0.7$. U_{inlet} is certainly inferior to the $\overline{u}_{local}$ since the flow is concentrated in a small distance , namely, the mainstream flow in the present work. Thus, U_{inlet} is not the good scale to carry

out the normalization. However, it allows to compare the experimental and numerical results[7].

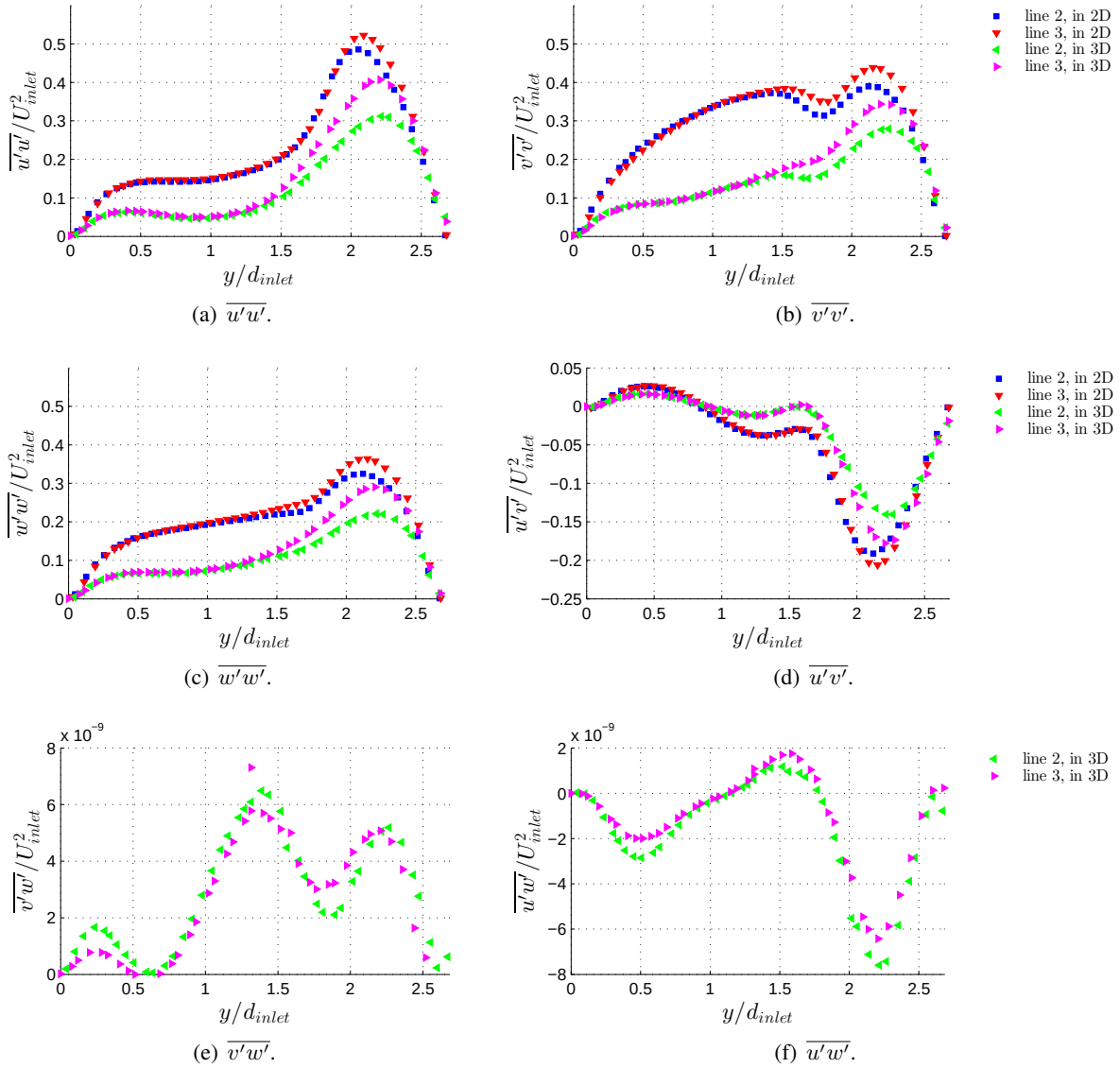

(a) $\overline{u'u'}$. (b) $\overline{v'v'}$.

(c) $\overline{w'w'}$. (d) $\overline{u'v'}$.

(e) $\overline{v'w'}$. (f) $\overline{u'w'}$.

Figure IV.2.47: Normalized Reynolds stresses for $Re = 800$, RSM model

2.6.3 Comparative study

[LS] $k - \epsilon$ model is based on the Boussinesq hypothesis. $\overline{u'^2}$ and $\overline{v'^2}$ are thus almost identical. $\overline{u'v'}$ is calculated from Eq.IV.2.10. There are some differences between the micro-PIV and the modelling results. Reynolds stresses $\overline{u'^2}$, $\overline{v'^2}$ and $\overline{u'v'}$ are larger in the experiments. This is clear in the mainstream flow for $Re = 800$ (Fig.IV.2.49). The ratios of $\overline{u'^2}$ for micro-PIV and RSM are about 30% and 100% for $Re = 400$ and $Re = 800$ (Fig.2.48(a) and Fig.2.49(a)). We can conclude that the [LS] $k - \epsilon$ and RSM models under-predict the Reynolds stress $\overline{u'^2}$ in the mainstream flow. While, the estimation of Reynolds stress $\overline{u'^2}$ is somewhat comparable in the swirl zone. Nevertheless, $\overline{v'^2}$ has the same order of magnitude. Large difference is predicted between the swirl zone and the mainstream flow ($y = 1.2{-}2\ mm$) where $\overline{v'^2}$ has higher values for the micro-PIV experiments than the modeling results (Fig.2.48(b) and Fig.2.49(b)). $\overline{u'v'}$ is negative in the main flow for both cases (micro-PIV experiments and modelling results). Reynolds stresses increase when Reynolds number increases since the turbulence increases, except for [LS] $k - \epsilon$

[7] U_{inlet} is the bulk velocity for numerical data

model where the size of swirl clearly decreases (see Fig.IV.2.30), therefore, the Reynolds stresses are more important for $Re = 400$. The evolution of Reynolds stresses is higher for [LS] $k - \epsilon$ model than for RSM model. This can be justified by the value of the exponent x.

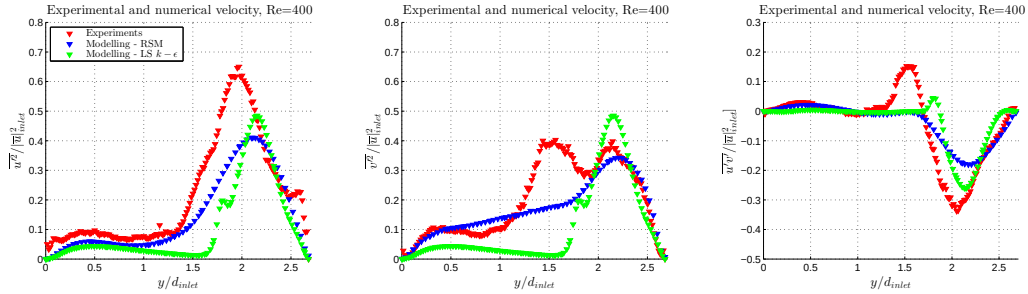

(a) $\overline{u'^2}$ (b) $\overline{v'^2}$ (c) $\overline{u'v'}$

Figure IV.2.48: Normalized Reynolds stress profiles comparison between micro-PIV, RSM and [LS] $k - \epsilon$ models along the line 3 in 3D, $Re = 400$

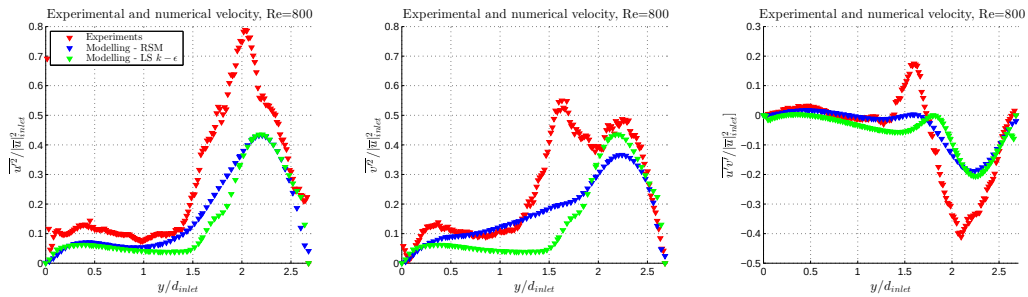

(a) $\overline{u'^2}$ (b) $\overline{v'^2}$ (c) $\overline{u'v'}$

Figure IV.2.49: Normalized Reynolds stress profiles comparison between micro-PIV, RSM and [LS] $k - \epsilon$ models along the line 3 in 3D, $Re = 800$

2.7 Axial development of the flow

2.7.1 Experimental flow consistency

2.7.1.1 Mean velocity

The flow inside the first three baffles evolves experimentally. Fig.IV.2.53. Fig.IV.2.28 shows the difference between the first and third baffles for $Re = 687$. Numerically this evolution varies from a model to another. However, the question is how the flow develops along the ten baffles. In order to answer this question, the experimental velocity profiles are plotted at the beginning (third baffle), the middle (fifth baffle) and the end of labyrinth-channel (ninth baffle) (Fig.IV.2.50). For $Re = 435$, a greater dispersion is observed ($0.08[m.s^{-1}]$ in the vortex zone). At $Re = 863$, in the mainstream flow, the velocity magnitude is the same for all positions but in the swirl zone, some differences are observed ($0.07[m.s^{-1}]$ in the vortex zone) which is relatively low. However, the dispersion is observed between the lines 3 and 9 in comparison with the line 5. This may be due to the deformation of labyrinth-channel when machining as the turning machine is not precise enough.

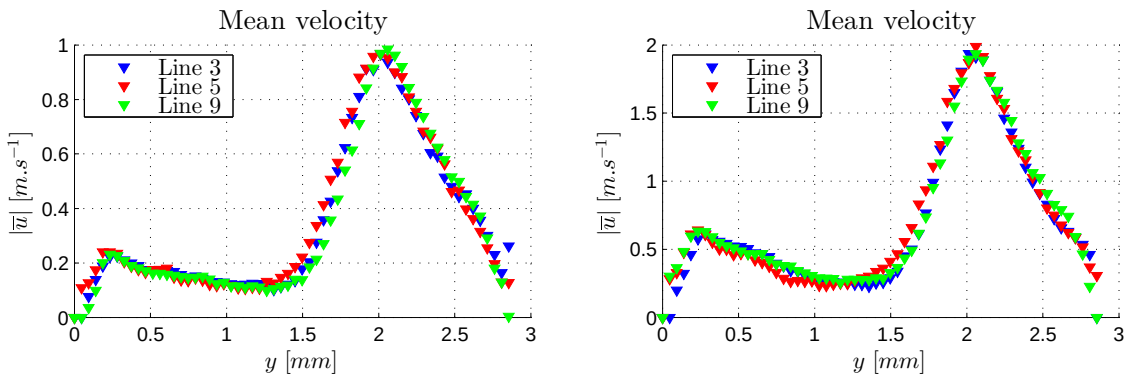

(a) $Re = 435$ (b) $Re = 863$

Figure IV.2.50: Mean velocity profiles along the lines 3, 5 and 9 (see Fig.II.1.6), $d_p = 5\mu m$

2.7.1.2 Fluctuating velocity second-order moments

The fluctuating velocity second-order moments are also calculated and plotted on Fig.IV.2.51 and Fig.IV.2.52. It appears that the fluctuating velocity second-order moments profiles are slightly different. $\overline{u'v'}$ values are close to zero in the vortex zones and higher in the main flow. $0.03-0.1$ $[m^2.s^{-2}]$ variation is observed in the main stream flow for both Reynolds numbers in terms of $\overline{u'^2}$. This variation decreases for $\overline{v'^2}$ and $\overline{u'v'}$ to about $0.02 - 0.04$. Fluctuating velocity second-order moments profiles confirm that third baffle is the one where the flow is well developed.

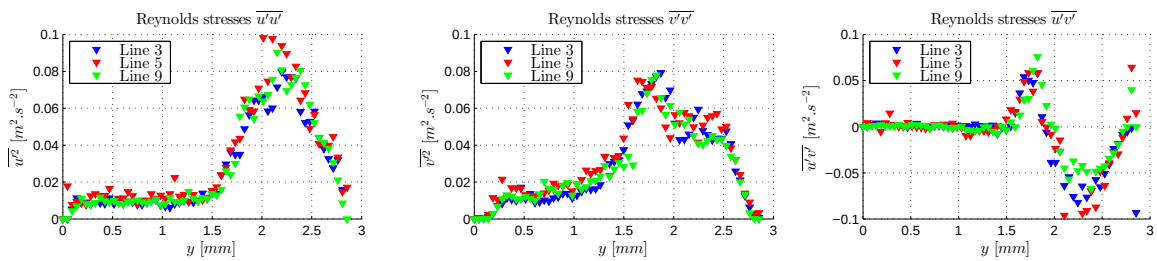

(a) $\overline{u'^2}$ (b) $\overline{v'^2}$ (c) $\overline{u'v'}$

Figure IV.2.51: Fluctuating velocity second-order moments profiles, $Re = 435$, $d_p = 5\mu m$

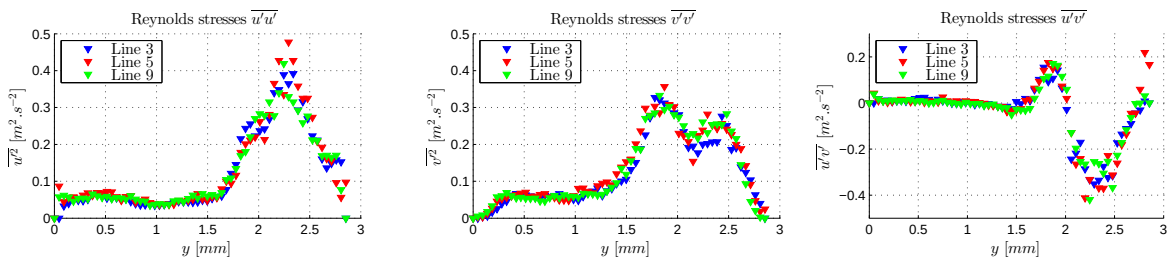

(a) $\overline{u'^2}$ (b) $\overline{v'^2}$ (c) $\overline{u'v'}$

Figure IV.2.52: Fluctuating velocity second-order moments profiles, $Re = 863$, $d_p = 5\mu m$

2.7.2 Numerical flow consistency

2.7.2.1 Mean velocity

It has been underlined that the flow for the low-Reynolds number [CHC] $k-\epsilon$ model, in 2D, is not yet developed. Therefore a fourth baffle was added to analyze the flow characteristics on this baffle and compare it with the other baffles. The flow modeled by [LS] $k-\epsilon$ model is well developed. This is seen when comparing the velocity profiles on lines 3 and 4 (Fig.2.53(a)). Results presented in Fig.2.53(b) confirm the hypothesis that the flow modeled by [CHC] $k-\epsilon$ model is no yet developed at the third baffle, since the velocity profiles on the line 4 is very different from the line 3. This model gives an exponent x much larger than the other models.

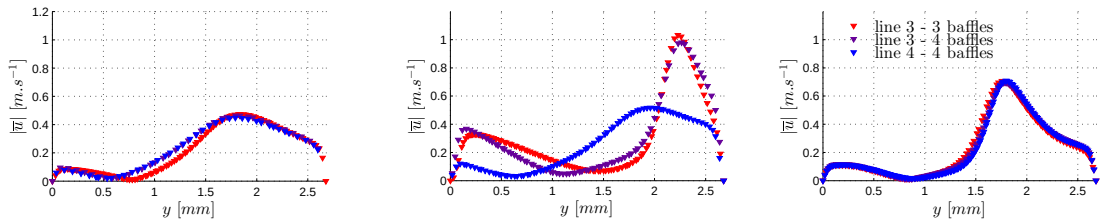

(a) LS $k-\epsilon$ model, $Re = 400$ (b) CHC $k-\epsilon$ model, $Re = 400$ (c) RSM model, $Re = 400$

Figure IV.2.53: The mean velocity modulus profiles for [LS] (a), [CHC] (b) $k-\epsilon$ and (c) RSM models on the lines 3 and 4 in the case of four baffles compared with the line 3 in the case of three baffles and $Re = 400$

2.7.2.2 Fluctuating velocity second-order moments

The fluctuating velocity second-order moments are plotted for RSM model at the lines 3 and 4 for the modelling performed on 4 baffles, and at the line 3 for the modelling performed on 3 baffles. As it is found when mean velocity profiles are considered, the flow seems to be established since the fluctuating velocity second-order moments profiles do not vary (Fig.IV.2.54).

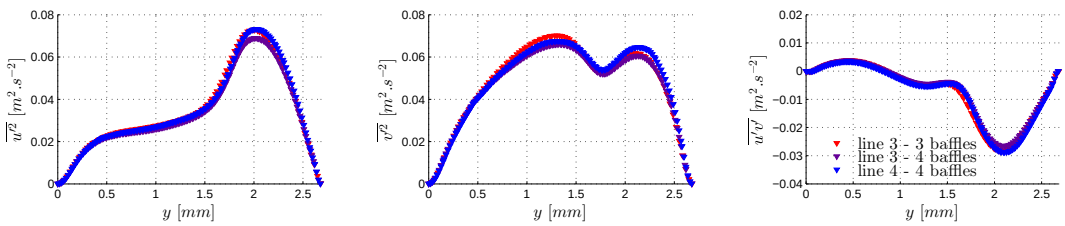

(a) $\overline{u'^2}$ (b) $\overline{v'^2}$ (c) $\overline{u'v'}$

Figure IV.2.54: The fluctuating velocity second-order moments profiles for RSM model on the lines 3 and 4 in the case of four baffles compared with the line 3 in the case of three baffles and $Re = 400$

2.8 Vertical evolution of the flow

Numerically, the flow is symmetric about $z = 0.5\ mm$ for all models. This result is deduced from Fig.IV.2.31 which represents the velocity in axis z. The modelling is performed assuming smooth wall. Nevertheless, as mentioned above, the labyrinth-channel is fabricated by machining and thus this

surface is not smooth. The surface roughness is characterized using an optical profilometer. The roughness average, $\mathcal{R}_a$, is the most widely used one-dimensional roughness parameter. This parameter is the arithmetic average of the absolute values. When measuring $\mathcal{R}_a$ for the fabricated labyrinth-channel, we found that $\mathcal{R}_a = 4.65\mu m$. The velocity profiles are plotted in Fig.IV.2.55, for the third baffle at $z = [0.25; 0.5; 0.75]\ mm$ above the rough wall using particle diameter $d_p = 5\mu m$. Velocity profiles for $0.25\ mm$ and $0.75\ mm$ are superimposed; the flow is symmetric about the z axis for this range. At this distance from the wall, the roughness has no effect on the mean velocity.

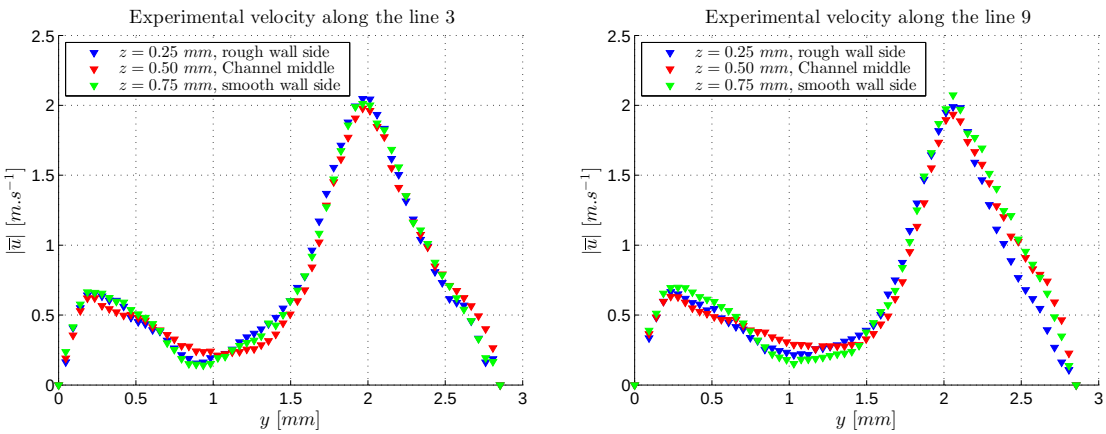

(a) baffle 3. (b) baffle 9.

Figure IV.2.55: Mean velocity profiles, $Re = 863$, $d_p = 5\mu m$

Once again, it can be concluded that the flow properties do not change after the third baffle, for the different flow rates.

2.9 Turbulent kinetic energy

2.9.1 Experimental analysis

The turbulent kinetic energy field must be calculated using the formula:

$$k = \frac{1}{2}\left(\overline{u'^2} + \overline{v'^2} + \overline{w'^2}\right) \quad . \tag{IV.2.11}$$

The third component $\overline{w'^2}$ has to be assumed in order to calculate this quantity. As mentioned above in the turbulence intensity calculation, at the entrance, the fluid motion is essentially in the y direction. The hypothesis of $\overline{w'^2} = \overline{u'^2}$ can be applicable. Root-mean-squared velocity fluctuations obtained by RSM and discussed in section IV.2.3.2 confirm that $u_{rms} = w_{rms}$ at the inlet. Inside the baffle, there is motion in the x and y directions. This hypothesis is not true anymore. With 2-D PIV data, there is no knowledge of the third rms velocity component (usually tangential or perpendicular) and k can only be estimated using a pseudo-isotropic assumption defined as follows:

$$\overline{w'^2} = \frac{1}{2}\left(\overline{u'^2} + \overline{v'^2}\right) \quad . \tag{IV.2.12}$$

This yields the following simplified formula:

$$k = \frac{3}{4}\left(\overline{u'^2} + \overline{v'^2}\right) \quad . \tag{IV.2.13}$$

This assumption was verified experimentally by Khan et al. (2006)[56] using stereoscopic PIV data in impeller of pitched-blade turbin. It is impossible to check this assumption experimentally with our

set-up. Nevertheless, numerical modelling can confirm this hypothesis. The numerical results indicate the third component $\overline{w'^2}$ is inferior to $\overline{u'^2}$ and $\overline{v'^2}$ for RSM (see Fig.IV.2.46 and Fig.IV.2.47). Another assumption seems to be more realisable. This assumption is based on the results of the boundary layers where $\overline{w'^2}$ is estimated as follow:

$$\overline{w'^2} = \min\left(\overline{u'^2}, \overline{v'^2}\right) \quad . \tag{IV.2.14}$$

A comparison of these two assumptions is presented in Fig.IV.2.56 for $Re = 346$ and $Re = 687$. In the swirl zone, the two assumptions give the same results, while the second assumption (Eq.IV.2.14) underestimates the turbulence kinetic energy with respect to the first assumption (Eq.IV.2.13). Therefore, the second assumption is taken into account when calculating the turbulence kinetic energy in micro-PIV. The differences for the two methods are very small and we then chose the easiest to calculate, since the two velocity variances are equal, therefore, the second method corresponds to the axisymmetric assumption.

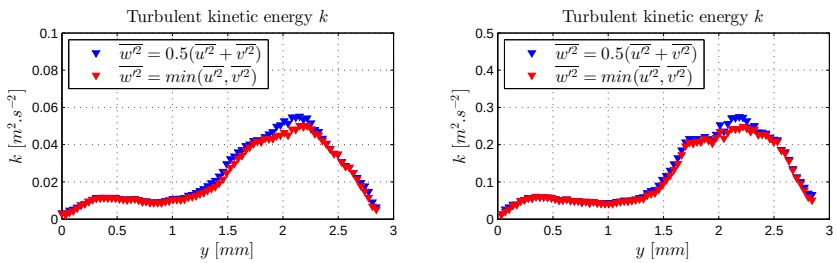

(a) $Re = 346$ (b) $Re = 687$

Figure IV.2.56: Comparison of turbulent kinetic energy for the two assumptions discussed along the line 3, $d_p = 1\mu m$

Turbulence kinetic energy fields are shown in Fig.IV.2.57 for $Re = 346$ and $Re = 687$ using $d_p = 1\mu m$. One can remark that the turbulence kinetic energy k is weak in the swirl zone. $k/|\overline{u}|^2_{inlet} \simeq 1$ in the mainstream region since the mean velocity is much greater than $|\overline{u}|_{inlet}$ as the flow narrows in this region. The numerical analysis is detailed in section IV.2.9.2

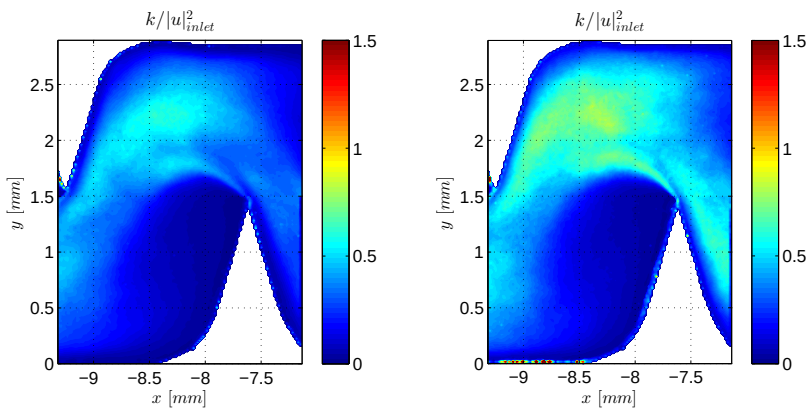

(a) $Re = 346$ (b) $Re = 687$

Figure IV.2.57: Normalized turbulent kinetic energy fields inside the third baffle, $d_p = 1\mu m$

2.9.2 Numerical analysis

The fields of the normalized turbulence kinetic energy (k) and the normalized dissipation rate (ϵ) are shown on Fig.IV.2.58 and Fig.IV.2.59 for $Re = 400$ and $Re = 800$ in 2D only. k and ϵ for S-A

model are calculated from Eq.A.25 and Eq.A.27 in annex A.4. The normalization by respectively U_{inlet} and U_{inlet}^3/d_{inlet} allows, in particular, to have almost the same levels for different Reynolds numbers, but also to analyze in a quantitative way departure of the present results from results obtained for wall flows with standard geometries. As an example, for a turbulent flow over a flat and smooth plate, Pope (2000)[85] shows that the dissipation term magnitude is about 0.5, with the maximum value of about 1 attained at the wall. Similarly, the normalized turbulence level k/u_τ^2 is about 5, corresponding to a maximum turbulence intensity k/U^2 of about 0.1, which is not very different from what is obtained in our case since U/U_{inlet} can be as large as 3.5 (Fig.2.32(g))(which is therefore compatible with values of k/U_{inlet}^2 larger than 1). It can be observed that k and ϵ for standard and [LS] $k-\epsilon$ models no longer evolve from just after the first baffle until the end, which has already been observed for the mean velocity fields (Fig.IV.2.33). For [CHC] $k-\epsilon$ model, k and ϵ are not impacted by the first baffle. The increase of k and ϵ can be observed after the third and the second baffle for $Re = 400$ and $Re = 800$ respectively (Fig.2.58(c) and Fig.2.58(i)). This could be linked to the value of the mean velocity in the principal flow which is high as the turbulence is not well developed (Fig.IV.2.32). The other models dissipate flow energy from the first baffle whereas the [CHC] $k-\epsilon$ model dissipates a large amount of energy only after the second baffle. The large difference between the CHC $k-\epsilon$ model data for $Re = 400$ and $Re = 800$ is probably directly connected to the very large value of the exponent x of the discharge-pressure curve for this model. RSM under-estimates the turbulence kinetic energy k in comparison with the other models Fig.2.58(e) and Fig.2.58(k), while S-A model over-estimates turbulence kinetic energy k, see Fig.2.59(d) and Fig.2.59(j). k is weak in the swirl region for RSM model. k will be even smaller is the swirl zone for 3D modelling.

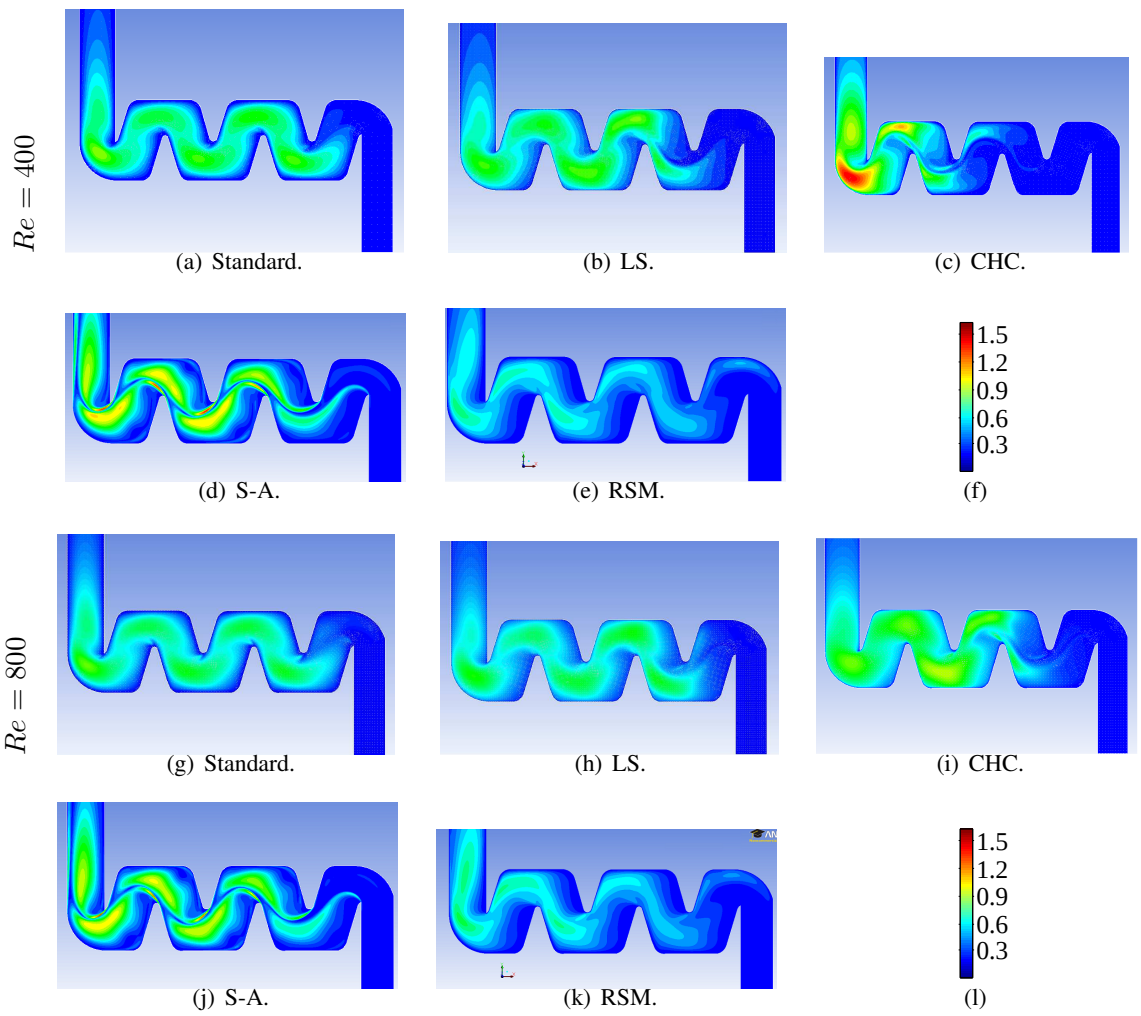

Figure IV.2.58: The normalized turbulence kinetic energy k/U_{inlet}^2, in 2D simulations

One can note that k is more important for the models where the swirl zone is of the second group (big swirl), and thus the dissipation of turbulence kinetic energy will be more important, see Fig.2.59(c) and Fig.2.59(d). k_d is small for the models where the dissipation rate fields are large. This result is coherent since small k_d gives great pressure losses for the same flow rate.

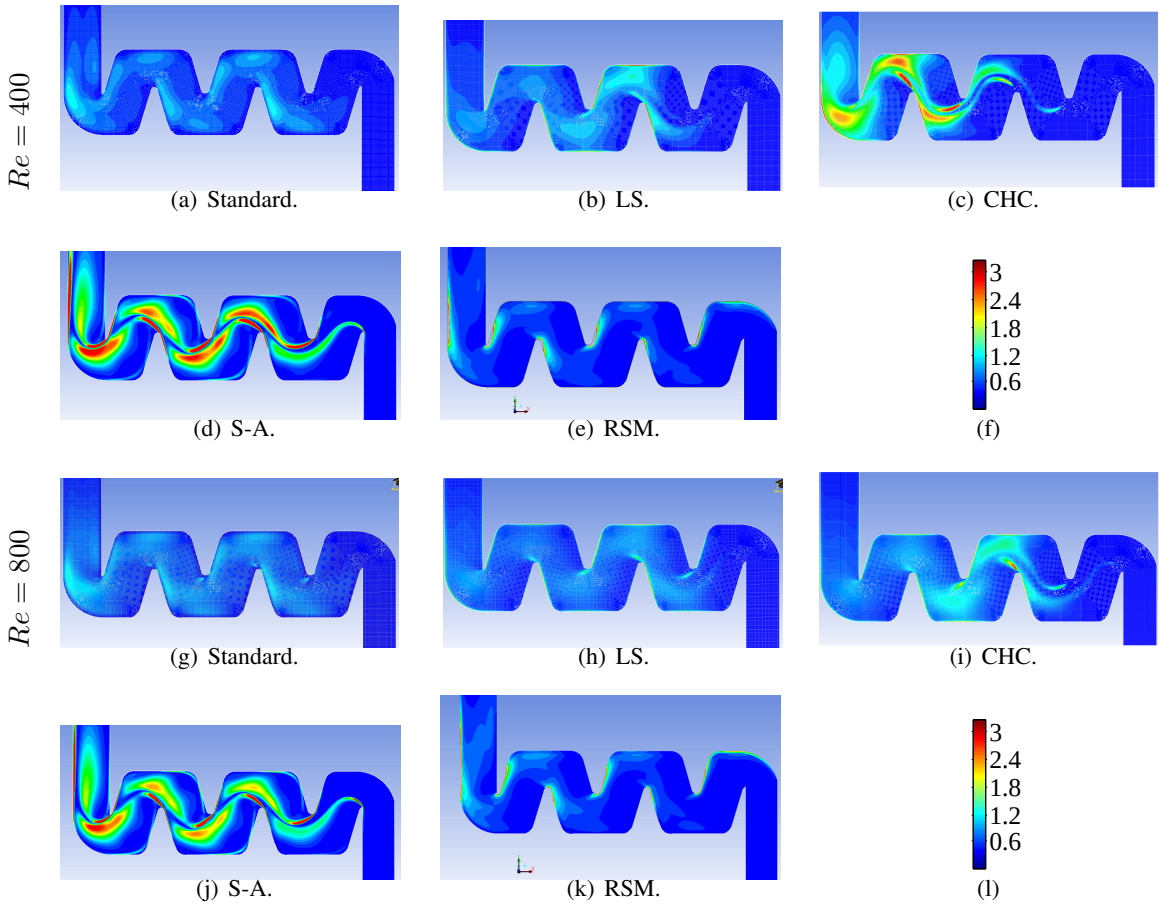

Figure IV.2.59: The normalized dissipation rate in 2D, where the red-colored regions have the values $3 > \epsilon / \frac{U^3_{inlet}}{d_{inlet}} > 5$ in order to visualize the transition between the main flow and the swirl region

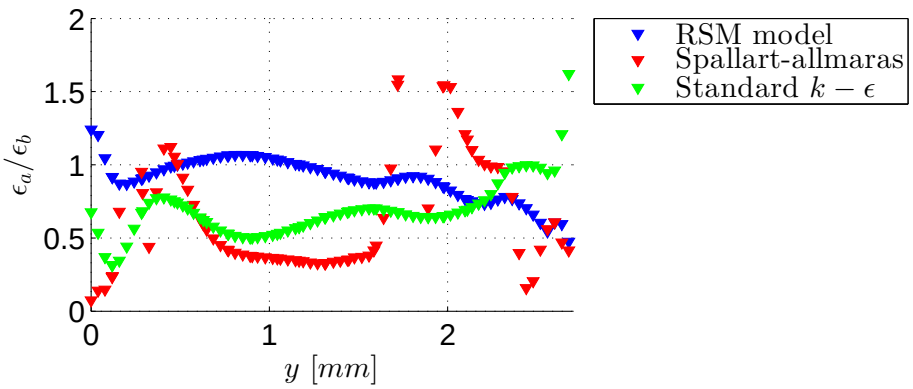

Figure IV.2.60: Ratio of ϵ_a/ϵ_b, where $\epsilon_a = \left(\epsilon / \frac{U^3_{inlet}}{d_{inlet}}\right)_{400}$ and $\epsilon_b = \left(\epsilon / \frac{U^3_{inlet}}{d_{inlet}}\right)_{800}$ along the line 3 in 3D.

Then, the ratio of normalized ϵ for $Re = 400$ (ϵ_a) to normalized ϵ for $Re = 800$ (ϵ_b) is calculated and presented in Fig.IV.2.60. It seems that the ϵ_a/ϵ_b ratio decreases for a large exponent x. Mean ϵ_a/ϵ_b,

along the line 3, are about 0.91 and 0.82 for RSM and standard models respectively. It is clear that this ratio increases when x exponent decreases. As a matter of fact, when x increases, the swirl zone size increases with Reynolds number and thus the dissipation rate. As except, for S-A model, this ratio undergoes rapid changes with y along the line 3. The evolutions of each term of k equations are then plotted for the line 3 (Fig.IV.2.61), for the standard, [LS] and [CHC] $k-\epsilon$ models. To allow quantitative comparison between results obtained for different flow rates, these terms are normalized by $\frac{\rho U_{inlet}^3}{d_{inlet}}$ (since they obviously all have the same dimension, namely, that of $\rho\epsilon$).

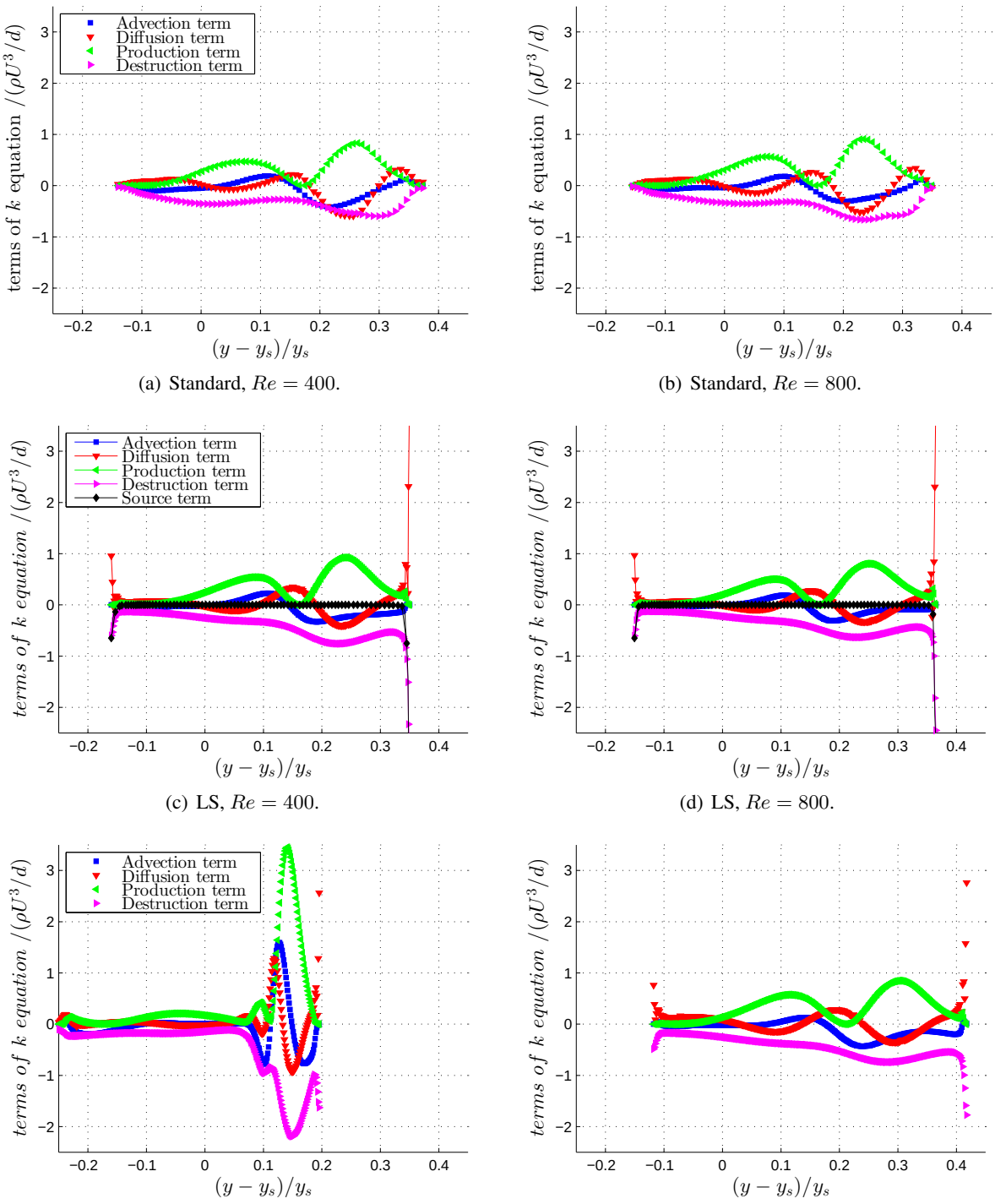

(a) Standard, $Re = 400$.

(b) Standard, $Re = 800$.

(c) LS, $Re = 400$.

(d) LS, $Re = 800$.

(e) CHC, $Re = 400$

(f) CHC, $Re = 800$.

Figure IV.2.61: Normalized terms of turbulence kinetic energy equation in 2D, where y_s is the radial position of the center of the swirl

In the middle of the flow, the normalized diffusion terms, in k equation, for standard, [LS] and [CHC] $k-\epsilon$ models give the same profile for $Re = 800$. For $Re = 400$, this term is different for [CHC] model. Far from the wall, the damping functions are equal to 1. Therefore, these factors do not affect the budget, hence they are the same for all models. The production term for k equation is identical for the different models. It has two peaks (Fig.IV.2.61): one is in the middle of the main flow and the other is at the contact between the main flow and the swirl region due to the shear rate. The advection term is also the same for all models: it is positive between the main flow and the center of the swirl region. That is due to the negative values of the mean velocity components (Fig.IV.2.32 and Fig.IV.2.33) and the gradients of k. Otherwise, the turbulent kinetic energy increases from the wall and the main flow to the center of the swirling region. The main difference is wall treatment: in [CHC] $k-\epsilon$ model, the boundary conditions imposed at the wall are $k = 0, \epsilon = 2\nu\left(\frac{\partial\sqrt{k}}{\partial y}\right)^2$. Therefore the dissipation at the wall has a high value. It can be linked with the high value of the destruction term for k equation which is related to ϵ. Consequently, the diffusion term of the turbulence kinetic equation for [LS] and [CHC] $k-\epsilon$ models reaches a significant value at the wall (Fig.2.61(d) and Fig.2.61(f)), as this term is then in equilibrium with the dissipation term.

2.10 Flow isotropy

The $k-\epsilon$ models imply, as noted above, that the flow is isotropic. $\overline{u'^2}/\overline{v'^2}$ is calculated within the third baffle to know whether the flow is isotropic or not; this is seen in Fig.IV.2.62. In order to better distinguish contour values, the high scale is fixed to be 2.5. However, the value of $\overline{u'^2}/\overline{v'^2}$ reaches about 10 near the wall. It is due to the values of $\overline{v'^2}$ which are much lower than those of $\overline{u'^2}$. The red zones highlight the zone where $\overline{u'^2}/\overline{v'^2}$ is greater than 3. We observe that RSM, in 3D, is in good agreement near the wall even if it predicts lower ratio than micro-PIV experiments. In practice, the boundary condition $|\overline{u}| = 0$ at wall determines the way in which the Reynolds stresses depart from zero for small wall distances. Kim et al. (1987)[58] demonstrate that the Reynolds stresses $\overline{u'^2}$ and $\overline{v'^2}$ are in function of y^2 and y^4 respectively. Therefore, $\overline{v'^2}$ decreases more quickly than $\overline{u'^2}$ when approaching closer to the wall. In the work of Kim et al. (1987)[58] reported by Pope (2000)[85], $\overline{u'^2}$ normalized by u_τ^2 reaches 7.3 while, $\overline{v'^2}$ normalized by u_τ^2 is about 0.36 at $y/\delta = 0.1$ which is equivalent to $0.05d_{inlet}$ in our study. In this case, the ratio is about 20. This situation is only applicable when u' is normal to the wall. One can remark this in micro-PIV experiments on Fig.2.62(b). This situation is not reproduced by RSM model Fig.2.62(a). The enhanced wall treatment used in the modelling and the method by which μ_t is calculed, are the two causes. The logarithmic value of $\overline{u'^2}/\overline{v'^2}$ is, then, calculated and represented in Fig.IV.2.63. Indeed, $\overline{u'^2} = \gamma\overline{v'^2}$ is equal to $\overline{v'^2} = (1/\gamma)\overline{u'^2}$ facing the symmetry with respect to the isotropy, where γ is a constant. This gives the logarithmic scale, with the same value in opposite sign. In Fig.IV.2.63, the positive values of $\log_{10}(\overline{u'^2}/\overline{v'^2})$ correspond to the regions where $\overline{u'^2}$ is superior to $\overline{v'^2}$ while the negative values are for the opposite case. As $10^{0.8} = 6.31$, $\overline{u'^2}/\overline{v'^2}$ is about 6.31. Therefore, the flow, globally, is not isotropic.

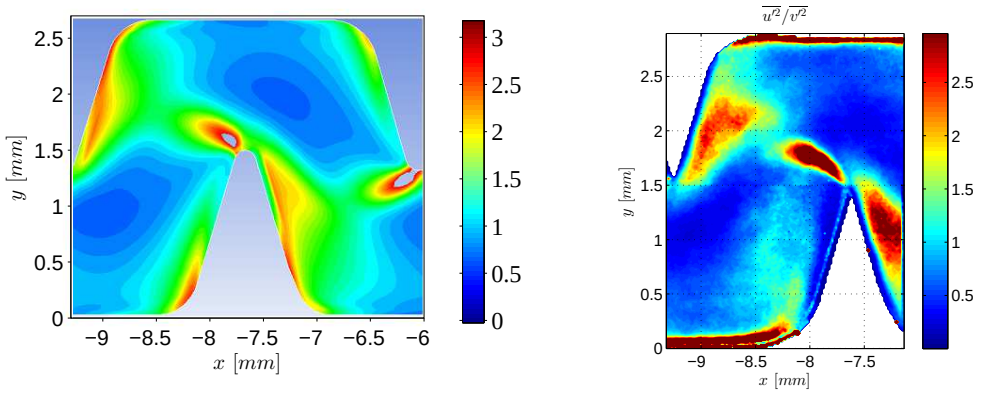

(a) RSM model in 3D, $Re = 800$ (b) Micro-PIV, $Re = 687$

Figure IV.2.62: $\overline{u'^2}/\overline{v'^2}$ ratio in the third baffle

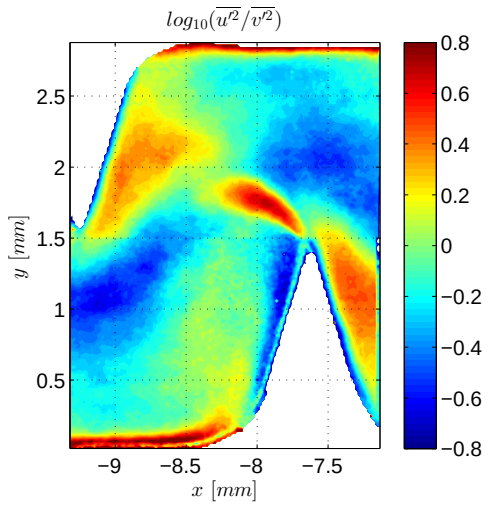

Figure IV.2.63: Anistropy of the flow in the third baffle, $\log_{10}(\overline{u'^2}/\overline{v'^2})$, $Re = 687$

2.11 Turbulence properties

Turbulence Reynolds number fields Re_t, defined in Eq.III.1.65 are shown in Fig.IV.2.64 for $Re = 400$ and $Re = 800$. The turbulence Reynolds number fields are developed from the second baffle. However, the turbulence Reynolds number is weak at the entrance as such at the first baffle. The ratio of turbulence Reynolds number and Reynolds number at the inlet boundary condition is shown in Fig.IV.2.65 where this ratio is more important for $Re = 400$. The turbulence Reynolds number Re_t has the same order of magnitude as the global Reynolds number Re of the flow. A detailed analysis of all the terms constituting this ratio is necessary:

$$\frac{Re_t}{Re} = \frac{k}{\epsilon}\frac{k}{|\overline{u}|^2_{inlet}}\frac{|\overline{u}|_{inlet}}{d_{inlet}} \quad . \tag{IV.2.15}$$

$\frac{|\overline{u}|_{inlet}}{d_{inlet}}$ has the magnitude of 10^3, while $\frac{k}{|\overline{u}|^2_{inlet}}$ has the magnitude order of 1 (see Fig.IV.2.58) and k/ϵ is in the order of 10^{-3}.

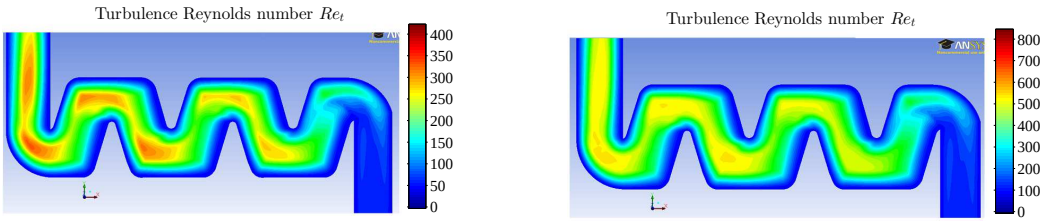

(a) $Re = 400$ (b) $Re = 800$

Figure IV.2.64: Turbulence Reynolds number Re_t defined in Eq.III.1.65 for RSM model in 2D.

It is important to compare the Re_t for both Reynolds numbers. The profiles of Re_t/Re are plotted along the line 3 and presented in Fig.IV.2.65. Re_t/Re for $Re = 400$ is slightly larger and closer to one than for $Re = 800$ in the mainstream region ($y = 1.75 - 2.25\ mm$). However, as expected, close to the walls, the ratio decreases to 0 as Re_t is zero at the walls.

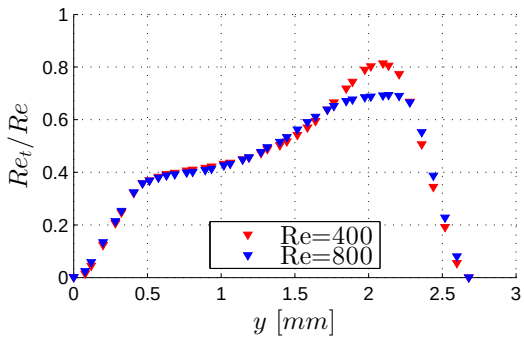

Figure IV.2.65: Ratio of turbulence Reynolds number Re_t to Reynolds number along the line 3 for RSM model in 3D

k/ϵ ratio is presented in Fig.IV.2.67 for $Re = 400$ and $Re = 800$ for RSM model in 3D. The time scale t_L is larger at the inlet than inside the baffles where the flow is almost laminar. In addition, this time scale is also relatively more important in the swirl zone than in the mainstream flow. The smaller the mixing time is, the more agitated and turbulent is the flow. The time scale increases when Reynolds number decreases. The turbulence Reynolds numberRe_t is then related to k and t_L. It is clear that the influence of k is more important than t_L in the estimation of Re_t. t_L justifies the good choice for the time between two laser pulses $6 - 12\ \mu s$ when performing the micro-PIV acquisition (see table II.2.2).

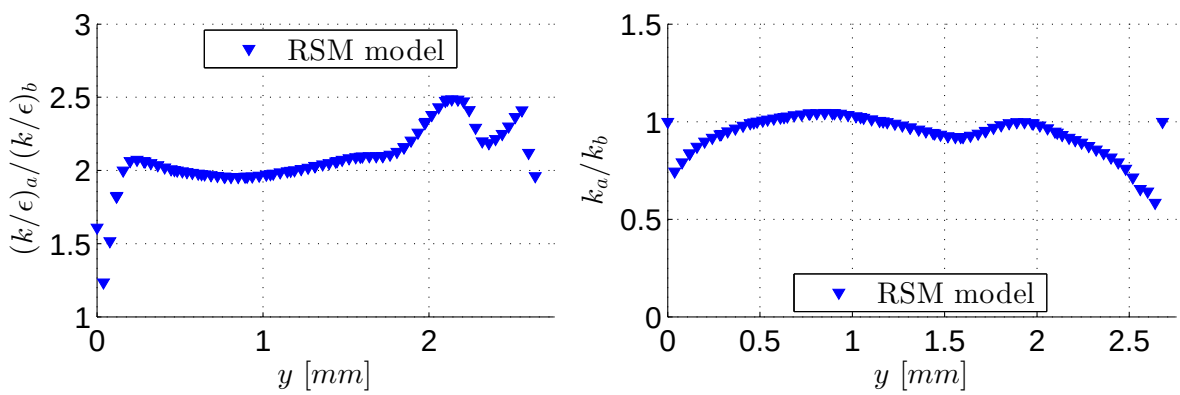

(a) $(k/\epsilon)_a/(k/\epsilon)_b$ (b) $(k/|\overline{u}|^2_{inlet})_a/(k/|\overline{u}|^2_{inlet})_b$

Figure IV.2.66: Ratios on line 3 for RSM model in 3D

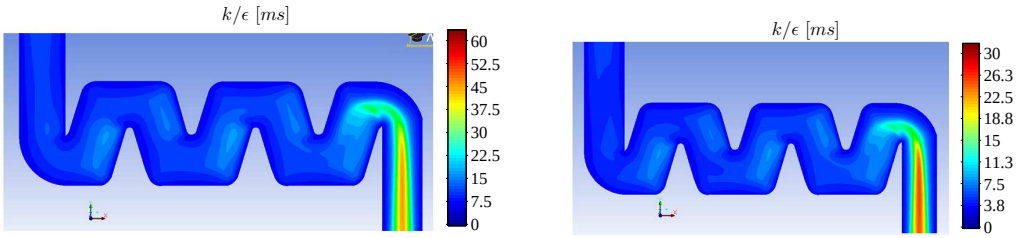

(a) $Re = 400$ (b) $Re = 800$

Figure IV.2.67: k/ϵ ratio for RSM model in 3D

When k/ϵ is normalized by the bulk velocity at the inlet, one finds:

$$\left(\frac{k}{\epsilon}U_{inlet}\right)_a / \left(\frac{k}{\epsilon}U_{inlet}\right)_b = \left[\left(\frac{k}{\epsilon}\right)_a / \left(\frac{k}{\epsilon}\right)_b\right] \times (U_{inlet\ a}/U_{inlet\ b}) \approx 2 \times 0.5 = 1$$

One can remark that the ratio 2 of k/ϵ is that of the bulk velocity for the two Reynolds numbers. When $y < 0.2\ mm$, the normalized values $t_{La}/t_{Lb} < 1$. Therefore, the swirl zone is quieter for greater Reynolds number $Re = 800$, even if Re_t/Re ratio is equal for both Reynolds numbers; whereas, for $y > 2\ mm$, the normalized values $t_{La}/t_{Lb} > 1$. Therefore, this zone is more agitated for greater Reynolds number $Re = 800$.

It is important to compare the values of k/ϵ in the swirl region to the characteristic time of particles from Stokes number. In general, the clay particles diameter is in the order of $d_p = 2\mu m$. Mean clay density is about 1700 $[kg.m^{-3}]$. When replacing these values in Eq.II.1.2, we find that $\tau_p = 0.37 \times 10^{-6}\ [s]$ and then Stokes number for $Re = 400$, $St = 19 \times 10^{-6}$ which is much smaller than 1. Whereas the sedimentation velocity is equal to $U_g = 1.526 \times 10^{-6}\ m.s^{-1}$.

2.12 Swirl detection and analysis

The study of flow velocity shows that the flow inside the baffle is composed of a mainstream flow and a recirculation zone. This recirculation zone is observed when considering the streamlines of velocity fields (Fig.IV.2.34). In order to quantify swirling motion, shearing motion zones and to distinguish between these two zones, deeper analysis is performed in this section to define with more accuracy the swirling zone. However, $\left(\frac{|\overline{u}|_{inlet}}{d_{inlet}}\right)_a / \left(\frac{|\overline{u}|_{inlet}}{d_{inlet}}\right)_b = 0.5$, where the indices a and b are defined for $Re = 400$ and for $Re = 800$ respectively. Re_t is mainly influenced by k and k/ϵ . k is somewhat equal for two Reynolds numbers, while normalized k/ϵ is larger for $Re = 400$ at $y = 1.75 - 2.75\ mm$, see Fig.IV.2.67.

The turbulence kinetic energy of the flow is proportional to U^2, while the dissipation rate is related to U^3/L. The ratio of k/ϵ is proportional to L/U. This term refers to the time scale of the large eddies (commonly referred to as the large eddy "turnover" time) t_L, the time scale for the small eddies can be generated using the viscosity and the dissipation $t_\eta = (\nu/\epsilon)$. The large scale structures in the flow are seen to have a much larger time scale (duration) than the smallest energy dissipation eddies. As the Reynolds number of the flow increases, the magnitude of the separation between both time and length scales increases.

2.12.1 Strain rate and vorticity

The deformation rate of the fluid is an important property. The deformation tensor describes how fluid elements deform as a result of fluid motion. This deformation (or velocity gradient) tensor is

represented by $D_{ij} = \nabla u_{ij}$ and defined by :

$$D_{ij} = \nabla u_{ij} = \frac{\partial u_i}{\partial x_j} = \begin{pmatrix} \frac{\partial u}{\partial x} & \frac{\partial u}{\partial y} & \frac{\partial u}{\partial z} \\ \frac{\partial v}{\partial x} & \frac{\partial v}{\partial y} & \frac{\partial v}{\partial z} \\ \frac{\partial w}{\partial x} & \frac{\partial w}{\partial y} & \frac{\partial w}{\partial z} \end{pmatrix} \quad . \tag{IV.2.16}$$

As this is a second order tensor it can be decomposed into a symmetric and an antisymmetric part. Applying this to the Jacobian matrix $J = (\nabla u)^T$, with symmetric and antisymmetric components, S and Ω respectively, $D_{ij} = S_{ij} + \Omega_{ij}$:

$$S = \frac{1}{2}\left(\nabla u + \nabla u^T\right) = \frac{1}{2}\begin{pmatrix} 2\frac{\partial u}{\partial x} & \frac{\partial u}{\partial y} + \frac{\partial v}{\partial x} & \frac{\partial u}{\partial z} + \frac{\partial w}{\partial x} \\ \frac{\partial v}{\partial x} + \frac{\partial u}{\partial y} & 2\frac{\partial v}{\partial y} & \frac{\partial v}{\partial z} + \frac{\partial w}{\partial y} \\ \frac{\partial w}{\partial x} + \frac{\partial u}{\partial z} & \frac{\partial w}{\partial y} + \frac{\partial v}{\partial z} & 2\frac{\partial w}{\partial z} \end{pmatrix} \quad ; \tag{IV.2.17}$$

$$\Omega = \frac{1}{2}\left(\nabla u - \nabla u^T\right) = \frac{1}{2}\begin{pmatrix} 0 & \frac{\partial u}{\partial y} - \frac{\partial v}{\partial x} & \frac{\partial u}{\partial z} - \frac{\partial w}{\partial x} \\ \frac{\partial v}{\partial x} - \frac{\partial u}{\partial y} & 0 & \frac{\partial v}{\partial z} - \frac{\partial w}{\partial y} \\ \frac{\partial w}{\partial x} - \frac{\partial u}{\partial z} & \frac{\partial w}{\partial y} - \frac{\partial v}{\partial z} & 0 \end{pmatrix} \quad . \tag{IV.2.18}$$

The diagonal components of the strain rate tensor S ($\frac{\partial u}{\partial x}$,$\frac{\partial v}{\partial y}$ and $\frac{\partial w}{\partial z}$) are the extensional strain rates. Note that $\frac{\partial u}{\partial x} > 0$ for an elongating body and $\frac{\partial u}{\partial x} < 0$ for a shortening body. The strain rate due to shearing in the x-y plane is defined in the components of the strain rate tensor as:

$$S_{xy} = \frac{1}{2}\left(\frac{\partial u}{\partial y} + \frac{\partial v}{\partial x}\right) \quad . \tag{IV.2.19}$$

The vorticity is a vector field $\overrightarrow{\omega}$, defined as the curl(rotational) of the flow velocity $\overrightarrow{u}$ vector. The definition can be expressed by the vector analysis formula:

$$\overrightarrow{\omega} = \nabla \times \overrightarrow{u} \quad ; \tag{IV.2.20}$$

where ∇ is the delta operator. However, the vorticity of a fluid at a point is equal to twice the angular velocity of the fluid particles at that point. The last definition allows to relate the vorticity to Ω. The vorticity of a two-dimensional flow is always perpendicular to the plane of the flow, and therefore can be considered as a scalar field. Micro-PIV experiment is performed in 2D. Therefore, there is one component of vorticity ω_z which is given as follow:

$$\omega_z = \frac{\partial v}{\partial x} - \frac{\partial u}{\partial y} \quad . \tag{IV.2.21}$$

The strain rate S_{xy} and the vorticity ω_z are calculated from Eq.IV.2.19 and Eq.IV.2.21. Then, these are normalized by (U_m/d_{inlet}) for two Reynolds numbers for the third baffle in both the micro-PIV experiments and the 3D modelling with RSM. One can conclude that the strain rate as well as the vorticity values are not much influenced by the Reynolds number when comparing the fields for these two Reynolds numbers (Fig.IV.2.68 to Fig.IV.2.71)[8]. The numerical results are close to those obtained experimentally. ω_z has a large value for the flow in the separation zone (red zone) Fig.IV.2.70 with a positive value for the bottom tooth and a negative value for the top tooth. Regarding the same zone in the fields of strain rate, one finds that the strain rate is also maximum in this zone. As a result of this, the vorticity can be used directly to identify vortices. A problem associated with this method is that vorticity cannot distinguish between swirling motions and shearing motions (Kida et al., 1998)[57]. In addition,

[8]As the field of view is $= 2.2 \times 2.2$ for $d_p = 1\mu m$, it is difficult to visualize an entire baffle. This is why the baffle is presented by juxtaposition of two fields of view. The line, in the middle, is the limit of these two fields.

contrary to what is found for the recirculation zone, the vorticity values in these zones are closer to zero. The variation of velocity occurs over a quite long distance (from $y = 0$ to $y = 1.5\ mm$).

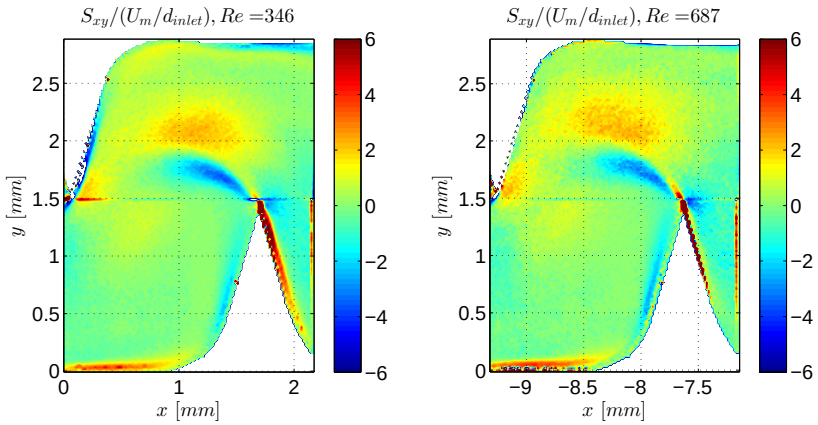

(a) $Re = 346$ (b) $Re = 687$

Figure IV.2.68: Strain rate fields, micro-PIV with $d_p = 1\mu m$

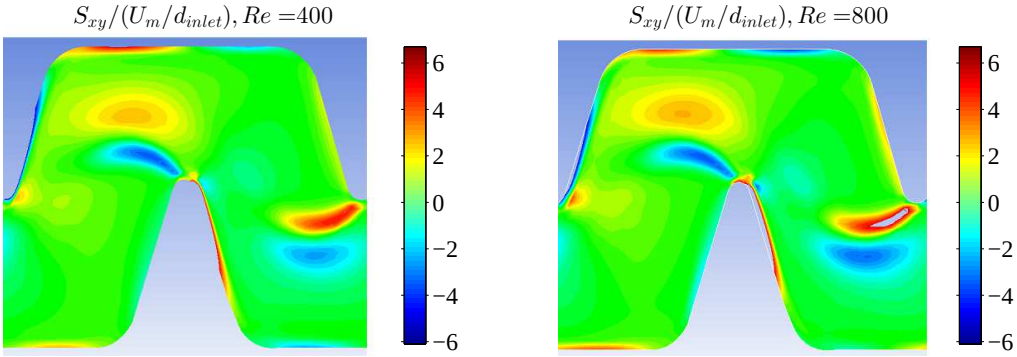

(a) $Re = 400$ (b) $Re = 800$

Figure IV.2.69: Strain rate fields, RSM model.

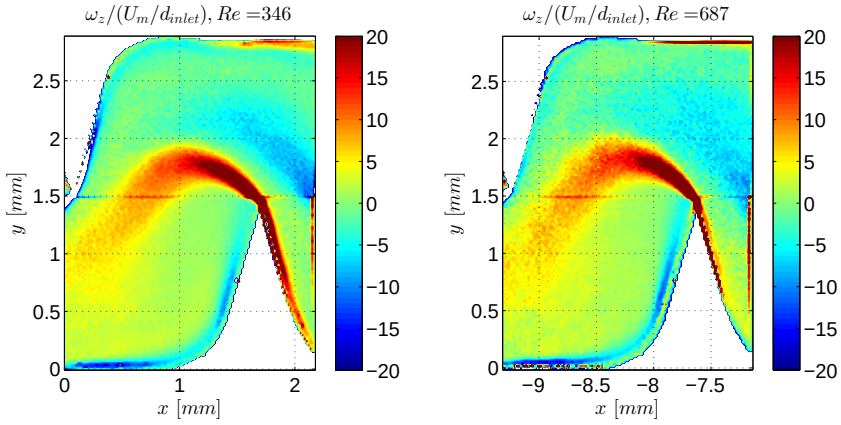

(a) $Re = 346$ (b) $Re = 687$

Figure IV.2.70: Vorticity fields, micro-PIV with $d_p = 1\mu m$

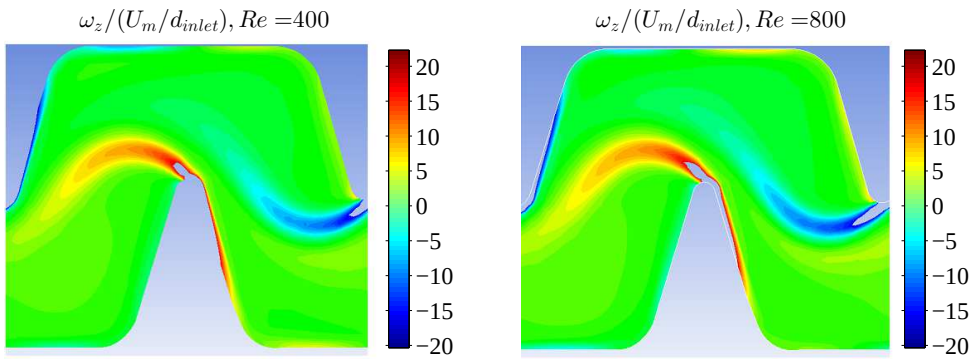

(a) $Re = 400$ (b) $Re = 800$

Figure IV.2.71: Vorticity fields, RSM model.

2.12.2 Advanced criterion

2.12.2.1 Definitions

The numerical and experimental data must be analyzed by advanced methods. There are several different kinds of methods to identify coherent turbulent structures (eddies) in a quantitative way. There is so far no universal accepted method to identify a coherent structure (Haller, 2005 [45]; Green, Rowley et al., 2007 [43]). Many of these methods involve the velocity gradient tensor (Chakraborty, Balachandar et al., 2005 [23]; Green, Rowley et al., 2007 [43]).

The characteristic equation[9] for the tensor ∇u is given by:

$$\lambda^3 + P\lambda^2 + Q\lambda + R = 0 \quad , \tag{IV.2.22}$$

where P, Q and R are the three invariants of the velocity gradient tensor. Using the decomposition into symmetric and anti-symmetric parts, these invariants can be expressed as follows:

$$P = -tr(\overline{D}) \quad ; \tag{IV.2.23}$$

$$Q = \frac{1}{2}\left(tr\left(\overline{D}\right)^2 - tr\left(\overline{D}^2\right)\right) = \frac{1}{2}\left(\|\overline{\Omega}\|^2 - \|\overline{S}\|^2\right) \quad ; \tag{IV.2.24}$$

$$R = -det(\overline{D}) \quad ; \tag{IV.2.25}$$

where $\|.\|$ is the Frobenius matrix norm.

λ_2-criterion A symmetric tensor is defined as follows:

$$A = S^2 + \Omega^2 \quad . \tag{IV.2.26}$$

A is considered to determine if there is a local pressure minimum that entails a vortex. A vortex is defined as "a connected region with two negative eigenvalues of A" (Jeong and Hussain, 1995)[52]. Since A is symmetric, it has real eigenvalues only. Thus its two eigenvalues (λ_1 and λ_2) are also real for a two-dimensional flow, and by ordering the eigenvalues $\lambda_1 \leq \lambda_2 \leq \lambda_3$ the definition becomes equivalent to requiring that $\lambda_2 < 0$. The local minimum of λ_2 corresponds to a vortex core. If the value of λ_2 is positive, the shear motion only exists but the swirling motion disappears in the local flow field. That is called the Lambda-2 (λ_2) vortex criterion.

[9]The characteristic equation is the equation which is solved to find matrix eigenvalues λ, also called the characteristic polynomial. For a general matrix A, the characteristic equation in variable λ is defined by $det(A - \lambda I) = 0$,

Q-criterion One commonly mentioned method is the Q-criterion (Green, Rowley et al., 2007)[43], defined in Eq.IV.2.24. The Q-criterion defines a vortex as a " connected fluid region with a positive second invariant of ∇u ". Coherent eddies are then defined as regions of the flow with positive values of Q and lower pressure than the immediate surroundings (Chakraborty, Balachandar et al., 2005)[23], these can easily be visualized as isosurfaces. Looking at the definition of the second invariant, we can see that Q represents the local balance between shear strain rate and vorticity magnitude, defining vortices as areas where the vorticity magnitude is greater than the magnitude of rate-of-strain (Hunt et al., 1988 [50], Vàclav Kolàr, 2007 [60]).

Eq.IV.2.24 is developed to implement the parameter Q in Fluent software and to process it under Matlab for micro-PIV experiments. Q can be written, in 2D and 3D, as follows:

$$Q = -\frac{1}{2}\left(\left(\frac{\partial u}{\partial x}\right)^2 + \left(\frac{\partial v}{\partial y}\right)^2\right) - \left(\frac{\partial u}{\partial y}\frac{\partial v}{\partial x}\right) \quad \text{in 2D} \quad . \tag{IV.2.27}$$

and

$$Q = -\frac{1}{2}\left(\left(\frac{\partial u}{\partial x}\right)^2 + \left(\frac{\partial v}{\partial y}\right)^2 + \left(\frac{\partial w}{\partial z}\right)^2\right) - \left(\frac{\partial u}{\partial y}\frac{\partial v}{\partial x} + \frac{\partial u}{\partial z}\frac{\partial w}{\partial x} + \frac{\partial v}{\partial z}\frac{\partial w}{\partial y}\right) \quad \text{in 3D} \quad ; \tag{IV.2.28}$$

Δ-criterion The Δ-criterion defines vortices as "regions in which the eigenvalues of ∇u are complex and the streamline pattern is spiraling or closed" (Vàclav Kolàr (2007) [60]). In order to determine if the eigenvalues are complex we examine the discriminant of the characteristic equation:

$$\Delta = \left(\frac{Q}{3}\right)^2 + \left(\frac{R}{2}\right)^2 > 0 \quad . \tag{IV.2.29}$$

This definition is valid for incompressible flows where $P = 0$. The streamlines are closed or spiralling if two of the eigenvalues form a complex conjugate pair. By looking at the Δ criterion we can see that $Q > 0$ is a more restrictive criterion than $\Delta > 0$ (Chakraborty, Balachandar et al., 2005) [23].

This criterion is not treated in this manuscript.

2.12.2.2 Criterion treatment

λ_2 criterion is plotted on Fig.IV.2.72 and Fig.IV.2.73 for micro-PIV and RSM respectively. This method allows to define the vorticity center for which λ_2 is the smallest of negative sign. In Fig.IV.2.70 and Fig.IV.2.71, the blue zone represents the vortices. As observed for vorticity fields the λ_2 criterion underlines that separation zone (just behind the baffle top) is the region with vortex cores.

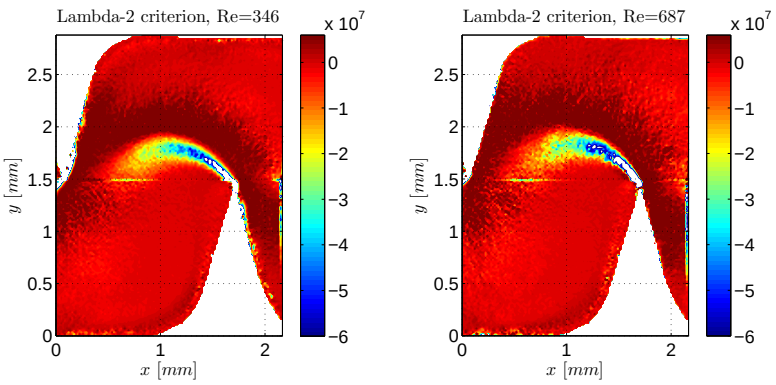

(a) $Re = 346$ (b) $Re = 687$

Figure IV.2.72: Normalized Lambda-2 criterion, $d_p = 1\mu m$

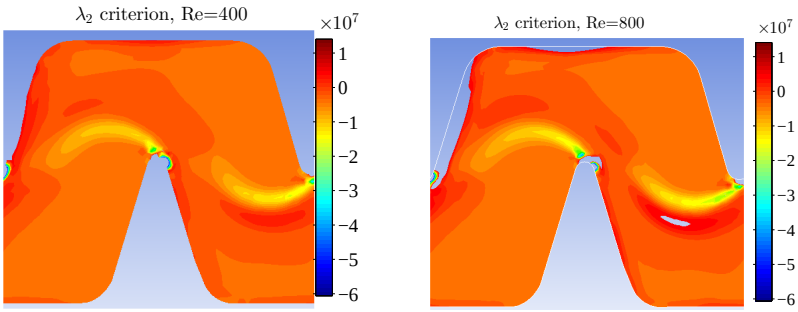

(a) $Re = 400$ (b) $Re = 800$

Figure IV.2.73: Normalized Lambda-2 criterion, RSM model in 3D

The Q-criterion identifies the cores of turbulent structures (Chakraborty, Balachandar et al., 2005) [23] while the λ_2-criterion is a somewhat looser criterion than the Q-criterion but guarantees local pressure minima within the 2D plane (Dubief and Delcayre, 2000 [37]; Chakraborty, Balachandar et al. 2005 [23]). The drawback of the Eulerian methods is that they are not independent of the reference frame, i.e. they are not objective. As Green et al. (2007) [43] also point out, this method requires the user to effectively choose the thresholds discretionally (as $Q > 0$ may be changed to a higher value for instance in order to visualize more easily the eddies).

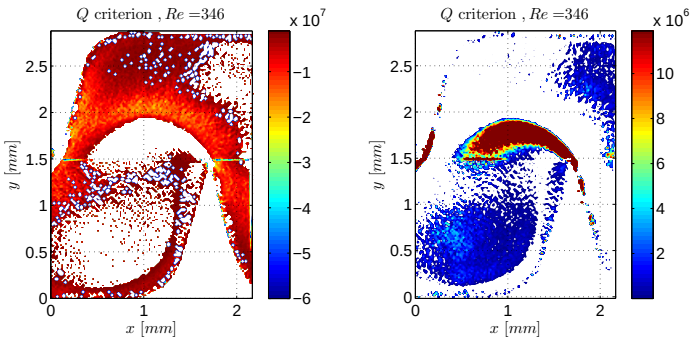

(a) Shear motion zone (b) Vortex zone

Figure IV.2.74: Rate of strain and vorticity regions, $Re = 346$, $d_p = 1\mu m$

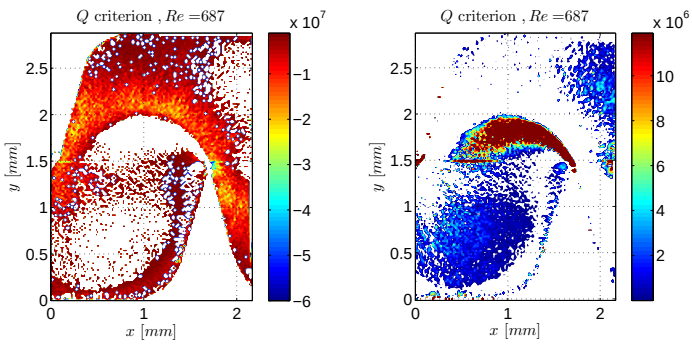

(a) Shear motion zone (b) Vortex zone

Figure IV.2.75: Rate of strain and vorticity regions, $Re = 687$, $d_p = 1\mu m$

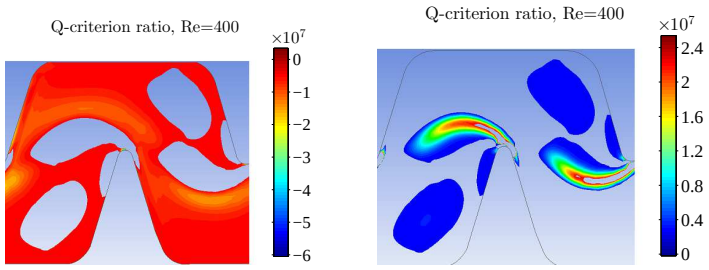

(a) Shear motion zone (b) Vortex zone

Figure IV.2.76: Rate of strain and vorticity regions in 3D, $Re = 400$, RSM model

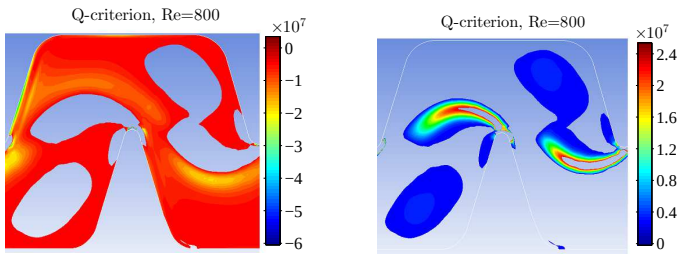

(a) Shear motion zone (b) Vortex zone

Figure IV.2.77: Rate of strain and vorticity regions in 3D, $Re = 800$, RSM model

The experimental Q-criterion fields are plotted in Fig.IV.2.74 and in Fig.IV.2.75 for both Reynolds numbers. The Q-criterion fields are plotted in Fig.IV.2.76 and Fig.IV.2.77 for RSM model. The advantage of Q-criterion is to separate and distinguish between the vortex zone and shear motion zone. The Q-criterion confirms what is found by the λ_2 criterion: the size and position of the region near the baffle teeth and that in which recirculation occurs depend very little on the Reynolds number. The Q-criterion is calculated in 2D and in 3D on the 3D geometry by Eq.IV.2.27 and Eq.IV.2.28 respectively. Nevertheless the figures presented above are for the 3D equation. In Fig.IV.2.78, the ratio of Q_{3D}/Q_{2D} is calculated and shown. This figure points out the limitations of the swirl zone where small positive values in 3D become small negative values in 2D when the third component is eliminated (as with micro-PIV data).

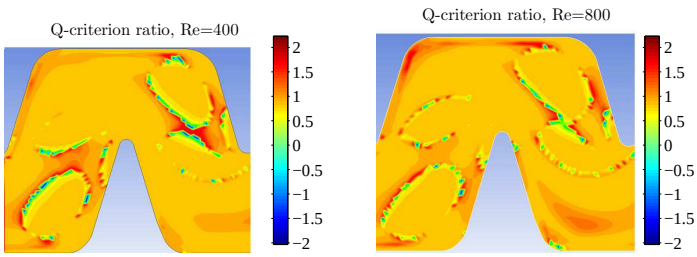

(a) $Re = 400$ (b) $Re = 800$

Figure IV.2.78: $\frac{Q_{3D}}{Q_{2D}}$ calculated on the 3D geometry, RSM model

2.13 Conclusion

The flow is analyzed in detail in this chapter. These velocity fields together with the discharge-pressure curves allow to visualize and qualify the flow and then to validate the numerical model.

Firstly, on one hand, experimental analysis reveals that the flow at the inlet section is, globally, laminar when $Re = 435$ while for $Re = 867$ this flow is slightly turbulent with a weak turbulent intensity (around 4%). The turbulence statistics, including correlation coefficients and skewness profiles, show that the 500 pairs of image number used in this manuscript are not enough to analyze with high accuracy the second order statistics at the inlet. A special acquisition micro-PIV and new parameters must be used to investigate with high accuracy these statistics. On the other hand, the turbulence models use the equations of turbulence to model the flow, therefore they provide a velocity profile corresponding to the turbulent state at the inlet (with 5% intensity).

Secondly, the flow within the labyrinth-channel is composed of a mainstream flow and a recirculation region as it is found by micro-PIV experiments. The most important flow evolution occurs in the first three baffles, where the flow develops along these baffles to reach a stable state in the third baffle where all the flow variables and parameters such as mean velocity, Reynolds stresses and turbulence Reynolds number Re_t reach their stable state. Nevertheless, slight variations in the turbulence quantities after the third baffle is observed, numerically, when some models such as CHC $k - \epsilon$ model are used. The velocity components values and turbulence quantities in the first baffle are very weak in comparison with the other baffles. Numerically, mainstream flow and recirculation region differ from one model to another. This variation has an impact on the pressure loss prediction. S-A model predicts high pressure losses even if it has an exponent closer to 0.59. This is due to the prediction of great swirl zone by this model. The pressure losses calculated for standard $k - \epsilon$ are close to those obtained experimentally. Nevertheless, standard $k - \epsilon$ model under-estimates the velocity in the labyrinth-channel emitter, in 2D and 3D. LS $k - \epsilon$ in 2D and RSM give the best results regarding the velocity, the x exponent is very close to the experimental one for LS $k - \epsilon$. As RSM has an exponent of 0.46 and 0.48 in 2D and in 3D, this model under-predicts the swirl zone for $Re = 400$, while the other models such as LS and CHC $k - \epsilon$ models over-predict the swirl zone for Re=400. Globally, almost all models predict the same mean velocity and the same swirl zone for $Re = 800$ in the third baffle where the flow is developed. LS $k - \epsilon$ model gives the closest exponent to the experiment. Nevertheless the velocity profiles are not exactly superposed. The mean velocity differs according to the model. Some models such as Standard $k - \epsilon$ and LS $k - \epsilon$ and RSM models are better to model the flow in the labyrinth-channel. Modelling the flow in 2D or 3D predicts the same results with standard $k - \epsilon$ and RSM models. The results emphasizes RSM model supremacy in simulating such a flow. The Reynolds number Re has no effect on the flow development, with a small effect on the mainstream flow and swirl zone. The results of RSM model are closer to the experimental results. The experimental results show that the roughness effect is insignificant from $0.25\ mm$ above the wall. Experimentally, the flow isotropy is analyzed calculating the $\overline{u'^2}/\overline{v'^2}$ ratio. This ratio reaches about 6 which indicates that the flow is anisotropic.

Thirdly, swirl regions are deeper analyzed. Q and λ_2 methods show that the vortex occurs mainly in the separation zone where the vorticity results from the change of direction. The vorticity values are large in this zone in comparison with the recirculation where the vorticity remains at small value. Q criterion allows to distinguish between the shear motion and swirl zones. Nevertheless, the limitations of these recirculation zones are somewhat inaccurate since the Q values are very low. Therefore, the ratio of Q in 3D to Q in 2D is calculated numerically. This ratio allows to determine with high accuracy the recirculation zone. As a conclusion, just downstream the baffle, there is , as expected, a recirculation zone but of weak intensity in comparison with the mainstream flow, where the strong vorticity value is generated by the flow direction change.

Finally, with the present results, we find that the RSM model is the best model to analyze and visualize the flow in the labyrinth-channel since the flow is not isotropic, the different pressure field and velocity fields are almost identical to those obtained experimentally.

Conclusion and perspectives

This thesis focuses on the study of the flow in millimetric-channel. This millimetric channel, also known as labyrinth-channel, is part of the micro-irrigation emitter. The micro-irrigation system has achieved a good development these last years. Nevertheless, this system is sensitive to clogging. This clogging increases the installation and maintenance cost. Since the hydrodynamic conditions play an important role in controlling the clogging, the flow in the emitter labyrinth-channel has to be understood and characterized in order to improve emitter performance. The flow characterization and analysis are the objectives of this thesis. For that purpose, two approaches are developed, namely, micro-PIV measurements and numerical modelling.

The flow characterization of the labyrinth-channel is essential. This characterization allows to predict and distinguish between the mainstream flow and the recirculation zone position and size. These zones are characterized by a low-velocity. Numerically, the prediction of recirculation zone position and size varies depending on the numerical model. Therefore, micro-PIV experiments help to analyze the flow within the labyrinth-channel and to validate the numerical model. Although micro-PIV technique is a powerful tool to perform the flow characterization in millimetric channel, is still little used, in such application (micro-irrigation). Indeed, the labyrinth scale is larger than the one classically used in micro-PIV. This technique is used in G-eau research laboratory in the framework of the present thesis for the first time. A particular care has been taken to choose the particles diameter on the one hand and to seed and mix particles but also to prevent them from depositing on labyrinth-channel wall on the other hand.

Micro-PIV experiments are performed in 2D. Thus, they define two instantaneous velocity components u and v which allows to calculate $\overline{u}$ and $\overline{v}$, three fluctuating velocity second-order moments $\overline{u'^2}$, $\overline{v'^2}$ and $\overline{u'v'}$, $\mathcal{C}$, ω_z and S_{xy}. These parameters are in some way enough to characterize the flow in the labyrinth-channel.

The manuscript reports the assessment of several turbulent models. In the literature, the choice of turbulent model is not yet established. Several models such as the $k-\epsilon$, RSM and LES models are studied. As LES model is not well adapted to simulate wall bounded flows and as it is time consuming, Spalart–Allmaras, RANS and RSM models are chosen to perform the present work. The numerical models used allow to compute the pressure losses and to have the discharge-pressure curves. This curve defines the hydraulic performance of emitter. These pressure losses are calculated numerically by the simulation, and the two major contributions, due to turbulent dissipation rate and wall friction, are discussed. To our knowledge, this analysis is quite innovative as it is the first time that it is conducted. The turbulent dissipation is the main responsible of the pressure losses in the labyrinth-channel. The pressure losses are strongly related to the recirculation zone size. x exponent is the variable which determines the flow uniformity in the labyrinth-channel. It depends on the change of recirculation zone size when Reynolds number change. $x = 0.5$ confirms that the flow is uniform within all the labyrinth-channel and well developed. The pressure loss coefficient (PLC), namely, φ relates the emitter discharge to the pressure head losses, Eq.IV.1.10, using a second-order polynomial model. PLC depends on the geometric parameters of the baffle. This coefficient can be used to rapidly predict the hydraulic performance for emitters depending on their geometries. However, φ decreases when Reynolds number increases since the flow develops more rapidly. The flow characteristics within each unit are identical when the flow is fully developed. This observation is of interest for manufacturers who could adjust the number of labyrinth units according to the discharge they want to achieve, in order to meet the plant needs.

The experimental results show that flow varies until the third baffle with small Reynolds number effects on the flow development and composition (mainstream flow and swirl zone). The effect of the roughness is negligible from $0.25\ mm$ above the wall. Generally speaking, RSM model fits correctly the experiments. Therefore, the RSM model will help to perform optimization studies in the future with the objective of minimizing the recirculation regions where particle deposition is likely to occur, while maintaining a sufficiently large pressure loss.

This optimization will have to take into account the balance between the emitter improvements for clogging and a good hydraulic performance at the same time. Thus, in order to design a good performance emitter, x exponent must be close to 0.5. This requires to have an uniform flow in all the labyrinth-channel units. Increasing the number of labyrinth-channel patterns can make the flow more uniform. However, the conditions of the outlet flow are not influenced by the number of labyrinth channels. This increasing of labyrinth-channel has no effect on the emitter clogging since the emitter is mostly vulnerable to clogging in the first baffle where the turbulence quantities are weak. This is likely to favor small clay particles to deposit, in particular, in the swirl region. These particles are suspended in water and passing through the micro-irrigation emitter. When clogging occurs at the end of labyrinth-channel, it is certainly caused by intermittent irrigation, more than particles /flow interaction.

The experimental and numerical results provide a lot of interesting elements and ideas to understand and improve the emitter performance. In order to enrich this understanding, PTV experiments can be performed with the labyrinth-channel prototype to track particles. Such experimentation could be achieved with inert particles to study fluid-particle interaction (coupling micro-PIV and PTV experiments) and then with real particles to analyze agglomeration and deposit mechanisms. The Eulerian and Lagrangian tracking model could be tested to investigate the influence of injecting particles on the flow and particles deposition varying the concentration and particle size. Also of interest, is to simulate how deposit modifies labyrinth-channel geometry and thus how it impacts the flow.

Part V

Présentation en français

Table of Contents

Résumé **163**

1 Introduction générale, matériels et méthodes **165**
1.1 Introduction 165
1.2 Méthodologie expérimentale 166
1.2.1 Outils expérimentaux 168
1.2.2 Paramètres expérimentaux 168
1.2.3 Le traitement des données 170
1.3 Approche numérique 171
1.3.1 Modèles $k - \epsilon$ 171
1.3.2 Le modèle RSM 172
1.3.3 Les lois de paroi 173
1.4 La résolution numérique 174

2 Résultats et conclusion générale **177**
2.1 Pertes de charge dans le labyrinthe 177
2.2 Caractérisation de l'écoulement dans le labyrinthe 179
2.2.1 La section d'entrée 179
2.2.2 Le labyrinthe 180
2.3 Le développement axial de l'écoulement 183
2.4 L'évolution verticale de l'écoulement 184
2.5 Méthodes avancées de détection de vorticité 185
2.6 Conclusion générale et perspectives 188

Résumé

Dans le contexte actuel de raréfaction de l'eau, une meilleure efficacité de l'utilisation de l'eau est essentielle pour maintenir une croissance économique durable. De plus, l'utilisation efficiente de l'eau couvre également des questions environnementales et sociales importantes. La micro-irrigation offre la meilleure efficience, cependant, son utilisation n'est pas très répandue. Dans le monde, ce système ne couvre que 3% des terres irriguées et 4% en France, du fait que ce système est très sensible au colmatage, ce qui augmente le coût de son installation et de sa maintenance.
Ce colmatage est fortement lié aux faibles sections de passage du distributeur de micro-irrigation. En effet, un labyrinthe constitué de chicanes est généralement inséré dans les distributeurs. Les chicanes existantes, qui jouent un rôle important pour générer des pertes de pression et assurent la régulation du débit sur le réseau d'irrigation, produisent des zones de recirculation où la vitesse est faible voire nulle. Ces zones de recirculation favorisent le dépôt de particules ou autre développement biochimique provoquant le colmatage du goutteur. La caractérisation de la topologie de l'écoulement dans le labyrinthe du goutteur doit être décrite pour analyser la sensibilité du goutteur au colmatage qui réduit considérablement ses performances.

Des expériences utilisant la micro-PIV et un ensemencement avec des particules de $1\mu m$ sont menées sur dix motifs répétitifs pour analyser les régions qui peuvent être sensibles au colmatage. Un goutteur fonctionne avec un débit faible, et la section transversale du labyrinthe est d'environ $1\ mm^2$. Le nombre de Reynolds varie de 400 à 800. Ainsi, cette étude expérimentale permet d'analyser le régime d'écoulement et son influence. Un algorithme de traitement est développé pour obtenir la moyenne et les fluctuations des vitesses. Puis, des méthodes avancées d'analyses tourbillonnaires ont été utilisées pour détecter précisément la vorticité et les zones de recirculations. Une attention particulière est accordée à la validation de la technique micro-PIV et aux courbes débit-pression qui quantifient la performance globale du goutteur.

Plusieurs modèles de turbulence, implémentés dans ANSYS/Fluent, sont utilisés pour modéliser l'écoulement au sein du labyrinthe. Les résultats des expériences de micro-PIV et des modélisations sont comparés afin de valider le modèle numérique. Puis, des méthodes avancées d'analyses tourbillonnaires ont été utilisées pour détecter précisément la vorticité et les zones de recirculations. L'objectif global de ce manuscrit est d'identifier le meilleur modèle qui permettra ensuite de prédire et analyser les zones sensibles au colmatage afin de les réduire grâce à l'optimisation de géométrie.

Chapter 1

Introduction générale, matériels et méthodes

1.1 Introduction

La micro-irrigation est un système d'irrigation sous pression qui distribue de l'eau par des goutteurs à proximité des racines des plantes. Malgré les nombreux avantages de ce système; tels que les faibles efforts humains, moins d'eau et d'énergie par rapport à l'irrigation par aspersion, son pourcentage d'utilisation est faible en comparaison avec les autres systèmes (irrigations par aspersion et gravitaire). Dans cette technique, les goutteurs sont les éléments les plus importants et les plus critiques. Cette technique est basée sur l'utilisation de tuyaux d'un diamètre de l'ordre d'un centimètre sur les quels sont insérés des goutteurs, souvent constitués d'un labyrinthe d'une section de $1\ mm^2$ qui comprend des chicanes, de sorte qu'ils peuvent facilement être bouchés par le développement biochimique ou par des particules qui ne sont pas capturées par les systèmes de filtrage. Par conséquent, l'uniformité de l'irrigation est perturbée et les coûts d'installation sont augmentés. Ainsi, le principal inconvénient de cette technique est le colmatage qui réduit considérablement la durée de vie du goutteur et constitue un obstacle à son développement. Ce colmatage est lié aux conditions hydrodynamiques de l'écoulement (Li et al., 2008[70]; Wei et al., 2006[101]; Wei et al., 2012[102]; Jun et al., 2007[110]). Ainsi, la caractérisation de l'écoulement est très importante pour l'amélioration des performances du goutteur. Les chicanes qui jouent un rôle important pour générer des pertes de pression (Ozekici and Sneed, 1995)[80] et assurer la régulation du débit sur le réseau d'irrigation, produisent des tourbillons à faible vitesse. Ces tourbillons favorisent le dépôt de particules ou le développement biochimique provoquant le colmatage du goutteur (Ozekici and Sneed, 1995)[80]. Lors de la conception des goutteurs, l'obstruction peut être évitée ou au moins fortement réduite en diminuant autant que possible la taille des zones tourbillonnaires. L'analyse de l'écoulement permet d'identifier et d'éviter autant que possible les zones vulnérables au colmatage. L'objectif global de cette étude est de comprendre et d'analyser l'écoulement dans le labyrinthe. Cette étape est essentielle pour optimiser la géométrie du labyrinthe afin d'améliorer la géométrie des goutteurs ce qui permettra d'avoir un goutteur anti-colmatage.

La micro-irrigation se caractérise par de faibles apports d'eau. Elle fonctionne avec un débit entre $0,5$ et $8\ l/h$ pour une pression comprise entre 0,5 et 4 bars. Le goutteur peut être autorégulant ou non autorégulant (figureV.1.1). Les goutteurs non autorégulants offrent une plus grande durabilité et longévité ainsi qu'une meilleure résistance au colmatage et une faible maintenance grâce à l'absence de pièces en mouvement. Les goutteurs GR[1] sont équipés d'un système de contrôle appelé canal de labyrinthe (ou labyrinthe) dans lequel l'eau suit un chemin long et complexe qui conduit à la dissipation de la pression sous la forme des pertes de charge.

[1]Ceci est le nom industriel, pas un acronyme

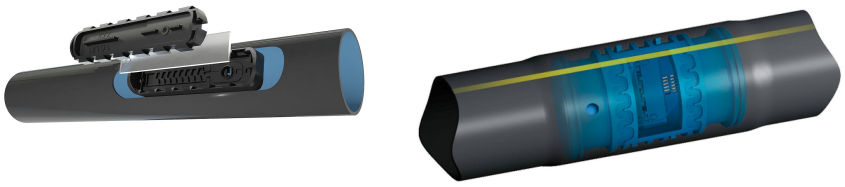

(a) (b)

Figure V.1.1: Illustration de goutteurs autorégulant (a) et non autorégulant (b).

L'augmentation de débit du goutteur avec la pression statique dans le tuyau latéral suit une relation du type (Karmeli, 1977)[54]:

$$q = k_d \Delta P^x \tag{V.1.1}$$

où q est le débit du goutteur, k_d est une constante de proportionnalité qui caractérise chaque goutteur, ΔP est la pression et x est l'exposant de la courbe débit-pression. La valeur de cet exposant dépend de la conception du goutteur. En effet, les fabricants tentent de créer des goutteurs dont le débit ne dépend pas directement de la pression ($x < 0,5$). Pour atteindre cet objectif, ils introduisent certains éléments au goutteur, comme un labyrinthe qui génère des pertes de charge. Le problème est que ce labyrinthe est très sensible aux phénomènes de colmatage qui est influencé par l'hydrodynamique.

Il semble que ce colmatage est fortement lié aux caractéristiques de l'écoulement. La caractérisation des écoulements au sein du labyrinthe a été réalisée expérimentalement et numériquement. Des mesures par micro-vélocimétrie par images de particules (micro-PIV) ont été réalisées afin de caractériser la structure de l'écoulement. Il apparaît que la micro-PIV dans un labyrinthe du goutteur de micro-irrigation est rarement utilisée (Jun et al., 2007)[110]. Dans cette thèse, les expériences sont effectuées sur un motif de dix chicanes répétitif fabriqué en plexiglas à l'échelle réelle avec une section de $1mm^2$. Cette méthode permet de mesurer des champs de vitesse instantanée et de déterminer jusqu'aux moments d'ordre deux des fluctuations de vitesse tout le long du canal en labyrinthe. Différents modèles de turbulence ont été utilisés pour modéliser l'écoulement à des nombres de Reynolds comprise entre 400 et 800 (Al-Muhammad et al., 2016) [10]. Comme il a été classiquement observé par Al-Muhammad et al. (2016) [10], il semble qu'il y a deux régions différentes; l'une est l'écoulement principal et l'autre est constituée de zones de recirculation qui sont caractérisées par une faible vitesse. Néanmoins, ces deux régions peuvent varier d'un modèle de turbulence à l'autre. Trois chicanes sont nécessaires pour stabiliser l'écoulement. De plus, la dissipation turbulente joue un rôle majeur dans les pertes de charge, contrairement à l'écoulement de canal classique où les contraintes de cisaillement de paroi gouvernent les pertes de charge (Al-Muhammad et al., 2016)[10]. L'objectif principal de ce travail est de caractériser cet écoulement et de l'analyser afin de vérifier les hypothèses d'écoulement turbulent utilisées dans la modélisation numérique.

1.2 Méthodologie expérimentale

Des expériences par micro-PIV ont été réalisées pour étudier l'écoulement dans le labyrinthe. Dix chicanes ont été utilisées. Le matériau est du PMMA transparent. L'étanchéité est assurée en serrant sur les deux plaques de PMMA deux plaques d'acier d'une épaisseur de 5 mm. La géométrie du labyrinthe et le support des prototypes sont présentés sur la figure V.1.2. Une géométrie détaillée en 2D, avec toutes les dimensions, du labyrinthe utilisé pour les expériences de micro-PIV est représentée sur la figure V.1.3. Toutes les dimensions sont détaillées dans le tableau V.1.1. Du fait des tolérances de fabrication, les deux prototypes n'ont pas rigoureusement les mêmes dimensions. Les écarts rendent d'autant plus nécessaire la normalisation des quantités analysées.

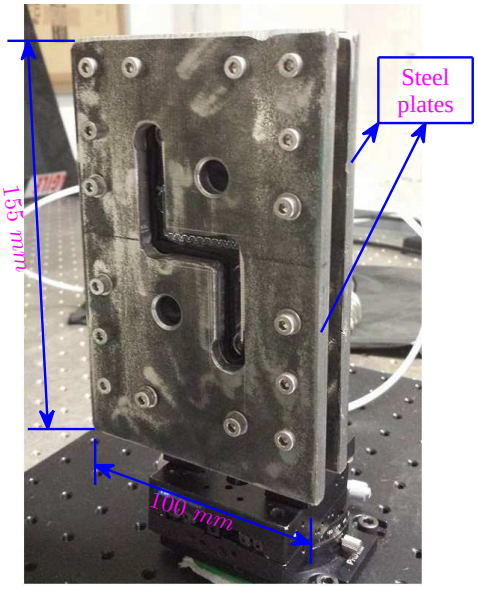

Figure V.1.2: Le prototype expérimental

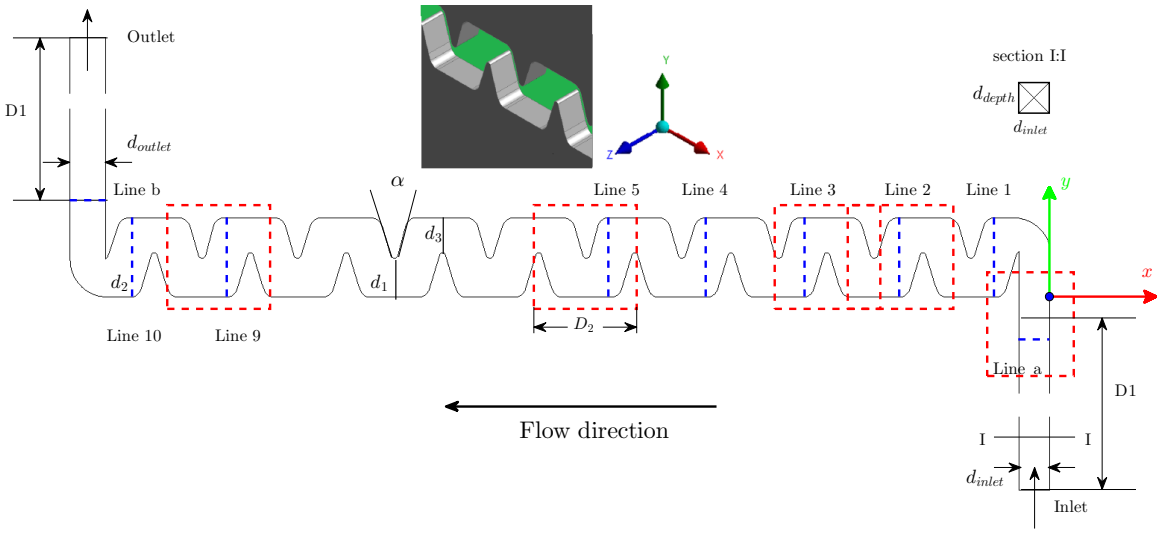

Figure V.1.3: Le labyrinthe

Table V.1.1: Les dimensions du labyrinthe.

		Géometrie 1 (pour $5\mu m$)	Géometrie 2 (pour $1\mu m$)	Modélisation	
La largeur de l'entrée	d_{inlet}	1.07	1.20	1.00	mm
La largeur de la sortie	d_{outlet}	1.25	1.40	1.20	mm
La profondeur du labyrinthe	d_{depth}	0.80	1.15	1.00	mm
	d_1	1.34	1.34	1.31	mm
	d_2	2.72	2.80	2.67	mm
	d_3	1.20	1.20	1.17	mm
	D_1	10.00	10.00	4.00	mm
La longueur du labyrinthe	D_2		3.24		mm
L'angle du labyrinthe	α		33		o

1.2.1 Outils expérimentaux

Le système hydraulique qui fait circuler le fluide avec des particules d'ensemencement, est composé de différents éléments; un filtre, une pompe, un débitmètre, des capteurs de pression relative. Le dispositif expérimental est représenté sur les figure V.1.4 et la figure V.1.5. Le débit est réglé par la pompe. Juste avant la pompe, il y a un filtre pour donner une meilleure filtration, spécialement lors de l'ensemencement. Ensuite, deux amortisseurs, un amortisseur fait main (qui est constitué par un tuyau qui contient de l'air) et un amortisseur commercial (type: PML 9962-FPD10, avec une efficacité maximale de 97%), absorbent les pulsations d'écoulement, avant de passer par un débitmètre (Mc Millan, précision de $\pm 3ml/min$) et le prototype du labyrinthe. La pression à l'entrée ainsi que la perte de pression sont mesurées par deux capteurs de haute précision ($PR - 33x/80794$ et $PD - 33x/80920$, la précision est de 0.01%).

Pour ensemencer l'écoulement, des particules fluorescentes sont ajoutées à l'eau. Elles sont faites de polystyrène avec de la fluorescéine. Deux diamètres sont utilisés, $5\ \mu m$ et $1\mu m$.

Le système optique est constitué par une source laser qui est un Litron laser Nd-YAG de $135\ mJ$, doublé en fréquence ($532nm$). Une caméra HiSence 4M avec la résolution de 2048×2048 pixels équipée d'un objectif Canon MP-E 65mm f/2,8, est montée pour étudier l'écoulement à l'intérieur du labyrinthe. Dans cette configuration, le champ de vision est $3 \times 3mm$. Pour caractériser l'écoulement avec des particules d'un diamètre de $1\mu m$, des tubes d'extension sont installés entre le boîtier de la caméra et l'objectif. Cela produit un champ de vision de $2,2 \times 2,2mm$.

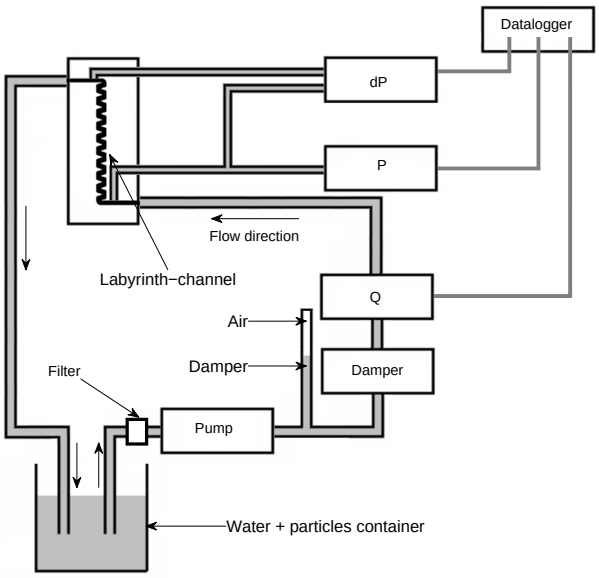

Figure V.1.4: Le schéma hydraulique

1.2.2 Paramètres expérimentaux

1.2.2.1 L'intervalle entre les impulsions laser

L'intervalle entre les impulsions d'illumination laser est un facteur important pour la réussite de l'acquisition et du traitement par micro-PIV. Donc, beaucoup d'attention doit être apportée pour déterminer cet intervalle. En général, le temps est défini à partir de la vitesse d'écoulement:

$$\Delta t = \frac{\Delta x}{U} \quad , \tag{V.1.2}$$

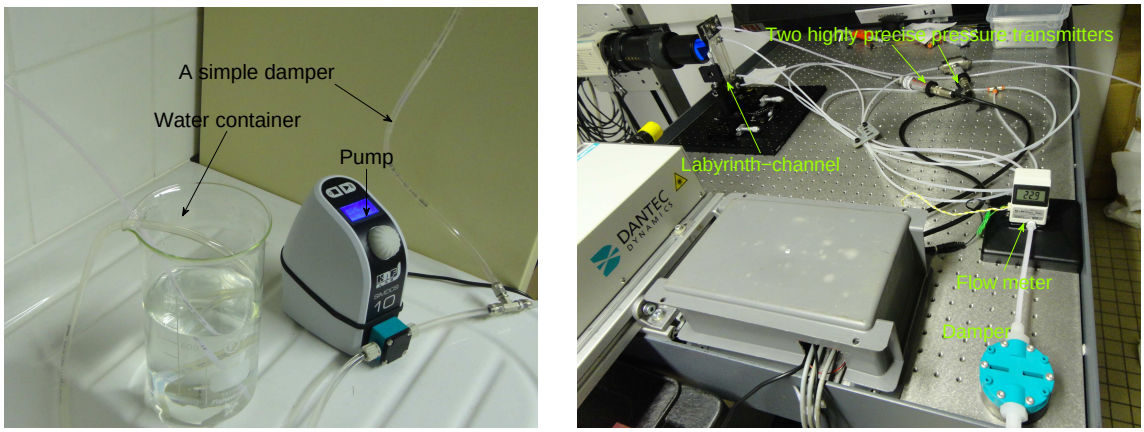

Figure V.1.5: Le montage expérimental

où $\Delta x =$ Taille de la fenêtre$/4$ est le déplacement typique d'une particule $[m]$,
U est la vitesse de l'écoulement $[m.s^{-1}]$.

Il doit être suffisamment long pour permettre de déterminer les déplacements entre deux images successives des particules et assez court pour éviter que des particules d'ensemencement ne quittent la fenêtre d'acquisition.

La difficulté de la détermination des intervalles entre deux impulsions laser vient du fait que l'écoulement, dans le canal-labyrinthe, est complexe. Selon Al-Muhammad et al. (2016) [10], il se compose de deux régions différentes: l'un est l'écoulement principal et l'autre est la zone de recirculation. Le profil du module de la vitesse est tracé sur une ligne arbitraire (la ligne 3 présentée sur la figure V.1.3) sur la figure V.1.6. Ce profil correspond aux résultats de la modélisation obtenus par le modèle RSM pour un nombre de Reynolds $Re = 800$ (voir la partie II de la version anglaise). Nous avons choisi deux vitesses correspondant aux valeurs extrêmes pour estimer Δt. Ensuite, Δt est calculé à partir de l'équation V.1.2 pour qu'une particule se déplace d'un quart de la fenêtre d'interrogation (tableau V.1.2 et tableau V.1.3).

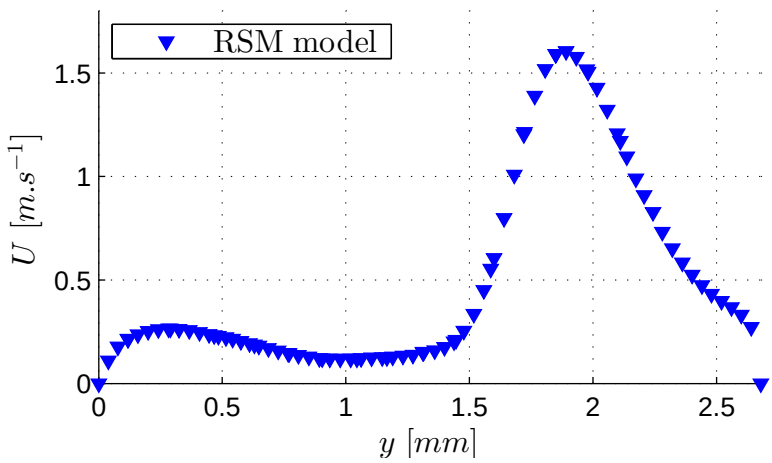

Figure V.1.6: Le profil du module de vitesse pour $Re = 800$ le long de la ligne 3 (voir la position des lignes sur la figure V.1.3)

Les expériences sont réalisées avec deux diamètres de particules, qui seront traités différemment (taille de la fenêtre d'interrogation).

Table V.1.2: Configuration pour l'acquisition

L'agrandissement d'acquisition	Les champs de vue $(mm \times mm)$	Le diamètre des particules (μm)	La fenêtres d'interrogation $(pixels)$	Le quart d'une fenêtre (μm)
$\times 5$	3×3	5	64×64	$\Delta x_1 = 23.28$
$\times 7.7$	2.2×2.2	1	32×32	$\Delta x_2 = 8.59$

Table V.1.3: Intervalle entre les impulsions laser.

Le débit $q\ (ml.min^{-1})$	Re	La vitesse $U\ (m.s^{-1})$	Le quart d'une fenêtre $\Delta x_1\ (\mu m)$	Le quart d'une fenêtrer $\Delta x_2\ (\mu m)$	Le temps $\Delta t_1\ (\mu s)$	Le temps $\Delta t_2\ (\mu s)$
48	800	1.6	23.28	8.59	15	6
		0.264			88	33
36	600	1.168	23.28	8.59	20	8
		0.17			137	51
24	400	0.76	23.28	8.59	30	12
		0.093			250	93

Le taux de dissipation ϵ obtenu avec la modélisation par le modèle $k - \epsilon$ standard pour les débits 24 et 48 $ml.min^{-1}$ est de 60 et 500 $[m^2.s^{-3}]$ respectivement. Les nombres de Stokes pour ces deux diamètres de particules sont $0,015$ (6×10^{-4}) pour $Re = 800$ et $0,005$ (2×10^{-4}) pour $Re = 400$ pour $d_p = 5\mu m$ et $d_p = 1\mu m$, respectivement. Les valeurs du nombre de Stokes sont donc très petites, de sorte que τ_p, défini comme $\tau_p = d_p^2 \frac{\rho_p}{18\mu}$, est en effet, comme prévu, beaucoup plus petite que τ_k défini comme $\tau_k = (\nu/\epsilon)^{1/2}$. Afin d'avoir une concentration de particules suffisante pour effectuer les expériences de micro-PIV, les particules d'ensemencement sont ajoutées à l'eau jusqu'à ce qu'il y ait quatre particules par fenêtre d'interrogation, qui a la dimension de 64×64 pixels pour $d_p = 5\ \mu m$ (32×32 pixels pour $d_p = 1\ \mu$ m). Cette concentration est obtenue en mélangeant $1\ ml$ de solution brute chargée en particules avec $150ml$ d'eau pure.

1.2.3 Le traitement des données

Les expériences de micro-PIV permettent de déterminer les champs de vitesses dans la région étudiée de l'écoulement. Chaque champ de vitesses contient une grille de vitesses u et v. A partir de ces champs de vitesses instantanées, le module de vitesse $|u|$, les fluctuations de vitesse autour de la moyenne (u' et v') sont dérivées et calculées.

$$|u| = \left(u^2 + v^2\right)^{1/2} \quad .$$

Cette formule peut être appliquée pour la vitesse moyenne $(\overline{u})$ au lieu de la vitesse instantanée (u) pour trouver $|\overline{u}|$, et les fluctuations de vitesses:

$$u' = u - \overline{u},$$

et

$$v' = v - \overline{v}.$$

Plusieurs quantités statistiques sont calculées à partir des ensembles de champs de vitesses instantanés contenant les composantes moyennes de vitesse selon les axes x et y ($\overline{u}$ et $\overline{v}$), les moments de l'ordre deux de la vitesse fluctuante ($\overline{u'^2}$, $\overline{v'^2}$ et $\overline{u'v'}$) et le module de la vitesse $|\overline{u}|$. Les quantités

statistiques servent à calculer les résidus de convergence. Bien que les quantités statistiques finales qui servent à tracer et calculer les champs de vitesse et des vecteurs sont calculées à partir de:

$$\overline{u_j(x,y)} = \frac{1}{\mathcal{N}_v}\sum_{k=1}^{\mathcal{N}_v} u_{jk}(x,y)$$

j=1,2

$$\overline{|u(x,y)|} = \frac{1}{\mathcal{N}_v}\sum_{k=1}^{\mathcal{N}_v} |u_k(x,y)|$$

où k est le numéro de l'image acquise et $\mathcal{N}_v$ est le nombre total des images. Les moments d'ordre deux des fluctuations de vitesse sont définis comme:

$$\overline{u_i'v_j'(x,y)} = \frac{1}{\mathcal{N}_v}\sum_{k=1}^{\mathcal{N}_v}\Big(u_{ik}(x,y) - \overline{u_i(x,y)}\Big) \times \Big(u_{jk}(x,y) - \overline{u_j(x,y)}\Big)$$

i et j=1,2.

Le nombre de paires d'images est choisi pour assurer les critères de convergence vers le module de la vitesse moyenne et de ses composantes u et v ainsi que pour les trois moments du second ordre de la vitesse fluctuante. Dans ces expériences, nous analysons 250 séries d'images pour 5 μm et 500 séries d'images pour $1\mu m$. Le nombre de paires d'images devrait être suffisant pour assurer la convergence des données. Sa détermination permet de réduire le temps d'enregistrement et d'éviter une trop grande quantité de données pendant la phase de traitement.

Des études de convergence ont été réalisées sur les données micro-PIV afin de vérifier si le nombre d'image est suffisant. Cette étude montre que ces nombres sont suffisants pour analyser avec une haute précision les champs de vitesse et les moments du second ordre de la vitesse fluctuante à l'intérieur des chicanes ainsi qu'à la section de sortie alors qu'à l'entrée ces nombres de paires d'image ne sont pas suffisants pour donner de bons résultats (voir la partie II.2.5.3 de la version anglaise pour plus de détails).

1.3 Approche numérique

1.3.1 Modèles $k-\epsilon$

Il apparaît que les modèles de turbulence classiques ne peuvent pas bien reproduire les caractéristiques d'un tel débit à un faible nombre de Reynolds. Donc, des modèles $k-\epsilon$ à faible nombre de Reynolds sont aussi introduits afin de modéliser l'écoulement dans le labyrinthe. Il y a environ une centaine de modèles $k-\epsilon$ à faible nombre de Reynolds. Les modèles à faible nombre de Reynolds utilisés ici sont les suivants: [Abid] (Abid) (1991), [LS] (Launder et Sharma 1974), ([CHC] (Chang, Hsieh et Chen 1995). Ces modèles sont comparés aux modèles $k-\epsilon$ standard et RNG. Les équations modélisées de l'énergie cinétique turbulente k et du taux de dissipation ϵ, pour les modèles $k-\epsilon$, sont:

$$\underbrace{\rho u_j \frac{\partial k}{\partial x_j}}_{\text{advection}_k} = \underbrace{\frac{\partial}{\partial x_j}\left[\left(\mu + \frac{\mu_t}{\sigma_k}\right)\frac{\partial k}{\partial x_j}\right]}_{\text{diffusion}_k} + \underbrace{G_k}_{\text{production}_k} - \underbrace{\rho\epsilon}_{\text{destruction}_k} - \underbrace{D}_{\text{terme source}_k} \quad ; \tag{V.1.3}$$

$$\underbrace{\rho u_j \frac{\partial \epsilon}{\partial x_j}}_{\text{advection}_\epsilon} = \underbrace{\frac{\partial}{\partial x_j}\left[\left(\mu + \frac{\mu_t}{\sigma_\epsilon}\right)\frac{\partial \epsilon}{\partial x_j}\right]}_{\text{diffusion}_\epsilon} + \underbrace{C_{1\epsilon} f_1 \frac{\epsilon}{k} G_k}_{\text{production}_\epsilon} - \underbrace{C_{2\epsilon} f_2 \rho \frac{\epsilon^2}{k}}_{\text{destruction}_\epsilon} + \underbrace{E}_{\text{terme source}_\epsilon} \quad . \tag{V.1.4}$$

G_k représente la production de l'énergie cinétique turbulente due aux gradients de vitesse moyenne:

$$G_k = -\rho\overline{\acute{u}_i\acute{u}_j}\frac{\partial u_j}{\partial x_i} = \mu_t S^2 \quad ; \tag{V.1.5}$$

où S est le module du tenseur de vitesse de déformation moyenne, défini comme $S = \sqrt{2S_{ij}S_{ij}}$. La viscosité turbulente peut être écrite comme un terme général multiplié par une fonction d'amortissement f_μ:

$$\mu_t = \rho f_\mu C_\mu \frac{k^2}{\epsilon} \quad . \tag{V.1.6}$$

Les fonctions d'amortissement f_μ, f_1 et f_2 pour les modèles de $k-\epsilon$ standard et RNG sont égales à 1. Les fonctions d'amortissement f_μ, f_1 et f_2 varient d'un modèle à l'autre. La fonction d'amortissement et le terme source pour $k-\epsilon$ standard et RNG et les modèles à faible nombre de Reynolds sont détaillés dans le document de Launder and Spalding (1972)[66], Yakhot and Orszag (1986)[109] et Karvinen et al. (2005)[55] respectivement (voir Al-Muhammad et al. (2016) [10] pour plus de détails).

1.3.2 Le modèle RSM

Les équations de Navier-Stokes-Reynolds moyennées (RANS) sont fermées en résolvant les équations de transport pour les tensions de Reynolds R_{ij}, avec une équation pour le taux de dissipation ϵ. Le mouvement du fluide est alors décrit par l'équation de continuité, l'équation de quantité de mouvement, les équations de transport exactes du tenseur de contraintes de Reynolds $\rho\overline{u_i'u_j'}$, l'équation de l'énergie cinétique turbulente k et de la dissipation turbulente ϵ. Pour un écoulement incompressible sans tenir compte de la flottabilité et la gravité, l'équation de R_{ij} peut être écrite comme suit:

$$\underbrace{C_{ij}}_{\text{Convection}} = \underbrace{D_{T,ij}}_{\text{Diffusion turbulente}} + \underbrace{D_{L,ij}}_{\text{Diffusion moléculaire}} + \underbrace{P_{ij}}_{\text{Production}} + \underbrace{\phi_{ij}}_{\text{Contrainte de pression}} - \underbrace{\epsilon_{ij}}_{\text{Dissipation}} \tag{V.1.7}$$

Les termes qui ne demandent aucune modélisation sont:

$$C_{ij} = \frac{\partial}{\partial x_k}\left(\rho u_k \overline{u_i'u_j'}\right) \quad ; \tag{V.1.8}$$

$$D_{L,ij} = \frac{\partial}{\partial x_k}\left(\mu \frac{\partial \overline{u_i'u_j'}}{\partial x_k}\right) \quad ; \tag{V.1.9}$$

$$P_{ij} = -\rho\left(\overline{u_i'u_k'}\frac{\partial u_j}{\partial x_k} + \overline{u_j'u_k'}\frac{\partial u_i}{\partial x_k}\right) \quad . \tag{V.1.10}$$

Les autres termes ont les définitions suivantes:

$$D_{T,ij} = -\frac{\partial}{\partial x_k}\left[\rho\overline{u_i'u_j'u_k'} + \overline{p'\left(\delta_{kj}u_i' + \delta_{ik}u_j'\right)}\right] \quad , \tag{V.1.11}$$

$$\phi_{ij} = \overline{p'\left(\frac{\partial u_i'}{\partial x_j} + \frac{\partial u_j'}{\partial x_i}\right)} \quad , \tag{V.1.12}$$

$$\epsilon_{ij} = 2\mu\overline{\frac{\partial u_i'}{\partial x_k}\frac{\partial u_j'}{\partial x_k}} \quad . \tag{V.1.13}$$

Ainsi, $D_{T,ij}$, ϕ_{ij} et ϵ_{ij} doivent être modélisés pour fermer les équations. Le terme de diffusion $D_{T,ij}$ est généralement modélisé en utilisant le modèle de Daly et Harlow simplifié [33]:

$$D_{T,ij} = C_s\frac{\partial}{\partial x_k}\left(\rho\overline{u_k'u_\ell'}\frac{k}{\epsilon}\frac{\partial\overline{u_i'u_j'}}{\partial x_\ell}\right) \quad \text{terme général} \tag{V.1.14}$$

avec $C_s = 0.22$.

Cependant, des instabilités numériques peuvent résulter de cette équation, donc une autre simplification en utilisant une diffusivité turbulente scalaire est faite (Lien and Leschziner, 1994)[71]:

$$D_{T,ij} = \frac{\partial}{\partial x_k}\left(\frac{\mu_t}{\sigma_k}\frac{\partial\overline{u_i'u_j'}}{\partial x_k}\right) \quad \text{terme simplifié} \tag{V.1.15}$$

ϕ_{ij} est le terme de corrélation pression - déformation. Chou (1945) [29] a montré que ce terme pourrait être divisé en trois contributions; la première ne contient que des interactions de turbulence, la seconde est générée par des interactions entre la turbulence et le gradient de vitesse moyenne et la dernière rend compte uniquement de la présence des parois. Par application de la divergence sur les équations de vitesse fluctuante, on obtient l'équation de Poisson pour les fluctuations de pression:

$$\frac{\partial^2 p'}{\partial x_i \partial x_i} = \underbrace{-2\rho \frac{\partial \overline{u_i}}{\partial x_j}\frac{\partial u'_j}{\partial x_i}}_{\text{Rapide}} - \underbrace{\rho \frac{\partial u'_i}{\partial x_j}\frac{\partial u'_j}{\partial x_i}}_{\text{Lent}} + \underbrace{\rho \frac{\overline{\partial u'_i \partial u'_j}}{\partial x_j \partial x_i}}_{\text{Paroi}} \quad . \tag{V.1.16}$$

Le terme de pression-déformation, ϕ_{ij}, est modélisé sur la base des propositions de Gibson and Launder (1978) [40], Fu et al. (1987) [38] et Launder (1989) [63]. La modélisation est composée de plusieurs termes comme suit:

$$\phi_{ij} = \phi_{ij,1} + \phi_{ij,2} + \phi_{ij,w} \tag{V.1.17}$$

où $\phi_{ij,1}$ est le terme de pression-déformation lente, aussi appelé le retour à l'isotopie, tandis que $\phi_{ij,2}$ est appelé le terme de pression-déformation rapide, et $\phi_{ij,w}$ est le terme de réflexion de la paroi. Le terme de pression-déformation lente, $\phi_{ij,1}$, est modélisé comme suit:

$$\phi_{ij,1} = -C_1 \rho \frac{\epsilon}{k}\left(\overline{u'_i u'_j} - \frac{2}{3}k\delta_{ij}\right) \quad . \tag{V.1.18}$$

Le terme de pression-déformation rapide, $\phi_{ij,2}$, est modélisé suivant:

$$\phi_{ij,2} = -C_2\left(P_{ij} - \frac{2}{3}P_k\delta_{ij}\right) \tag{V.1.19}$$

où les constantes C_1 et C_2 sont 1.8 et 0.6 respectivement.
La viscosité turbulente, μ_t, est calculée de manière similaire aux modèles $k-\epsilon$ avec l'hypothèse habituelle:

$$\epsilon_{ij} = \frac{2}{3}\delta_{ij}\epsilon \tag{V.1.20}$$

Les valeurs de k et ϵ sont résolues par les équations modélisées suivantes:

$$\frac{\partial}{\partial x_i}(\rho k u_i) = \frac{\partial}{\partial x_j}\left[\left(\mu + \frac{\mu_t}{\sigma_k}\frac{\partial k}{\partial x_j}\right)\right] + \frac{1}{2}G_k - \rho\epsilon \quad , \tag{V.1.21}$$

$$\frac{\partial}{\partial x_i}(\rho \epsilon u_i) = \frac{\partial}{\partial x_j}\left[\left(\mu + \frac{\mu_t}{\sigma_\epsilon}\frac{\partial \epsilon}{\partial x_j}\right)\right] + \frac{1}{2}C_{\epsilon 1}G_k\frac{\epsilon}{k} - C_{\epsilon 2}\rho\frac{\epsilon^2}{k} \quad , \tag{V.1.22}$$

où $C_\mu = 0.09$, $\sigma_k = 0.82$, $\sigma_\epsilon = 1.00$, $C_{\epsilon 1} = 1.44$ et $C_{\epsilon 2} = 1.92$.

1.3.3 Les lois de paroi

Les écoulements turbulents sont affectés de façon significative par la présence de parois car les effets de la viscosité moléculaire deviennent de plus en plus prédominants par rapport à l'effet de la turbulence - qui disparait à la paroi- lorsque la paroi est approchée. Le champ de vitesse moyenne doit satisfaire à la condition de non-glissement à la paroi. Cependant, la turbulence est également modifiée par la présence de la paroi. Très proche de la paroi, l'amortissement visqueux réduit les fluctuations de vitesse tangentielle, alors que le blocage cinématique réduit les fluctuations normales. Vers la partie extérieure de la zone proche de la paroi, cependant, la turbulence est rapidement augmentée par la production d'énergie cinétique de la turbulence due aux forts gradients de vitesse moyenne. Cependant, le traitement de la région proche de la paroi peut être réalisé en utilisant les fonctions de paroi, uniquement dans la région de la paroi, ou en utilisant des fonctions d'amortissement modifiant les propriétés de la turbulence près de la paroi tandis que les propriétés de la turbulence dans l'écoulement de base restent

inchangées. Les régions de proche-paroi et les fonctions d'amortissement sont présentées dans cette section.

Les équation de μ_t, k et ϵ sont modifiées à l'aide de fonctions algébriques pour représenter la réalité physique. Afin de tenir compte des effets complexes en proche paroi, il faut adapter les équations standard en ajoutant les fonctions d'amortissement. En effet, les équations sont intégrées à la paroi sans supposer une loi universelle pour le profil de vitesse, ni une condition d'équilibre pour k et ϵ (voir Al-Muhammad et al. (2016) [10] pour plus de détails).

1.4 La résolution numérique

La géométrie est représentée sur la figure V.1.7. Un labyrinthe composé de trois chicanes a été choisi. Les sections d'entrée et de sortie sont décalées par rapport à la région étudiée, afin d'éviter des perturbations. Toutes les dimensions du labyrinthe sont détaillées dans le tableau V.1.1.

La qualité du maillage a été vérifiée ainsi que l'indépendance des résultats au maillage pour tous les modèles numériques en 2D et 3D. y^+ ($y^+ = u_\tau \rho y/\mu$ où u_τ est la vitesse du frottement à la paroi) est autour de 5 pour les modèles $k-\epsilon$ à haut nombre de Reynolds, S-A et RSM et de l'ordre de 1 pour les modèles $k-\epsilon$ à bas nombre de Reynolds (tableau V.1.4).

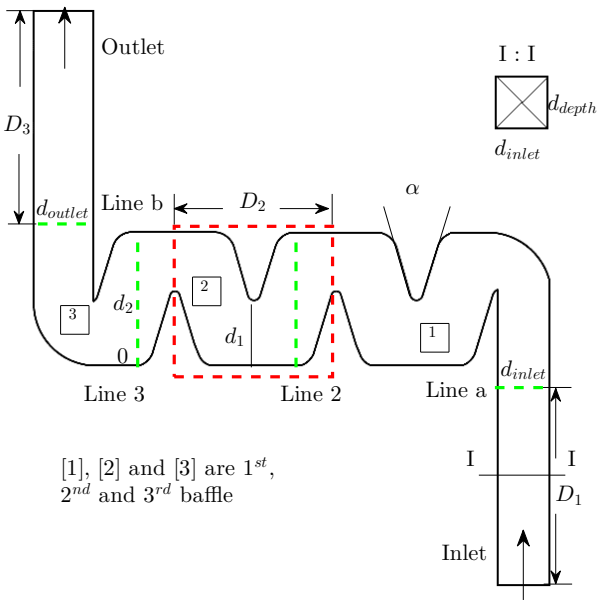

Figure V.1.7: Le labyrinthe utilisé pour la modélisation.

Table V.1.4: Caractéristiques des maillages.

Modèle	2D		3D	
	nombre de mailles	max de y^+	nombre de mailles	max de y^+
$k-\epsilon$ Standard, RSM	1.33×10^5	3.5- 4	5.3×10^5	7-8
$k-\epsilon$ à bas nombre de Reynolds, S-A	5.33×10^5	1.8- 2.5	5.3×10^5	8
$k-\epsilon$ LS	5.33×10^5	1.8- 2.5	1.2×10^6	8

Le débit $[kg.s^{-1}]$ [2] est imposé à l'entrée et à la sortie. Toutes les simulations sont effectuées avec un débit initial de 0.4 $[kg.s^{-1}]$ en 2D (0.0004 $[kg.s^{-1}]$ en 3D), puis on l'a augmenté régulièrement jusqu'à 0.8 $[kg.s^{-1}]$ en 2D (0.0008 $[kg.s^{-1}]$ en 3D); ce qui correspond à un nombre de Reynolds de 400 à 800.

Le diamètre hydraulique est de 2 mm et 1 mm en 2D et 3D respectivement, alors que l'intensité turbulente est supposée 5% à l'entrée.

[2] $[kg.s^{-1}]$ est l'unité de débit utilisé sous Fluent. Cette unité est convertie en $[l.h^{-1}]$ pour avoir la même unité utilisée pour l'acquisition expérimentale. Il est important de noter que:

- en 2D, 1 $[kg.s^{-1}]$ est équivalent à 3.6 $[l.h^{-1}]$
- en 3D, 1 $[kg.s^{-1}] = 3600$ $[l.h^{-1}]$

Chapter 2

Résultats et conclusion générale

2.1 Pertes de charge dans le labyrinthe

Les contours de pression statique sont représentés sur la figureV.2.1 en utilisant le modèle RSM en 3D. L'évolution de la pression statique le long des chicanes est présentée. L'influence du nombre de Reynolds sur cette pression est discutée. La pression diminue légèrement à l'entrée et à la sortie car la chute de pression est générée uniquement par le frottement sur la paroi (Pope, 2000) [85]. Elle est fortement diminuée le long des chicanes où les contributions de plusieurs types de pertes de charge interviennent. La pression atteint sa valeur minimale à la sortie, en aval de la dernière chicane,(la zone en couleur bleue foncée la figure V.2.1). Les résultats de la littérature sur un canal labyrinthe similaire donnent quantitativement les mêmes champs de pression Wei et al. (2006) [101].

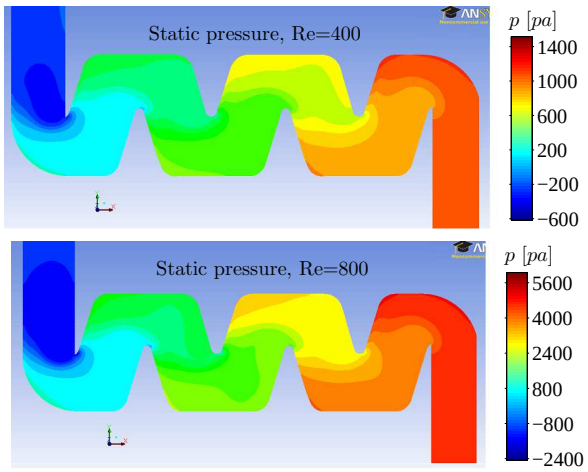

Figure V.2.1: Contour de pression statique en utilisant le modèle RSM en 3D

Le ratio des pertes de charge pour deux nombres de Reynolds ($Re = 400$ et $Re = 800$) est d'environ 4. Ce ratio est lié au carré du rapport des nombres de Reynolds ou plutôt au carré du rapport des vitesses débitantes à l'entrée. On peut conclure de cette comparaison que le nombre de Reynolds dans cette gamme de variation n'a aucun effet sur les pertes de pression.

Les courbes de débit-pression ($q = f(\Delta P)$), où ΔP représente la perte de charge entre l'entrée et la sortie, sont tracées pour chaque modèle de turbulence en 2D et quatre modèles en 3D. Elles sont comparées aux données expérimentales (figure V.2.2). Comme mentionné ci-dessus, dans la section I.1.2.3.2, à partir du papier de Karmeli (1977) [54], on peut noter que pour les goutteurs à long chemin, qui sont utilisés dans notre étude, l'exposant de la courbe débit-pression x, Eq.V.1.1, est compris entre 1 et 0.5. Ces valeurs sont respectivement celles pour un écoulement laminaire et pour un écoulement

turbulent pleinement développé. En 2D (figure 2.2(a).), les exposants des modèles standard, RNG et [LS] $k-\epsilon$, Spalart-Allmaras et RSM sont ceux du régime pleinement turbulent (pour lequel le coefficient de frottement C_f, qui est proportionnel à $\Delta P/q^2$, ne dépend plus du nombre de Reynolds Re). Ils sont proches, mais légèrement plus petits que, les exposants du modèle [LS] $k-\epsilon$ et des expériences $(0.57-0.59)$, de sorte que C_f diminue légèrement avec Re (voir White (2000)[105]). Les modèle $k-\epsilon$ à bas nombre de Reynolds [Abid], [AKN] et [CHC] ont un comportement plutôt laminaire puisque les exposants de ces modèles sont près de 1 et donc tels que C_f diminue fortement avec Re (voir tableau V.2.1). Il semble que, lorsque le débit augmente, tous les modèles $k-\epsilon$ prédisent presque la même perte de charge. Même s'il est assez difficile de commenter et d'analyser en détail les résultats présentés dans la figure 2.2(a) et la figure 2.2(b), une distinction claire peut être faite entre les deux types de régime d'écoulement, avec le modèle [LS] $k-\epsilon$ qui est le seul modèle qui peut simuler le régime turbulent pour lequel C_f diminue légèrement avec Re.

En trois dimensions, quatre modèles sont choisis: les modèles standard et [LS] $k-\epsilon$, S-A et RSM. On peut observer que les exposants de la courbe, en 3D, sont proches de 0.5. Ces résultats indiquent que l'écoulement est turbulent. L'exposant expérimental de cette courbe est 0.59 qui est proche des résultats numériques. Néanmoins, certaines différences dans la prédiction des pertes de charge peuvent être observées entre les valeurs expérimentales et numériques. On pourrait soupçonner que cela est dû à l'hypothèse 2D (figure 2.2(a)). Cependant, en regardant les résultats 3D, un plus grand écart est noté (figure 2.2(b)): les pertes de charge sont plus grandes que dans le cas 2D. La perte de charge est liée à la vitesse. Les profils et les champs de vitesse sont discutés dans le chapitre IV.2, et pour comprendre ces pertes, l'analyse des principaux facteurs de pertes de charge a été effectuée et présentée en détail dans la section IV.2.1.3 et la section IV.2.1.3 de la version anglaise.

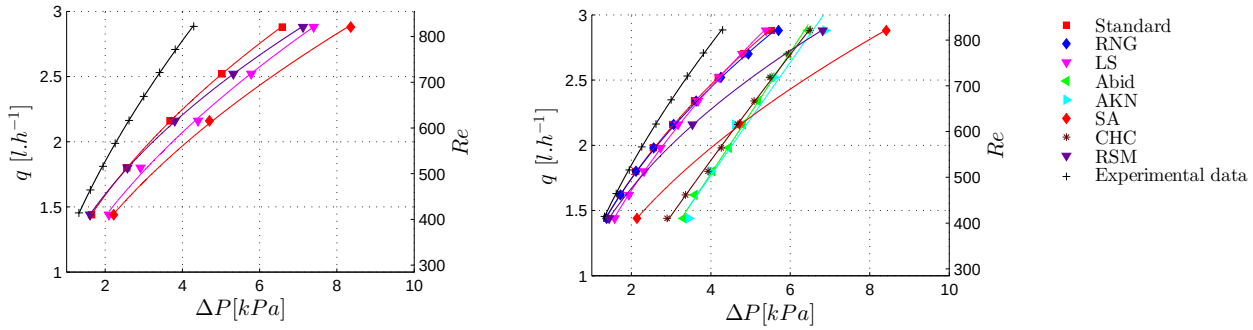

(a) 3D. (b) 2D.

Figure V.2.2: Les courbes de débit-pression en trois dimensions (3D) (a) et en deux dimensions (2D) (b).

Table V.2.1: Les valeurs de l'exposant x dans l'équation V.1.1 pour tous les modèles tracés dans la figure V.2.2.

	Modèle	Standard	RNG	Abid	LS	AKN	CHC	S-A	RSM	expérimentation
l'exposant x	2D	0.50	0.49	0.99	0.56	0.98	0.86	0.51	0.46	–
	3D	0.50	–	–	0.54	–	–	0.52	0.48	0.59

2.2 Caractérisation de l'écoulement dans le labyrinthe

2.2.1 La section d'entrée

Le prototype de labyrinthe est conçu en tenant compte du fait que l'écoulement doit être établi avant l'entrée dans le labyrinthe. Les champs de vitesse, à l'entrée, sont présentés pour deux nombres de Reynolds la figure V.2.3. Les champs de vitesses expérimentales, à l'entrée, sont tracés pour ces deux nombres de Reynolds la figure V.2.3[1]. Pour voir l'évolution de la vitesse le long de l'entrée du canal, les profils de vitesse, avant la première courbe de chicane, sont tracés le long du canal d'entrée (dans la direction y) afin de déterminer si l'écoulement évolue ou non. Ces profils sont présentés dans la figure V.2.4 pour $Re = 435$ et $Re = 863$ avec $d_p = 1\ \mu m$. Ils montrent que la vitesse est soumise à un petit changement quand l'écoulement approche de la courbure de la première chicane pour $Re = 863$. Cependant, les profils de vitesse ne se modifient pas le long d'une distance de $1.9D_h$. Par conséquent, le profil est considéré comme établi. La forme parabolique du profil de vitesse pour $Re = 435$ assure ce fait. Pour $Re = 863$, on peut remarquer que le profil de vitesse est aplati au milieu du canal. Les vitesses centrales (au centre du canal) U_c sont $1.03\ m.s^{-1}$, $1.39\ m.s^{-1}$ et $1.64\ m.s^{-1}$ pour $Re = 400$, $Re = 600$ et $Re = 800$ respectivement. Ensuite, le rapport de la vitesse centrale à la vitesse débitante, U_c/U_m est presque 2.16 pour $Re = 435$, 2 pour $Re = 642$; et 1.743 pour $Re = 863$ (figure V.2.5). Les ratios de U_c/U_m pour les modèles [LS] $k - \epsilon$ et RSM, sont d'environ $1.4 - 1.5$ lorsque le nombre de Reynolds est dans la gamme 400-800. Les modèles [LS] k- ϵ et RSM sont choisis pour effectuer ces analyses à l'entrée et à la sortie car (i) [LS] $k - \epsilon$ est le modèle le plus proche des expériences pour la valeur de l'exposant x, et (ii) Chaudhary et al. (2013) [26] ont démontré que le modèle RSM avec "Enhanced wall treatment" offre une grande précision grâce à la possibilité de capturer des turbulences anisotropiques et les flux secondaires, mais son coût de calcul est très élevé. Leurs calculs ont été effectués pour un faible nombre de Reynolds $Re = 4586$.

Dans un tube circulaire, la vitesse débitante pour un écoulement laminaire pleinement développé est la moitié de la vitesse sur la ligne centrale (maximum) (White, 2010)[105]. Il est clair que le rapport U_c/U_m diminue lorsque Re augmente pour les données expérimentales et numériques la figure V.2.6. Pour une position x/D_h donnée, les résultats expérimentaux obtenus dans cette étude sont plus proches des données de Targ dans un tube (Sparrow et al., 1964)[98], tandis que les résultats numériques sont plus proches du cas d'un canal plan (ce ratio ne dépasse pas 1.5).

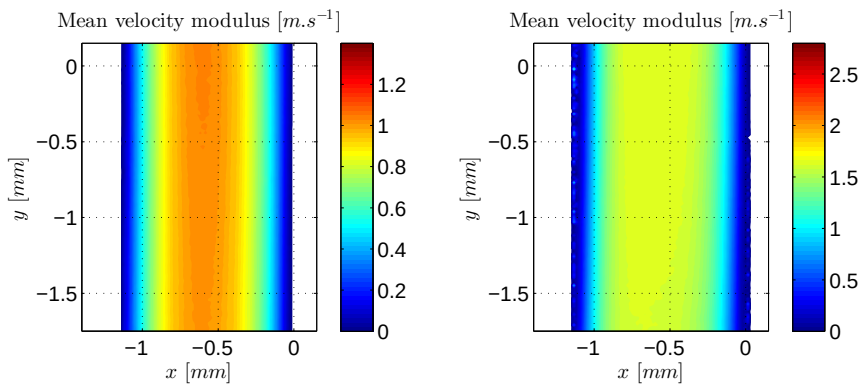

(a) $Re = 435$. (b) $Re = 863$.

Figure V.2.3: Les champs de vitesse à l'entrée, $d_p = 1\ \mu m$

[1]L'axe x, dans la figure, passe par le côté droit de la section d'entrée, tandis que l'axe y passe pour le côté inférieur du labyrinthe. L'origine du système de coordonnées est soulignée en bleu sur la figure V.1.3. Par conséquent, l'entrée est à $y = -35\ mm$ et $y = -4\ mm$ expérimentalement et numériquement, respectivement.

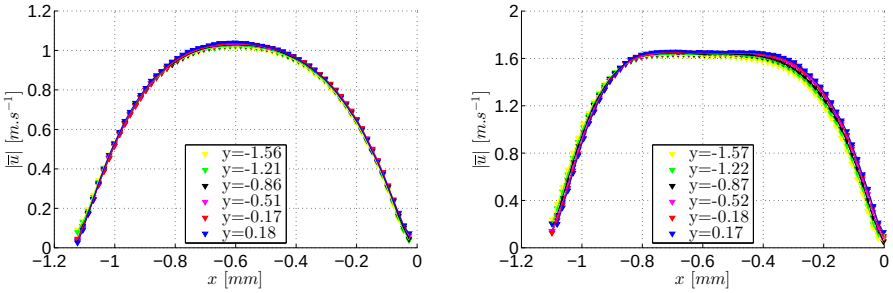

(a) $Re = 435$. (b) $Re = 863$.

Figure V.2.4: Les profils de vitesse pour plusieurs positions y à l'entrée, $d_p = 1\ \mu m$

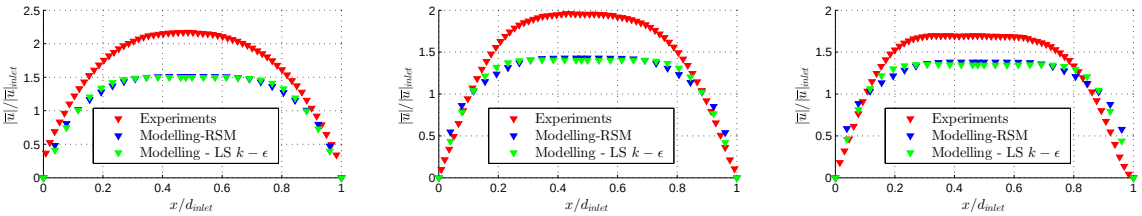

(a) $Re = 400$ (b) $Re = 600$ (c) $Re = 800$

Figure V.2.5: Les profils de vitesse normalisés sur la ligne a, $d_p = 1\mu m$, où la ligne a est à $y = 4\ D_h$ de l'entrée dans la modélisation numérique et à $y \simeq\ 38 D_h$ pour les expériences par micro-PIV.

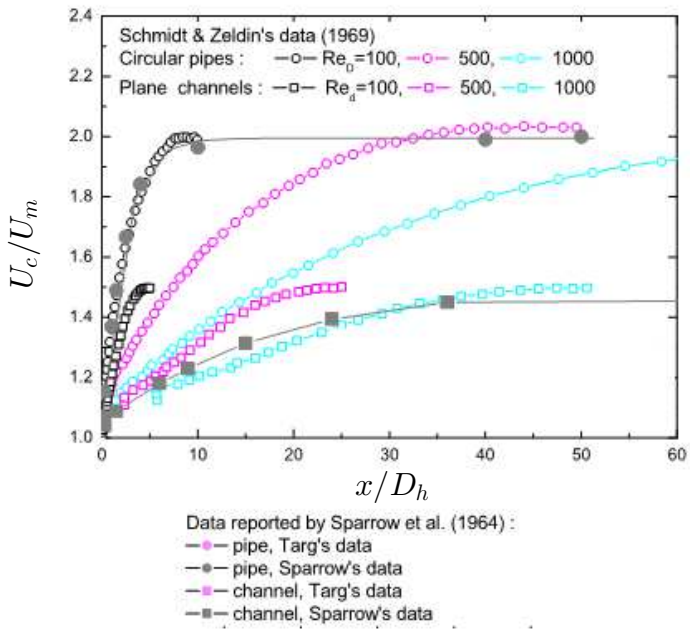

Figure V.2.6: Rapports U_c/U_m issue de l'étude de Sparrow et al. (1964)[98]

2.2.2 Le labyrinthe

Les champs de vitesse et les lignes de courant du module de la vitesse moyenne à l'intérieur des trois premières chicanes en utilisant des particules $d_p = 1\mu m$ sont représentés de la figure V.2.7 à la figure V.2.10. Derrière l'obstacle, nommé chicane dans ce manuscrit, l'écoulement est composé de deux

petits vortex pour la première chicane et d'un seul grand tourbillon dans la troisième chicane. Cette région est appelée une zone de recirculation (ellipse rouge), qui se caractérise par une très faible vitesse.

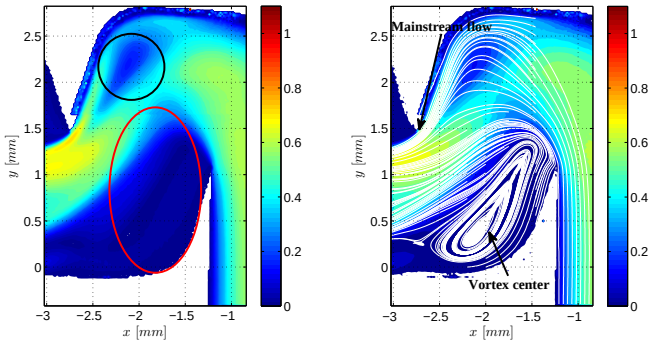

(a) Champ du module de vitesse moyenne

(b) Les lignes de courant

Figure V.2.7: Les champs de vitesse à l'intérieur de la première chicane, $Re = 346$, $d_p = 1\mu m$

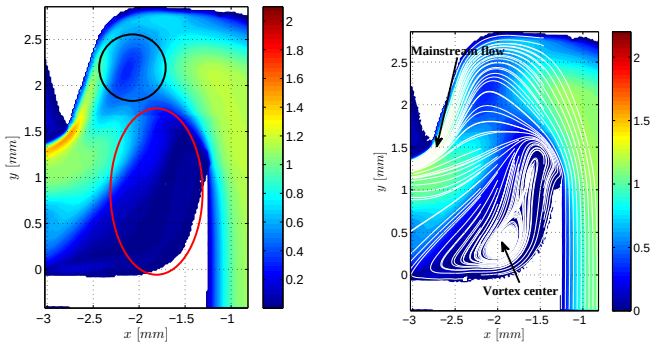

(a) Champ du module de vitesse moyenne

(b) Les lignes de courant

Figure V.2.8: Les champs de vitesse à l'intérieur de la première chicane, $Re = 687$, $d_p = 1\mu m$.

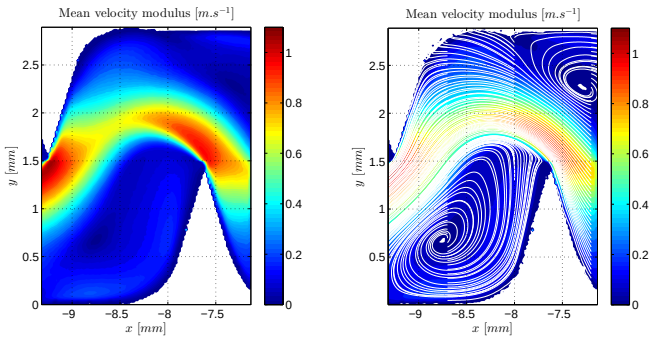

(a) Champ du module de vitesse moyenne

(b) Les lignes de courant

Figure V.2.9: Les champs de vitesse à l'intérieur de la troisième chicane, $Re = 346$, $d_p = 1\mu m$.

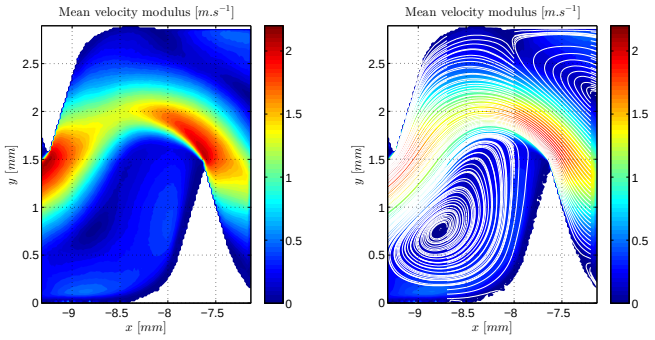

(a) Champ du module de vitesse moyenne

(b) Les lignes de courant

Figure V.2.10: Les champs de vitesse à l'intérieur de la troisième chicane, $Re = 687$, $d_p = 1\mu m$.

Le module de la vitesse moyenne varie de 0.05 à $0.2\ m.s^{-1}$ pour $Re = 346$ (respectivement 0.1 à $0.4\ m.s^{-1}$ pour $Re = 687$). L'écoulement principal est interrompu par une zone de stagnation (ellipse noire) dans la première chicane. La forme du vortex à l'intérieur de la troisième chicane ne change pas lorsque l'on augmente le débit. Le centre du tourbillon se déplace un peu vers le coté inférieur pour $Re = 346$. Le centre du tourbillon est à $x = -8.78\ mm$ et $y = 0.76\ mm$ pour $Re = 687$, puis à $x = -8.78mm$ et $y = 0.66\ mm$ pour $Re = 346$. Dans le milieu du labyrinthe, l'écoulement a une vitesse élevée qui atteint 1.1 et $2.2\ m.s^{-1}$ pour $Re = 346$ et $Re = 687$ respectivement à l'intérieur de la troisième chicane. La zone étroite à forte vitesse est appelée l'écoulement principal.

Modélisation en deux dimensions: Des simulations sont effectuées avec les modèles $k - \epsilon$ standard, [LS] et [CHC], S-A et RSM. Les champs de vitesses moyennes obtenus à partir des simulations pour les débits minimum et maximum, $Re = 400$ et 800, respectivement, sont reportés à la figure V.2.11. Ces champs de vitesses indiquent qu'il existe deux régions. L'une est l'écoulement principal caractérisé par de grandes valeurs de vitesse. L'autre est la zone de recirculation caractérisée par une valeur de vitesse faible et des valeurs de vitesse négatives. La même typologie d'écoulement est obtenue avec l'expérience de micro-PIV. Il peut également être observé (figure V.2.11) que la vitesse maximale est au coin de la chicane, où l'eau frappe la paroi dans les différentes chicanes.

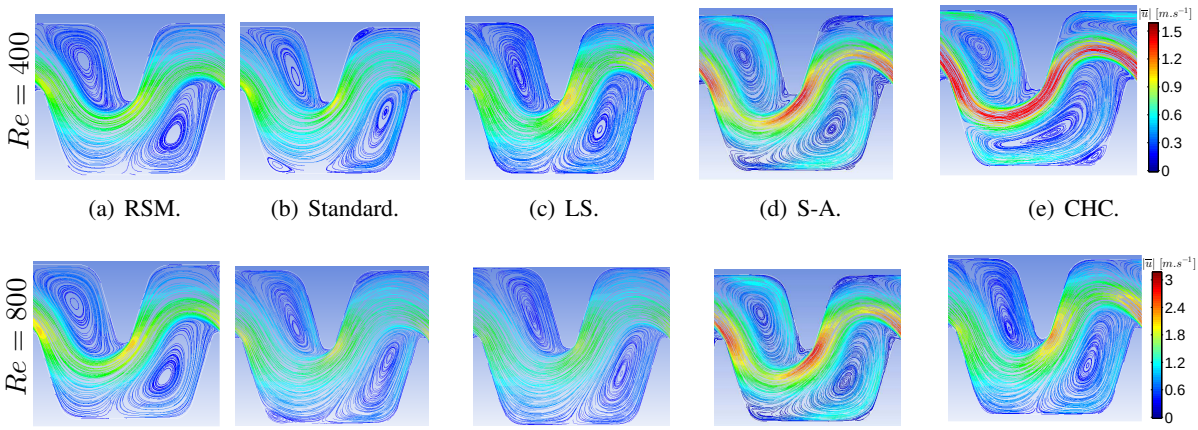

(a) RSM. (b) Standard. (c) LS. (d) S-A. (e) CHC.

(f) RSM. (g) Standard. (h) LS. (i) S-A. (j) CHC.

Figure V.2.11: Les champs de vitesse moyenne dans le carré rouge (Fig.V.1.7) en 2D, $[m.s^{-1}]$.

Modélisation en trois dimensions: Des simulations sont effectuées avec les modèles $k-\epsilon$ standard et [LS], RSM et S-A. Certains modèles prédisent la même topologie d'écoulement en 2D et 3D comme $k-\epsilon$ standard et RSM alors que d'autres modèles prédisent une topologie différente en 2D et 3D comme $k-\epsilon$ [LS] et S-A (figure V.2.12). Afin de caractériser la façon dont le débit évolue dans la profondeur du canal labyrinthe, une section transversale au niveau de la ligne 2 est prise pour analyser l'écoulement suivant l'axe z. Le débit est, en général, symétrique autour de l'axe z pour tous les modèles. Néanmoins, une variation importante de l'écoulement et de la forme de la zone de recirculation apparaît principalement pour le modèle [LS] $k-\epsilon$ lorsque le nombre de Reynolds change. Cette variation change d'un modèle à l'autre. Comme on s'y attendait, avec une zone de recirculation plus grande, l'écoulement principal possède une vitesse plus élevée (voir la version anglaise pour plus d'informations).

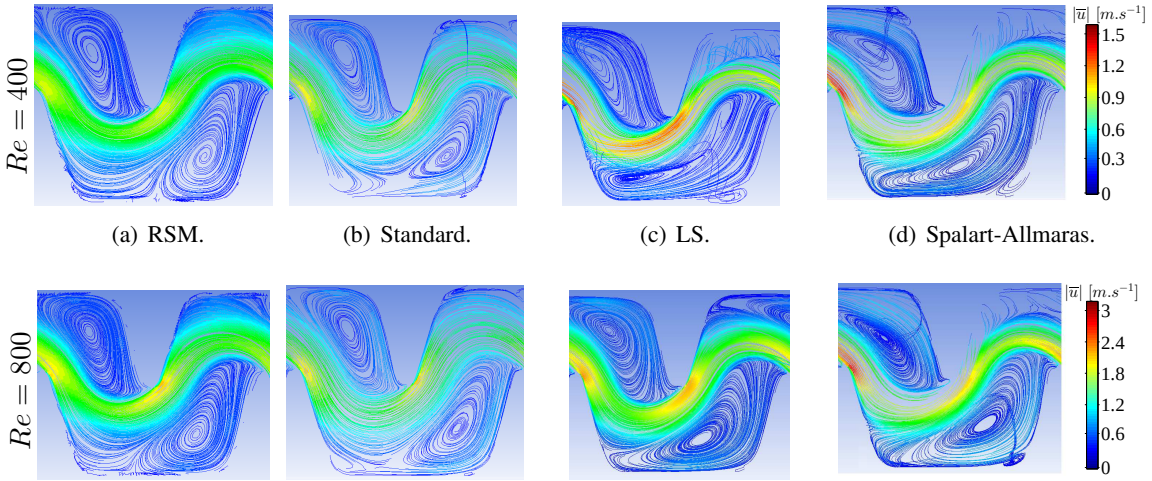

(a) RSM. (b) Standard. (c) LS. (d) Spalart-Allmaras.

(e) RSM. (f) Standard. (g) LS. (h) Spalart-Allmaras.

Figure V.2.12: Les champs de vitesse moyenne dans le carré rouge (figure V.1.7) Dans les simulations 3D.

Les champs de moments du second ordre de la vitesse fluctuante $\overline{u'^2}$, $\overline{v'^2}$ et $\overline{u'v'}$ sont également calculés et tracés dans la troisième chicane pour $Re = 400$ et $Re = 800$. On peut observer que les tensions de Reynolds sont trois fois plus élevées pour $Re = 800$ en comparaison avec $Re = 400$. Pour les deux, $\overline{u'^2}$ et $\overline{v'^2}$ sont maximum dans l'écoulement principal à proximité de la zone de séparation. Les tensions de Reynolds sont proches de zéro au niveau des zones de recirculation, ce qui pourrait faciliter le dépôt des particules et le colmatage du goutteur (ces résultats sont détaillés et discutés dans la version anglaise).

2.3 Le développement axial de l'écoulement

L'analyse de l'écoulement à l'intérieur des trois premières chicanes montre que l'écoulement évolue expérimentalement jusqu'à la troisième chicane. Numériquement cette évolution varie d'un modèle à l'autre. Cependant, la question est de savoir comment l'écoulement se développe le long des dix chicanes. Afin de répondre à cette question, les profils de vitesse expérimentaux sont tracés au début (troisième chicane), au milieu (cinquième chicane) et à la fin du labyrinthe (neuvième chicane) (figure V.2.13.) Pour $Re = 435$, une plus grande dispersion est observée (0.08 $[m.s^{-1}]$ dans la zone du vortex). Pour $Re = 863$, dans l'écoulement principal, l'amplitude de la vitesse est la même pour toutes les lignes, mais dans la zone de recirculation, des différences sont observées (0.07 $[m.s^{-1}]$ dans la zone du vortex) qui sont relativement faibles. Cependant, la dispersion est observée entre les lignes 3 et 9 par rapport à la ligne 5. Ceci peut être dû à la déformation du canal lors de l'usinage où l'uniformité n'a pas pu être suffisamment respectée.

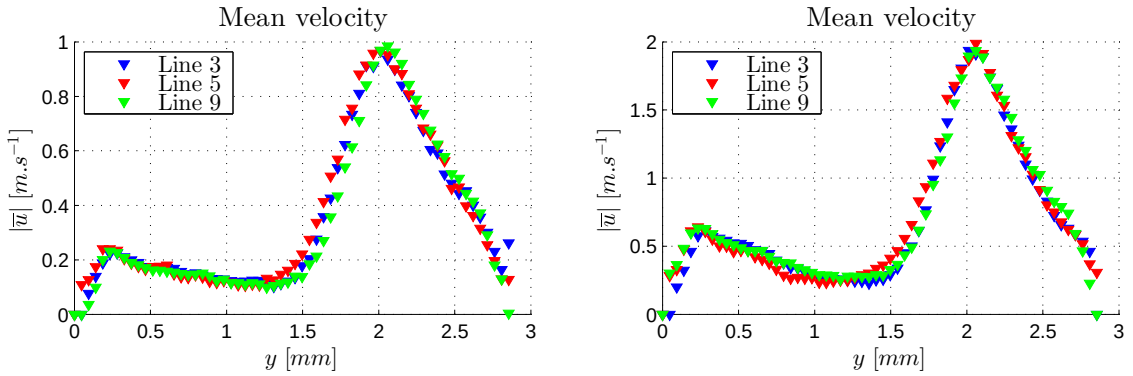

(a) $Re = 435$ (b) $Re = 863$

Figure V.2.13: Les profils de vitesse suivant les lignes 3, 5 et 9, $d_p = 5\mu m$.

Les moments du second ordre de la vitesse fluctuante sont également calculés et présentés sur la figure V.2.15 et la figure V.2.14. Il semble que les profils des moments du second ordre de la vitesse fluctuante sont légèrement différents. Les valeurs de $\overline{u'v'}$ sont proches de zéro dans les zones des recirculation et atteignent la valeur maximale dans l'écoulement principal. Une variation de $0.03-0.1$ $[m^2.s^{-2}]$ est observée dans l'écoulement principal pour les deux nombres de Reynolds en termes de $\overline{u'^2}$. Cette variation diminue pour $\overline{v'^2}$ et $\overline{u'v'}$ à environ $0.02 - 0.04$. Les profils des moments du second ordre de la vitesse fluctuante confirment que la troisième chicane est celle où l'écoulement est bien développé.

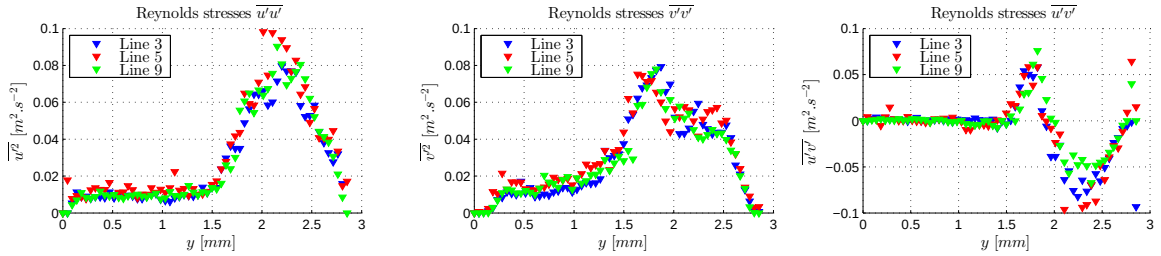

(a) $\overline{u'^2}$ (b) $\overline{v'^2}$ (c) $\overline{u'v'}$

Figure V.2.14: Les profils des moments du second ordre de la vitesse fluctuante, $Re = 435$.

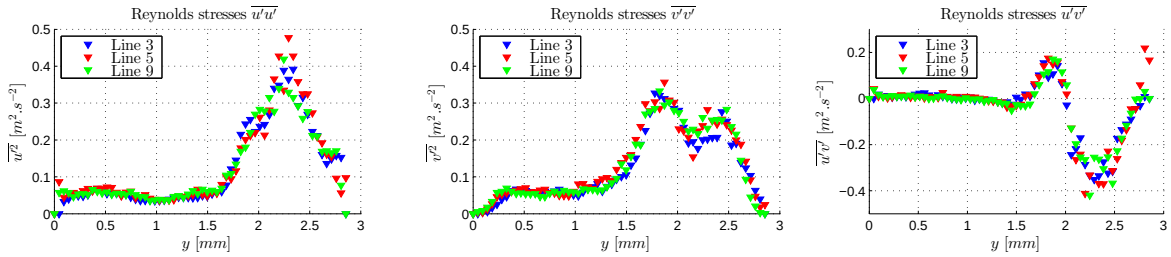

(a) $\overline{u'^2}$ (b) $\overline{v'^2}$ (c) $\overline{u'v'}$

Figure V.2.15: Les profils des moments du second ordre de la vitesse fluctuante, $Re = 863$.

2.4 L'évolution verticale de l'écoulement

Numériquement, l'écoulement est symétrique par rapport à $z = 0.5mm$ pour tous les modèles. La modélisation est réalisée en supposant que la paroi est lisse. Néanmoins, comme mentionné ci-dessus,

le labyrinthe est fabriqué par usinage, et donc cette surface n'est pas lisse. La rugosité de surface est caractérisée à l'aide d'un profilomètre optique. La rugosité moyenne, $\mathcal{R}_a$, est le paramètre de rugosité le plus largement utilisé. Ce paramètre correspond à la moyenne arithmétique des valeurs absolues. Lors de la mesure de $\mathcal{R}_a$ pour le labyrinthe fabriqué, nous avons constaté que $\mathcal{R}_a = 4.65\mu m$. Les profils de vitesse sont représentés sur la figure V.2.16, pour la troisième chicane à $z = [0.25; 0.5; 0.75]\ mm$ au-dessus de la paroi rugueuse en utilisant des particules de diamètre $d_P = 5\mu m$. Les profils de vitesse pour $0.25\ mm$ et $0.75\ \ mm$ se superposent; l'écoulement est symétrique autour de l'axe z pour cette plage. A cette distance de la paroi, la rugosité n'a aucun effet sur la vitesse moyenne. Encore une fois, il peut être observé que les propriétés de l'écoulement ne changent pas après la troisième chicane pour les différents débits.

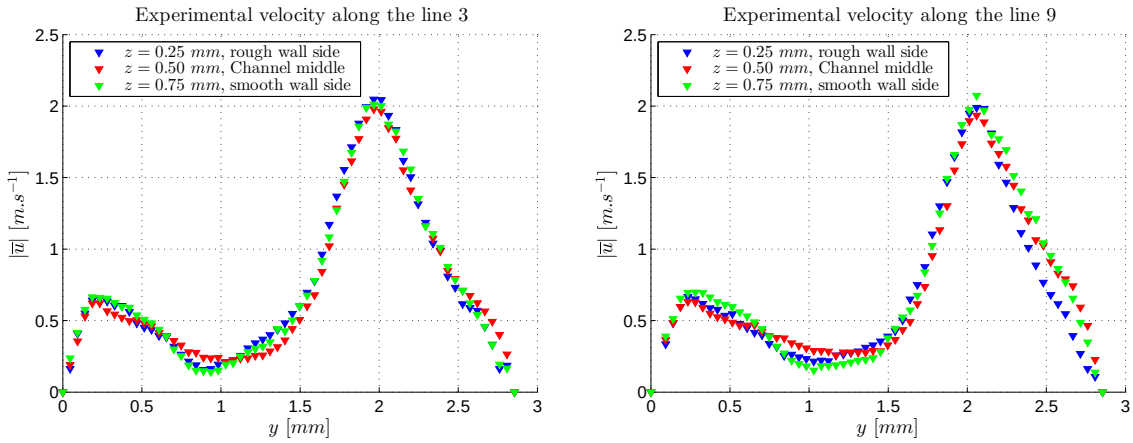

(a) Chicane 3. (b) Chicane 9.

Figure V.2.16: Les profils de vitesse, $Re = 863$, $d_p = 5\mu m$.

2.5 Méthodes avancées de détection de vorticité

Les données numériques et expérimentales ont été analysées par des méthodes avancées de détection de vorticité. Il existe plusieurs méthodes pour identifier les structures turbulentes cohérentes (tourbillons) d'une manière quantitative. Il n'y a jusqu'à présent aucune méthode acceptée universellement pour identifier une structure cohérente (Haller, 2005 [45]; Vert, Rowley et al., 2007 [43]). Beaucoup de ces méthodes impliquent le tenseur gradient de vitesse (Chakraborty, Balachandar et al., 2005 [23]; Vert, Rowley et al., 2007 [43]).

L'équation caractéristique[2] pour le tenseur ∇u est donnée par:

$$\lambda^3 + P\lambda^2 + Q\lambda + R = 0 \quad , \tag{V.2.1}$$

où P, Q et R sont les trois invariants du tenseur gradient de vitesse. En utilisant la décomposition en parties symétriques et antisymétriques, ces invariants peuvent être exprimés comme suit:

$$P = -tr(\overline{D}) \quad ; \tag{V.2.2}$$

$$Q = \frac{1}{2}\left(tr\left(\overline{D}\right)^2 - tr\left(\overline{D}^2\right)\right) = \frac{1}{2}\left(\|\overline{\Omega}\|^2 - \|\overline{S}\|^2\right) \quad ; \tag{V.2.3}$$

$$R = -det(\overline{D}) \quad ; \tag{V.2.4}$$

où $\|.\|$ est la norme de la matrice.

Le critère λ_2 est tracé sur la figure V.2.17. Cette méthode permet de définir les centres de vorticité

[2]L'équation caractéristique est l'équation qui est résolue pour trouver les valeurs propres d'une matrice, aussi appelée le polynôme caractéristique. Pour une matrice A, l'équation caractéristique de la variable λ est définie par $Det(A - \lambda I) = 0$,

pour lesquels λ_2 est la plus négative. Comme observé pour la vorticité (voir la version anglaise), le critère λ_2 souligne que la zone de séparation (juste derrière le sommet de la chicane) est la région où se trouvent les cœurs des vortex (la figure V.2.18).

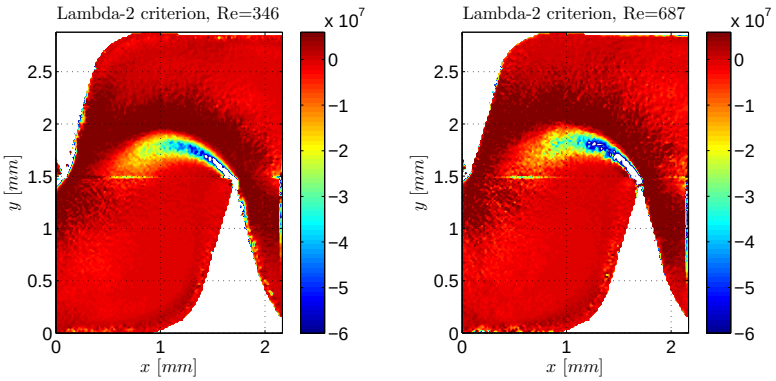

(a) $Re = 346$ (b) $Re = 687$

Figure V.2.17: Le critère λ_2 normalisé, $d_p = 1\mu m$.

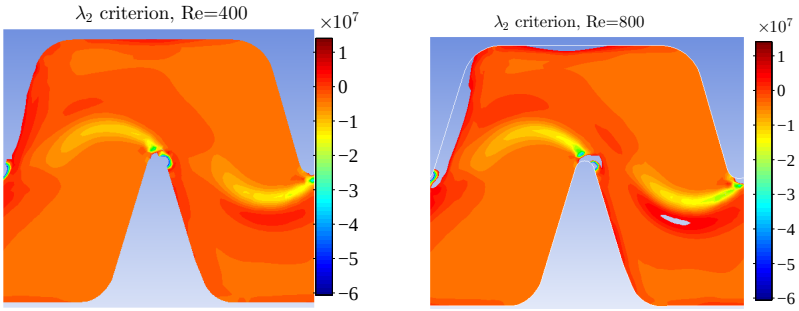

(a) $Re = 400$ (b) $Re = 800$

Figure V.2.18: Le critère λ_2 normalisé, le modèle RSM en 3D.

Le Critère Q identifie les cœurs des structures turbulentes (Chakraborty, Balachandar et al., 2005) [23] tandis que le critère λ_2 est un critère un peu plus lâche que le critère Q, mais qui garantit des minima de pression locale dans le plan 2D (Dubief and Delcayre, 2000 [37]; Chakraborty, Balachandar et al., 2005[23]).

L'équation de Q est développée pour extraire le paramètre Q des simulations sous ANSYS/Fluent et le traiter sous Matlab pour des expériences de micro-PIV. Q peut être écrit en 2D et 3D, comme suit:

$$Q = -\frac{1}{2}\left(\left(\frac{\partial u}{\partial x}\right)^2 + \left(\frac{\partial v}{\partial y}\right)^2\right) - \left(\frac{\partial u}{\partial y}\frac{\partial v}{\partial x}\right) \quad \text{en 2D} \quad . \tag{V.2.5}$$

et

$$Q = -\frac{1}{2}\left(\left(\frac{\partial u}{\partial x}\right)^2 + \left(\frac{\partial v}{\partial y}\right)^2 + \left(\frac{\partial w}{\partial z}\right)^2\right) - \left(\frac{\partial u}{\partial y}\frac{\partial v}{\partial x} + \frac{\partial u}{\partial z}\frac{\partial w}{\partial x} + \frac{\partial v}{\partial z}\frac{\partial w}{\partial y}\right) \quad \text{en 3D} \quad ; \tag{V.2.6}$$

Les champs de critère Q expérimental sont représentés sur la figure V.2.19 et sur la figure V.2.20 pour les deux nombres de Reynolds. Les champs de critère Q sont tracés sur la figure V.2.21 et la figure V.2.22 pour le modèle RSM. L'avantage du critère Q est de séparer et de distinguer entre la zone de vortex et la zone de cisaillement. Le critère Q confirme ce que l'on trouve par le critère de λ_2 : la taille

et la position de la région à proximité des dents des chicanes et dans laquelle la recirculation se produit dépendent très peu du nombre de Reynolds.

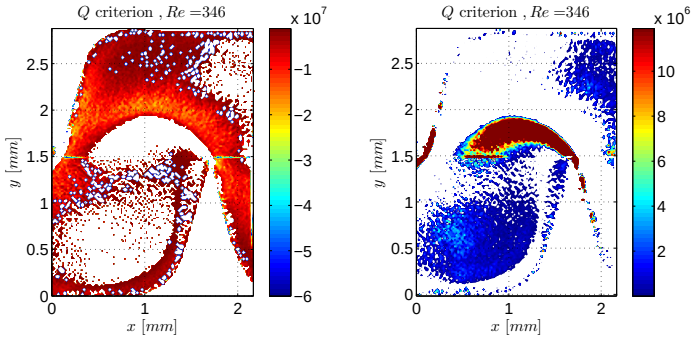

(a) Zone cisaillée (b) Zone de vortex

Figure V.2.19: Les régions cisaillées et les zones de vortex, $Re = 346$, $d_p = 1\mu m$.

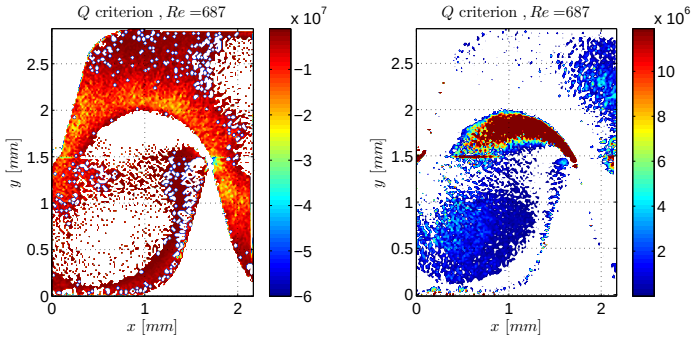

(a) Zone cisaillée (b) Zone de vortex

Figure V.2.20: Les régions cisaillées et les zones de vortex, $Re = 687$, $d_p = 1\mu m$.

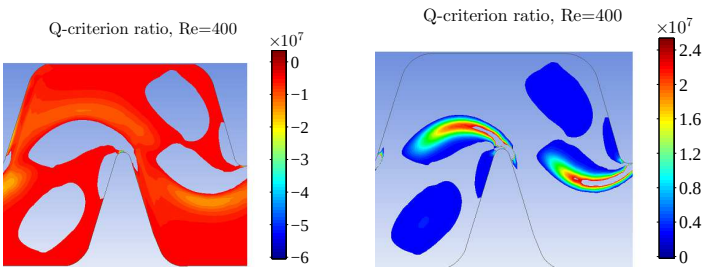

(a) Zone cisaillée (b) Zone de vortex

Figure V.2.21: Les régions cisaillées et les zones de vortex en 3D, $Re = 400$, le modèle RSM.

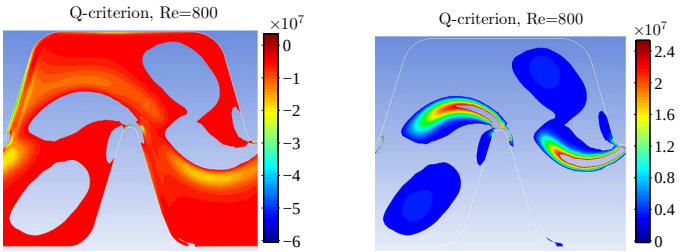

(a) Zone cisaillée (b) Zone de vortex

Figure V.2.22: Les régions cisaillées et les zones de vortex en 3D, $Re = 800$, le modèle RSM.

Le critère Q est calculé en 2D et en 3D sur la géométrie 3D par l'équation V.2.5 et l'équation V.2.6 respectivement. Les résultats présentés ci-dessus sont pour l'équation 3D (voir la version anglaise pour plus d'informations). Dans la figure V.2.23, le rapport de Q_{3D}/Q_{2D} est présenté. Cette figure met en évidence les limites de la zone de recirculation, où de petites valeurs positives en 3D deviennent de petites valeurs négatives en 2D lorsque la troisième composante est éliminée. Cela permet aussi de vérifier que, à ces petites différences près, l'approche expérimentale basée sur la micro-PIV dans le plan axial permet d'obtenir des résultats pertinents.

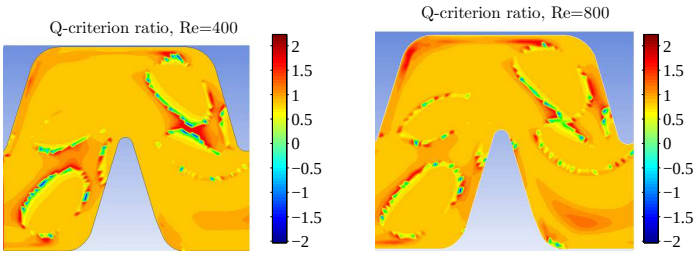

(a) $Re = 400$ (b) $Re = 800$

Figure V.2.23: $\frac{Q_{3D}}{Q_{2D}}$ calculated on the 3D geometry, RSM model.

2.6 Conclusion générale et perspectives

Cette thèse a porté sur l'étude de l'écoulement dans un canal millimétrique. Ce canal millimétrique est le labyrinthe qui constitue le goutteur du système de micro-irrigation. Le système de micro-irrigation a atteint un bon développement ces dernières années. Néanmoins, ce système est encore peu utilisé dans le monde parce que le goutteur est sensible au colmatage. Ce colmatage augmente le coût de l'installation. Etant donné que les conditions hydrodynamiques jouent un rôle important dans le contrôle du colmatage, la caractérisation de l'écoulement dans le labyrinthe est nécessaire pour améliorer les performances du goutteur. La caractérisation et l'analyse de l'écoulement sont les objectifs de cette thèse.

La caractérisation expérimentale de l'écoulement est essentielle dans le labyrinthe. Cette caractérisation permet de prédire et de distinguer entre l'écoulement principal et la position et la taille des zones de recirculation propices au colmatage. Ces zones se caractérisent par une faible vitesse. Numériquement, la prédiction de la position et la taille de la zone de recirculation varie selon le modèle. Par conséquent, des expériences par micro-PIV permettent d'analyser l'écoulement dans le labyrinthe et de valider le modèle numérique. La technique de micro-PIV a été utilisée pour effectuer la caractérisation des écoulements dans le canal millimétrique. La technique de micro-PIV a encore été peu utilisée pour visualiser et analyser l'écoulement dans ce type de labyrinthe du fait de sa difficile mise en œuvre. Généralement, les expériences 2D de micro-PIV définissent deux composantes de la vitesse $\overline{u}$ et

$\overline{v}$ et trois moments du second ordre de la vitesses fluctuant $\overline{u'^2}$, $\overline{v'^2}$ et $\overline{u'v'}$.

Le manuscrit rapporte l'évaluation de plusieurs modèles de turbulence, des modèles $k-\epsilon$ à haut nombre de Reynolds et des modèles $k-\epsilon$ à bas nombre de Reynolds, et les modèles Spalart-Allmaras et RSM. Les modèles numériques utilisés permettent de calculer les pertes de charge et d'avoir les courbes débit-pression. Cette courbe définit les performances hydrauliques du goutteur. La dissipation turbulente est le principal responsable des pertes de pression dans le labyrinthe. Les pertes de charge sont fortement liées à la taille de la zone de recirculation. Les caractéristiques de l'écoulement à l'intérieur de chaque unité sont identiques lorsque l'écoulement est complètement développé. Cette observation est d'intérêt pour les fabricants qui pourraient régler le nombre d'unités de labyrinthe selon le débit qu'ils veulent atteindre, afin de répondre aux besoins de la plante.

Ce travail souligne la difficulté d'identifier et quantifier les zones de recirculation. Il apparait cependant que le critère Q soit le mieux adapté pour caractériser ces zones. Le modèle RSM correspond bien aux expériences micro-PIV, ne serait-ce qu'en regard de la forte anisotropie de l'écoulement qui ne peut être prise en compte par les autres modèles étudiés. Par conséquent, le modèle RSM aidera dans le futur à réaliser des études d'optimisation.

Les outils numériques seront utilisés pour optimiser la géométrie du labyrinthe, avec l'objectif de minimiser les régions de recirculation où le dépôt de particules est susceptible de se produire, tout en maintenant une assez grande perte de charge. Cette optimisation doit tenir compte de l'équilibre entre l'amélioration du goutteur pour le colmatage et avoir une bonne performance débit/perte de charge dans le même temps.

Les résultats expérimentaux et numériques fournissent beaucoup d'éléments intéressants et des idées pour comprendre et améliorer la performance du goutteur. Afin d'enrichir cette compréhension, des expériences complémentaires par micro-PIV en injectant des particules d'argile dans l'écoulement comme l'argile bentonite pourraient être effectuées. Ces expériences permettraient d'analyser l'impact de l'ajout de particules réelles sur la dynamique de l'écoulement. Parallèlement, des expériences PTV seront effectuées pour caractériser les trajectoires des particules ainsi que les phénomènes d'agglomération et de dépôt. Ces expériences seront également couplées à des travaux numériques, en utilisant le modèle de turbulence RSM et une approche lagrangienne ou eulérienne.

Appendix A

A.1 Optical system

Since micro-PIV is based on the optical measurements of particles displacements, it is important to understand how experimental parameters affect the scattering and collection of light in micro-PIV (see Adrian and Yao (1985) for more details [7])[3].

A.1.1 Imaging of small particles

Some basic knowledge about the imaging must be introduced first to understand. In general, the following formulae and terms are used to characterize imaging systems for a single-lens system Fig.A.1:

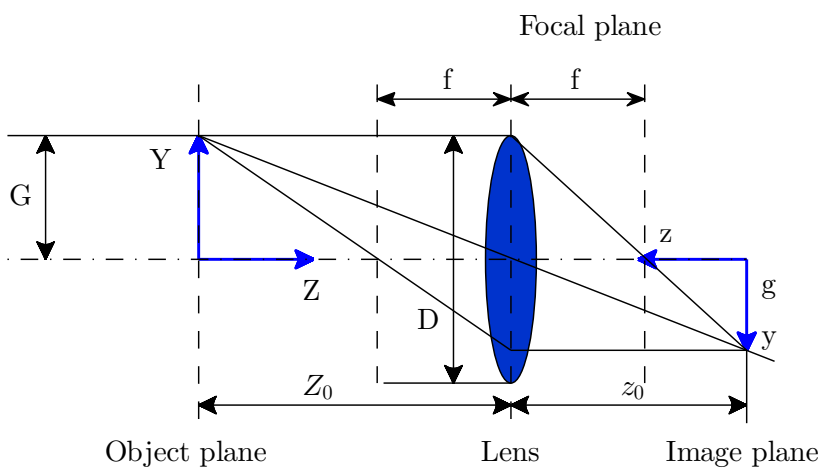

Figure A.1: Image reconstruction system

Single-lens formula:

$$\frac{1}{Z_0} + \frac{1}{z_0} = \frac{1}{f} \tag{A.1}$$

[3]The section A.1 is extracted from Raffel et al. (2007)[89]

The magnification factor is based on the two distances:

$$M = \frac{z_0}{Z_0} = \frac{g}{G}$$

Another term used in imaging is the scale factor which is the inverse of the magnification:

$$S = \frac{1}{M} = \frac{G}{g}$$

F-number (lens stop):

$$f_{\#} = \frac{f}{D}$$

where Z_0 is the distance between the lens and the object plane $[m]$,
f is the focal distance $[m]$,
z_0 is the distance between the image plane and the lens $[m]$,
D is the aperture lens diameter $[m]$.

A.1.2 Diffraction limited imaging

This paragraph provides a summary of the description of diffraction limited imaging, for more detail see (Raffel et al., 2007)[89].

When plane light waves impinge on a lens (camera objective), they generate a far-field diffraction pattern on a distant observing screen. The image of a distant point source (e.g. a small scattering particle inside the light laser sheet) does not appear as a point in the image plane. A circular pattern (Fraunhoofer diffraction pattern), namely, the Airy disk will be obtained for a low exposure and surrounding Airy rings can be observed for a very light exposure.

Using the approximation of Fraunhofer for the far field it can be shown that the intensity of Airy pattern represents the Fourier transform of the aperture transmissivity distribution [[42],[68]]. Taking into account the scaling theorem of the Fourier transform, it becomes clear that large aperture diameters correspond to small Airy disks and small apertures to large disks as can be seen in Fig.A.2.

The value of the radius of the ring and therefore of the Airy disk can be found for a given aperture diameter D and wavelength λ. From normalized intensity distribution of the Airy pattern and its approximation by a Gaussian curve Fig.A.3, one can find.

$$\frac{I(x)}{I_{\text{max}}} = 0 \Rightarrow \frac{d_{\text{diff}}}{2x_0} = 1.22 \tag{A.2}$$

where λ is the wavelength of the illuminating light source $[\mu m]$ and :

$$x_0 = \frac{\lambda}{D} \quad . \tag{A.3}$$

The image size of a seeding particle which is recorded by a camera is determined by the particle diameter, image magnification, and the point response of the imagining lens and affected by diffraction on the aperture of the lenses so that the formulae mentioned above are not applicable to calculate the diameter. The diffraction-limited minimum image diameter can be obtained by the following formula:

$$d_{\text{diff}} = 2.44 f_{\#} \lambda \left(M + 1\right) \quad , \tag{A.4}$$

where d_{diff} is the diameter of Airy disk $[m]$.

In the present experiments, $f_{\#} = 2.8$ and $\lambda = 0.532\mu m$. $M = 5$ ($M = 6.7$) are used in this study for particles diameters $d_p = 5\ \mu m$ ($1\ \mu m$) respectively. This gives d_{diff} with the values of $21.8\ \mu m$ ($28\ \mu m$). The image diameter of particle is the convolution of the diffraction-limited image with the

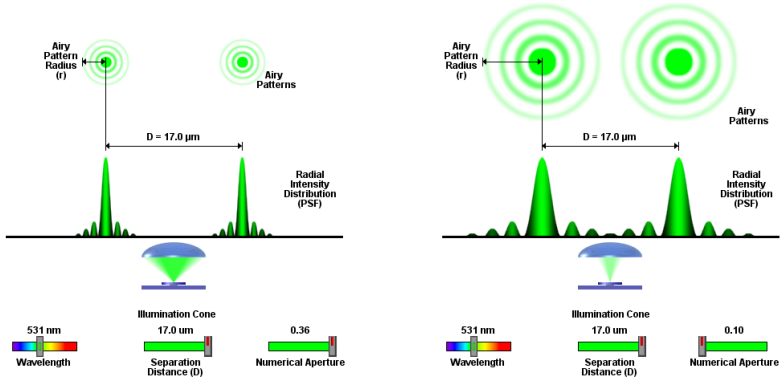

Figure A.2: Airy patterns for a large aperture and a smaller aperture diameter - source: www.olympusmicro.com

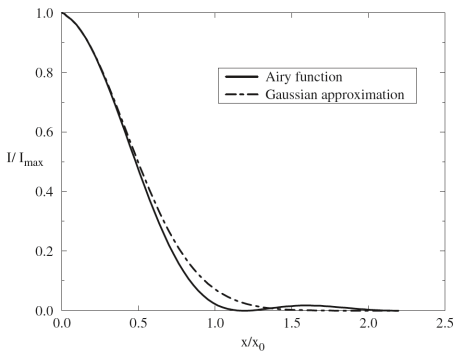

Figure A.3: Normalized intensity distribution of the Airy pattern and its approximation by a Gaussian curve (Raffel et al., 2007)[89]

geometric image. The convolution is a Gaussian function with an image diameter given by (see Adrian and Yao 1985 [7], Adrian 1991 [8]):

$$d_{\text{image}} \simeq \sqrt{(M.d_p)^2 + d_{\text{diff}}^2} \tag{A.5}$$

For the previous configurations, d_{image} is 33.93 μm (28.79 μm). The image particle diameter when projected back into the flow is 6.80 μm (4.30 μm). As it is found by Prasad et al. (1992)[86] if a particle image diameter is resolved by $3-4$ pixels, the location of a particle-image correlation peak can be determined to within $1/10th$ the particle-image diameter. The measurement uncertainly is then of $\delta x \approx d_{\text{image}}/10M$. With the parameters of present experiments, the errors are 0.68 μm (0.43 μm).

The previous expression is dominated by diffraction effects and reaches a constant value of d_{diff} when the size of the particle's geometric image $M\ d_p$ is considerably smaller than d_{diff} (less than $\simeq$ 1.5 μm). Likewise, it is dominated by the geometric image size for geometric image sizes considerably larger than d_{diff} where $d_{\text{image}} \approx M dp$ (greater than $\simeq$ 14 μm).

In practice the point spread function is often approximated by a normalized Gaussian curve also shown in Fig.A.3 and defined by:

$$\frac{I(x)}{I_{\text{max}}} = exp\left(-\frac{x^2}{2\sigma^2}\right) \tag{A.6}$$

where σ must be set $\sigma = f_{\#}(1+M)\lambda\sqrt{2}/\pi$, in order to approximate diffraction limited imaging. In practice, there are two good reasons for optimizing the particle image diameter:

- An analysis of PIV evaluation shows that the error in velocity measurements strongly depends on the particle image diameter. For most practical situations, the error is minimized by minimizing both the image diameter d_{image} and the uncertainty in locating the image centroid or correlation peak centroid respectively.

- Sharp and small particle images are particularly essential in order to obtain a high particle image intensity I_{max}, since at constant light energy scattered by the tracer particle the light energy per unit area increases quadratically with decreasing image areas ($I_{\text{max}} \sim 1/d_{\text{image}}$). This fact also explains why increasing the particle diameter not always compensates for insufficient laser power.

In order to obtain a sharp particle image, the particle must be within the depth of field of the lens, δz. Offuft (1995) [79] reformulated the conventional result for the value of M not equal to unity. Eq.A.7 is used to estimate the depth of field δz:

$$\delta z = 2 f_{\#} d_{\text{diff}} (M+1)/m^2 = 4.88(1+1/M)^2 f_{\#}^2 \lambda \quad . \tag{A.7}$$

Some theoretical values for the diffraction limited imaging of small particles ($dp \approx 1\mu m$) are shown in table 2.6 (calculated with a wavelength of $\lambda = 532\ nm$ and a magnification of $M = 5$). It can be seen that a large aperture diameter is needed to get sufficient light from each individual particle within the light sheet, and to get sharp particle images, because – as already shown in Fig.A.2 – the size of the diffraction pattern can be decreased by increasing the aperture diameter. Unfortunately, a big aperture diameter yields a small focal depth which is a significant problem when imaging small tracer particles. Since lens aberrations become more and more important for an increasing aperture, see Raffel et al. (2007)[89] for more detail.

A.2 Standard Wall function

[4]The logarithmic law-of-the-wall representing the mean velocity profile in the fully turbulent region of the inner layer is written in Eq.III.1.60. This equation provides the wall boundary conditions for momentum equation. In order to specify the turbulence quantities at the wall-adjacent cell in term of the wall-shear stress supposing the local equilibrium and constant shear in the logarithmic region, the turbulence equations for k and ϵ are solved.

$$k_P = \frac{u_\tau^2}{\sqrt{C_\mu}} \quad , \quad \epsilon_P = \frac{u_\tau^3}{\kappa y_P} \tag{A.8}$$

where E is an empirical constant ($= 9.793$),
y_P distance from point P to the wall,
k_P is the turbulence kinetic energy at the near-wall node P.
When using Eq.A.8 in complex flow situations, the turbulent velocity scale (u_τ) becomes zero at the points of flow detachment or attachment where the wall-shear vanishes. k and ϵ vanish also according to this equation, while experimental test indicates quite the contrary. Therefore, the standard wall function, described by Launder and Spalding (1974) [67], becomes more popular in the computation of industrial turbulent flows. In this approach, the universal law-of-the-wall for mean velocity is replaced by:

$$\frac{U_p C_\mu^{1/4} k_P^{1/2}}{\tau_\omega/\rho} = \frac{1}{\kappa} ln(E \frac{\rho C_\mu^{1/4} k_P^{1/2} y_P}{\mu}) \quad . \tag{A.9}$$

where U_P is the mean velocity of the fluid at the near-wall node P.
The Eq.A.9 can be written in the same way as Eq.III.1.60 replacing u^+ by u^*, and y^+ by y^* as following:

$$U^* = \frac{1}{\kappa} ln(E y^*) \tag{A.10}$$

where U^* is the dimensionless velocity

$$U^* = \frac{U_P C_\mu^{1/4} k_P^{1/2}}{\tau_\omega/\rho} \tag{A.11}$$

[4]The section A.2, A.3 and A.5 are extracted from the following document:
ANSYS FLUENT Theory Guide, ANSYS Inc., 2003.

and y^* is the dimensionless distance from the wall

$$y^* = \frac{\rho C_\mu^{1/4} k_P^{1/2} y_P}{\mu} \tag{A.12}$$

The log-law is employed when $y^* > 11.225$. When the mesh is such that $y^* < 11.225$ at the wall-adjacent cells, the stress-strain relationship $u^* = y^*$ is applied. In $k - \epsilon$ models and in the RSM, the k equation is solved in the whole domain including the wall-adjacent cells. The boundary condition for k imposed at the wall is:

$$\frac{\partial k}{\partial n} = 0 \tag{A.13}$$

where n is the local coordinate normal to the wall.
At the wall-adjacent cells, the production of k and its dissipation rate are assumed to be equal. Thus, the production of k is based on the logarithmic law and is computed from:

$$G_k \approx \tau_w \frac{\partial U}{\partial y} = \tau_w \frac{\tau_w}{\kappa_P C_\mu^{1/4} \kappa_P^{1/2} y_P} \tag{A.14}$$

and dissipation rate ϵ is calculated from:

$$\epsilon_P = \frac{C_\mu^{3/4} \kappa_P^{3/2}}{\kappa y_P} \tag{A.15}$$

The ϵ equation is not solved at the wall-adjacent cells, but instead is computed using this equation Eq.A.15.

A.3 Non-equilibrium wall function

The standard wall function is not applied when the flows are under severe pressure gradients, and in strong non-equilibrium, which means that the turbulence production term and the dissipation term are not equal. The log-law for mean velocity is sensitized to pressure-gradient effects Launder and Splanding [66]:

$$\frac{\widetilde{U} C_\mu^{1/4} \kappa^{1/2}}{\tau_w/\rho} = \frac{1}{\kappa} ln \left(E \frac{\rho C_\mu^{1/4} \kappa^{1/2} y}{\mu} \right) \tag{A.16}$$

where :

$$\widetilde{U} = U - \frac{1}{2}\frac{dp}{dx}\left[\frac{y_\nu}{\rho\kappa\sqrt{k}} ln\left(\frac{y}{y_\nu}\right) + \frac{y - y_\nu}{\rho\kappa\sqrt{k}} + \frac{y_\nu^2}{\mu}\right] \tag{A.17}$$

and y_ν is the physical viscous sub-layer thickness and is computed from :

$$y_\nu = \frac{\mu y_\nu^*}{\rho C_\mu^{1/4} k_p^{1/2}} \tag{A.18}$$

where $y_\nu^* = 11.225$. The two-layer-based concept is adopted to compute the budget of turbulence kinetic energy ($\overline{G_k}$, $\overline{\epsilon}$) in the wall-neighboring cells.

$$\tau_t = \begin{cases} 0, & y < y_\nu \\ \tau_\omega, & y > y_\nu \end{cases} \quad k = \begin{cases} \left(\frac{y}{y_\nu}\right)^2 k_P, & y < y_\nu \\ k_P, & y > y_\nu \end{cases} \quad \epsilon = \begin{cases} \frac{2\nu k}{y^2}, & y < y_\nu \\ \frac{k^{3/2}}{C_\ell^* y}, & y > y_\nu \end{cases} \tag{A.19}$$

where $C_\ell^* = \kappa C_\mu^{-3/4}$. Using these profiles, the cell-averaged production of k , $\overline{G_k}$, and the cell-averaged dissipation rate, $\overline{\epsilon}$ can be computed from the volume averages of G_k and ϵ of the wall-adjacent cells.

For quadrilateral and hexahedral cells for which the volume average can be approximated with a depth-average,

$$\overline{G_k} = \frac{1}{y_n}\int_0^y \tau_t \frac{\partial U}{\partial y} dy = \frac{1}{\kappa y_n}\frac{\tau_\omega^2}{\rho C_\mu^{1/4}\kappa_p^{1/2}} ln\left(\frac{y_n}{y_\nu}\right) \tag{A.20}$$

and

$$\bar{\epsilon} = \frac{1}{y_n}\int_0^y \epsilon dy = \frac{1}{y_n}\left[\frac{2\nu}{y_\nu} + \frac{\kappa_p^{1/2}}{C_\ell^*} ln\left(\frac{y_n}{y_\nu}\right)\right] k_p \tag{A.21}$$

where y_n is the height of the cell ($y_n = 2y_p$). For cells with other shapes, the appropriate volume averages are used.

A.4 Spalart-Allmaras: k and ϵ

The turbulent viscosity ν_t is defined so that the Reynolds shear stress is given by[5]:

$$-\overline{u'v'} = \nu_t \frac{d\overline{u}}{dy} \tag{A.22}$$

The turbulent viscosity is given by the relation which constitute Prandtl's mixing-length hypothesis as follows:

$$\nu_t = \ell_m^2 |\frac{d\overline{u}}{dy}| \tag{A.23}$$

One of the fundamental properties of the log-law region is:

$$-\overline{u'v'}/k = 0.3 = \sqrt{C_\mu} \tag{A.24}$$

Turbulence kinetic energy k is given as:

$$k = \frac{-\overline{u'v'}}{\sqrt{C_\mu}} = \frac{\nu_t}{\sqrt{C_\mu}}\frac{d\overline{u}}{dy} \tag{A.25}$$

in $k-\epsilon$ model, the turbulent viscosity is given by:

$$\nu_t = C_\mu \frac{k^2}{\epsilon} \tag{A.26}$$

By replacing k in this eqation, we find:

$$\nu_t = C_\mu \frac{\nu_t^2}{C_\mu}\frac{\frac{d\overline{u}}{dy}^2}{\epsilon} \quad \Rightarrow \epsilon = \nu_t\left(\frac{d\overline{u}}{dy}\right)^2 \tag{A.27}$$

A.5 RSM: supplementary informations

The wall-reflection term, $\phi_{ij,w}$, is responsible for the redistribution of normal stresses near the wall. It tends to damp the normal stress perpendicular to the wall, while enhancing the stresses parallel to the wall. This term is modeled as :

$$\phi_{ij,w} = -C_1'\frac{\epsilon}{k}\left(\overline{u_k'u_m'}n_k n_m \delta_{ij} - \frac{3}{2}\overline{u_i'u_k'}n_j n_k - \frac{3}{2}\overline{u_j'u_k'}n_i n_k\right) \times \frac{k^{3/2}}{C_\ell \epsilon d} + C_2'\left(\phi_{km,2}n_k n_m \delta_{ij} - \frac{3}{2}\phi_{ik,2}n_j n_k - \frac{3}{2}\phi_{jk,2}n_i n_k\right)\frac{k^{3/2}}{C_\ell \epsilon d} \tag{A.28}$$

where $C_1' = 0.5$, $C_2' = 0.3$ n_k is the x_k component of the unit normal to the wall, d is the normal distance to the wall, and $C_\ell = C_\mu^{3/4}/\kappa$, where $C_\mu = 0.09$ and $\kappa = 0.41$.

[5]The main equations are extracted from (Pope, 2000)[85].

A.6 Image recording devices

The introduction of digital image recording was the real revolution for PIV. In fluid mechanics, special cross-correlation CCD (charge-coupled devices) sensors are more frequently used than CMOS (Complementary Metal Oxide Semiconducteurs) sensors. Theses cameras provided with CCD sensors, which are capable of recording two subsequent images on separate frames. A CCD sensor is formed from an $M \times N$ array Fig.A.4. Each element (pixel) is a silicium rectangle of the order of a few micron. Charge accumulated in the pixel must be rapidly transferred before being converted in electric tension. Therefore, storage cells are necessary to decouple integration time from the data transfer time. There are two technologies to do it, Interline transfer and Frame transfer. The first one is the most used for the cameras at which the frame straddling is functioned. This method of transfer takes its name from additional vertical transfer registers located between the active pixels. Such chips comprise light-sensitive cells and an equal number of storage cells. After recording the first image, the charges of the light-sensitive cells are quickly transferred to the storages cells, while recording on the second image, the data of the storage cells are sequentially transferred to the output register. Therefore, the shortest time between two recordings is approximately determined by the time which is necessary to transfer the charges from the light sensitive cells to the storage cells (time of transfer is lower than 1 μs). One disadvantage of this sensor is that the storage cells occupy about 50% of CCD-ships which are therefore not light sensitive. Adding an array of micro-lens can diminish this problem.

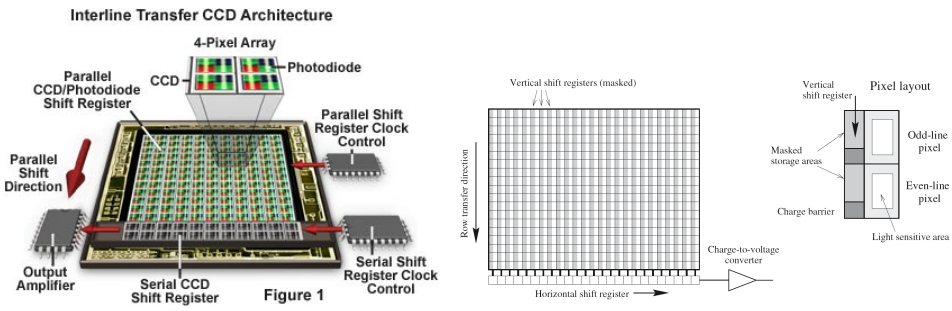

Figure A.4: Imaging system

The maximum frame rate of a CCD camera is determined by the time which is needed to read out the data. Although the read-out time for the camera in Fig.A.5 is 91 ms, the shortest time between two subsequent recordings is as low as 0.2 (table II.1.6). This is achieved by employing the so-called frame straddling technique (Wernet, 2000)[103]. The first image is recorded after triggering the camera, while the image of frame $\#1$ is exposed by firing laser $\#1$. The image data of frame $\#1$ are then transferred to the storage cells and frame $\#2$ is exposed by firing laser $\#2$. Since reading out of the data from frame $\#1$ takes for the given example 91 ms frame $\#2$ is exposed for the same time. It is therefore necessary to prevent firing the laser again during this time otherwise frame $\#2$ would have been exposed twice. It is also recommended to perform PIV measurements with low ambient light or best in dark to achieve two images with comparable exposure.

A.7 Camera

Camera spectral sensitivity functions relate scene radiance with captured RGB triplets. They are important for many computer vision tasks that use color information, such as multispectral imaging, and color constancy. The spectral response is shown in Fig.A.6.

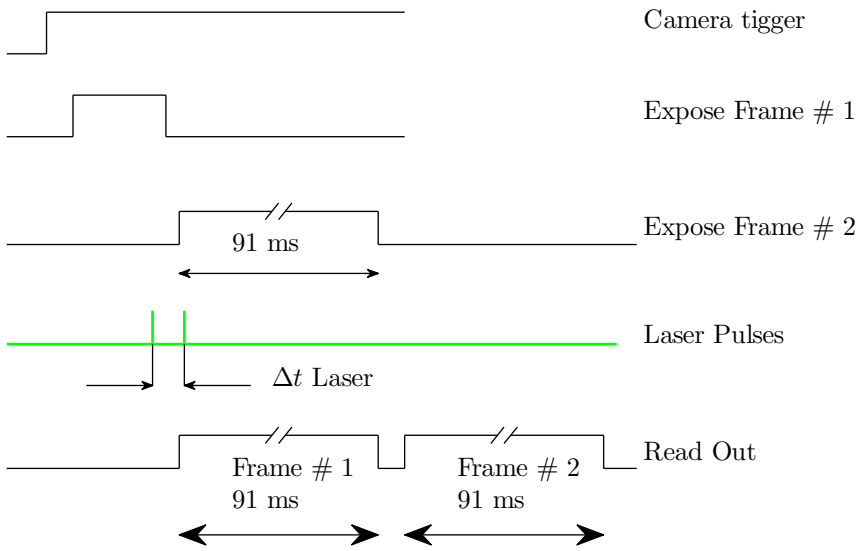

Figure A.5: Timing Diagram for Double-Frame Camera and Frame Straddling Technique

A.8 Treatment method

After the images acquisition, the data treatment is performed by the Dynamic Studio software. The algorithm procedure is organized as follows:

- Mask the labyrinth-channel boundary,
- Calculate the average image,
- Remove the background noise by substracting the average image from each image (image arithmetic),

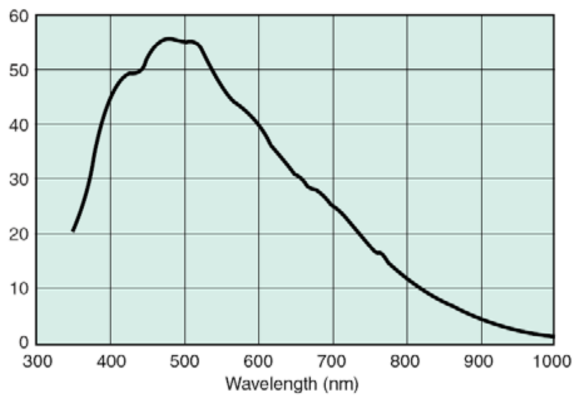

Figure A.6: Spectral response HiSense 4M
- source : www.dantecdynamics.com

- Apply adaptive correlation on the image arithmetic.

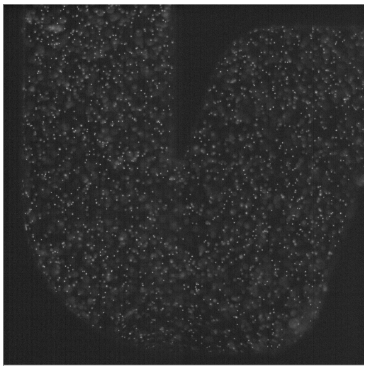

(a) Raw image

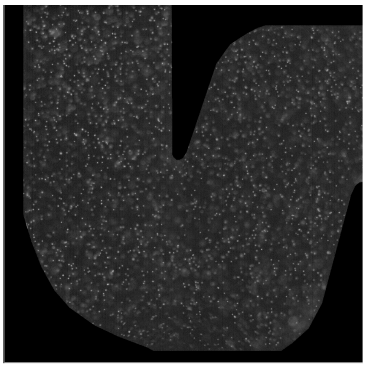

(b) Image masked

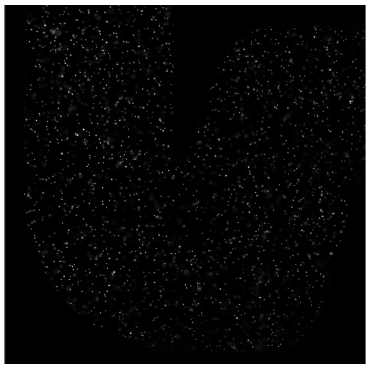

(c) Image arithmetic

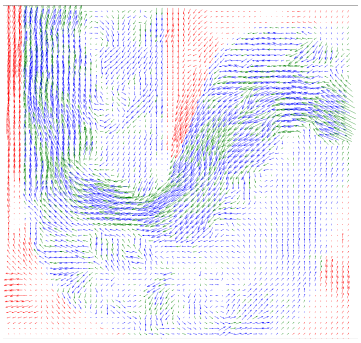

(d) Adaptive correlation

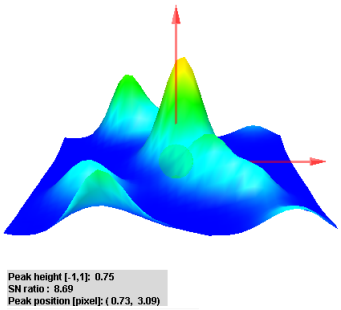

(e) Correlation peak

Figure A.7: An example of micro-PIV Data Processing

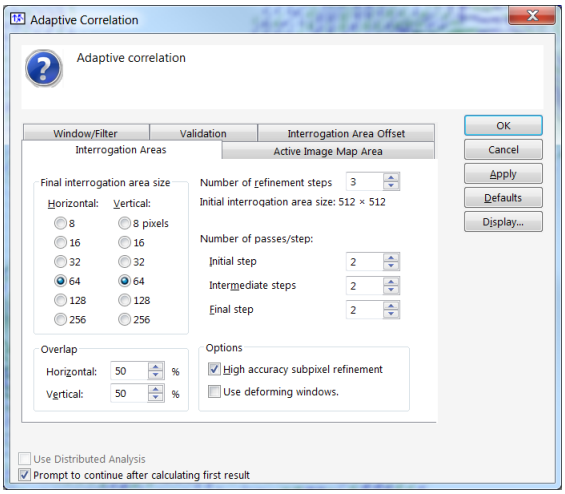

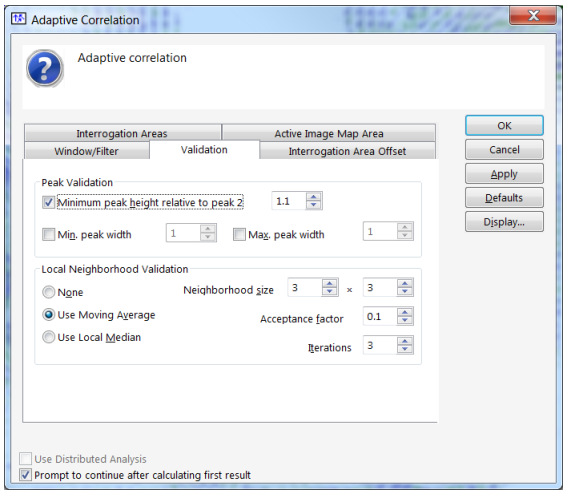

Figure A.8: Adaptive correlation parameters

A.9 Cross correlation

The Fourier transform is used to first compute the Fourier transform of interrogation cells from images 1 and 2, then the product in the spectral space of signals before performing an inverse Fourier transform to obtain the correlation signal in real space. If we define a wave number, k, as function of

wavelength, λ, to be:

$$k = 1/\lambda \tag{A.29}$$

then the Fourrier transform, $\mathcal{F}$, and the inverse Fourier transform, $\mathcal{F}^{-1}$, can be defined as:

$$H(k) = \mathcal{F}[h(x)] = \int_{-\infty}^{+\infty} h(x) e^{2\pi i k x} dx \quad ; \tag{A.30}$$

$$h(k) = \mathcal{F}^{-1}[H(x)] = \int_{-\infty}^{+\infty} H(x) e^{-2\pi i k x} dx \quad . \tag{A.31}$$

Now the correlation can be comptued

$$\begin{aligned}
C_{fg}(\Delta x) &= \int_{-\infty}^{+\infty} f^{\star}(x) g(x+\Delta x) dx \\
&= \int_{-\infty}^{+\infty} \left(\int_{-\infty}^{+\infty} \mathcal{F}^{\star}(k) e^{2\pi i k x} dk \int_{-\infty}^{+\infty} G(k') e^{-2\pi i k' \Delta x} e^{-2\pi i k' x} dk' \right) dx \\
&= \int_{-\infty}^{+\infty} \left(\int_{-\infty}^{+\infty} \mathcal{F}^{\star}(k) e^{2\pi i k x} dk \int_{-\infty}^{+\infty} G(k') e^{-2\pi i k' (\Delta x + x)} dk' dx \right. \\
&= \int_{-\infty}^{+\infty} \int_{-\infty}^{+\infty} \int_{-\infty}^{+\infty} \mathcal{F}^{\star}(k) G(k') e^{-2\pi i (k'-k) x} e^{-2\pi i k' \Delta x} dx dk' dk \\
&= \int_{-\infty}^{+\infty} \int_{-\infty}^{+\infty} \mathcal{F}^{\star}(k) G(k') e^{-2\pi i k' \Delta x} \left(\int_{-\infty}^{+\infty} e^{-2\pi i (k'-k) x} dx \right) dk' dk \\
&= \int_{-\infty}^{+\infty} \int_{-\infty}^{+\infty} \mathcal{F}^{\star}(k) G(k') e^{-2\pi i k' \Delta x} \delta(k'-k) dk' dk \\
&= \int_{-\infty}^{+\infty} \mathcal{F}^{\star}(k) G(k) e^{-2\pi i k \Delta x} dk \\
&= \mathcal{F}^{-1} \left[\mathcal{F}^{\star}(k) G(k) \right] \quad .
\end{aligned} \tag{A.32}$$

This is known as the correlation theorem. For the special case of having real functions $f(x)$ and $g(x)$ we have $\mathcal{F}^{\star}(k) = \mathcal{F}(-k)$ but this cannot be exploited anymore in evaluating the correlation.

A.10 Comparative study between $1\mu m$ and $5\mu m$ particles diameters

A comparative study has been performed between $1\mu m$ and $5\mu m$ to see the influence of the use of smaller particles on the flow parameters. One of the goals for using $d_p = 1\ \mu m$ is to allow to treat the micro-PIV data using an interrogation window 32×32 pixels. The number of points is 127 instead of 63 using an interrogation window size, 64×64 pixels for $d_p = 5\ \mu m$. Smoothing the data confirms that the interrogation window size 64×64 pixels or 32×32 pixels has no influence on the treatment of velocity.

Velocity profiles are plotted using the two particles diameters $1\mu m$ and $5\mu m$ on the line 3. These profiles are shown in Fig.A.9. When comparing velocity modulus and its components $\overline{u}$ and $\overline{v}$ values for the two particle diameters, the profiles show that there is a small difference between the velocity profiles. This difference occurs for $Re = 435$. The velocity in the mainstream flow is larger in the case of $d_p = 1\ \mu m$. That is related to the two velocity components $\overline{u}$ and $\overline{v}$. Fig.9(b) show the velocity components $\overline{u}$. This velocity component is related to the flow rate. The flow rate is 23.96 $ml.min^{-1}$ for $d_p = 5\mu m$ and 23.93 $ml.min^{-1}$ for $d_p = 1\mu m$. Thus, this variation is not related to the flow rate. Regarding the velocity components $\overline{v}$, in Fig.9(c), it can be concluded that the difference is only occurred in the mainstream flow. However, a convergence study is performed in point (-8.50, 2.00) to see whether the difference is related to the number of valid vectors in this point. The number of valid vectors is about 130 when $d_p = 5\mu m$ and about 180 when $d_p = 1\mu m$ from 250 pairs of images. The ratios of velocities

for $d_p = 1\mu m$ and $d_p = 5\mu m$ are about 1.22, 1.22 and 1.25 for $\overline{|u|}$, $\overline{u}$ and $\overline{v}$ respectively. The mean value of these velocities is converging toward its stable value.

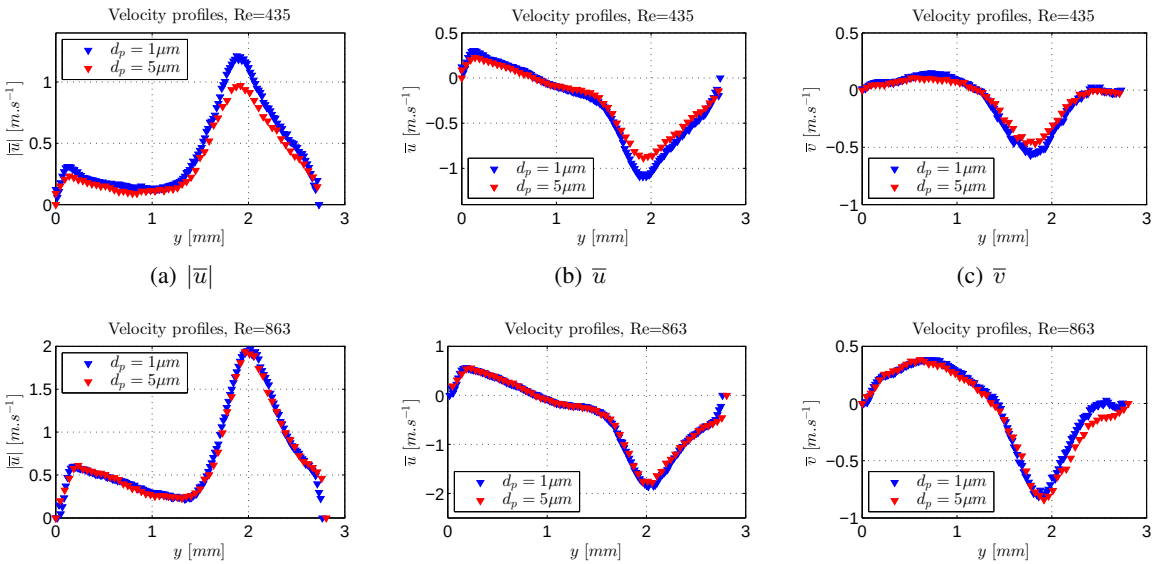

(a) $|\overline{u}|$ (b) $\overline{u}$ (c) $\overline{v}$

(d) $|\overline{u}|$ (e) $\overline{u}$ (f) $\overline{v}$

Figure A.9: Velocity profiles along the line 3, for two particle diameters ($d_p = 1\mu m$ and $d_p = 5\mu m$).

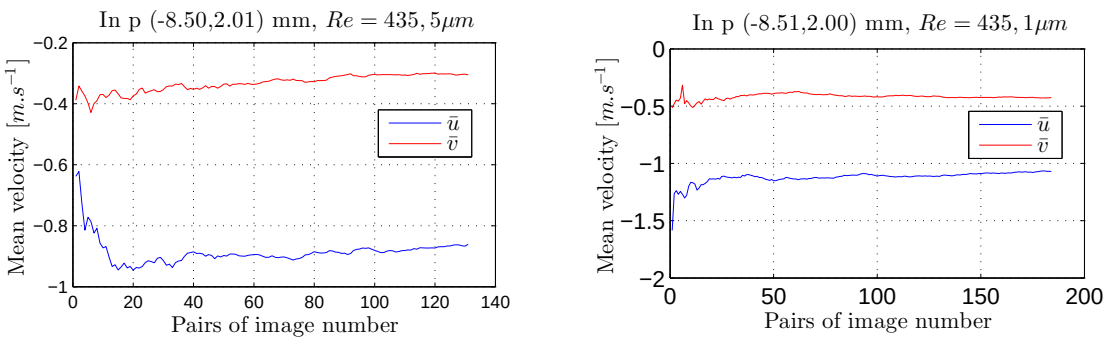

(a) $d_p = 5\mu m$ (b) $d_p = 1\mu m$

Figure A.10: Mean velocities convergence profiles in point $y = 2mm$ along the line 3, $Re = 435$.

Fluctuating velocity second-order moments profiles are, also, plotted for the two particles diameters on the line 3 Fig.A.11. $\overline{u'^2}$ and $\overline{v'^2}$ are superposed for the two particle diameters, in the case of $Re = 863$ whereas, for $Re = 435$, these profiles are higher with $1\mu m$ particles diameter. The same calculation is performed on the fluctuating velocity second order moments. The ratios of fluctuating velocities for $d_p = 1\mu m$ and $d_p = 5\mu m$ are about 1.57,1.55 and 1.28 for $\overline{u'^2}$, $\overline{v'^2}$ and $\overline{u'v'}$ respectively. This can be related to the prediction of mean velocity components shown in Fig.9(e) and to the convergence to their mean values. However, fluctuating velocity second-order moments values are more accurate with $1\mu m$ particle diameter.

Accordingly to this comparative study, one can conclude that the use of $d_p = 1\mu m$ predicts better and accurately the flow inside the labyrinth-channel in comparing with the use of $d_p = 5\mu m$. In order to have a high precision for the prediction of flow quantity and variable, it is advised to perform the micro-PIV acquisition with more pairs of images. Subsequently, micro- PIV acquisitions with 500 pairs of image number using $d_p = 1\mu m$ is performed inside the first three baffles to characterize and visualize with high precision the flow. The largest deviations are obtained at $y = 2\ mm$ in the region where the

streamlines curvature is the strongest. We can conclude that the particles of $5\mu m$ are very large to follow the trajectory curvature. The detailed results in the point $p(-8.51, 2)\ mm$, which is in the mainstream flow where the largest deviation is remarked, is presented in Fig.A.10 and Fig.A.12.

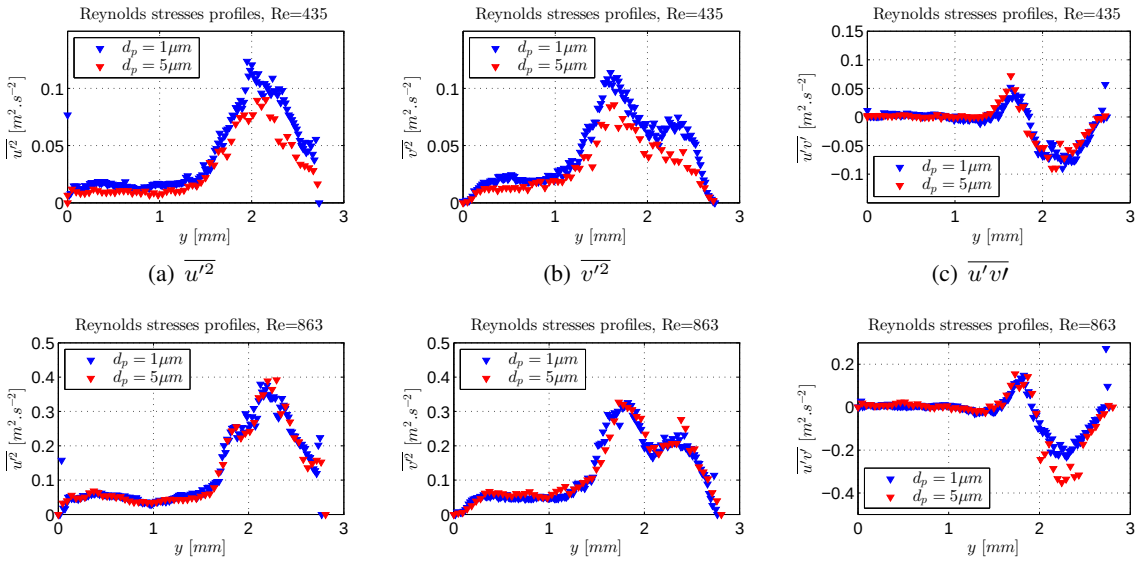

(a) $\overline{u'^2}$ (b) $\overline{v'^2}$ (c) $\overline{u'v'}$

(d) $\overline{u'^2}$ (e) $\overline{v'^2}$ (f) $\overline{u'v'}$

Figure A.11: Fluctuating velocity second-order moments profiles along the line 3, for two particle diameters ($d_p = 1\mu m$ and $d_p = 5\mu m$).

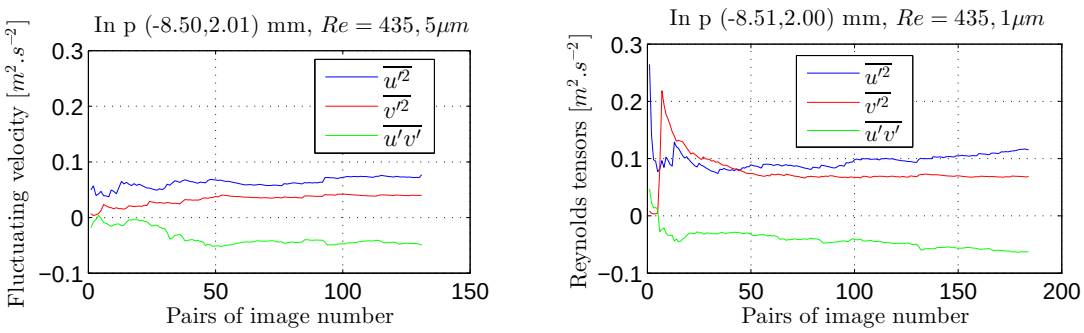

(a) $d_p = 5\mu m$ (b) $d_p = 1\mu m$

Figure A.12: Convergence of fluctuating velocity second order moments in point $y = 2mm$ along the line 3, $Re = 435$.

A.11 Diagram

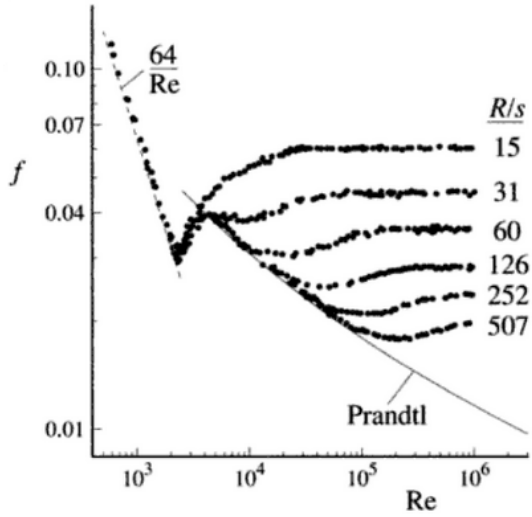

Figure A.13: The friction factor f against the Reynolds number for fully developed flow in pipes of various roughness. (Pope, 2000)[85]

A.12 Friction factor k_f

Table A.1: Friction factor for fully developed laminar flow in pipes with various cross section.

a/b	1	2	3	4	6	8	inf
k_f	56.92	62.20	68.36	72.92	78.80	82.32	96.0

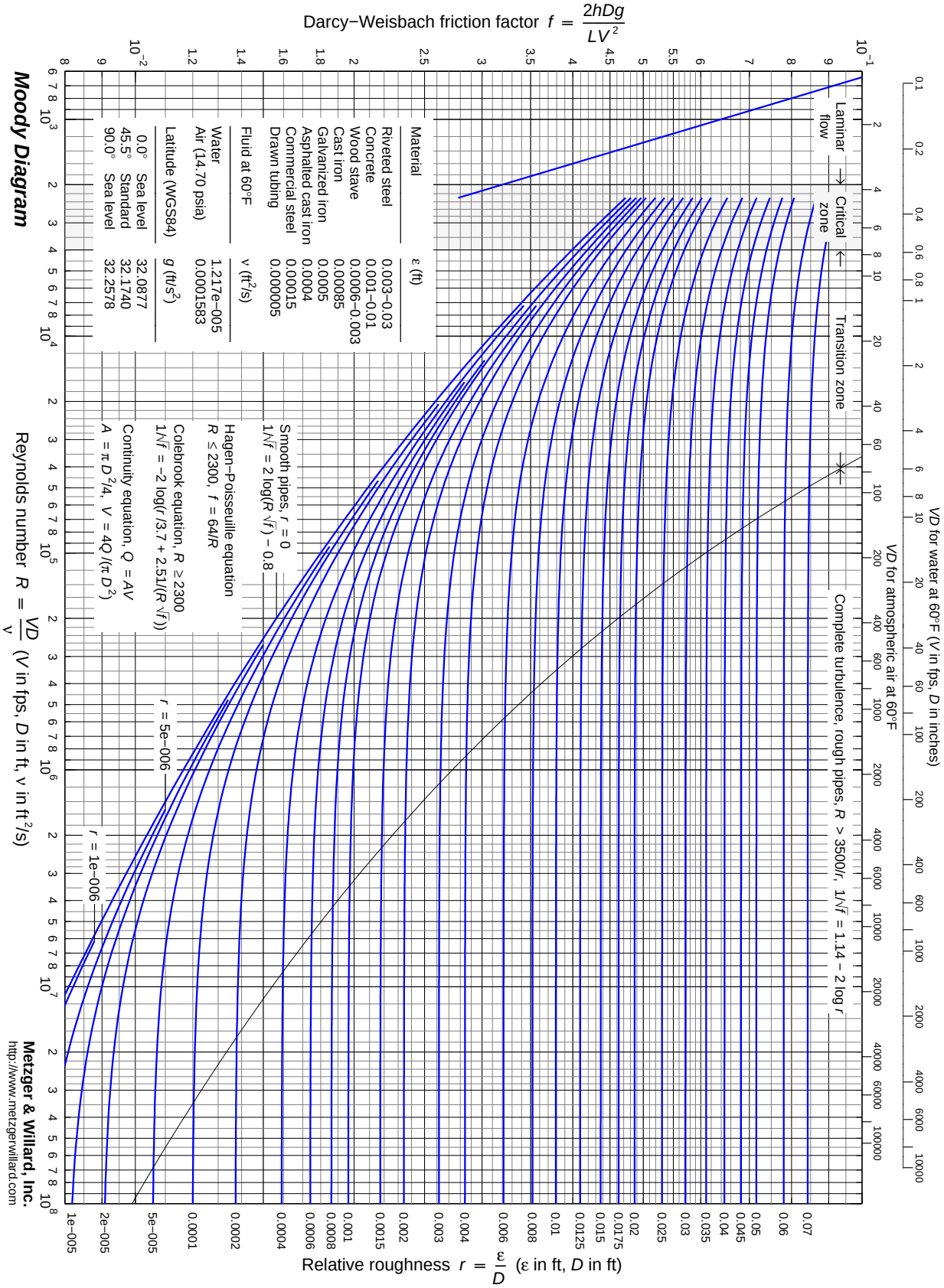

Figure A.14: Moody diagram. Moody (1944) [74]

Bibliography

[1] L'agriculture dans le monde http: //agriculture.gouv.fr/IMG/pdf/HS$_2 6_4 - 5_c le85d799.pdf$. page 21, 23

[2] L'histoire de la micro-irrigation http://www.gardenguides.com/79735-history-drip-irrigation.html. page 25

[3] Abe, K., Kondoh, T., Nagano, Y. (1994) A new turbulence model for predicting fluid flow and heat transfer in separating and reattaching flows-I. Flow field calculations. International Journal of Heat and Mass Transfer. 37: 139-151. page 80

[4] Abid, R. (1991) A modified low-Reynolds-number turbulence model applicable to recirculating flow in pipe expansion. Technical report AIAA-91-a781, AIAA 22nd fluid dynamics, plasma dynamics and laser conference. page 80

[5] Adachi, T., Hasegawa, S. (2006) Transition of the flow in a symmetric channel with periodically expanded grooves. Chemical Engineering Science. 61(8):2721-2729. page 103

[6] Adin, A., Sacks, M. (1991) Dripper Clogging Factors in Wastewater Irrigation. Journal of Irrigation and Drainage Engineering. 117(6):813-826. page 29, 31

[7] Adrian, R. J., Yao, C. S. (1985) Pulsed laser technique application to liquid and gaseous flows and the scattering power of seed materials. Applied Optics. 24(1):44-52. page 191, 193

[8] Adrian, R. J. (1991) Particle-imaging techniques for experimental fluid mechanics. Annual review of fluid mechanics. 23(1):261-304. page 193

[9] Ali, A. A. M.(2013) Anti-clogging drip irrigation emitter design innovation. European International Journal of Science and Technology. 2(8): 154-164. page 34

[10] Al-Muhammad, J., Tomas, S., Anselmet, F. (2016) Modeling a weak turbulent flow in a narrow and wavy channel: cas of micro irrigation. Irrigation Science. 34(5):361-377. page 57

[11] Anselmet, F., Ternat, F., Amielh, M., Boiron, O., Boyer, P., Pietri, L. (2009) Axial development of the mean flow in the entrance region of turbulent pipe and duct flows. Comptes Rendus Mécanique. 337(8):573-584. page 116

[12] Bakker, A. (2002) Lecture 7 – Meshing, Applied Computational Fluid Dynamics. http://www.bakker.org/dartmouth06/engs150/07-mesh.pdf (last accessed: 08.12.16). page 90

[13] Bastiaans, R. J. M. (1993) Cross-correlation PIV : theory, implementation and accuracy.(EUT reports; Vol. 99-W-001). Eindhoven: Technische Universiteit Eindhoven. ISBN: 90-386-2851-X. page 61

[14] Benouniche, M., Kuper, M., Hammani, A., Boesveld, H. (2014) Making the user visible: analysing irrigation practices and farmers' logic to explain actual drip irrigation performance. Irrigation Science. 32(6):405-420. page 28

[15] Bounoua, S. (2010) Étude du colmatage des systèmes d'irrigation localisée. Thèse, Aix Marseille Université. 109p. page 30

[16] Bounoua, S., Tomas, S., Labille, J., Molle, B., Granier, J., Haldenwang, P., Izzati, S. N. (2016) Understanding physical clogging in drip irrigation: in situ, in-lab and numerical approaches. Irrigation Science. 34(4):327–342. page 30

[17] Bralts, V. F., Wu, I. P., Gitlin, H. M. (1981) Drip irrigation uniformity considering emitter plugging. Transactions of the ASAE. 24(5): 1234-1240. page 28

[18] Bucks, D. A., Nakayama, F. S., Gilbert R. G. (1979) Trickle irrigation water quality and preventive maintenance. Agricultural Water Management. 2(2): 149-162. page 30, 31

[19] Burt, C. M., Styles, S. W. (1994) Drip and microirrigation for trees, vines, and row crops. Irrigation Training and Research Center. California Polytechnic State University. San Luis Obispo, CA. 261 p. page 29

[20] Burt, C. M., O'connor, K., Ruehr, T. (1995) Fertigation. Irrigation Training and Research Center. California Polytechnic State Univ. San Luis Obispo, CA. 295 p. page 29

[21] Carpa, A., Scicolone, B. (2004) Emitter and filter tests for wastewater reuse by drip irrigation. Agricultural Water Management. 68(2):135-149. page 31

[22] Carpa, A., Scicolone, B. (2005) Assessing dripper clogging and filtering performance using municipal wastewater. Irrigation and Drainage. 54:71-79. page 31

[23] Chakraborty, P., Balachandar, S., Adrian, R. J. (2005) On the relationships between local vortex identication schemes Journal of Fluid Mechanics. 535:189-214. page 151, 153

[24] Chang, K. C., Hsieh, W. D., Chen, C. S. (1995) A two-equation turbulence model for compressible flows. Journal of fluids Engineering. 117:417-423. page 80

[25] Chassaing, P. (2000) Turbulence en mécanique des fluides. Cépaduès. page 95

[26] Chaudhary, R., Thomas, B. G., Vanka, S. P. (2013) Evaluation of turbulence models in MHD channel and square duct flows. Continuous Casting Consortium Report No. CCC 201011, University of Illinois Urbana-Champaign, IL. page 114

[27] Chen, H. C., Patel, V. C. (1988) Near-wall turbulence models for complex flows including separation. AIAA Journal. 26(6):641-648. page 85

[28] Chengappa, P. G., Nagaraj, N., Kanwar, Ramesh. (2007) International Conference on 21st Century Challenges to Sustainable Agri-Food Systems: biotechnology, environment, nutrition, trade and policy. 15th-17th March, 2007. New Delhi. page 23.

[29] Chou, P. Y. (1945) On velocity correlations and the solutions of the equations of turbulent uctuation. Quarterly of Applied Mathematics 3(1):38–54. page 82.

[30] Christensen, K. T. (2004) The influence of peak-locking errors on turbulence statistics computed from PIV ensembles. Exp. Fluids 36: 484-497. page 68

[31] Compaoré, M. L. (2006) Panorama des techniques d'irrigation et éléments de choix. In : Tiercelin J.-R. Vidal A., eds. Traité d'irrigation. 2e éd. Paris : Lavoisier, 489-512. page 25

[32] Dacles-Mariani, J., Zilliac, G. G., Chow, J. S., Bradshaw. P. (1995) Numerical/Experimental Study of a Wingtip Vortex in the Near Field. AIAA Journal, 33(9):1561-1568. page 78

[33] Daly, B. J., Harlow, F. H. (1970) Transport equations in turbulence. Phys Fluids 13:2634–2649. page 82

[34] Dazhuang, Y., Peiling, Y., Shumei, R., Yunkai, L., Tingwu, X. (2007) Numerical study on flow property in dentate path of drip emitters. New Zealand Journal of Agricultural Research. 50:705-712. page 40, 37, 37

[35] DehghaniSanij, H., Yamamoto, T., Rasiah, V., Utsunomiya, J., Inoue, M. (2004) Impact of biological clogging agents on filter and emitter discharge characteristics of microirrigation systems. Irrigation and drainage. 53(4):363-373. page 31

[36] Dosoretz, C., Tarchitzki, J., Katz, I., Kenig, E., Chen, Y. (2011) Development and effects of fouling layer in distribution and irrigation systems applying treated wastewater effluents. In: Levy G, Fine P, Bar-Tal A (eds) Use of treated sewage water in agriculture: impacts on crops and soil environment. Blackwell Publishing, Oxford, pp 328–350. page 28

[37] Dubief, Y., Delcayre, F. (2000) On coherent-vortex identification in turbulence. Journal of Turbulence 1:1-22. page 153

[38] Fu, S., Launder, B. E., Leschziner, M. A. (1987) Modelling strongly swirling recirculating jet flow with Reynolds-stress transport closures. In sixth symposium on Turbulent Shear Flows, Toulouse, France. page 82

[39] Gamri, S., Soric, A., Tomas, S., Molle, B., Roche, N. (2014) Biofilm development in microirrigation emitters for wastewater reuse. Irrigation Science. 32(1):77-85. page 29, 29

[40] Gibson, M. M., Launder, B. E. (1978) Ground effects on pressure fluctuations in the atmospheric boundary layer. J. Fluid Mech. 86:491–511. page 82

[41] Gilbert, R. G., Nakayama, F. S., Bucks, D. A., French, O. F., Adamson, K. C. (1981) Trickle irrigation: emitter clogging and other flow problems. Agricultural Water Management. 3(3):159-178. page 28, 30, 29

[42] Goodman, J. W. (2004): Introduction to Fourier optics, Roberts Company Publishers, Greenwood village. page 192

[43] Green, M.A., Rowley, C. W., Haller, G.(2007) Detection of Lagrangian coherent structures in three-dimensional turbulence. J. Fluid Mech. 572: 111-120. page 152, 153

[44] Häfeli, R., Altheimer, M., Butscher, D., Rudolf von Rohr, P. (2014) PIV study of flow through porous structure using refractive index matching. Experiments in Fluids 55:1717. page 121

[45] Haller, G. (2005) An Objective Definition of a Vortex. J. Fluid Mech. 525:1-26. page 151

[46] Hanjalic, K., Launder, B.E. (2011) Modelling turbulence in engineering and the environment. Cambridge University Press. page 85

[47] Harley, J. C., Huang, Y., Bau, H., Zemel, J. (1995) Gas flow in micro-channels. Journal of Fluid Mechanics. 284:257-274. page 34

[48] Hills, D. J., Nawaar, F. M., Waller, P. M. (1989) Effects of chemical clogging on drip-tape uniformity. Transactions of the ASAE. 32(4):1202-1206. page 29

[49] Hinze, J. O. (1975) Turbulence. McGraw-Hill Publishing Co. edition 2. page 76

[50] Hunt, J. C. R., Wray, A. A., Moin, P. (1988) Eddies, stream, and convergence zones in turbulent flows. Center for Turbulence Research. Report CTR-S88:193-208. page 152

[51] Huser, A., Biringen, S. (1993) Direct numerical simulation of turbulent flow in a square duct. Journal of Fluid Mechanics. 257: 65-95. page 118

[52] Jeong, J., Hussain, F. (1995) On the identicaiton of a vortex. Journal of Fluid Mechanics. 285:69-94. page 151

[53] Kandilikar, S. G., Joshi, S., Tian, S. (2003) Effect of surface roughness on heat transfer and fluid flow character at low Reynolds numbers in small diameter tubes. Heat Transfer Eng. 24(3):4–16. page 34

[54] Karmeli, D. (1977) Classification and flow regime analysis of drippers. Journal of Agricultural Engineering Research. 22: 165-173. page 27, 28, 102

[55] Karvinen, A., Ahlstedt, H. (2005) Comparison of turbulence models in case of jet in crossflow using commercial CFD code. Engineering Turbulence Modeling and Experiments. 6:399-408. page **??**

[56] Khan, F. R., Rielly, C.D., Brown, D. A. R. (2006) Angle-resolved stereo-PIV measurements close to a down-pumping pitched-blade turbine. Chemical Engineering Science 61(9):2799-2806. page 140

[57] Kida S., Miura, H. (1998) Identication and Analysis of Vortical Structures. Eur. J. Mech. B/Fluids. 17(4): 471-488. page 149

[58] Kim, J., Moin, P., Moser, R. (1987). Turbulence statistics in fully developed channel flow at low Reynolds number. Journal of Fluid Mechanics. 177:133-166. page 118, 119, 134, 145

[59] Knudsen, J. G., Katz, D. L. (1958) Fluid dynamics and heat transfer. New York, McGraw-Hill. page 84

[60] Kolàr, V. (2007) Vortex identication: New requirements and limitations. International Journal of Heat and Fluid ow. 28:638-652. page 152, 152

[61] Kumar, B. V. K. V., Hassebrook, L. (1990) Performance measures for correlation filters. Applied Optics.29(20):2997-3006. page 70

[62] Lankford, B., Mdemu, M., Machibya, M. (2004) Draft Irrigation Efficiency and Productivity Manual. International Water Management Institute. Private Bag X 813 Silverton 0127, South Africa. page 24

[63] Launder, B. E. (1989) Second-moment closure and its use in modelling turbulent industrial flows. International Journal for Numerical Methods in Fluids. 9(6):963-985. page 82

[64] Launder, B. E., Jones, W. P. (1972) The prediction of laminarization with a two-equation model of turbulence. International Journal of Heat and Mass Transfer. 15:301-314. page 79

[65] Launder, B. E., Sharma, B. I. (1974) Application of the energy-disssipation model of turbulence to the calculation of flow near a spinning disc. Lett. Heat Mass Transfer. 1:131-138. page 80

[66] Launder, B. E., Spalding, D. B. (1972) Lectures in mathematical models of turbulence. Academic Press. London, New York. page 79, 195

[67] Launder, B. E., Spalding, D. B. (1974) The numerical computation of turbulent flows. Computer Methods in Applied Mechanics and Engineering. 3(2):269-289. page 79, 84, 194

[68] Lauterborn, W., Kurz, T., Wiesenfeldt, M. (1995) Coherent optics:Fundamentals and applications. Springer-Verlag Berlin Heidelberg. page 192

[69] Levy, G., Fine, P., Bar-Tal, A. (2011) Treated Wastewater in Agriculture: Use and impacts on the soil environments and crops. Wiley-Blackwell.446 p. page 30

[70] Li, Y., Yang, P., Xu, T., Ren, S., Lin, X., Wei, R., Xu, H. (2008) CFD and digital particle tracking to assess flow characteristics in the labyrinth flow path of a drip irrigation emitter. Irrigation Science. 26(5):427-438. page 165

[71] Lien, F. S., Leschziner, M. A. (1994) Assessment of turbulence-transport models including non-linear rng eddy-viscosity formulation and second-moment closure for flow over a backward-facing step. Computers Fluids 23(8):983-1004. page 82

[72] Liu, H. S., Li, Y. K., Liu, Y. Z., Yang, P. L., Ren, S. M., Wei R. J., Xu, H. B. (2010) Flow characteristics in energy dissipation units of labyrinth path in the drip irrigation emitters with DPIV technology. Journal of Hydrodynamics, Ser. B 22(1):137-145. page 35, 36, 38, 39

[73] Merkley, G. P., Allen, R. G. (2003) Sprinkle and trickle irrigation lecture notes (BIE 5110/6110). Dept. of Biological and Irrig. Engrg., Utah State Univ., Logan, UT. page 25, 28

[74] Moody, L. F. (1944) Friction factors for pipe flow. Transactions of the ASME 66(8): 671–684. page 204

[75] Nakayama, F. S., Bucks, D. A. (1981) Emitter clogging effects on trickle irrigation uniformity. Trans American Society of Agricultural and Biological Engineers. 24(1):77-80. page 28

[76] Nakayama, F. S., Bucks, D. A. (1986) Trickle Irrigation for Crop Production: Design, Operation and Management. Developments in Agricultural Engineering 9. Elsevier Science. New York. 383 pp. page 29

[77] Nakayama, F. S., Bucks, D. A. (1991) Water quality in drip/trickle irrigation: a review. Irrigation Science. 12(4):187-192. page 30

[78] Nishimura, T., Ohori, Y., Kawamura Y. (1984) Flow characteristics in a channel with symmetric wavy wall for steady flow. Journal of Chemical Engineering of Japan. 17:466-471. page 34

[79] Offutt, P. W. (1995) Development of experimental technique and studies of spatial structure in turbulent thermal convection. PhD thesis, University of Illinois, Urbana, Illinois. page 194

[80] Ozekici, B., Sneed, R. E. (1995) Anaysis of pressure losses in tortuous path emitters. ASAE meeting Paper. No.912155. page 165

[81] Palau Salvador, G., Arviza Valverde, J., Bralts, V. F. (2004) Hydraulic flow behavior through an in-line emitter labyrinth using CFD techniques. ASAE/CSAE Annual International Meeting. Paper Number: 042252 Ottawa, Ontario, Canada. page 34

[82] Pfahler, J., Harley, J., Bau, H. H., Zemel, J. (1990) Liquid and gas transport in small channels. AMSE DSC. 19:149-157. page 34

[83] Philipova, N., Nikolov, N., Pichurov, G., Markov. (2009) A mathematical model of emitter discharge depending on geometric parameters of drip emitter labyrinth channel. Proceedings of the 11th National Congress on Theoretical and Applied Mechanics. 2-5 Sept. 2009, Borovets, Bulgaria (CD-ROM). pp. 1-6. page 34

[84] Pitts, D. J., Haman, D. Z., Smajstria, A. G. (1990) Causes and prevention of Emitter plugging in Mico irrigation Systems. Bulletin 258. Florida Cooperative Extension Service. Institute of Food and Agricultural Sciences. University of Florida. page 30

[85] Pope, S. B. (2000) Turbulent flows. Cambridge university press. page 33, 75, 101, 106, 142, 145, 196, 203

[86] Prasad, A. K., Adrian, R. J., Landreth, C. C., Offutt, P. W. (1992) Effect of resolution on the speed and accuracy of particle image velocimetry interrogation. Experiments in Fluids. 13(2):105-116. page 193

[87] Press, W. H., Teukolsky, S.A., Vetterling, W.T., Flannery, B.P. (1992) Numerical Recipes in FORTRAN. The Art of Scientific Computing. Second Edition. Cambridge University Press. page 61

[88] Puig-Bargués, J., Arbat, G., Barragan, J., Ramirez de Cartagena, F. (2005) Hydraulic performance of drip irrigation subunits using WWTP effluents. Agricultural Water Management. 77(1-3):249–262. page 30, 31

[89] Raffel, M., Christian, E., Willert S. T., Wereley J. (2007) Particle Image Velocimetry A Practical Guide. Springer. édition 2. page 45, 46, 192, 193, 194

[90] Rav-Acha, C., Kummel, M., Salamon, I., Adin, A. (1995) The effect of chemical oxidants on effluent constituents for drip irrigation. Water Research. 29(1): 119-129. page 31

[91] Ravina, I., Paz, E., Sofer, Z., Marcu, A., Shisha, A., Sagi, G. (1992) Control of emitter clogging in drip irrigation with reclaimed wastewater. Irrigation Science. 13(3):129-139. page 31

[92] Ravina, I., Paz, E., Sofer, Z., Marm, A., Schischa, A., Sagi, G., Yechialy, Z., Lev, Y. (1997) Control of clogging in drip irrigation with stored treated municipal sewage effluent. Agricultural Water Management. 33(2):127-137. page 31

[93] Reynolds, O. (1895) On the Dynamical Theory of Incompressible Viscous Fluids and the Determination of the Criterion. Philosophical Transactions of the Royal Society of London. A, 186:123-164. page 75

[94] Rieul, L., Ruelle, P. (2003) Guide Pratique. Irrigation. 3rd edition. Paris: Cemagref. page 26, 28

[95] Santiago, J. G., Wereley, S. T., Meinhart, C. D., Beebe, D. J., Adrian, R. J. (1998) A micro particle image velocimetry system. Experiments in Fluids. 25: 316-319. page 45

[96] Shiklimanov, I. A. (2000) World water resources at the beginning of the 21st century. Summary of the monograph. IHP Unesco. page 22

[97] Spalart, P., Allmaras, S. (1992) A one-equation turbulence model for aerodynamic flows: Technical report. American Institute of Aeronautics and Astronautics. page 77

[98] Sparrow, E. M., Lin, S. H. (1964) The Developing Laminar Flow and Pressure Drop in the Entrance Region of Annular Ducts. ASME. J. Basic Eng. 86(4):827-833. page 114, 116, 118

[99] Üzen, N., Çetin, O., Karaer, M. (2013) The Role of Micro Irrigation for Modern Agriculture. http://www.researchgate.net/publication/259744265. page 25

[100] Vickers, A. (2002) Water Use and Conservation. Amherst, MA Waterplow Press. 43. page 23

[101] Wei, Q., Shi, Y., Dong, w., Lu, G., Huang, S. (2006) Study on hydraulic performance of drip emitters by computational fluid dynamics. Agricultural Water Management. 84(1-2):130-136. page 34, 35, 36, 101, 105, 165

[102] Wei, Z., Cao, M., Liu, X., Tang, Y., Lu, B. (2012) Flow behaviour analysis and experimental investigation for emitter micro-channels. Chinese Journal of Mechanical Engineering. 25(4):729-737. page 34, 35, 39, 165

[103] Wernet, M. P. (2000) Development of digital particle imaging velocimetry for use in turbomachinery. Experiments in Fluids. 28(2):97-115. page 197

[104] Westerweel, J. (2000) Theoretical analysis of the measurement precision in particle image velocimetry. Experiments in Fluids. Springer-Verlag. 29(Suppl 1):S003-S012. page 68

[105] White, F. M. (2010) Fluid Mechanics (7th Edition). McGraw-Hill. page 55, 83, 95, 102, 103, 114

[106] Wolfshtein, M. (1969) The velocity and temperature distribution in one-dimensional flow with turbulence augmentation and pressure gradient. International Journal of Heat and Mass Transfer. 12(3):301-318. page 85

[107] Wu, D., Li, Y. k., Liu, H. S., Yang, P. L., Sun, H. S., Liu, Y. Z. (2013) Simulation of the flow characteristics of a drip irrigation emitter with large eddy methods. Mathematical and Computer Modelling. 58(3-4):497-506. page 34

[108] Xue, Z., Charonko, J. J., Vlachos, P. P. (2013) Signal-to-noise ratio, error and uncertainty of PIV measurement. Conference proceedings. 10th Int. Symp. Particle Image Velocimetry (PIV). pp.1-18. page 70

[109] Yakhot , V., Orszag, S. A. (1986) Renormalization group analysis of turbulence. I. Basic theory. Journal of Scientific Computing. 1(1):3-51. page 79

[110] Zhang, J., Zhao, W., Wei, Z., Tang, Y., Lu, B. (2007) Numerical investigation of the clogging mechanism in labyrinth channel of the emitter. International Journal for Numerical Methods in Engineering. 70:1598-1612. page 34, 35, 165

[111] Zhang, J., Zhao, W., Tang, Y., Lu, B. (2010) Anti-clogging performance evaluation and parameterized design of emitters with labyrinth channels. Computers and Electronics in Agriculture. 74(1):59-65. page 34

[112] Zhang, J., Zhao, W., Tang, Y., Lu, B. (2011) Structural optimization of labyrinth-channel emitters based on hydraulic and anti-clogging performances. Irrigation Science. 29(5): 351-357. page 15, 104

[113] Zhang, J., Zhao, W., Lu, B. (2013) Rapid Prediction of Hydraulic Performance for Emitters with Labyrinth Channels. Journal of Irrigation and Drainage Engineering. 139(5):414-418. page 104